Improving the Figure of Merit in N-Type Thermoelectric Oxides Using Low Temperature Synthesis and Cold Sintering

Stephanie Mudd

A thesis submitted in partial fulfilment of the degree of
Doctor of Philosophy

Supervisors:
Primary – Dr Rebecca Boston
Secondary – Professor Derek Sinclair

The University of Sheffield
Faculty of Engineering
Department of Materials Science and Engineering

October 2023

Abstract

Thermoelectric materials convert heat directly into electricity according to the Seebeck effect. Thermoelectric generators (TEGs) use two types of TE materials: n-type (electron dominated conductor) and p-type (hole dominated conductor) to increase the efficiency of electricity generation from a given temperature gradient. High electrical and low thermal conductivities are required to enhance the figure of merit, ZT. These characteristics are often mutually exclusive in naturally occurring materials. Some p-type materials have been found with greater than unity ZT however, current n-type materials are seriously underperforming their p-type counterparts. This work shows a study of two methods designed to enhance ZT in an n-type oxide by reducing thermal conductivity. These are: controlled impurities to enhance phonon scattering and a novel cold sintering method designed for complex stoichiometry oxides with incongruent dissolution rates which allows nano-scale grains to be retained in a sintered ceramic, increasing the density of grain boundaries which scatter phonons. Nanoscale particles are produced using by ionic liquid synthesis method, what's more a new compositional series was made using this method: $La_{0.15-x}Eu_xSrTiO_3$. The results demonstrate the cooperative fine tuning of thermoelectric properties to improve ZT. The initial densities of ceramics made using the novel cold sintering method are relatively low, ~55%, but this technique has the potential to be greatly improved. These results show novel compositions and methods which make incremental steps towards improving the efficiency of TEGs, in order to begin recuperating some of the 72% of primary energy lost globally in the form of waste heat.

Acknowledgements

Table of Contents

Thesis Structure

This thesis begins with an introduction to relevant scientific theories and published research which contextualise the experimental chapters. The methodology then describes the techniques used to synthesise and characterise materials throughout this work. The experimental work is separated into three distinct chapters: Ionic Liquid Synthesis of Lanthanum-Doped Strontium Titanate, Europium Doping of Lanthanum Strontium Titanate and Novel Cold Sintering Method. These chapters are self-contained with their own aims, objectives, introduction, results, discussions, conclusions and references.

Chapter three covers the initial synthesis of Lanthanum doped, A-site deficient strontium titanate (LST) using the ionic liquid method and comparing the product to that of the same composition made using the conventional solid state synthesise which usually requires a temperature upwards of 1000 ℃. The main reasons for using a low temperature synthesis method was to reduce the grain size of the LST and reduce the embodied energy of this material which would not only help to improve the thermoelectric performance of the material (if the small grain size could be retained in a sintered product) but would also reduce the environmental impact of ceramic synthesis.

Chapter four covers a compositional series introducing europium doping into LST. This present a novel combination of dopants in strontium titanate which would aim to reduce the thermal conductivity through scattering caused by mass fluctuation on the A-site. A low thermal conductivity must be coupled with a high powder factor and so the electronic properties were also investigated to calculate the thermoelectric figure of merit for each composition in the series.

Chapter five introduces a novel take on the Cold Sintering Process, in which ceramics are sintered at temperatures < 300 ℃. This novel method was inspired by the ionic liquid synthesis method and Reactive Cold Sintering. In this chapter the initial development of the novel process is detailed in which the density/ porosity was examined. Key findings from the previous two chapters on the nature of the ionic liquid synthesised LST and the inherent impurities were integrated into the examination of the bulk ceramics to determine densification mechanisms and potential improvements.

1.0 Literature Review

1.1 Thermoelectric Principles

The depletion of fossil fuels and rising CO_2 levels are a well-known crisis in our society, with increasing urgency we look to increase the sustainability of our practises and halt the rise in global temperatures. A lesser known aspect of this crisis, is that two thirds of the energy converted from our primary sources (petroleum, coal, natural gas etc.) is lost as heat.[1] Not only do we need to look for renewable sources of our energy but we must learn to use our resources more efficiently. Thermoelectric generators (TEGs) are able to recapture waste heat and convert this directly into usable electricity in an emission free process. Furthermore, with no moving parts TEGs are a reliable and scalable solution to tackle the waste heat crisis.

TEGs are already used in deep space probes (e.g. Cassini mission to Saturn) in the form of Radioisotope Thermoelectric Generators(RTGs), where decaying radioactive materials are the heat source and the TEG converts this into electricity.[2] The current state of the art thermoelectric materials (chalcogenides) are expensive and toxic materials, which is acceptable for RTG applications, however to open up the use of TEGs into commercial and domestic applications their cost and toxicity must be reduced. Currently the search is on to provide low cost, highly efficient and sustainable alternatives.

1.1.1 Discovering Thermoelectricity

In 1821, Thomas Seebeck observed that the needle of a compass moved when the junctions of two dissimilar metals were held at different temperatures. Seebeck initially termed this effect 'thermo-magnetism', though it is now known as the thermoelectric effect.[3,4] This effect is observed when a potential difference is generated due to a temperature gradient. It is now known that what Seebeck observed was a magnetic field generated by the flow of electricity across the two junctions, due to the thermoelectric effect.[5]

When a temperature gradient is present the majority charge carriers will move from the hot to cold side, which leads to a potential difference between the two sides. Two types of charge carries are defined: electrons and holes (holes being considered the absence of an electron) allowing the separation of two types of thermoelectric materials. For *n*-type materials electrons are the majority carrier and for *p*-types holes are the majority carrier.[6]

A thermoelectric generator (TEG) utilizes both *n*-type and *p*-type 'legs' thermally in parallel, electrically in series between a hot and cold contact (Figure 1.1.1) to create a current from which heat energy can be converted to electricity then stored or immediately utilised. For example, the cold contact could be attached to a water-cooling system and the hot contact could be attached the external face of a tail pipe in a combustion engine.[7]
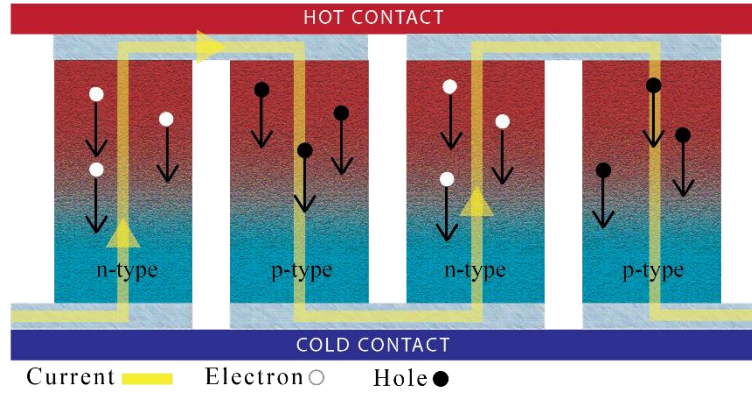
Figure 1.1.1 Schematic of thermoelectric device showing current flow in thermoelectric 'legs' between a hot and cold contact.

The maximum conversion efficiency of a thermoelectric device is given in Equation 1.1.1.[8] This is ultimately limited by the temperature differential between the hot and cold contacts and the thermoelectric of merit, ZT, of the *n* and *p* components.

$$\eta_{max} = \frac{\sqrt{1+ZT}-1}{\sqrt{1+ZT}+\frac{T_C}{T_H}} \frac{T_H-T_C}{T_H} \qquad Eqn.\ 1.1.1$$

ZT is a dimensionless figure of merit which is determined by the materials electrical and thermal properties, shown in Equation 1.1.2. Where *S* is the Seebeck coefficient (V/K), σ is the electrical conductivity (S/m), *T* is the absolute temperature (K) and κ is the thermal conductivity (W/mK).

$$ZT = \frac{S^2\sigma T}{K} \qquad Eqn.\ 1.1.2$$

In order for a material to generate the largest potential across the thermal gradient, the charge carriers must move unimpeded through the material whilst heat transfer is minimal to maintain the temperature gradient. In 1995, Glen Slack termed a phonon-glass electron-crystal (PGEC), which is a material with the high electrical conductivity of a crystal and low thermal conductivity of glass and therefore an extremely high ZT.[9,10] For this technology to be commercially viable it is necessary for TE materials to have a ZT > 3 in order to compete with other energy recovery technologies. [11,12]

Part of the numerator in Equation 1.1.2, $S^2\sigma$, is known as the power factor, which describes the electronic characteristics of the material. Due to the interdependencies of S, σ and κ, which will be discussed in this section and throughout the literature survey, no one naturally-occurring material possessing all the desirable properties is currently known, therefore strategic materials engineering is required to achieve optimisation.[13,14]

The band structure of a material is an important factor, as this determines the environment in which the charge carriers flow, and so has a large impact on the power factor. Band theory is a popular theory to predict the conduction behaviour of insulators, semiconductors and metals.[15]

Both the position and momentum of an electron are impossible to determine due to the interaction of our observing instruments and the electrons. Therefore, we refer to electron densities which describe the possibility of an electron being in a particular space.[15]

In an atom an electron resides in an orbital. When a covalent bond forms between two atoms, the orbitals overlap and form molecular orbitals. In 3D materials this idea can be extended until a continuum of energy levels form bands: a valance band, and a conduction band at a higher energy level.[15]

In semiconductors, at 0 K, there is a full valence band and an empty conduction band between which there is an area of forbidden energy, the band gap. In insulators the band gap is much larger. Metals are represented by a partially filled band, or overlapping valence and conduction bands.[15]

The fermi energy is the highest filled energy level at 0 K. Electrons in the vicinity of the fermi level are of particular importance as these are the electrons which generally can be induced to take part in electrical conduction. The fermi level can change position with temperature and level of doping.[15]

This is a highly simplified way to look at the electronic structure of the material. In fact, within a band there are variations in the density of states (available sites for electrons to occupy) due to the specific chemical and crystal structures. Density Functional Theory (DFT) modelling looks further into this, mapping the density of states for a specific material in order to predict its electronic properties.[16–18]

1.1.2 Seebeck Coefficient

The Seebeck coefficient is a measure of the potential difference, ΔV, generated per unit temperature, T, shown by Equation 1.1.3. The larger the potential generated by a material the larger the Seebeck coefficient; the square of the S is directly correlated to ZT. This potential is generated by a majority charge carrier of holes or electrons, so the sign of the Seebeck reflects which type of conduction the material possesses. *n*-type materials have a majority of electron charge carriers and so the Seebeck coefficient is negative, whereas *p*-type materials have a majority of hole charge carriers so the Seebeck coefficient is positive. Current flows in opposing directions in these two materials and so the potential sign reverses from *p*-type to *n*-type.

$$S = \frac{\Delta V}{\Delta T} \qquad \textit{Eqn. 1.1.3}$$

$$S = \frac{8\pi^2 k_B^2 T}{3eh^2} m^* \left(\frac{\pi}{3n}\right)^{2/3} \qquad \textit{Eqn. 1.1.4}$$

Equation 1.1.4 can be used to further understand the factors affecting the Seebeck coefficient. Where k_B is the Boltzmann constant, T is temperature in Kelvin, m^* is the effective mass of charge carriers, h is Plank's constant, n is the carrier concentration, and e is the electron charge. [19,20]

Therefore, three important values can be extracted which strongly affect the Seebeck coefficient. These are: the absolute temperature, the effective mass and the charge carrier concentration.

The Seebeck coefficient is directly proportional to the effective mass. The effective mass describes ability of the outermost electrons, those which take part in conduction, to travel through the lattice. It takes into account not only the mass of the electron but the effect of the surroundings, the band, on the electron. A large effective mass will also lower charge carrier mobility, which also reduces the electrical conductivity.[21]

The effective mass is dependent on the density of states (DOS). Sharp gradients in the DOS map lead to a large effective mass. A large number of energy levels occupying a very small energy range increases the effective mass, which can be caused by a highly symmetrical crystal structure inducing degenerate energy levels, or an impurity band introduced by dopants (this is also referred to as a resonant level).[13] Manipulating the band structure in this way is called band convergence, Pei *et al.* used this technique in PbTe by alloying with MgTe which converged the valence band at low temperatures which gave them a 40 % increase in the ZT.[22]

On the other hand, the Seebeck coefficient is decreased by a large number of charge carriers. In a very highly electrically conductive material such as a metal, the Seebeck values are typically around 10 μV/K due to the large number of charge carriers.[23] Insulators, with the lowest amount of charge carriers (usually only from small levels of impurities) typically have a Seebeck coefficient greater than 200 μV/K. A semiconductors Seebeck coefficient lies somewhere between the two. Figure 1.1.2 shows how the Seebeck coefficient decreases with an increase in charge carrier.[23]

Typically, in a semiconductor due to thermal excitation the number of charge carriers increases with temperature, therefore the absolute Seebeck coefficient reduces with an increase in temperature.
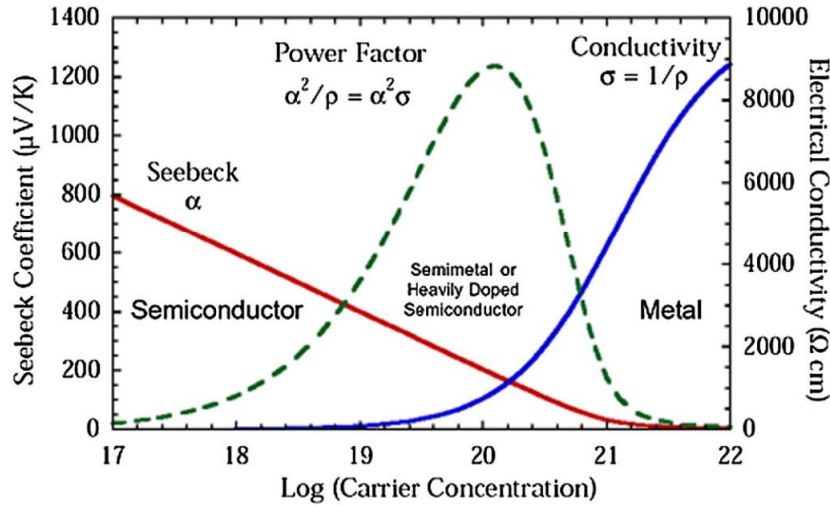
Figure 1.1.2 Seebeck and electrical conductivity versus carrier concentrations from Gayner.[23]

1.1.3 Electrical Conductivity

The electrical conductivity is determined by the electron mobility, μ, the number of charge carriers, n and the charge of the charge carrier, q according to Equation 1.1.5.

$$\sigma = nq\mu \qquad\qquad Eqn.\ 1.1.5$$

The Mott transition is the transition between insulator and metallic conduction behaviour, which occurs when the carrier concentration exceeds a value n_e, according to Equation 1.1.6. Where n_e is the electron carrier concentration and a_0 is the Bohr radius of the carrier and dopant. For oxygen deficient STO the Mott criterion is $\sim 1 \times 10^{18}\ cm^{-3}$.[24]

$$n_e^{1/3}.a_0 \sim 0.25 \qquad\qquad Eqn.\ 1.1.6$$

Both the lattice itself and any impurities present, or purposefully added (dopants), can scatter electrons which reduces the mobility of charge carriers and therefore the electrical conductivity.

A semiconductor or small band gap insulators' electrical conductivity will increase with temperature as thermal energy provides enough energy for electrons to overcome an activation energy and take part in conduction. Whereas, a metal's electrical conductivity will decrease with increasing temperature, as all the electrons in a metallic structure are free to take part in conduction at all temperatures. However, the level of scattering increases with temperature and so interactions between electrons and phonons cause a decrease in electrical conductivity.

Muta *et al.* found that for single crystals of $EuTiO_3$, $SrTiO_3$ and $CaTiO_3$, doped with lanthanum, the electrical conductivities all decreased with temperature between 300 and 900 K so that $\sigma \propto T^{-x}$. This is because the conductivity is dominated by the charge mobility, μ, in this region and $\mu \propto T^{-x}$. At lower temperatures (300-500K) the T exponent of the electrical conductivities reduction was -2.7, indicating optical phonon-electron scattering. At higher temperatures (500- 900K) the T exponent was -1.6 which is caused by dominant acoustic phonon-electron scattering according to their findings.[25] See the section entitled 'Thermal Conductivity' for a description of the two phonon-electron scattering modes. The electrical conductivity-temperature behaviour of single crystal and polycrystalline $La_{0.003}Sr_{0.997}TiO_{3-\delta}$ normalised for charge carrier density, *n*, and elementary charge, *e* are given in Figure 1.1.3. [26] Moos *et al.* proposed that acceptor type stated exist on the surface of the grains which trap the conduction electrons from the adjacent grains, reducing the electrical conductivity. [26]
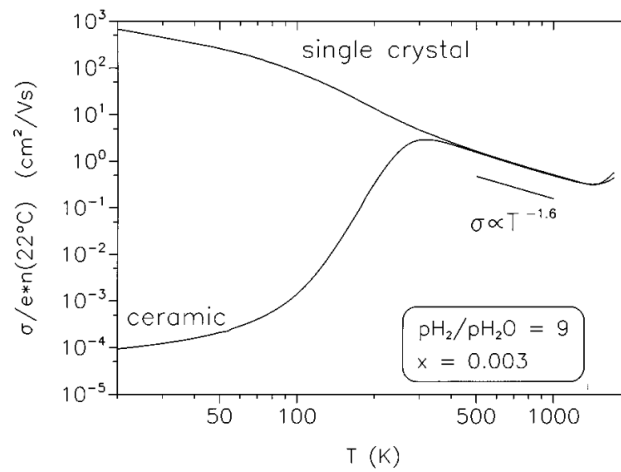
Figure 1.1.3 Electron mobility as a function of temperature for single crystal and polycrystalline $La_{0.003}Sr_{0.997}TiO_{3-\delta}$ normalised for charge carrier density, n, and elementary charge, e.

1.1.4 The Power Factor

The power factor is a useful metric summarising electronic properties of the material, and is the numerator of the ZT equation. It is calculated using Equation 1.1.7 from the Seebeck coefficient, S, and the electrical conductivity, σ. It is particularly useful when trading off Seebeck coefficients and the electrical conductivity during band engineering to determine what level of doping *etc.* will ultimately lead to the highest ZT.

$$PF = S^2\sigma \qquad \textit{Eqn. 1.1.7}$$

Consider a semiconductor at room temperature in which the fermi level lies between the conduction and the valence band. When the fermi level is in the centre of the band gap the Seebeck coefficient is maximized as the number of charge carriers is almost zero. However,

this region has a low electrical conductivity due to low to no charge carriers, so the power factor is not maximized.

The charge carrier concentrations are clearly largest when the fermi level is within the conduction band- as is the case with metals. Metals have a large electrical conductivity but low Seebeck coefficients due to overly the large number of charge carriers.

Therefore, the ideal position for the fermi level, to achieve a high power factor, is on the band extrema where there is a sharp change in the density of states. Here the effective mass is large (leading to high Seebeck coefficient), and a small temperature increase can allow high energy electrons to take part in conduction. This can be achieved by careful defect engineering and/or doping of semiconductors.

Of course the temperature also affects the position of the fermi level so that the power factor changes with temperature. Therefore, the material will also have an optimal temperature window where the power factor is maximized. Typically, in *n*-type systems the fermi level moves further to the conduction band, and in *p*-type systems the fermi level will move towards the valence band with an increase in temperature.

In order to maximize the power factor, the ideal charge carrier concentration depends on the material (as effective mass and mobility change) though the ideal concentration is between 10^{19} and 10^{21} carriers/cm^3. This is lower than those of typical metals and higher than that found in typical semiconductors which is why heavily doped semiconductors are ideal thermoelectric materials.[27]

Wei *et al.* showed an example of fermi level optimization for *p*-type GeTe.[28] For pristine GeTe the fermi level lies deeply into the valence band where the carrier concentration is ~ 8.7 x10^{20} cm^{-3}. This results in a very low Seebeck coefficient of ~ 25 µV/K. By doping GeTe with Bi the fermi level can be moved to a higher energy, towards the edge of the valence band to improve the power factor. $Ge_{0.88}Bi_{0.12}Te$ has a reduced carrier concentration of 7 x10^{19} cm^{-3} and a much larger Seebeck coefficient of 150 µV/K. The power factor is maximized by a trade-off between carrier concentration and Seebeck leading to the highest value for $Ge_{0.94}Bi_{0.06}Te$ which was ~ 4.5 mW/mK^2.[28]

1.1.5 Thermal Conductivity

$$\mathrm{K}_{tot} = \mathrm{K}_e + \mathrm{K}_{lat} \qquad \textit{Eqn. 1.1.8}$$

The equation for the total thermal conductivity is given in Equation 1.1.8, where K_e is the contribution of thermal energy carried by the electrons and K_{lat} is the contrition from the lattice. The majority of thermal energy is carried through the lattice via phonons. In order to reduce the thermal conductivity, it is necessary to prevent phonons from making efficient progress through the lattice. This can be done by scattering and reducing their mean free path via means of introducing scattering centres and/or reducing the strength of bonds between atoms. Strong rigid bonds limit the amplitude of vibrations so allow greater mobility of carriers and phonons.[29] Nonharmonic vibrations in filled skutterudites, for example Ba, La,

Yb doped $CoSb_3$ have, for example, been used to destructively interfere with heat carrying phonons to reduce thermal conductivity down to 2.7 W/mK at room temperature.[30]

If a unit cell has more than one atom, then the crystal has two phonon modes: acoustic and optical. In the acoustic mode atoms in the unit cell move together, and their frequency is near to that of sound waves.[31,32] Whereas in optical mode adjacent atoms move against each other and their frequency is close to that of infrared light.[31,32]
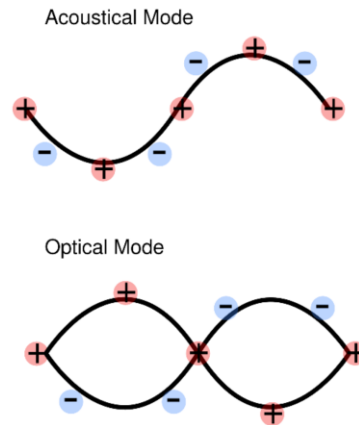
Figure 1.1.3 Schematic of optical and acoustic phonon modes.[31]

Optical phonons are dominant at lower temperatures (300-500K). Their thermal conductivity is relatively low due to low velocity and small heat capacity. Acoustic phonons are dominant at higher temperatures (500-900K) and responsible for the majority of thermal conductivity.[33]

A portion the total thermal conductivity is carried by the conduction electrons, shown in Equation 1.1.9 where L is the Lorentz number, σ is the electrical conductivity and T is temperature.[19]

$$K_e = L\sigma T \qquad\qquad Eqn.\ 1.1.9$$

This equates to a small portion of the total, for example at room temperature an electrical conductivity 500-1000 S/cm only corresponds to a K_e of 0.4-0.8 Wm/K.[34] When considering the total thermal conductivity of most materials are between 2 and 10 Wm/K, this is not by any means a large contributor to the overall thermal conductivity, therefore, the lattice contribution is the focus of most efforts when trying to reduce the thermal conductivity.

Scattering centres are only effective at scattering phonons which have a similar wavelength to their own dimensions. It is known that many different wavelengths of phonons are involved with thermal transport. Therefore, a hierarchy of scattering centres are required to effectively reduce the thermal conductivity.[35] Scattering centres include point defects such as vacancies or interstitials which are effective in scattering low wavelength phonons, nanoparticles and grain boundaries which scatter medium wavelength phonons.[35] However, these additions can also scatter electrons, decreasing their mobility, therefore decreasing the electrical

conductivity. Balancing the reduction in thermal conductivity with the preservation of electrical conductivity is an important yet challenging task.

For a typical metal or semiconductor, the thermal conductivity reduces as the temperature increases due to an increase in lattice vibrations which scatter phonons. This temperature dependence can be lost if the lattice contribution to the thermal conductivity is low. Guélou, *et al.* showed that in the semiconductor $Cu_5Sn_2S_7$ the total value and temperature dependence of the thermal conductivity was largely reduced due to Cl doping which caused an increase in the level of cation disorder. [36]

1.1.6 Summary

Therefore, it has been shown that a large degree of interconnection exists between the parameters S, σ and K. Phonon-Glass Electron-Crystal (PGEC) materials with high electrical conductivity and low thermal conductivity are desired, though extremely difficult to achieve in practice due to the conflicting structures which produce a low thermal conductivity and those which produce a high electrical conductivity. Figure 1.1.4 shows the general trend of the key parameters versus the carrier concentration. Current research aims to achieve a trade-off between the three key properties to achieve a maximum ZT. This can only be achieved by carrier concentration refinement as well as the use of complex materials and hierarchical structures to achieve a high ZT.

With these underlying theories in mind let the next section delve into the state of the art in thermoelectric materials. There are a huge number of thermoelectric materials that have been created and discovered though for brevity, only the highest performing categories of materials are put forward and discussed.
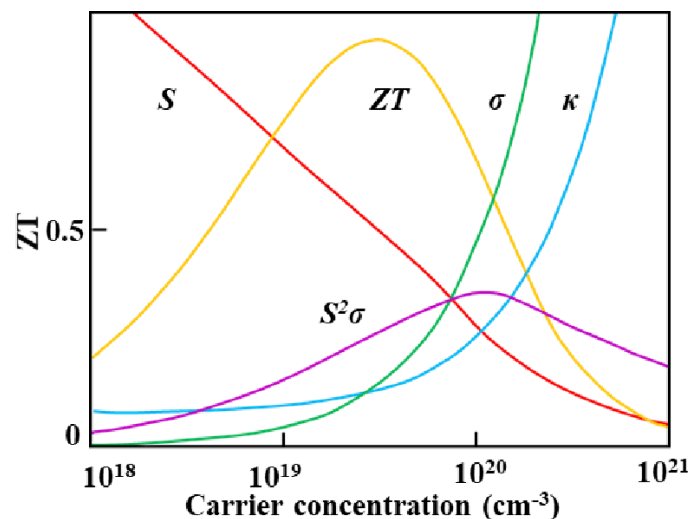
Figure 1.1.4 The interdependencies of thermoelectric properties in maximizing ZT. [37]

1.2 p-Type Thermoelectric Materials

1.2.1 Bismuth Telluride – Antimony Telluride Alloys

The most mature and widely used of the thermoelectric materials are bismuth telluride (Bi_2Te_3) based compounds. The small band gap of the intrinsic material, 0.13 eV, leads to degradation of ZT at high temperatures due to flooding of minority charge carriers, therefore these materials function best close to room temperature.
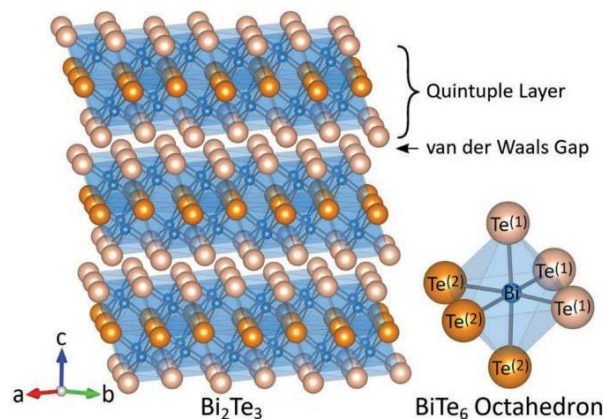
Figure 1.2.1 Tetradymite crystal structure of bismuth telluride taken from work published by Witting et al.[38]

Bismuth telluride has a tetradymite crystal structure with the large Te atoms forming hexagonal close packed layers, and Bi occupying octahedral holes. For every 5 close packed layers there is a layer with no Bi atoms. The bonds between the Te and Bi are polar covalent (slight negative charge on the tellurium due to higher electronegativity and positive on the Bi), with weak Van der Waals forces between the close packed layers.[38] This layered structure leads to anisotropy in the electrical conductivity - conduction within basal planes is much larger than across the planes in the c direction.

Importantly, the anisotropy is lower in p-type materials (3:1) than in the n-type tellurides (6:1).[38–40] This fact will be discussed further in the section 1.3.1 'Bismuth Telluride - n-type'. Though the Seebeck values remain isotropic due to isotropic density of states.[38,39]

These compounds have high band degeneracy, high carrier mobility and relatively low thermal conductivity leading to outstanding figures of merit. The large Te atoms with weak bonds between them lead to low thermal conductivity – single crystals of Bi_2Te_3 have an average thermal conductivity of 1.37 W/mK at 300K.[38]

The complexity of the fermi surface, originating from spin orbit coupling, leads to high Seebeck coefficients. Without the spin orbit interactions, the band gap in Bi_2Te_3 would be positioned at a high symmetry point in the Brillouin zone (Γ). Though due to interactions between the Bi and Te orbitals the conduction band becomes lower in

energy, moving towards the valence band, which in order to avoid a crossing, inverts.[38] This results in a complex fermi surface, a small band gap and a high level of degeneracy, which leads to a large Seebeck coefficient.
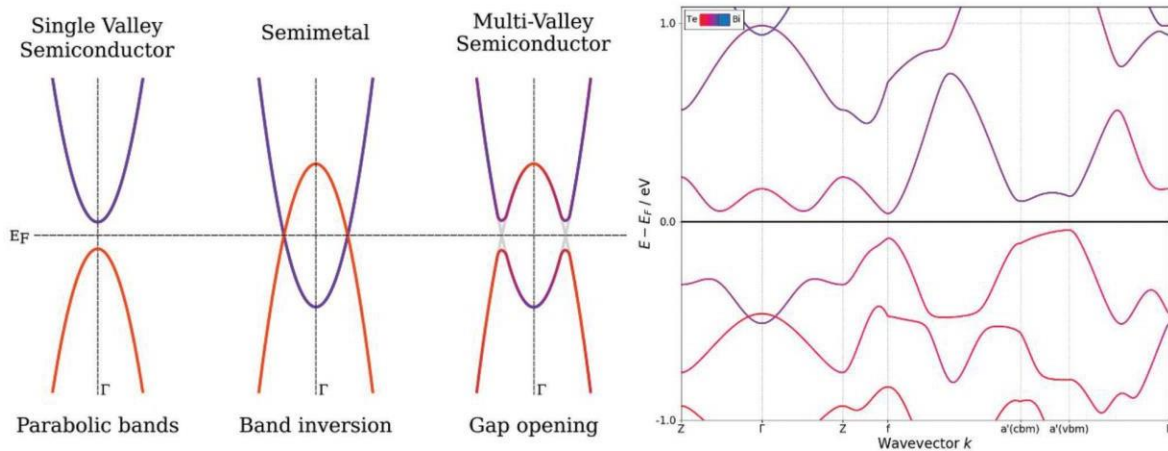
Figure 1.2.2 Diagram showing how band inversion creates a complex fermi surface in BiTe (left) and a DFT band model of BiTe (right).[38]

p-type conduction can be induced by alloying Bi_2Te_3 with Sb_2Te_3 which also increases the band gap, increasing the maximum service temperature.[1] In 2017 Kim *et al.* tuned the carrier concentration of Bi_2Te_3-Sb_2Te_3 by adding excess Te. Reducing the carrier concentration improved the Seebeck coefficient but reduced the electrical conductivity, however, tuning of the carrier concentration can overall improve the power factor. Stoichiometric $(Bi_{0.25}Sb_{0.75})_2Te_3$ had a carrier concentration of 6.7×10^{19} cm^{-3} which gave a ZT of 0.6 at 27 °
C. When adding excess Te the carrier concentration was tuned to 2.6×10^{19} which gave a ZT of 1.05 at 27 °C.[41]

Additional doping e.g. with Indium, can help to expand the band gap of Bi_2Te_3 which upshifts the service temperature. Operating at higher temperatures allows for larger ZTs to be accessed and the energy conversion efficiency increases, as the difference between the cold and hot contacts is proportional to the conversion efficiency of thermoelectric materials. In 2016 Xu *et al.* showed this by doping $(Sb,Bi)_2Te_3$ with indium, resulting in a peak ZT of 1.4 at 227 °C, rather than the usual peak around room temperature seen in Bi_2Te_3.[42]

Controlling the microstructure with techniques such as ball milling and hot pressing have been used to create nanostructured materials which reduce the thermal conductivity due to grain boundary and dislocation scattering, expanding the ZT of $Bi_{0.5}Sb_{1.5}Te_3$ to 1.4 at 100 °C.[43] In 2015 Kim *et al.* introduced a high dislocation density at grain boundaries of $Bi_{0.5}Sb_{1.5}Te_3$ (through a liquid phase compaction synthesis technique) which reduced the thermal conductivity compared to a ingot solidification, increasing the ZT from 1.00 to 1.86 at 47 °C.[44]

Table 1.2.1 Thermoelectric properties of Bi$_2$Te$_3$ and Sb$_2$Te$_3$ based alloys.

Composition	ZT	Temp. / ºC	Electrical conductivity / Scm^{-1}	Thermal / Wm^{-1}K^{-1}	Seebeck coefficient / μVK^{-1}	Source
(Bi$_{0.25}$Sb$_{0.75}$)$_2$Te$_3$	1.05	27	1900	1.75	180	Kim, 2017 [41]
Bi$_{0.3}$Sb$_{1.625}$In$_{0.075}$Te$_3$	1.4	227	700	1.1	220	Xu, 2016 [42]
Bi$_{0.5}$Sb$_{1.5}$Te$_3$	1.4	100	850	1.0	210	Poudel, 2008 [43]
Bi$_{0.5}$Sb$_{1.5}$Te$_3$ (melt solidification)	1.00	47	830	1.3	225	Kim, 2015 [44]
Bi$_{0.5}$Sb$_{1.5}$Te$_3$ (liquid phase compacted)	1.86	47	650	0.65	242	Kim, 2015 [44]

Although bismuth telluride is a high performing *p*-type material its low service temperature severely limits its applications in anything above a room temperature environment. Large temperature differences between hot and cold contacts lead to the largest energy conversion so other materials are required to aim for this.

1.2.2 Tin Selenide

Tin Selenide (SnSe) on the other hand does not suffer from the same issue as bismuth telluride, its optimum temperature range is 500-800 ºC. SnSe is a 2D anisotropic material with low symmetry, and an intrinsically very low thermal conductivity, <0.4 W/mK (at 923 K) due to strong anharmonic bonding.[45] This is already beneficial in reaching high ZTs if the electronic properties can be engineered to match this.
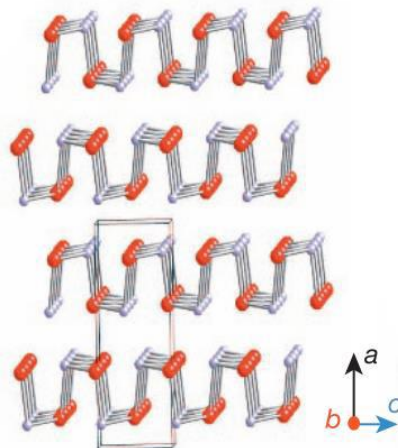
Figure 1.2.3 Schematic of the atomic arrangement of SnSe taken from work published by Zhao et al. [46]

Understanding the structure of SnSe is key to engineering high ZTs as its layered structure

leads to a large degree of anisotropy. In single crystals of SnSe, Se and Sn form two atom thick layers, by corrugation in the b-c plane of a single atom think sheet in an accordion-like pattern. ZT is highest in the b and c axis for hole doped specimens, though much smaller along the a-axis due to reduced mobility between layers. This material operates at moderate temperatures, ultimately limited by a phase transition from *Pnma* to *Cmcm* at ~ 527 ºC. Much beyond this temperature (~ 700 ºC) the ZT drops, due to bipolar conduction mechanisms (holes and electrons) being activated in the *Cmcm* structure (*Cmcm* has half the band gap of *Pnma* so electrons can overcome this gap at elevated temperatures leading to electron conduction which interferes with the hole conduction mechanism).[46]

ZT is maximized in the b-axis, followed by the *c* then *a* axis, due to the differences in the power factors. The electrical conductivity is greater along the Sn-Se planes which have strong Se-Sn bonds, and much lower along the *a* axis which has weaker bonds.[46] The thermal conductivity is also much lower along the *a* axis, though this is not compensation enough to increase the ZT as the thermal conductivity is already intrinsically low in all directions (<0.5 W/mK at 680 ºC). [46]

Anharmonicity means that mechanical and thermal exchange energy and cause a dampening effect.[47] The scale of the effect can be quantified by the Grüneisen parameter. Along the a, b and c axes the average Grüneisen parameters are: 4.1, 2.1 and 2.3, which follow the same trend as the thermal conductivities. [46]

In *n*-type selenides such as bromine doped SnSe, charge density overlap between the layers facilitates conduction in the out of plane direction (a-axis) where the thermal conductivity is at its lowest, therefore reaching a higher ZT ~2.8 at 773K.[29]

Table 1.2.2 Thermoelectric properties of tin selenides.

Composition	ZT	Temp. / ºC	Electrical conductivity / Scm^{-1}	Thermal / $Wm^{-1}K^{-1}$	Seebeck coefficient / μVK^{-1}	Source
SnSe (a-axis)	0.2	680	14	0.23	390	Zhao, 2014 [46]
SnSe (c-axis)	2.3	680	71	0.31	320	Zhao, 2014 [46]
SnSe (b-axis)	2.6	680	89	0.35	340	Zhao, 2014 [46]
SnSe (b-axis)	1.5	500	33	0.33	440	Zhao, 2014 [46]
$Sn_{0.985}Na_{0.015}Se$ (b-axis)	2.0	500	150	0.55	300	Zhao, 2016 [45]
Polycrystalline SnSe	0.5	550	33	0.62	350	Sassi, 2014 [48]

In 2016 Zhao *et al.* showed a huge increase in the PF of single crystal SeSn from ~6.4 $\mu Wcm^{-1} K^{-2}$ (500 ºC) to ~14 $\mu Wcm^{-1} K^{-2}$ when acceptor doped with Na.[45] Doping with sodium pushed the fermi level deeper into the valence band where there are multiple valence bands in a small energy range. This changed the electrical conductivity character to metallic

rather than semiconducting. [45] This vastly increased the number of charge carriers and enhanced the electrical conductivity. A huge loss in Seebeck coefficient would be expected to accompany this, however, Zhao *et al.* only found a small degrease due to the effective masses of holes in these bands being greater than in the first valence band, which enhanced the Seebeck coefficient.

Sassi *et al.* showed the properties of polycrystalline SnSe. The maximum ZT was much lower as the anisotropy of the electrical properties becomes averaged as the grains are no longer perfectly orientated.[48] Though their sample did show some preferred orientation, which led to a small degree of anisotropy in electrical and thermal conductivities. Still an element of random grain orientation heavily reduced the power factor. Not only this but the thermal conductivity overall did not decrease in the polycrystalline sample, as would be expected due to grain boundaries causing phonon scattering. They reported that the increase in thermal conductivity of the polycrystalline samples was due to increased diffusivity and specific heat capacities measured. This resulted in an overall ZT of 0.5 at 550 ℃.[48]

Furthermore, at higher temperatures above the phase transition to *Cmcm* (~ 527 ℃) Sassi *et al.* recorded significant mass loss from the samples indicating that the polycrystalline material was not stable at higher temperatures.[48]

This is a disadvantage for SnSe thermoelectric as polycrystalline materials are generally more mechanically stable than layered single crystals and much easier to manufacture.[48]

Another intriguing family of layered oxides are the calcium and sodium cobaltites. Though their thermal conductivities are not as low as SnSe, they have been shown to possess electron-crystal phonon-glass characteristics which is highly attractive for thermoelectric materials.[49,50]

1.2.3 Sodium and Calcium Cobaltite

Unlike most other high performance thermoelectric materials, layered cobaltite materials such as Na_xCoO_2 and Ca_xCoO_y consist of light elements and show metallic conduction at room temperatures.[51,52] This is in stark contrast to bismuth telluride which is a semiconductor consisting of heavy elements.

Oxides usually have high thermal conductivities due to strong bonds and light elements which make phonon transport easier. However, in this material the alternating layers of ordered CoO_2 and highly disordered Ca_xCoO_y or sodium ion nanoblock layers play an important role in reducing the thermal conductivity below 1 W/mK at room temperature whilst maintaining high electrical conductivity. [51,52]

CoO_2 layers are responsible to the electrical conductivity whist the intermediate layers are a source of holes and act as a glass in terms of phonon transport.[49] Therefore, electrical properties show a large anisotropy, with larger values in plane. For single crystals the larger in-plane values are quotes from now on.[50]
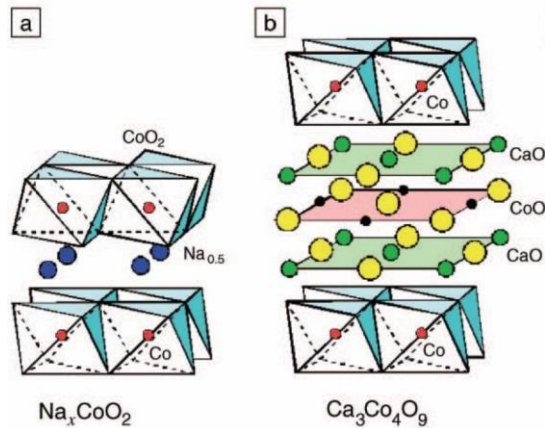
Figure 1.2.4 Crystal structure of a) Na_xCoO_2 which consist of CoO_2 layers and sodium nanoblock layers b) $Ca_3Co_4O_9$ which consists of layers of CoO and Ca_2CoO_3.[52]

These materials have been found to have very low charge carrier mobility though are highly abundant in charge carriers leading to a high electrical conductivity. Unlike in most semiconductors where the number of charge carriers has an optimal level above which S is too low, so the thermopower is maximised by the mobility of charge carriers.

The Seebeck coefficient is usually highly negatively correlated to the number of charge carriers, though the opposite effect is observed with layered cobaltites. Funahashi *et al.* showed that for "whisker like" single crystals of $Ca_2Co_2O_5$ the electrical conductivity and the Seebeck coefficient simultaneously rose with temperature up to the maximum measure temperature, 700 °C, typical of semiconductor behaviour.[53]

On the other hand, the electrical conductivity of Na_xCoO_2 shows metallic behaviour, electrical conductivity, reducing with an increase in temperature, between 50 and 800 K.[49,50,52,54] Koumoto *et al.* compared the thermoelectric properties of Na_xCoO_2 and $Ca_3Co_4O_9$ between 25 and 300 K. They found that, of the two, $Ca_3Co_4O_9$ had lower thermal conductivity and highest Seebeck coefficient, but also lower electrical conductivity due to the increased disorder of the interlayer between CoO_2 planes.[52]

Fujita *et al.* showed the effect of moving from single crystal to polycrystalline $Na_xCoO_{2-\delta}$, which reduced the thermal conductivity but also the electrical conductivity and Seebeck coefficient.[54] This drastically lowered the ZT at 527 °C from 1.2 to 0.31. This effect was also confirmed at 27 °C by Takahata *et al.*[49]

A similar value of ZT was found by Miyazaki *et al.* for polycrystalline $Ca_3Co_4O_9$, though in contrast this was an improvement on the single crystal thermoelectric properties reported by Koumoto *et al.* due to the marked decrease in thermal conductivity due to grain boundary scattering.[51,52]

Table 1.2.3 Thermoelectric properties of layered cobaltite materials.

Composition	ZT	Temp. / °C	Electrical conductivity / Scm^{-1}	Thermal / $Wm^{-1}K^{-1}$	Seebeck coefficient / μVK^{-1}	Source
$Ca_3Co_4O_9$ single crystal	0.01	27	41	2.9	160	Koumoto, 2006 [52]
Na_xCoO_2 single crystal	0.06	27	1000	5.0	100	Koumoto, 2006 [52]
$Na_xCoO_{2-\delta}$ single crystal	1.2	527	1900	5.1	200	Fujita, 2001 [54]
$Na_xCoO_{2-\delta}$ polycrystalline	0.31	527	280	2.1	170	Fujita, 2001 [54]
$NaCa_2O_4$ polycrystalline	0.03	27	330	2.0	80	Takahata, 2000 [49]
$Ca_3Co_4O_9$ polycrystalline	0.035	27	67	0.98	133	Miyazaki, 2000 [51]

1.2.4 Closing Remarks on *p*-type Materials

A material will generally perform better as a *p*-type or an *n*-type material due to idiosyncrasies in the microstructure and band properties making them unable to perform as well in both conduction mechanisms. There is a large abundance in high performance *p*-type materials, however there is no guarantee that when inducing *n*-type conduction the performance is as great - and in most cases it is not, with the exception of bismuth telluride. Currently in the literature *n*-type thermoelectric materials are falling short of their *p*-type counterparts, though high figure of merit *n* and *p* types are essential for a high efficiency thermoelectric device. Some of the highest performing *n*-type materials in the literature are described and discussed in the following section 1.3 '*n*-type Thermoelectric Materials'.

1.3 *n*-type Thermoelectric Materials

This section discusses the state of the art of *n*-type thermoelectric materials. It lists the most common classes of materials in this field, providing the details of their crystal structures which lead to desirable characteristics for *n*-type thermoelectric materials.

1.3.1 Bismuth Telluride – *n*-type

Bismuth telluride is able to perform as a *p*-type or *n*-type thermoelectric material, depending on the doping strategy and so this material features in both the state of the art for *p*-types and this section which will cover its performance as an *n*- type. The crystal structure of bismuth telluride was shown in the section '1.2 p-Type Thermoelectric Materials' Figure 1.2.1. It has a complex tetradymite structure with hexagonal close packed Te atoms with Bi occupying the octahedral sites. In order to induce *n*-type conduction bismuth telluride can be doped with bismuth selenide (Bi_2Se_3) which induces Se vacancies.

n-type tellurides have a larger power factor than *p*-types in the basal planes (~45 µW/Kcm for *n*-types, compared to ~35 µW/Kcm for *p*-types) due to the weighted higher mobility of electrons than holes.[38] However, the ZT of *n*-types is lower than *p*-types due to the increased anisotropy in the *n*-type's electrical conductivity. The lower anisotropy in p-types generally matches that of the thermal conductivity anisotropy so that the ZT is virtually isotropic in *p*-type materials whether in a single crystal or polycrystalline material.[39] In contrast, the anisotropy in *n*-type conductivity is much larger (~6) so it remains anisotropic unless all the grains are oriented in the same direction.[39] This means that strategies to increase ZT by reducing the grain size are less applicable to *n*-type bismuth telluride, as random grain orientations reduce the power factor.

Table 1.3.1 Thermoelectric properties of n-type Bismuth Tellurides

Composition	ZT	Temperature / °C	Electrical conductivity/ Scm^{-1}	Thermal / $Wm^{-1}K^{-1}$	Seebeck coefficient / μVK^{-1}	Source
$Bi_2Te_{2.7}Se_{0.3}I_{0.0075}$	1.13	150	1400	1.1	-150	Lee, 2015[55]
$Bi_2Te_{2.79}Se_{0.21}$	1.2	102	800	1.1	-200	Hu, 2015[56]
Bi_2Te_3	1.16	147	1000	0.75	-150	Wu, 2013[57]

By alloying Bi_2Te_3 with Bi_2Se_3 Lee *et al.* induced an *n*-type material which had a ZT of 0.55 at 150 ºC, a relatively low value for this material compared to its *p*-type counterparts. When further doped with iodine this improved the electrical conductivity by increasing the carrier concentration and reduced the lattice thermal conductivity, achieving a ZT of 1.13 at 150 ºC.[55]

Also achieving a similarly low thermal conductivity was Hu *et al.* who performed hot zone melting of $Bi_2Te_{2.79}Se_0.21$. This gave a lighter deformation, than say ball milling, and maintained some texture of the grains, meaning that the power factor can be preserved (otherwise negatively affected by anisotropy) whilst introducing point defects and microscale grains. This resulted in a ZT of 1.2 at 102 ºC.

Wu *et al.* also investigated microstructure control, looking at three different morphologies of *n*-type Bi_2Te_3: nanowires, flower-like nanosheets and nanoparticles.[57] They found that the flower like nanosheets gave the highest ZT due to the preservation of the electrical conductivity that was not shown in the other two morphologies. This is likely also due to the retained texture in these microstructures. This need to maintain grain orientation or single crystals is a complication for these materials as it makes synthesis of high performance *n*-type bismuth tellurides complex and costly compared to a material which can perform well in polycrystalline form as these are much easier to make on an industrial scale than single crystals. Furthermore, the expensive and toxic nature of Te and Se resign these materials to niche high value applications.

A material which can be made polycrystalline whilst maintain high electrical conductivity and very low thermal conductivity, due to their unique crystal structure are Skutterudites.

1.3.2 CoSb$_3$ Based Skutterudites

Based on MX_3 formula skutterudites are composed of corner sharing MX_6 octahedra which form nanoscale cages which can be filled with a variety of atoms. *n*-type filler atoms donate electrons to the lattice inducing semi conduction and create inharmonious vibrations which interfere with lattice vibrations, therefore inhibiting thermal transport. The greatest improvement in thermal transport reduction has been seen in multiple filled cages, the key to this being that multiple size fillers produce vibrations of multiple magnitudes which interfere with a broader range of phonons, rather than in the case of one filler species. The parent structure $CoSb_3$ possesses a thermal conductivity of around 10 W/mK at room temperature but by adding Ba, La and Yb Shi *et al.* found a reduction in thermal conductivity to 2.7 W/mK at 27 ºC.[30,58] This was accompanied by a large increase in the electrical conductivity whilst maintaining the Seebeck coefficient value which resulted in a ZT of 0.42 at 27 ºC.[30]

The increase of the electrical conductivity from unfilled to filled skutterudites, whilst maintaining a high absolute Seebeck coefficient is an unusual effect amongst materials. This effect is attributed to the large effective mass of the electrons, therefore the Seebeck coefficient remains high, despite the rise in the number of conduction electrons.[9]

For filled skutterudites the electrical conductivity reduces with an increase in temperature, whilst the absolute Seebeck coefficient increases. This metallic behaviour is typical of heavily doped semiconductors.[58] As temperature is increased the electrons become more scattered by the lattice vibrations therefore the electrical conductivity drops.

Table 1.3.2 Thermoelectric properties of CoSb$_3$ based Skutterudites.

Composition	ZT	Temperature / °C	Electrical conductivity/ Scm^{-1}	Thermal / $Wm^{-1}K^{-1}$	Seebeck coefficient / μVK^{-1}	Source
$CoSb_3$	0.017	27	400	10	-120	Nolas, 2000[58]
$Ba_{0.08}La_{0.05}Yb_{0.04}Co_4Sb_{12}$	0.42	27	2398	2.7	-126	Shi, 2011[30]
$Ba_{0.08}La_{0.05}Yb_{0.04}Co_4Sb_{12}$	1.71	577	1428	2.6	-192	Shi, 2011[30]

1.3.3 *n*-type Oxides

Oxides are an attractive group of materials for thermoelectric applications as their constituents are generally low cost, non-toxic and are stable up to high temperatures – features which many other thermoelectric materials such as Bi_3Te_3 selenium and cobalt containing materials not able to claim. This is a significant consideration when trying to expand the viable applications of thermoelectric devices from niche applications with large budgets e.g. RTG in space probes to wider scale applications within homes, commercial and domestic vehicles etc.

Thermoelectric generators present a unique opportunity to convert the vast amount of energy humans waste in the form of heat directly into electricity, reliably and portably. In order to grasp this opportunity, the constituent materials must be of low cost, have low environmental impact and be efficient (possess high figure of merit). As previously stated this is proving a challenge in the current state of the art for *n*-type materials, though some of the most well documented and promising *n*-type thermoelectric oxides are described in this section.

1.3.4 ZnO

ZnO is a direct band gap semiconductor with a hexagonal wurtzite crystal structure at room temperature, Figure 1.3.1. Through doping the electrical conductivity can be increased to significant levels though the ZT is limited by its thermal conductivity.[59,60]
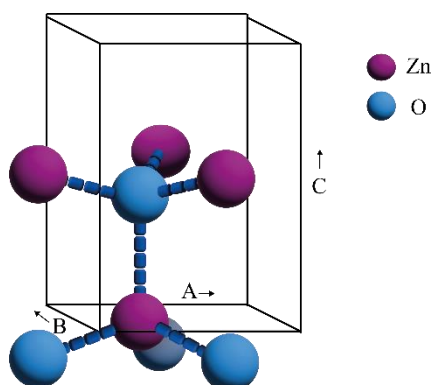
Figure 1.3.1 Hexagonal wurtzite crystal structure of ZnO

The c/a ratio of the crystal structure pays an important role in the electronic properties as shown by Wiff *et al.* when adding small amounts of Al in place of Zn. Al decreased the c/a ratio thereby compressing the distance between hexagonal layers.[61] The smaller c/a ratio led to larger concentration of charge carriers at room temperature as well as a small increase in the effective mass leading to large improvement in the power factor at small c/a ratios, onset by increasing Al doping levels.[61]

Qu *et al.* corroborated this effect by showing the increase of the electrical conductivity with Al content across three samples, shown in Table 1.3.3. The largest ZT achieved by this study was 0.16 at 800 ℃ in $Zn_{0.97}Al_{0.03}O$.[62]

The largest ZT for ZnO based materials was reported by Ohtaki *et al.* in 2009 who reported much higher electrical conductivities than Qu *et al.* Their Al doped ZnO showed nearly 6 times the electrical conductivity and gave a ZT of 0.37 at 1000 ℃. Co-doping with Al and Ga increased the ZT further by increasing the absolute Seebeck value and reducing the thermal conductivity.[63] The disparity of these results may be down to their contracting synthesis routes with Qu *et al.* using a co-precipitation method and Ohtaki *et al.* using a solid state synthesis route. The co-doped sample by Ohtaki *et al.* also contained an unknown peak in their XRD analysis as well as small amounts of $ZnAl_2O_4$ in the Al dopes composition. This makes it hard to determine if the properties are soley down to the composition, though the fact stands that these are the highest thermoelectric properties of *n*-type ZnO to date.

Table 1.3.3 Thermoelectric properties of zinc oxides.

Composition	ZT	Temperature / ℃	Electrical conductivity / Scm^{-1}	Thermal / $Wm^{-1}K^{-1}$	Seebeck coefficient / μVK^{-1}	Source
ZnO	0.007	800	33	6.0	-174	Qu, 2011[62]
$Zn_{0.99}Al_{0.01}O$	0.04	800	130	5.1	-154	Qu, 2011[62]
$Zn_{0.97}Al_{0.03}O$	0.16	800	170	3.6	-117	Qu, 2011[62]
$Zn_{0.98}Al_{0.02}O$	0.37	1000	816	~7.7	-152	Ohtaki, 2009[63]
$Zn_{0.96}Al_{0.02}Ga_{0.02}O$	0.65	1000	458	~4.8	-255	Ohtaki, 2009[63]

1.3.5 Perovskites
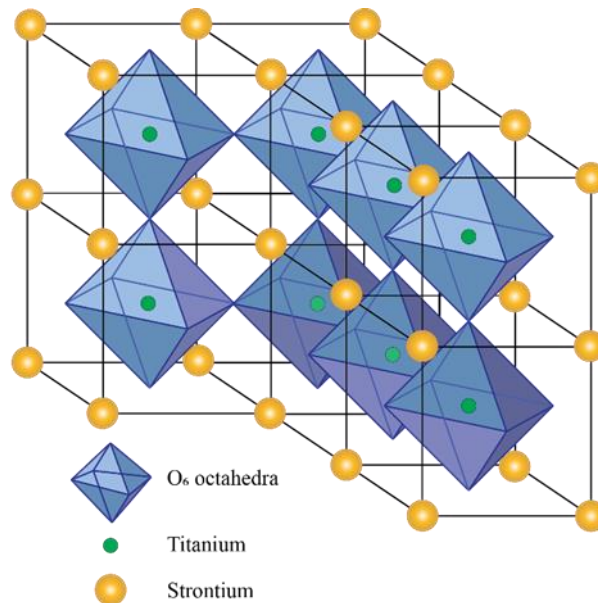
Figure 1.3.2 Cubic perovskite crystal structure of SrTiO₃

Perovskites in general are a highly attractive structure for a wide range of applications such as solar cells, MLCCs, super conductors and thermoelectric materials.[64–67] With the general structure ABX_3 they can accommodate a variety of atoms as the A and B sites vary largely in size, smaller atoms can occupy the B site whereas larger atoms can occupy the A and X site. An ideal cubic perovskite is $SrTiO_3$, (STO) shown in Figure 1.3.2. Ti and O form corner sharing octahedra, Sr occupy cavities between the octahedra. It contains mixed boding: covalent bonding within the octahedra and ionic bonds between strontium and oxygen.

The tolerance factor is essentially a measure of stability of the cubic perovskite and can be used to predict and explain crystal structure distortions. In Equation 1.3.1, r_A, r_B, r_O are the ionic radii of the A-site, B-site and oxygen atoms respectively, and t is the tolerance factor.

$$t = \frac{r_A + r_O}{\sqrt{2}(r_B + r_O)} \qquad Eqn.1.3.1$$

The tolerance factor for $SrTiO_3$ is 1 meaning that the ionic radii are ideally sized to form a cubic perovskite arrangement. The further the tolerance factor is away from one the less stable the cubic perovskite is. Small changes in atomic size and bond lengths can be accommodated by distortions which relieve strain such as, octahedral distortions in $CaTiO_3$. Ca is a smaller ion than Sr and so the A-O bond is reduced in length and t drops below 1. This is compensated for by octahedral tilting giving rise to an orthorhombic distortion of the cubic perovskite. Larger ions like Ba can cause tetragonal and rhombohedral distortions.[68]

The flexibility of perovskites mean that the material properties can be largely changed which is an advantage for an application such as thermoelectric materials where careful balance of the Seebeck coefficient, electrical and thermal conductivity needs to be employed.

Electron transport in *n*-type perovskites occurs via the large polaron mechanism.[69,70] When charge carriers interact with the lattice they can be referred to as polarons.[71] The coherence length is the size of the polarisation cloud, effectively the range of influence the charge carrier has on the lattice. If the coherence length is larger than one lattice parameters length, then this is called a large polaron.[69]

For example, the electron induced by the loss of oxygen in STO is localised to the Ti species, reducing it from Ti^{4+} to Ti^{3+}. The electrons radius of influence on the surrounding ions is larger than one unit cell and is therefore a large polaron. This polaron hops between Ti atoms aided by the overlapping 3d orbitals. This is the large polaron conduction mechanism.

1.3.6 $CaMnO_3$

Stoichiometric $CaMnO_3$ (CMO) has an orthorhombic perovskite crystal structure. Molinari *et al.* found that undoped CMO has a ZT 0.03 at 950 K, with a power factor of 0.5 $\mu W/K^2cm$ and a Seebeck coefficient of -230 $\mu V/K$.[72] Typical donor dopants for CMO are Yb on the A-site and Nb on the B-site (ref. Fergus *et al.* and those therein).[59] Through Yb doping ($Ca_{0.9}Yb_{0.1}MnO_3$) to increase the electrical conductivity the ZT can be increased to 0.2 at 1000 ℃. The Seebeck coefficient of this sample was -150 $\mu V/K$ at 1000 ℃.[59]

1.3.7 $SrTiO_3$

Doped $SrTiO_3$ (STO) based structures with the cubic perovskite structure have a higher electrical conductivity, thermal conductivity and absolute Seebeck coefficient than CMO. The high degree of symmetry in cubic perovskites induce a high level of degeneracy in the density of states and therefore lead to a high effective mass and Seebeck coefficient. Highly directional Ti 3d electrons (states occupied when STO is donor doped) lead to a high electrical conductivity. Though the strength of these covalent bonds also leads to high thermal conductivity. High power factors of 28- 36 mW/K^2cm have been reported for La doped STO which rival that of Bi_2Te_3.[73] The ideal charge carrier concentration for strontium titanate, to maximise the power factor is ~ 2 $x10^{21}$ cm^{-3}.[74,75] This can be achieved through doping and or oxygen deficiency.

Due to these properties, strontium titanate based oxides form the basis of the remainder of this work. Though already many works have been published engineering the properties of *n*-type STOs this is a young material compared to bismuth telluride and much is yet to be done with the material thanks in large part, to the highly flexible perovskite structure. One of the key obstacles in oxides is their high thermal conductivity, which negatively impacts the ZT, therefore much research is done to reduce the thermal conductivity whilst retaining high power factor.

1.4 Strategies to Improve the Figure of Merit in Strontium Titanate

Pure strontium titanate ($SrTiO_3$) is a wide band gap insulator (indirect band gap of 3.20 - 3.25 eV at room temperature) with a large thermal conductivity.[76,77] A high performance thermoelectric material requires a high electrical conductivity and low thermal conductivity to give a high ZT, this clearly is not achieved by pure strontium titanate. For this reason, strontium titanate is commonly doped with substitutional elements or its stoichiometry is changed in order to improve the thermoelectric performance.[78] Some of the most common strategies are described in the following section.

1.4.1 Oxygen Vacancies

Inducing oxygen vacancies into strontium titanate is a common strategy to increase the electrical conductivity. Oxygen vacancies lead to the generation of electrons and the subsequent reduction of Ti^{4+} according to Equations 1.4.1 and 1.4.2 respectively.

$$SrCO_3 + TiO_2 \rightarrow Sr_{Sr}^x + Ti_{Ti}^x + (3-\delta)O_O^x + \frac{\delta}{2}O_2(g) + \delta V_O^{\bullet\bullet} + 2\delta e' + CO_2(g) \quad Eqn.\ 1.4.1\ ^{[70,79]}$$

$$Ti^{4+} + e' \rightarrow Ti^{3+} \qquad Eqn.\ 1.4.2\ ^{[70]}$$
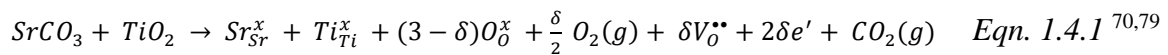
The creation of oxygen vacancies is encouraged by high temperature and low oxygen partial pressures.[79] The electrons produced in equation 1.4.1 then occupy the Ti 3d band which form the conduction band leading to higher electrical conductivity than stoichiometric STO. As Ti^{3+} is a larger ion than Ti^{4+} this mechanism is commonly associated with a lattice parameter increase.[80,81]

As oxygen vacancies are defects which can cause the scattering of phonons, as well as a means to increase the electrical conductivity, it is possible that they can decouple the interaction of power factor and thermal conductivity. Rahman *et al.* show this as they increased the H_2 content in their H_2/Ar reducing gas from 1 to 20% (therefore increasing the level of reduction) they saw an increase in electrical conductivity from ~ 0 S/cm to 13 S/cm as well as a reduction in thermal conductivity from 4.5 to 4.0 W/mK at 400 ℃.[24] Though the Seebeck coefficient also reduced from -800 to -450 µV/K, this resulted in a modest ZT value of 0.047 at 400 ℃.[24]

The charge carrier concentration in this sample was 10.66 x10^{19} cm^{-3} and was accompanied by an increase in lattice parameter to 3.9047 Å, compared to 3.8991 Å when sintering in 1% H_2/Ar (carrier concentration in this case was 0.106 x 10^{19} cm^{-3}). Both the lattice parameters given appear to be smaller than the standard STO cubic lattice parameter of 3.905 Å.[82] This could be due to the fact that they are working with highly pure single crystals therefore the amount of impurities and oxygen vacancies in their starting material was much lower resulting in a smaller lattice parameter.

Yamada *et al.* also show a study of single crystal STO heat treatments in increasing temperatures and reduced oxygen partial pressures which show a direct correlation to the free electron density.[79] Their maximum free electron density reached 5.8 x10^{19} cm^{-3} at the highest sintering temperature (1400 ℃) and the lowest oxygen partial pressure (9.6x10^{-12} atm). This sample had a lattice parameter of 3.9053 Å, however, in general this study found no trend between lattice parameter and number of charge carriers - though they make a comment on

the accuracy of their lattice parameter measurements and do see a trend in the density of samples after heat treatment, which reduces in correlation to the temperature and partial pressure of the heat treatment.[79] This represents loss of oxygen from the lattice.

Cao *et al.* showed the effect of reducing $La_{0.08}Sr_{0.9}TiO$ (LSTO) in three different environments: 1) 5% H_2 / Ar, 2) 5% H_2 / Ar with sacrificial carbon powder not in contact with the sample and, 3) 5% H_2 / Ar sample in direct contact with sacrificial carbon powder.[83] These were sintered at 1437 ℃ for 12 h, though they increased this to 24h for the samples with carbon to induce more oxygen vacancies. Between the conditions 1 and 3, the degree of reduction increased which was evidenced by an increase in lattice parameters from 3.9080 Å to 3.9095 Å and an increase in the Ti^{3+}/Ti ratio found from XPS data Figure 1.4.1.[83] This increased the electrical conductivity from 85 S/cm to 1288 S/cm at 57 ℃, Figure 1.4.2. The increase in electrical conductivity is mainly seen at lower temperatures, by ~ 600 K (327 ℃) the electrical conductivity values become comparable between all three samples of LST at a value around 183 S/cm. Cao *et al.* hypothesised that this is due to the modulation of the grain boundary potential barrier height. The barrier is caused by a difference in concentration of oxygen vacancies between the bulk and the re-oxygenated grain boundary, the boundary remains relatively oxygen rich compared to the bulk due to trapped oxygen. This property is discussed further in the section 'Reducing Thermal Conductivity Via Alternate Synthesis and Processing Routes'. Cao *et al.* do not provide thermal conductivity data so the ZT could not be determined.
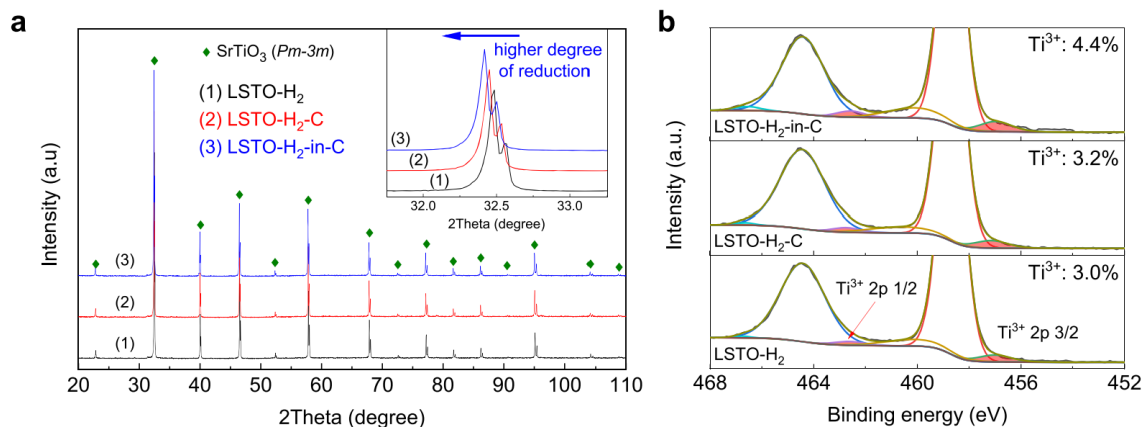
Figure 1.4.1 a) XRD of LSTO samples and b) XPS data of LSTO samples. [83]
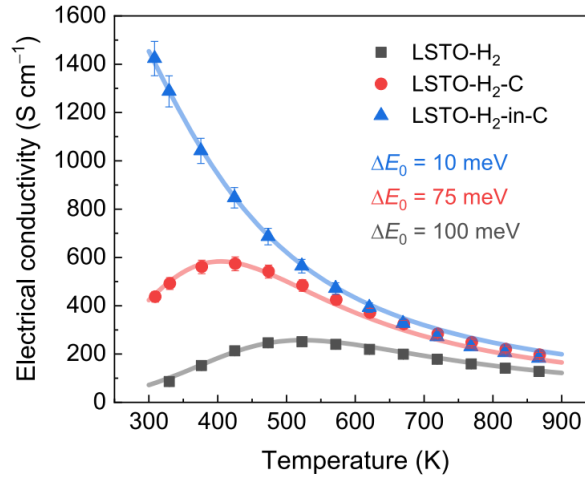
Figure 1.4.2 Electrical conductivity of LSTO found experimentally are represented by symbols and lines show that predicted by the model with band off set values, ΔE. [83]

The obvious strategy would be to increase the level of oxygen deficiency until a high ZT is achieved, but beyond maximum oxygen nonstoichiometric the cubic perovskite structure (desirous for its highly symmetrical structure leading to large Seebeck coefficient) becomes unstable.[24,52] Furthermore, once the optimum number of charge carriers for STO is reached the Seebeck coefficient begins to reduce, limiting the value of ZT. Therefore, the strategy to increase the electrical conductivity through the generation of oxygen vacancies is a successful one, but this strategy alone does not achieve the electrical conductivities required to bring ZT above 1.

Table 1.4.1 Thermoelectric properties of oxygen deficient strontium titanate.

Composition	ZT	Temp. / °C	Electrical conductivity/ S/cm	Thermal Conductivity / $Wm^{-1}K^{-1}$	Seebeck coefficient / μVK^{-1}	Source
$SrTiO_{3-\delta}$	0.047	400	13	4.0	-450	Rahman, 2019[24]
$La_{0.08}Sr_{0.9}TiO_{3-\delta}$ Sintering in 5% H_2	/	57	85	/	-129	Cao, 2021[83]
$La_{0.08}Sr_{0.9}TiO_{3-\delta}$ Sintering in 5% H_2 on carbon bed	/	57	1288	/	-115	Cao, 2021[83]
$La_{0.08}Sr_{0.9}TiO_{3-\delta}$ Sintering in 5% H_2 on carbon bed	/	600	183	/	-208	Cao, 2021[83]

1.4.2 A-site Doping

A second common strategy to increase the figure of merit in n-type strontium titanate is the addition of A-site donor dopants. Perovskites, given their flexible structures in terms of substitution, have the possibility of doping with many elements. The relative ionic radii of the dopant compared to the parent A-site species dictates what site the dopant will occupy; large to mid-size ionic radii e.g. La, Dy, Y, Nd, Ba, Sr, Ca generally occupy the A-site rather than the B-site, whereas smaller ionic radii will occupy the B-site e.g. Ti, Nb, Yb.[25,70,74,84–88] Some mid-size dopants may occupy both the A and B site, for example Eu^{3+} has been shown to dope onto both the A and B site in barium titanate, as Eu is much smaller than the Ba ion but larger than the Ti ion.[84,86] This is undesirable as this leads to a self-compensation mechanism which cancels out the donor doping effect. The aim of donor doping on the A-site it to induce defects which cause phonon scattering and reduce the thermal conductivity. This is commonly done by doping with a 3+ species: a rare earth element.

The replacement of the Sr^{2+} with a 3+ ion (M^{3+}) requires charge compensation to retain overall charge neutrality. The possible compensation mechanism for replacing the Sr^{2+} with M^{3+} (representing any donor 3+ ion) are given in the equations below, using the Kroger-Vink notation.

$$2M_2O_3 + 3TiO_2 \rightarrow 4M_{Sr}^{\bullet} + 3\,Ti_{Ti}^{x} + 12O_O^{x} + V_{Ti}'''' \qquad \text{Eqn. 1.4.3 } [89]$$

$$M_2O_3 + 3TiO_2 \rightarrow 2M_{Sr}^{\bullet} + 3Ti_{Ti}^{x} + 9O_O^{x} + V_{Sr}'' \quad \text{Eqn. 1.4.4}[89]$$

$$M_2O_3 + 2TiO_2 \rightarrow 2M_{Sr}^{\bullet} + 2Ti_{Ti}^{x} + 6O_O^{x} + \frac{1}{2}O_2 + 2e' \quad \text{Eqn. 1.4.5}[89]$$
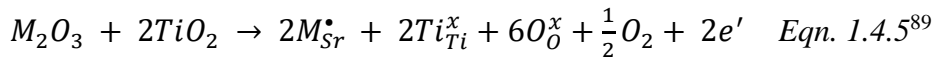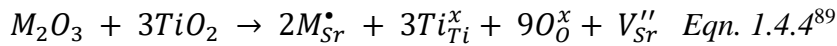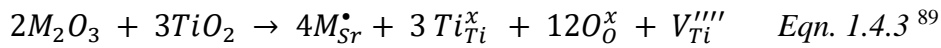
It is generally accepted that the most energetically favourable of these compensation mechanisms is equation 1.4.4, which describes the formation of A-site vacancies to retain charge neutrality. [86,90–93]. Commonly used levels of doping are between 10 and 20 mol.% as this achieves the optimum charge carrier concentration for strontium titanate of around 2 $\times 10^{21}$ cm^{-3}.[74,75]

Table 1.4.2 Thermoelectric properties of A-site doped strontium titanate.

Composition	ZT	Temp. / °C	Electrical conductivity/ S/cm	Thermal Conductivity / Wm^{-1}K^{-1}	Seebeck coefficient / uVK^{-1}	Source
$Sr_{0.9}Y_{0.1}TiO_3$	0.15	680	60	2.5	-220	Muta, 2003[88]
$Sr_{0.9}Dy_{0.1}TiO_3$	0.051	680	15	2.3	-230	Muta, 2003[88]
$Sr_{0.9}Gd_{0.1}TiO_3$	0.051	680	19	2.5	-215	Muta, 2003[88]
$Sr_{0.9}La_{0.1}TiO_3$	0.03	680	15	3.2	-215	Muta, 2003[88]
$Sr_{0.9}Sm_{0.1}TiO_3$	0.03	680	11	2.7	-215	Muta, 2003[88]
$Eu_{0.9}La_{0.1}TiO_{3-\delta}$	0.25	570	380	4.2	-180	Muta, 2005[25]

$Sr_{0.9}La_{0.1}TiO_{3-\delta}$	0.20	570	350	4.7	-180	Muta, 2005[25]
$Sr_{0.9}La_{0.1}TiO_{3\pm\delta}$	0.19	800	102	3.5	-246	Kovalevsky, 2014[94]
$Sr_{0.9}Nd_{0.1}TiO_{3\pm\delta}$	0.39	800	150	2.2	-231	Kovalevsky, 2014[94]
$Sr_{0.9}Sm_{0.1}TiO_{3\pm\delta}$	0.36	800	130	2.6	-259	Kovalevsky, 2014[94]
$Sr_{0.9}Gd_{0.1}TiO_{3\pm\delta}$	0.35	800	116	2.2	-249	Kovalevsky, 2014[94]
$Sr_{0.9}Dy_{0.1}TiO_{3\pm\delta}$	0.41	800	113	2.1	-266	Kovalevsky, 2014[94]
$Sr_{0.9}Y_{0.1}TiO_{3\pm\delta}$	0.25	800	112	3.4	-266	Kovalevsky, 2014[94]

In 1981 Chan *et al.* proposed that, in terms of a defect model, strontium titanate could be considered a two phase material of SrO and TiO_2. They stated that a dopant reacts only with one of the binary oxides depending on which site they occupy.[70,95] For an A-site dopant this would lead to interaction with the SrO binary oxide only. Since then other studies have agreed and found that the dopant species of the A-site ion is compensated for within this binary system and does not largely affect the TiO_6 octahedra.[25,88] Further to this it is suggested that the SrO binary oxide is responsible for the thermal conductivity whilst the TiO_2 is responsible for the electronic properties. Separating these two characteristics is an important step in achieving a high ZT, though in practice the separation is not so clear.

In 2003 Muta *et al.* showed $SrTiO_3$ doped with a selection of 3+ ions: La, Sm, Gd, Dy or Y at a level of 10 mol.%.[88] They found that the electronic properties (electrical conductivity and Seebeck coefficient) between all these samples reached the same maxima and were comparable across the whole temperature range. Whereas the thermal conductivity decreased with increasing atomic mass and ionic radii of the dopant species.[88] These results support the school of thought that the A-site dopant species does not affect the electric conductivity, only the thermal conductivity.

Adding dopant ions with a smaller ionic radius than Sr would be expected to reduce the lattice parameter. This trend was observed for all dopants except La, which actually increased the lattice parameter in this study. [90,92] Lu *et al.* also confirmed that this lattice expansion effect is also seen in La doped STO sintered in a reducing atmosphere.[90] On the other hand, other studies have shown that for La doped STO, when allowed to slowly air cool, additions of La did decrease the lattice parameter. These are two contrasting effects on the lattice parameter seen from La doping.

In the 2003 study Muta *et al.* showed STO with three levels of La doping, 5, 10 and 20 mol.%, and found that the lattice parameter increased with level of doping, along with the

electrical conductivity.[88] They showed that the absolute Seebeck coefficient also decreased from 180 to 150 S/µV/K at 1000 K with increasing La content. This is likely evidence of the number of charge carriers increasing. Therefore, by increasing the level of La doping they appeared to be increasing the number of charge carriers. Though the fact remains that A-site vacancy creation is more energetically favourable so it is unlikely that La is doping is directly causing the increase in charge carriers. More likely is that the presence of La and A-site vacancies encourage oxygen vacancy creation and titanium species reduction, which leads to lattice expansion (Ti^{3+} is a much larger atom than Ti^{4+}).

In 2005 Muta *et al.* studied the lanthanum doping of europium titanate (LETO) compared to lanthanum doped strontium titanate (LSTO) and found electrical conductivity much higher than the 2003 work.[25] It is clear in this work that the conductivity is due to reduction of the titanium species from Ti^{4+} to Ti^{3+}, providing electrons to the conduction band, as they observe that the sintered pellets appeared black, which is commonly associated with Ti^{3+}. No observation of sample colour was made in their previous study. It is therefore likely that the same effect is seen in both these works, though to a greater extent in the 2005 study leading to larger amounts of oxygen vacancies and charge carrier creation.

Muta's conclusion from both these papers is that the electrical conductivity is not greatly affected by the identity of A-site species, but is affected by the level of doping. The thermal conductivity however is greatly affected by the species of the A-site ion. In order of effectiveness of reducing the thermal conductivity was: Dy, Y, Gd, Sm, La. Overall Dy doping gave the largest ZT due to the reduction in thermal conductivity. This correlates to the ionic radii of the dopant species with smaller ions reducing the thermal conductivity the most.

Table 1.4.3 Ionic radii and atomic mass of A-site species. Where CN 12 was not given in Shannon Radii the next largest CN is quoted.

A-site Species	Ionic radii in CN 12 (Å)[80]	Atomic mass (g/mol)
Dy^{3+}	1.038 (CN 9)	162.5
Y^{3+}	1.075 (CN 9)	88.905
Gd^{3+}	1.107 (CN 9)	157.25
Sm^{3+}	1.24	150.36
La^{3+}	1.36	139.905
Eu^{3+}	1.12 (CN 9)	151.964
Nd^{3+}	1.27	144.242
Sr^{2+}	1.44	207.2

However, Kilner *et al.* suggest, and Hui *et al.* concur, that in order to predict the effect of a dopant rather than just looking at the ionic radii it is more helpful to consider the pseudocubic lattice parameter. Doing this means that the effect of both the ionic size and the Ti^{3+} produced under reducing conditions is considered. For $SrTiO_3$ the pseudocubic lattice parameter is 3.905 Å, $LaTiO_3$ is 3.956 Å due to the creation of Ti^{3+}.[70,96] This would explain the increase in lattice parameter when La is added.

Hui *et al.* stated that although the electrical properties are mainly determined by the Ti-O bond, the A-O interaction can modify the Ti-O interaction.[70] This is because of the pi bond which surrounds the Ti-O-Ti bond is optimised when the bonding angle is 180 °, any

distortions to the lattice, cubic to orthorhombic perovskite for example, can change the angle of this bond and therefore reduce the electrical conductivity. The pi bond is optimised in a cubic structure, with the tolerance factor close to 1. A-site dopants of course have the ability to reduce the tolerance factor depending on their ionic radii and factional occupancy.

Further to this increasing the electronegativity of the A site ion can weaken the Ti-O covalent bond.[70] By pulling the electrons more towards itself rather than becoming fully ionised and donating electrons to the O, this affects the ability of the O to form the covalent bond with the Ti which requires electron sharing.

Hui *et al.* found that a smaller ionic radii dopant allows the lattice parameter to contract which increased the level of overlap of the Ti 3d orbitals, responsible for conduction, therefore increases the electric conductivity.[70] Furthermore the addition of small ionic radii dopants compensate for the creation of the larger Ti^{3+} ion which reduces strain in the lattice and therefore encouraged reduction.[70] Comparing dopants Yb, Y, Gd, Sm, Pr, La they found that all but Y fit this trend, though the change in electrical conductivity was very small and all were below 10 S/cm except for Y which was ~60 S/cm at 800 ºC.[70] The cause of the large electrical conductivity in Y doped STO is unknown.

Similarly, an important study by Kovalevsky *et al.* was published which studied the effect of doping strontium titanate with: La^{3+}, Nd^{3+}, Sm^{3+}, Gd^{3+}, Dy^{3+} and Y^{3+} at a level of 10%.[94] All but the La dopant created tetragonal perovskites. These samples where sintered in a heavily reducing atmosphere to intentionally create oxygen vacancies and boost the electrical conductivity. Through using thermo-gravimetric analysis they found that the final material had a stoichiometric or excess level of oxygen. They proposed that vacancies were being created and Ti species reduced in the reducing atmosphere, evidenced by the high level of electrical conductivity, but that the compensation mechanism was not the creation of a site vacancies as proposed in previous studies. Rare earth [3+] ions were being compensated for by a mix of titanium reduction and the creation of layered perovskite structure.[94]

They also stated that in order to understand the effects of dopants it is more effective to consider the pseudo cubic lattice parameter containing the dopant ion because this accounts for the specific defect creation present, the level of overlap in the Ti 3d orbitals and the symmetry distortions. Smaller dopants can distort the TiO_6 octahedra, thereby reducing the symmetry. All but the La dopant reduced the symmetry to tetragonal in this study, shown by peak splitting in the XRD.[94] A high level of symmetry is important to the Seebeck coefficient and therefore this would be reduced by the addition of small dopants. Furthermore, a smaller lattice parameter increases the level of Ti 3d overlap and so increases the electrical conductivity.

Kovalevsky *et al.* showed a less clear trend between the ionic radii of the dopants and the power factor than with the pseudocubic lattice parameter and the power factor, which sloped down with increasing pseudo cubic lattice parameter, Figure 1.4.3.[94] Their highest power factor was recorded in Nd doped STO which was 1.54 W/mK^2 at 673 K.[94] An exception was seen for Y, which was also seen by Hui et al., though this time the power factor was much lower for Y.[70] This was put down to the presence of a secondary pyrochlore phase present in the XRD.[94]

At 950 ºC the lattice contribution to thermal conductivity was lowest for the smaller dopants Gd and Dy, followed by Nd. This was attributed to the distortion of the crystal lattice with smaller ionic radii dopants.[94]

The largest ZT of 0.41 at 800 ºC was shown in $Sr_{0.9}Dy_{0.1}TiO_{3-\delta}$ as this had the most effective balance of high power factor, from small pseudo lattice parameter, and low thermal conductivity as it has a large atomic mass.[94]
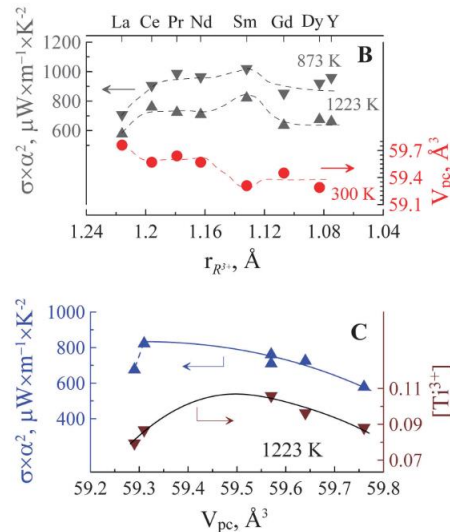
Figure 1.4.3 Power factor versus ionic radii of rare earth dopant and pseudocubic lattice volume for A-site doped strontium titanate by Kovalevsky et al.[94]

To summarise these findings, it is not clear that the specific identity of the A-site ion does not directly control the electronic properties of doped strontium titanate, despite some claims to the contrary. The A-site ion in some cases has been shown to dictate the power factor through manipulation of the symmetry, Ti-O-Ti bond length and Ti 3d band overlap and have little to no effect in other cases.

What is clear is that the A-site species in all cases has an effect on the thermal conductivity due to its ability to scatter phonons. This is controlled by the mass of the atom and the distortion of the unit cell.

1.4.3 Co-doping on the A-site

Co-doping on the A-site has been employed to reduce the thermal conductivity further by creating varying levels of strain in the lattice, which scatter phonons.

Iyasara *et al.* reported the thermoelectric properties of co-doped $La_xSm_xSr_{1-2x}TiO_{3-\delta}$.[97] They did not report their own values for single doped (La,Sr)TiO₃ for direct comparison of single and double doped STO. Though comparing the thermal conductivity of 3.8 W/mK at 700 ºC they reported for $La_{0.05}Sm_{0.05}Sr_{0.9}TiO_{3-\delta}$, with that of $Sr_{0.9}La_{0.1}TiO_3$ reported by Muta *et al.* in 2003 (3.3 W/mK at 680 ºC), the conductivity is in the same realm as the single doped species. However, it is difficult to compare samples between studies as properties vary greatly with

synthesis and processing conditions as has been shown above. Despite this the ZT was a modest value of 0.21 at 700 ℃.

Table 1.4.4 ionic radii and atomic mass of A-site species in STO by Iyasara et al.[97]

A-site species	Ionic radii in CN 12 / Å	Atomic mass /g/mol
Sr^{2+}	1.44	87.62
La^{3+}	1.36	138.905
Sm^{3+}	1.24	150.36

Lin *et al.* showed a study systematically varying the composition between $Sr_{0.8}Nd_{0.2}TiO_{3-\delta}$ and $Sr_{0.9}Dy_{0.1}TiO_{3-\delta}$ which were reduce sintered.[98] It is important to note that the level of donor doping in each composition was different which makes the elucidation of the electrical conductivity patterns more difficult. What was interesting is that the single doped Nd-STO (3.9096 Å) had a larger lattice parameter than that of pure STO (3.9050 Å), despite Nd having a smaller ionic radius than Sr. This is demonstrative of the effect previously mentioned where not only does the ionic radii influence the pseudo cubic lattice parameter but also the compensation mechanism. One would expect the lattice parameter to decrease if only considering the ionic radii though in this case the increase of the lattice parameter was suggested to be because of the creation of Ti^{3+}.[98] Though this could also be an A-site vacancy with a none zero radius due to electrostatic repulsion between oxygen ions.

Table 1.4.5 Ionic radii and atomic mass of A-site species used by Lin et al.[98]

A-site species	Ionic radii in CN 12 / Å	Atomic mass /g/mol
Sr^{2+}	1.44	87.62
Nd^{3+}	1.27	144.242
Dy^{3+}	1.083 (CN 9)	162.5

Then when Dy content was increased in steps of 3, 5, 7, 10 mol.% the lattice parameter decreased, as shown by the shift in the (110) peak to higher angles in Figure 1.4.4. In this case the Nd decreasing at twice the rate of the Dy increasing. Therefore, the overall level of doping is decreasing bringing the lattice parameter closer to the ideal cubic perovskite but the lattice parameter drops below that of pure STO when Dy doping level reaches 7 mol.% (3.9033 Å) and is even further reduced at 10 mol.% doping level (3.9027 Å) as Dy has a smaller ionic radius than Sr.
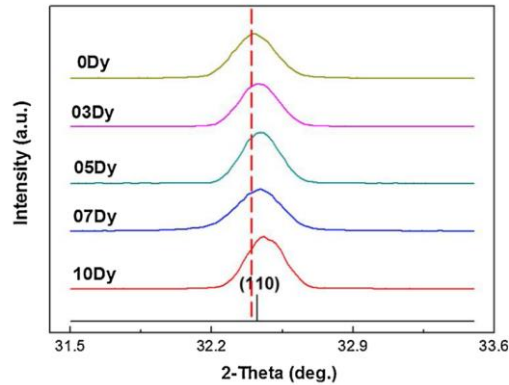
Figure 1.4.4 XRD of the (110) peak in the cubic perovskite with increasing Dy content.[98]

These lattice parameters have a direct correlation to the thermal conductivities seen in each sample. The thermal conductivity first increased with increasing Dy doping level up to to 5 mol.%, these lattice parameters are above the ideal cubic perovskite lattice parameter. However, for 7 and 10 mol.%, where the lattice parameter is below that of the ideal cubic perovskite lattice parameter, the thermal conductivity decreases. This is due to strain in the lattice causing phonon scattering.

The other factor that would affect thermal conductivity is the grain size. There is a clear increase in grain size from 0 mol.% Dy (5-8 μm) to the other samples with larger Dy concentrations (8-30μm).[98] This could also be the cause of the sudden increase in the thermal conductivity between 0 and 3 mol.% samples which then steadily decrease with increasing Dy.

A-site dopants have been shown to have an effect on diffusion of atoms in other work. Yang *et al.* showed that low levels of sodium doping in bismuth titanate led to an electrically two phase composite.[99] This was because the dopant was in homogenously mixed throughout the material due to the solid state synthesis method, leading to areas with effectively no dopant and areas of rich dopant levels. The presence of the dopant increased the diffusion coefficient in those areas and lead to larger grains. Sintering and grain growth are diffusion controlled processes so an uneven diffusion coefficient led to a distribution of small (low electrical conductivity, due to grain boundaries) and large grains (higher electrical conductivity due to pristine matrix).[99]

Returning to the work by Lin, the electrical conductivity reduced with increasing Dy content, which was also corroborated by XPS data which showed a steady reduction in Ti^{3+}/Ti^{4+} ratio. This is likely due to the fact that the overall dopant level (Nd + Dy) was also decreasing, leading to less requirement of the compensation mechanism which produces Ti^{3+}. This seemed to outweigh the effect that larger grains would be expected to have on the electrical conductivity, as electrical conductivity of the 3 mol% Dy was less than the 0 mol.% sample which had much small grains. Grain boundaries usually cause electron scattering, leading to lower electrical conductivity.

The highest ZT they achieved was 0.19 at 400 ℃ for $Sr_{0.87}Dy_{0.07}Nd_{0.06}TiO_{3-\delta}$ as this had a low thermal conductivity that was balanced by a higher power factor than the 10 mol% Dy sample.

Zhang *et al.* took co-doping to the nth degree by studying high entropy perovskites. High entropy alloys typically contain more than five elements. They showed (Ca $_{0.2}$Sr$_{0.2}$Ba$_{0.2}$La$_{0.2}$Pb$_{0.2}$)TiO$_3$, which had an extremely low thermal conductivity of 2.2 W/mK at 800 ºC, which was attributed to the short range chemical disorder from the variation of A site species.[100] Table 1.4.6 shows the ionic radii and atomic mass of these ions. It can be seen that the high entropy perovskite had a greater variation in the atomic mass of A-site dopants, which likely caused a greater strain on the lattice leading to low thermal conductivity. Using high resolution TEM Zhang showed the large density of dislocations and strain fields in their material, confirming this theory.[100] The presence of Pb in particular, being a large and heavy atom, would make thermal transport more difficult as it is a large scattering centre.

Table 1.4.6 ionic radii and atomic mass of A-site species in STO by Zhang et al.[100]

A-site species	Ionic radii in CN 12 / Å	Atomic mass g/mol
Sr^{2+}	1.44	87.62
La^{3+}	1.36	138.905
Ca^{2+}	1.34	40.078
Ba^{2+}	1.61	137.327
Pb^{2+}	1.49	207.2

Table 1.4.7 shows a summary of the thermoelectric properties of the co-doped STO discussed so far. These show generally higher electrical conductivity than the only oxygen deficient or a single doped STO shown so far. Therefore, are closer to achieving a high ZT thermoelectric material.

Table 1.4.7 Thermoelectric properties of co-doped strontium titanates.

Composition	ZT	Temp. / ºC	Electrical conductivity / S/cm	Thermal Conductivity/ Wm^{-1}K^{-1}	Seebeck coefficient / uVK^{-1}	Source
La$_{0.075}$Sm$_{0.075}$Sr$_{0.85}$TiO$_{3-\delta}$	0.21	700	250	3.6	-176	Iyasara, 2017[97]
La$_{0.05}$Sm$_{0.05}$Sr$_{0.9}$TiO$_{3-\delta}$	0.21	700	207	3.8	-200	Iyasara, 2017[97]
Sr$_{0.87}$Dy$_{0.07}$Nd$_{0.06}$TiO$_{3-\delta}$	0.19	400	514	4.1	-156	Li, 2020[98]
(Ca$_{0.2}$Sr$_{0.2}$Ba$_{0.2}$La$_{0.2}$Pb$_{0.2}$)TiO$_3$	0.10	700	65.6	2.4	-172	Zhang, 2022[100]

1.4.4 A-site Vacancies and Oxygen Loss

As well as dopants, an A-site vacancy can also affect diffusion of atoms in the material. There are contradicting claims in the literature about the effect that an A-site vacancy has on oxygen migration. According to Walsh *et al.* interaction with a strontium vacancy reduced the oxygen diffusion but an oxygen vacancy enhances the diffusion of strontium.[101] For thermoelectricity it is the oxygen diffusion which is most important as this leads to oxygen vacancy creation which is an important strategy for increasing electrical conductivity, and will be discussed further in the next section.

They show that oxygen follows a curved path around the neighbouring titanium cation, rather than a direct path between two oxygen lattice sites in order to follow a path of energy minima. Through first principle studies they calculate the activation energy for an oxygen to move past a strontium atom is 0.53 eV and the activation energy to move past an A-site vacancy is 0.89eV.[101] Though the reason for this is not claimed by this group.

Ubic *et al.* show that oxygen's surrounding an A-site vacancy do not relax inwards when vacancy concentration is above 1.5 mol %.[102] The vacancies in fact have a non-zero positive size, possibly due to the repulsion of surrounding oxygen anions. [102] This may explain why it is difficult for oxygen to migrate around an A-site vacancy due to the high level of repulsion between oxygen anions in that area.

Contradictory to the work by Walsh *et al.*, Akin *et al.* claim that A-site vacancies in fact encourage oxygen loss. [93] They found that compared to non-doped STO, La doped STO showed a dramatic increase in electric conductivity regardless of being sintered in O_2 or an inert gas at 1450 ºC.[93] They deduce that this is because of the A-site vacancies generated by the doping compensation, encourage oxygen loss and titanium reduction leading to high electric conductivity.[93] Specific conductivities of the highly conductive samples are not given as they used impedance spectroscopy of the samples, so when a large electrical conductivity was seen the sample could not be measured.

Despite this contradictory school of thought when A-site deficient La doped and reduced STO is combined high ZTs are observed. The composition $Sr_{0.775}La_{0.15}TiO_{3-\delta}$ by Lu *et al.* shows one of the largest ZTs for n-type strontium titanate to date, combining a record high power factor with moderately low thermal conductivity.

Table 1.4.8 Thermoelectric properties of A-site deficient, donor doped and reduced strontium titanate.

Composition	ZT	Temp. / ºC	Electrical conductivity/ S/cm	Thermal Conductivity / $Wm^{-1}K^{-1}$	Seebeck coefficient / μVK^{-1}	Source
$Sr_{0.775}La_{0.15}TiO_{3-\delta}$	0.41	700	416	2.7	-163	Lu, 2016[90]
$Sr_{0.5}La_{0.33}TiO_{3-\delta}$	0.27	797	200	3.5	-180	Azough, 2017[103]

1.4.5 Summary

In summary the some of the most common individual strategies to increase the thermoelectric figure of merit are doping onto the A-site donor dopants, oxygen deficiency and A-site deficiency. These strategies each have benefits of their own which can be compounded when applied simultaneously. The great advantage of the perovskite structure is that it is flexible enough to be able to accommodate multiple dopants and vacancies to some degree whilst maintaining its structure. The best n-type thermoelectric performances reported to date have been dysprosium dopes and oxygen deficient strontium titanate by Kovalevsky *et al.,* which had a ZT of 0.41 at 800 ºC, and an A-site deficient, La doped and oxygen deficient strontium titanate made by Lu *et al.* which had a ZT of 0.41 at 700 ºC.[90,94] These values are still below the desired ZT of 1 which will be able to compete with existing materials such as bismuth telluride and so more work is needed to improve the thermoelectric figure of merit. There is opportunity for this in the reduction of the thermal conductivity which could become lower – the thermal conductivity of the high ZT material bismuth telluride has a thermal conductivity ~1 W/mK whereas the strontium titanate based materials have only got as low as ~2 W/mK.[57]

1.5 Reducing Thermal Conductivity Via Alternate Synthesis and Processing Routes

1.5.1 Grain Boundary Properties

Increasing the density of grain boundaries can be used to reduce the thermal conductivity of materials as phonons are scattered by grain interfaces.[23] The specific grain boundary properties vary from sample to sample.[83] Herein the grain boundary properties of strontium titanate based materials are the focus. In strontium titanate the grain boundaries highly affect the electrical conductivity as well as the thermal conductivity. This is because of the build-up of electrostatic potential at the barriers which act as a barrier for the charge carriers.[104]

Dylla *et al.* showed that in oxygen deficient STO grain boundaries have an electronegative potential.[104] This is attributed to the lower concentration of positivity charged oxygen vacancies at grain boundary regions, compared to the bulk.[104] A schematic to demonstrate this is shown in Figure 1.5.1. With this in mind a polycrystalline material can be considered a two phase material: bulk and grain boundary. The electrical conductivity is largely affected by the grain boundary region because the resistivity can be so high in this region.[104]
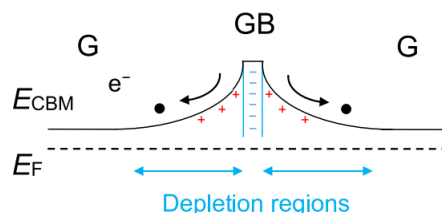
Figure 1.5.1 Grain boundary potential demonstrated by Cao et al.[83]

Comparatively, the Seebeck coefficient is less affected by the grain boundary density as the values within the boundary and in the bulk are not so widely dispersed. Polycrystalline and single crystal Seebeck coefficients, where the carrier concentration is equal, are largely

comparable.[104] An energy filtering effect occurs when low energy electrons are not able to overcome energy barriers at grain boundaries, thus improving the Seebeck coefficient as fewer charge carriers are taking part in conduction. Though this only prominent for grain sizes around 50nm or less.[105] Whether this has an overall improvement on the power factor is uncertain as this can result in a significant reduction in the electrical conductivity.[105,106]

Cao *et al.* modelled the effect of varying grain boundary potentials heights and how this would affect the electrical conductivity, Figure 1.5.2. At low temperatures in particular, the electronic thermoelectric properties are subdued by a large density of grain boundaries. In higher temperature regions, > 500 ℃, electronic properties are less dominated by grain boundary resistivity.[104]
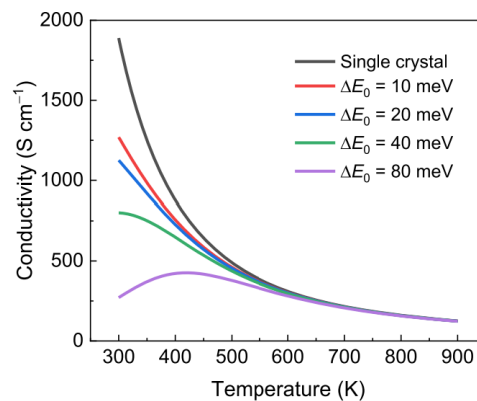
Figure 1.5.2 Modelled temperature dependency of electrical conductivity for SrTiO$_3$ using a two phase model (grain and grain boundary) with different band offset values (ΔE0) and a fixed BD thickness.[83]

Due to the ability of grain boundaries to affect the thermoelectric properties, nanoscalling has reignited the research for high ZT thermoelectric materials. Simply by changing the processing or grain boundary conditions, new ZTs emerged.

1.5.2 Applying Grain Boundary Engineering

Buscaglia *et al.* investigated the effect grain sizes ranging from 6μm to 24nm had on the thermoelectric properties of $Sr_{0.9}La_{0.1}TiO_3$ between 0 and 300 K. [107] Due to the lower temperature using high-pressure field assisted sintering (HP-FAST) most of the La was compensated for by A-site vacancies so conductivity was very low compared to other studies whose dopants and processing conditions induced the reduction of Ti.[90] They saw that the specimen with 24nm had a thermal conductivity of 1.2 W/mK at RT which was one order of magnitude less than the largest grain size sample.[107] The thermal conductivity generally decreased with decreasing grain size, becoming predominantly lower below 35nm. The group also saw a marked reduction in the electrical conduction of the smaller grained samples; interfaces between randomly orientated grains scatter electrons as well as phonons, reducing electrical conductivity.

A reduction in Hall mobility was measured by Ohta *et al*. in 200 nm grained Nb doped STO compared to 20μm or single crystal samples. [108] In this case all three grain sizes reached the same ZT value of 0.35 at 1000 K at which temperature ZTs converged suggesting that grain boundary effects are less prominent above 1000 K. They attribute this to the narrowing of the double Schottky barrier formed at the interface between grains as temperature is increased, due to the rapid increase of the relative static dielectric constant of the material at high temperatures.[108]

A massive increase in the Seebeck coefficient can be achieved by inducing electron confinement by reducing dimensions, which increases the density of states at the edge of the conduction band.[109] Ohta *et al*.[110] created a 2D electron gas in $SrTi_{0.8}Nb_{0.2}O_3$ confined between insulating layers of $SrTiO_3$ which showed approximately five times the Seebeck coefficient to bulk $SrTi_{0.8}Nb_{0.2}O_3$ (108 µV/K at 300 K). The Seebeck coefficient of a one-unit cell layer sample had a $|S|$ of 480 µV/K at 300 K. [110]

Wang *et al*.[111] intentionally manipulated the grain boundary (GB) composition by coating reduced La-STO powders in NbO_x compounds before densification, creating Nb doped grain boundaries. Nb doping for Ti can lower the bottom of the conduction band which forms a band offset, forming quantum wells at the GB. Trapped electrons lead to negatively charged GB which enhance the potential barrier height; creating greater energy filtering effect. This technique enhanced the power factor from ~5 to 5.75 x10-4 W/mK^2 at 600 K due to increased $|S|$, -190 to -220 µV/K and only slightly decreased electrical conductivity.

1.5.3 Solid State Synthesis

The conventional route to synthesise oxides is solid state synthesis. This concerns the combining of constituent elements in their carbonate or oxides forms. For example, for La doped STO, La_2O_3, $SrCO_3$ and TiO_2 are used as raw materials which typically have starting grain sizes on the scale of microns. Stoichiometric masses of raw materials are dried, combined and typically go through several milling, grinding, sieving and calcining steps to achieve a homogenous product. This technique relies on solid state diffusion limited by interfacial contact between grains, therefore, high temperatures and long hold times are required to achieve homogenisation. Typical calcination regimes for doped strontium titanate are 1050 -1300 ℃ for 3 - 6 h. [24,25,70,88,90,93,100,102,103]

Densification is then encouraged by pressing the powers and sintering at high temperature. Typical sintering conditions for doped strontium titanate vary between 1250 – 1600 ℃ for 2 - 20 h, in either air or low oxygen partial pressure atmospheres, depending if the oxygen deficient material is desired. [24,25,70,88,90,93,100,102,103] The densification process is driven by the reduction of surface energy and so grain growth is key to this process. Typical grain sizes in the sintered products are between 2-20 µm.[24,90,93,99,100,103]

This method is highly energy intensive resulting in a large embodied energy of ceramics which create a significant CO_2 burden associated with solid state sintered ceramics. Not only this but this technique makes manipulation of grain sizes or textures very difficult. In order to access the possible ZT improvements described from reducing grain size then alternative calcination and sintering routes must be explored.

1.5.4 Low Temperature Calcination Routes

Wet chemical synthesis methods are advantageous for creating nano sized functional oxides because the precursors become atomically dispersed in a liquid or gel. This allows much faster rates of diffusion than solid state diffusion, and so products can form much faster and at much lower temperatures, resulting in smaller grained products and energy savings compared to solid state synthesis.

Furthermore, particularly in the production of titanates such as $SrTiO_3$ a common impurity seen in final products is TiO_2.[112] TiO_2 is used as the source of Ti species in solid state synthesis, it is a highly stable compound which requires very high temperatures to break down and encourage transformation into other structures. These conditions also promote significant grain growth. Titania impurities in the final product inevitably alter the stoichiometry of the product from that which was set out to produce, and possibly cause additional effects to the materials properties so they must be avoided. A solution to this is to avoid TiO_2 as a precursor, instead using a low viscosity medium capable of chelating titanium ions.

In the following sections some of the most common low temperature calcination routes for oxides are described. These techniques demonstrate the use of alternative precursors to solid oxide and carbonates, which lead to energy savings and grain size reductions compared to solid state synthesis.

1.5.5 Sol- gel

The sol-gel method generally describes a method in which set of precursors, typically metal alkyoxides, are dissolved in water or alcohol which undergoes hydrolysis/alcoholysis and condensation reactions to form a gel.[113] This gel is then dried, where nano powders, fibres or layers can be formed, then calcined. [113] Figure 1.5.3 shows an overview of the types of processing that can be done with the sol-gel method and the resulting morphologies.
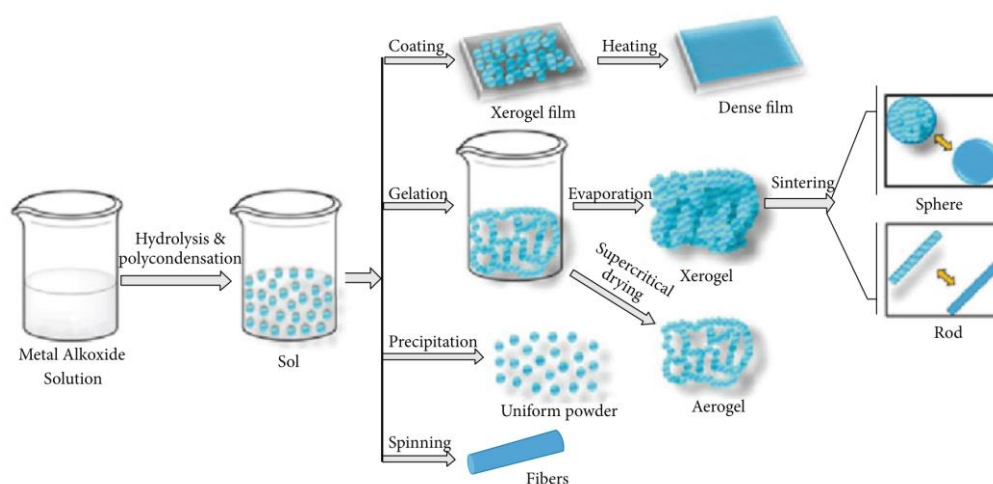
Figure 1.5.3 Overview of the sol-gel process and morphologies that can be synthesised.[113]

Yue *et al.* synthesised ZnO nanotubes using the sol-gel method in which zinc acetate and diethanolamine were dissolved in ethanol.[114] They then dipped an ultra-thin aluminium oxide honeycomb structured membrane into the solution, whose surface became coated in the sol. Once removed this was allowed to dry then calcined at 500 ℃ for 2 hr which crystallised ZnO.[114] The membrane was then dissolved with sodium hydroxide, leaving individual ZnO nanotubes as shown in Figure 1.5.4.
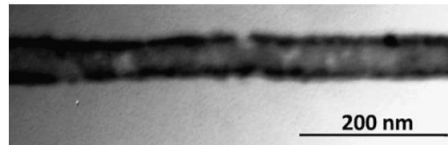
Figure 1.5.4 TEM micrograph of ZnO nanotube.[114]

The sol-gel method has also been widely used to synthesise nanoparticles of TiO_2.[115–117] Li *et al*. synthesised titania nanoparticles by dropping tetra-*n*-butyl titanate into deionized water whilst stirring.[117] Then the gel was allowed to dry at 105 ℃ for several hours, before milling the into a powder. This was then calcined for 2 h between 350 ℃ and 1000 ℃. Their XRD indicated that partial crystallisation occurred after the drying step. This was in the form of anatase. At ~550 ℃ rutile was also visible in the XRD which increased in relative intensity until finally only rutile titania was present after calcining above 800 ℃.[117] The grain sizes of the calcined powders are shown in Figure 1.5.5 which varied between 6nm for the lowest temperature and 120 nm for the highest calcination temperature.
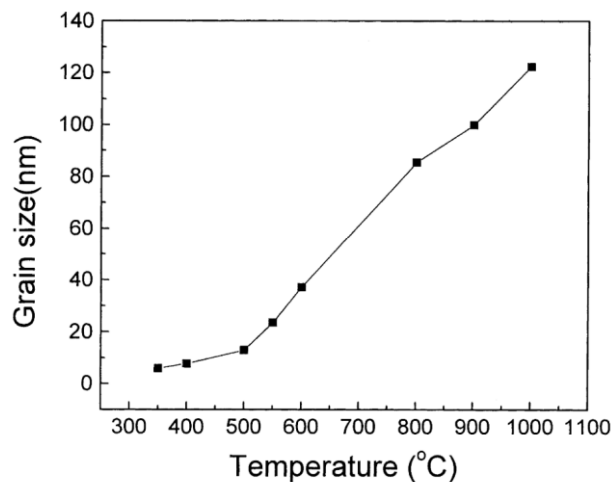
Figure 1.5.5 Grain sizes of titania synthesised by Li et al. using the sol-gel method, vs the calcination temperature. [117]

The main advantages of the sol-gel process are that it is a simple process, with high production efficiency and the flexibility to make products with special shapes.[113]

1.5.6 Pechini's Method

Pechini's method is a modified sol-gel process. In Pechini's method α-hydroxycarboxylic organic acids (e.g. citric acid) chelate cations in an aqueous-organic medium. The addition of a polyhydroxylic alcohol to this mixture polymerises the chelate creating a homogeneous distribution of cations. The organic portion is burnt off at temperatures leaving the pure final product.[118]

Liu *et al.* synthesised $Ca_3Co_4O_9$ using this method from calcium nitrate, cobalt nitrate hexahydrate and citric acid which forms a gel that was calcined at 800 ºC to produce fine grained pure phase product.[119] This group did not state the grain size produced from this calcination, though after sintering at 900 ºC for 8 h the grains were less than 2μm in dimension.[119] Dhiman *et al.* demonstrated the pechini method for $LaRe_xFe_{1-x}O_3$ (Re = Eu, Gd, Dy, Nd) using lanthanum, iron and RE hydrates, citric acid and ammonia.[120] Their final product showed high purity under the scrutiny of TEM and EDS, with crystallite sizes of 28-38 nm after annealing at 400 ºC.

1.5.7 Hydrothermal Synthesis

Hydrothermal synthesis uses the assistance of pressure above 1 bar and temperatures above 100 ºC to encourage reactions.[121] It allows uniform, nanosized particles to be made at low temperature using high pressure.[122] Cirkovic *et al.* used a hydrothermal treatment on a solution of barium strontium titanate (BST) synthesised using the Pechini method (complex polymerisation method). Highly pure and a homogeneous microstructure are important for the application of BST as dielectric materials.[122] A BST precursor solution was placed in an autoclave for 5h at 225 ºC and 67.1 atmospheres.[122] This created an amorphous powder which was then calcined at 700 ºC to crystallize the final product. They stated that stoichiometry is hard to control using the hydrothermal treatment, so the complex polymerisation technique was used to ensure the correct stoichiometry and the hydrothermal treatment improved the purity (removing carbonate phases, though there was another off-stoichiometry phase present) and created uniformly nano-sized powders < 50 nm which were less agglomerated compared to the complex polymerisation route.[122] This procedure required a Teflon lined high pressure autoclave – this method is expensive and harder to upscale.[122]

1.5.8 Co-precipitation

Co-Precipitation is the mixing of two or more different solids or liquids which are mixed and stirred continuously to form a precipitate.[123] Hikmah *et al.* performed this for $SrTiO_3$ by combining strontium nitrate $(Sr(NO_3)_2)$, oxalic acid dihydrate $(C_2H_2O_4.2H_2O)$ and titanium tetrabutoxide $(Ti(OCH_2CH_2CH_2CH_3)_4)$. All were individually dissolved in isopropanol before combining. This solution is continuously stirred, titrated in distilled water, washed with ethanol, then hydrolysed for 10h.[123] This produced a precipitate which they then sintered between 800-900 ºC for 2-4 h.[123] The low cost of these precursors comparative to ionic liquids make this a cost effective synthesis method.

Hikmah *et al.* reported impurities of $SrCO_3$ based carbonates due to reactions between the metal ions and the organics.[123] They show from FTIR analysis the presence of additional O-H bonds at 3406 cm^{-1}, 2458 cm^{-1} and 857 cm^{-1}, C=O stretching vibration at 1747 cm^{-1}, C-H at 1439 cm^{-1} as well as the characteristic bending and stretching of Ti-O bonds within TiO_6 octahedra in $SrTiO_3$ ~540 cm^{-1}.[123,124] The FTIR absorptions corresponding to Ti-O and the C=O at 1746 cm^{-1} were confirmed by Xian *et al.* though they also stated that the C=O overlaid with a O-H from H_2O absorption.[124] Xie *et al.* confirmed O-H absorptions at similar values of 3436 cm^{-1} and 1630 cm^{-1} in the spectra of pure BiOCl, pure $SrFe_{12}O_{19}$ and BiOCl–$SrFe_{12}O_{19}$ made via hydrolysis. The C-H absorption at 1439 cm^{-1} found by Hikmah *et al.* could not be confirmed from other sources, and in fact matches better with an O-H bending mode.[125]
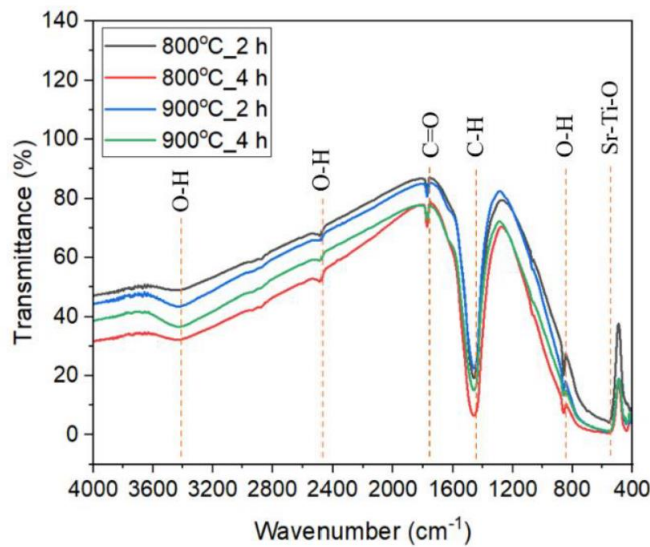
Figure 1.5.6 FTIR of SrTiO$_3$ made via the co-precipitation method by Hikmah[123]

Hasanah *et al.* also performed co-precipitation to produce Nd-doped STO.[87] In their FTIR additional C=H, C-H and O-H bonds were also found in the final product, Figure 1.5.7. Here the C-H bond is shown at 854 cm^{-1}, the C=H bond at 1490 cm^{-1}, O-H bond at 3407 cm^{-1} and the characteristic large absorption of the TiO_6 octahedra at 576 cm^{-1}. The Nd-doped STO was sintered at 900 and 1000 ℃ for 4 h which yielded crystallite sizes of 42 nm and 64 nm respectively. As well as grain growth the increased sintering temperature increased the level of crystallinity from 94.8 % to 95.7 %. [87]
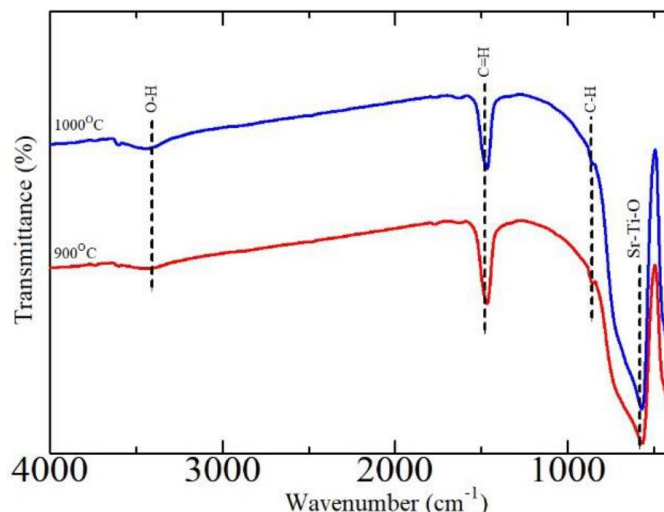
Figure 1.5.7 FTIR of Nd- doped SrTiO₃ made via co-precipitation method by Hasanah[87]

So far none of the methods presented are able to synthesise titanates such as STO or BTO using a simple technique at atmospheric pressure. The sol-gel process is highly simple but hydrolysis reactions induce the formation of TiO_2 which requires high temperatures to remove. Other methods use harsh chemicals such as acids or ammonia or use involved processes like titration or high pressures. There is another low temperature calcination method not yet covered which uses solvents considered green and can be performed at atmospheric pressure in a couple of steps. This technique is Ionic Liquid Synthesis.

1.5.9 Ionic Liquid Synthesis

An Ionic Liquid (IL) is a salt with a melting point below 100 ºC. They consist of a complex cation, such as 1-ethyl-3-methlyimidazolium (emim), and a hard anion, e.g. acetate (OAc) which are shown in Figure 1.5.8.[126] They are an attractive solvent in many synthesis applications because of their fast ion transport, low viscosity, wide liquid temperature ranges and structure forming properties on the nanoscale.[127] Low viscosity is a particularly important property because this facilitates fast mass transfer and avoids the formation of impurity phases in the final product.[128] Other successful applications of ionic liquids include: solvents for the ligation of peptides, electrolytes in batteries.[129,130]
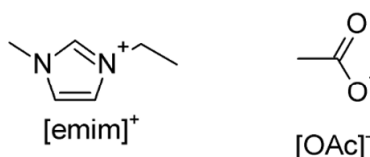
Figure 1.5.8 Structure of IL cation emim and anion OAc. [126]

They are a highly flexible class of materials, their properties can be tuned by selecting combinations of anions and cations. For example, their water solubility can be decreased by using the hydrophobic anion, [NTf₂], increased by using the hydrophilic anion [BF₄].[131] ILs have also been described as "green solvents" due to their low environmental toxicity, although are typically a high cost solvent.[131]

ILs are particularly useful in the synthesis of complex titanates, as titanium ions, from for example titanium alkoxide precursors, readily and exothermically form poorly crystalline TiO_2 in contact with water, and so water is not a suitable solvent for the wet chemical synthesis of titanates. Whereas, ionic liquids such as 1-ethly-3-methlyimidazolium acetate, can chelate Ti ions, holding them in suspension where they are able to take part in reactions to form titanates.

An IL synthesis method was demonstrated by Green *et al.* and Mottram *et al.* for the synthesis of complex functional oxides: (La,Sr)TiO$_3$, $YBa_2Cu_3O_{7-x}$ (YBCO) and $Bi_2Sr_2CaCu_2O_8$ (BSCCO). [128,132] This process involved first mixing aqueous solutions of soluble metal ions with the ionic liquid (e.g. 1-ethyl- 3-methylimidazolium acetate or nitrate), dehydrating this mixture to remove water, and then adding insoluble species as alkoxide precursors (if required) before calcining the entire mixture for 2 h to form the crystallised product.[128,132] Calcination temperatures varied between 600 ºC and 920 ºC depending on the material.[128,132] Green showed highly crystalline and pure YBCO and BSCCO confirmed by SEM, TEM and EDX calcined at 920 ºC and 850 ºC respectively. Using the solid state synthesis method YBCO requires calcining in the range of 850 ºC for 16 h and BSCCO at 775 ºC for 12 h.[133,134] The calcination times, therefore the energy inputs, are much reduced when using the ionic liquid method owing to the greater rate of mass diffusion using this method.

Mottram *et al.* showed the formation of (La,Sr)TiO$_3$ from an ionic liquid solution though combined TG and DSC alongside XRD analysis taken at set temperature intervals during the calcination which revealed the reaction process.[132] Initially small particles of anatase, mixed La and Sr carbonate species were formed, which they suggested act as reaction sites for the formation of the final product: the perovskite. Due to the large surface area of the intermediate species, this occurred rapidly.[132] Phase pure cubic perovskite LST was achieved at 600 ºC using this ionic liquid synthesis method. The size of the particles was 36 ± 12 nm. The lattice parameter found by Mottram *et al.* was 3.9076 ± 0.0009 Å, which is larger than that recorded by Lu *et al.* (3.8467 Å) who synthesised the same composition using solid state synthesis.[90,132] As these are supposed to be the exact same composition, this difference in lattice parameter is significant and must be explained by some change in stoichiometry or templating effect which was not explained by Mottram *et al.*

Alternatively, several studies have shown that highly crystalline titania can be synthesised using ILs at ambient pressure and temperatures.[135–139] The water-immiscible IL 1-butyl-3 methyl imidazoloium hexafluorophosphate ([Bmim][PF$_6$]) acts as a capping agent to prevent direct contact of water and titanium source (titanium tetraisopropoxide). This prevents fast hydrolysis that would result in amorphous TiO_2, and instead encourages crystalline TiO_2.[135] In this method titanium isopropoxide and propanol are added to the IL which is then added drop wise to water, where precipitations of titania are formed. The crystalline titania can then be extracted via through filtration, washing and drying at 100 ºC. Using this method Yoo *et al.* found that titania crystallised in the anatase structure, which showed the same level of crystallinity as a sol-gel synthesised anatase calcined at 400 ºC.[137] In the same conditions with no IL the titania came out amorphous.[137] Using this same method Choi *et al.* recorded a crystallinity of 37% with 5nm crystallite size, the crystallinity could be improved by a further heat treatment of 900 C for 1 hr which grew the crystallite size to 40nm and remained anatase.[135]

The imidazolium units form π-π bonds between one another which form an ordered structure around which the titania is hydrolysed and condensed.[137]The anions in IL form hydrogen bonds with water. By changing the anions, the strength of the hydrogen bonds is changed. This has an important effect on the structure forming properties. Strong hydrogen bonds between the water and anion can mask the π-π bonds which prevents stacking. Yoo *et al.* showed that with an increase in the hydrogen bond strength from $[PF_6]^-$, $[BF_4]^-$ to $[CF_3SO_3]^-$ the degree of crystallinity in the product decreased because of this effect.[137] Yu *et al.* also showed that by changing the anion from $[PF_6]^-$ to $[Cl]^-$ a rutile phase was formed instead of anatase.[138]

1.5.10 Surface properties of Solution Processed Thermoelectric Materials

There is a caveat of using wet chemical methods to synthesise thermoelectric materials at low temperature. This was recently highlighted by a research group led by Maria Ibanez who in 2021 published a paper Entitled 'The Importance of Surface Adsorbates in Solution Processed Thermoelectric Materials: The Case of SnSe'.[140] Though this paper used SnSe as an example the findings are relevant to all solution processed thermoelectric materials. Scientists must at least be aware of this and perhaps take methods to remove them before further processing. Using wet chemical synthesis methods allows the production of much smaller grained powders compared to solid state synthesis, however the use of additional solvents can lead to the presence of impurities on the surface of final product which if not sintered at high temperatures likely remain in the final product.

In the paper 'The Importance of Surface Adsorbates in Solution Processed Thermoelectric Materials: The Case of SnSe' the products of a typical solution processed SnSe, using Na salts, is assessed and revealed to contain significant surface adsorbates which cannot be removed from the surface of particles through purification.[140] This is because of the presence of a surface charge on the particles originating from an Se rich surface (-22 ±5 mV). This creates an immobile layer of Na^+ ions adsorbed, held by electrostatic forces, to the surface when synthesised using $NaBH_4$, Se powder, NaOH and $SnCl_2.H_2O$. [140]

The consequence of this impurity is doping of the SnSe (Na^+ is a p-type dopant in SnSe and leads to three times the concentration of holes in the material), Na complexes formed at grain boundaries (this leads to an increased energy barrier at the grain boundary causing an energy filtering effect which enhanced the Seebeck coefficient) and Na precipitates within the grains nucleated by the high defect concentration.[140]

The group compared this to SnSe solution processed using Me_4NBH_4 and Me_4NOH instead of Na containing species. This replaced the Na^+ surface adsorbates with Me_4N^+ which could be removed in the annealing step at 500 ℃ leaving minimal C and N impurities. In this case much smaller grains were found in the sintered pellets. The group attributed this to the larger Me_4N^+ which covered the dissolved particles with fewer molecules than Na^+ increasing the electrostatic repulsion between particles. Furthermore, they state that the Se rich surface reacts with Na to form Na_2S_x which has two consequences: this phase melts during annealing pulling grains together through capillary action whilst also providing a liquid phase which enhances mass transport. Hence the present of the Na promotes grain growth.[140]

Although the impurity level of Na was found to be as low as 1.6 at. % it had a marked effect on the ZT by increasing the electrical conductivity and Seebeck coefficient, doubling the figure of merit. They found no effect on the thermal conductivity.[140]

This study draws important attention to the impurities which may unwittingly be adsorbed to the surface of solution processed thermoelectric materials such as in the ionic liquid, sol-gel and precipitation processes. Though the effect was overall positive in this case as Na^+ is an effective dopant for p-type SnSe, for other materials and impurities this many not have the same effect. This is clearly shown in the work by Hikmah (Figure 1.5.6) and Hasanah (Figure 1.5.7) who show unexpected elements in their FTIR. With this context in mind it may be likely these are surface adsorbed though further work would be needed to confirm this in light of the work published by Liu and Ibanez *et al.*[140]

This goes to say that solution processed materials are by no means unusable because of potential surface adsorbates, however, the likelihood of the material containing surface impurities should be acknowledged. Lui *et al.* have done important work to bring this topic of discussion to light and have provided techniques, such as Zeta potential measurements, to assess the surface properties. [140] The effect of surface impurities within the sintered product should be considered in order to determine if they have any negative or positive impact on the properties of the material. This new information could explain previously un explainable effects in properties of solution processed materials.

1.5.11 Low Temperature Sintering Methods

In order to preserve small grain sizes produced from low temperature calcination methods and continue the trend of reducing energy input, low temperature sintering methods are required. Typical solid state synthesis requires high temperatures > 1000 ºC which coarsens grain structures and required large amount of energy input.[90,141,142] Ceramics currently have a large embodied energy, meaning it takes a lot of energy to produce them, potentially making them an unattractive material in a new sustainable culture. For this reason, low temperature sintering methods have gained much interest within research.

The investigation into Ultra Low Energy Sintering began in the 1960's and now several techniques are known that can achieve densification between room temperature and 300 ºC.[143–149] Grasso *et al.* published a comprehensive review of Ultra Low Energy Sintering techniques and mapped the emergence of techniques between 1970 and 2020.[141] The first of these techniques was Hydrothermal Reaction Sintering developed by Hirano and Somiya in 1976.[150]

1.5.12 Hydrothermal Reaction Sintering (HRS)

Hirano and Somiya first demonstrated the use of HRS to create >95 % dense Cr_2O_3.[150] This technique involved combining water and ~50 μm sized metallic chromium powder in a 3 x 5 mm platinum vessel. A pressure of 98 MPa and temperature of 1000 ºC were applied to the vessel for 3 h which caused a reaction between supercritical water and the metal which resulted in Cr_2O_3 formation and a by-product of hydrogen which diffused out through the platinum vessel.[150] At the time of publishing they state that the densification mechanism was not fully understood.

The requirement of platinum to diffuse the hydrogen made this a very expensive technique, as well as the ability to make only small amounts of the chromium oxide at one time. Therefore, this technique had very little application, though it is the start of an important journey to low temperature sintering.

1.5.13 Cold Sintering

The next significant milestone was Cold Sintering which was proposed by Gutman *et al*. in 1979. This technique applied pressures of up to 1 GPa to metallic powders at room temperature to achieve a dense final product. Densification was achieved by the plastic flow of the material and thus could not be applied to brittle materials.[151] Cold welding is now a term understood in which primary bonds form between two clean interfaces of metals when pressure is applied.[152] Some metals such as silver and gold can form primary bonds without the application of pressure, this is called spontaneous cold welding.[141,152]

Where HRS achieved sintering through diffusion this technique achieves sintering through plastic flow. Cold Sintering in this form can only be used for materials which are ductile and so oxides will not sinter in this way.

1.5.14 Hydrothermal Hot Pressing (HHP)

Continuing with the application of pressure to achieve densification at low temperatures, Yamasaki developed HHP in 1984.[153] Originally designed for encapsulation of radioactive waste, Yamasaki took inspiration from the lithification process which transforms loose particles into sedimentary rocks through compaction and cementation.[153,154] Taking silica powder, 28 wt. % radioactive waste and a mineraliser solution (in this case sodium hydroxide solution, 1 cm^3 of solution to 4 g of powder) they compressed the mixture in a hot press cell. This hot press cell was placed inside an autoclave filled with more of the NaOH solution. See Figure 9 for a diagram of this apparatus.

a)

A: Push rod
B: Gland packing
C: Cone
D: Hot press cell
E: Thermocouple well

(a) Hot-press autoclave

b)

The upper figure is the
cross section of AA.
A: Upper rod
B: Ring
C: Inner case
D: Raw material
E: Outer case
F: Lower rod

(b) Hot-press cell
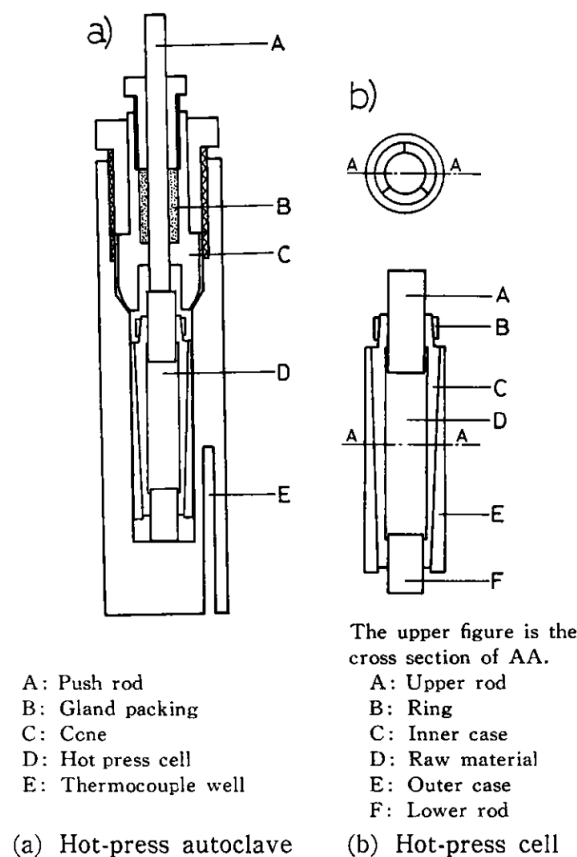
Figure 9 Yamasaki et al. apparatus for hydrothermal hot pressing

The autoclave was sealed and heated to up to 350 ℃ at a pressure of 16 MPa for 30 minutes. The elevated temperature increased the solubility of silica in the NaOH solution, resulting in a silica paste flowing from the hot press cell into the autoclave. By varying the concentration of the NaOH they could reduce the amount of silica dissolved and improve the final compressive strength of the final body. Yamasaki *et al.* concluded that in this case the densification was achieved by dissolution and deposition of the silica in NaOH, with the applied pressure keeping grain surfaces in contact.[153] The use of a hydrothermally sealed autoclave was useful in this application because this prevent the loss of potentially harmful volatiles, however for more general applications the use of a hot press cell and an autoclave adds unnecessary cost and complexity.

1.5.15 Reactive Hydrothermal Liquid-Phase Sintering (RHLPS)

Following on from HHP Riman *et al.* proposed RHLPS which they patented in 2012.[143] In this method a pre-compacted ceramic is pressed in a sealed hydrothermal environment. A schematic of this apparatus is shown in Figure 10. The pre-compaction makes a porous matrix into which a reactive medium infiltrates voids.[143] The hydrothermal conditions encourage the partial dissolution of the matrix and the formation of a reactant product which fills the voids.[147] This mechanism using the example of $BaTiO_3$ is shown in Figure 11 where the starting matrix is TiO_2 infiltrated with $Ba(OH)_2$.[147]
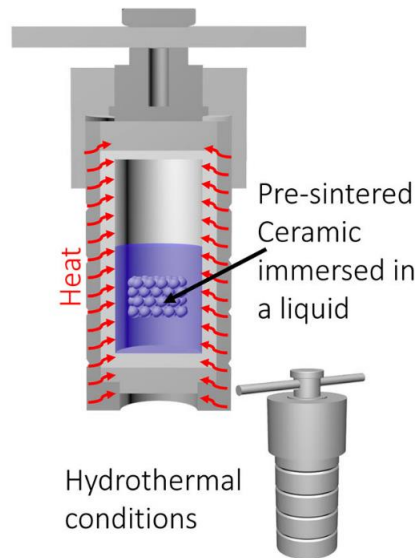
Figure 10 reactive hydrothermal liquid phase densification apparatus.[141]
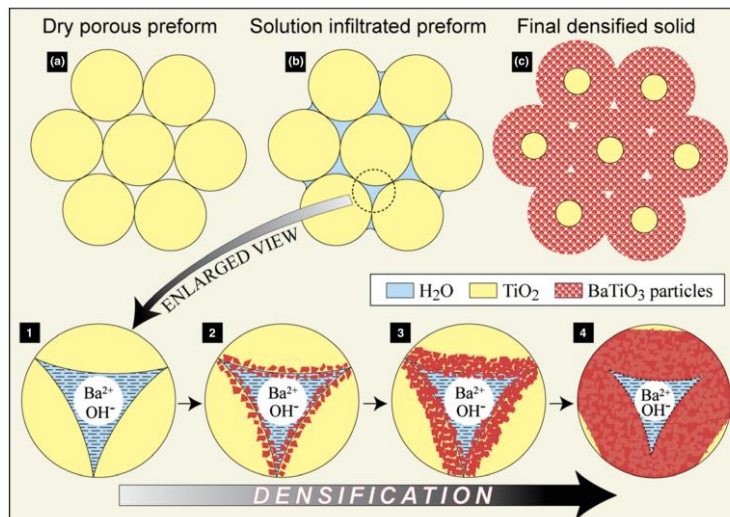
Figure 11 Reaction mechanism of the RHLPS process.[147]

Vakifahmetoglu *et al.* performed the RHLPS process to prepare $BaTiO_3$ and varied the sintering temperature between 90 and 240°C and holding time between 6 to 72 h.[147] The TiO_2 remained present in the XRD analysis of the final product in all but the samples made at 240 ºC held for 72 h; the final porosity of this sample was 10 vol %. The extensive reaction times and requirements of an autoclave are significant draw backs in this method.

1.5.16 Summary of Ultra Low Temperature Sintering Mechanisms

Mechanisms shown to induce primary bond formation so far have included:
- Plastic deformation
- Cold sintering (exclusive to metals)
- Dissolution- precipitation
- Chemical reactions

The majority of these methods have used complex apparatus (a Pt vessel or an autoclave/hydrothermally sealed cell) or are only applicable to a small set of materials, which is costly and limits the upscaling of these techniques. In order to compete with the practicality of solid state sintering, which can be done in any furnace, a simpler experimental set up is required. A new technique emerged into the state of the art which posed a much simpler apparatus to sinter at low temperatures. This was first proposed by Kähäri *et al.* which was then further developed and patented as Cold Sintering Process (CSP) in 2016 which became patented in 2021 by Clive Randall and colleagues at The Penn State Research Foundation.[155,156] Its foundation was the moistening of ceramic powder which were then compressed and heated to form a dense ceramic.

1.5.17 Cold Sintering Process

In 2014 Kähäri *et al.* achieved between 87 - 93% density Li_2MoO_4 by spraying starting powder with deionised water before applying uniaxial pressure (130 MPa) to a steel mould which was heated to 120 ℃ for 4 h.[144] They compared the dielectric properties of their low temperature sintered ceramic to one sintered using the conventional solid state sintering route which required a temperature of 540 ℃ for 2 h. Similar permittivity values were achieved with only a small decrease in the Q x f (a figure of merit in dielectric materials) believed to be caused by residual water in the samples.[144]

In 2016 Clive Randall's group published several papers based on the same principle which they called the Cold Sintering Process (CSP). [157–159] This method begins from ceramic powders whose surfaces are moisturized with a small amount of aqueous solution (1-25 wt. %) and compacted in a die between heated platens. [157] The liquid phase encouraged dissolution and precipitation, aided by local hydrothermal conditions created by the applied pressure (~350 MPa) and temperature (120 – 200 ℃).[157,159] The compaction is performed in an un-sealed environment so that the water is able to evaporate. Using this method Randall's group achieved densities between 85 – 98 % of the theoretical density in materials such as PbTe, $Ca_3Co_4O_9$, ZrO_2 and $Li1.5Al_{0.5}Ge_{1.5}(PO_4)_3$ in under 30 minutes.[157]

An additional benefit of CSP is the possibility of ceramic- polymer composites. When relying on solid state sintering to sinter ceramics the combination of a polymer and a percolated ceramic (randomly dispersed ceramic powder creates an interconnected pathway through a composite) in a dense body is a complex process. The high temperatures required to sinter ceramics (>900 ℃) would degrade the polymer, therefore a ceramic body would be sintered first before sections are machined away and the polymer infiltrated.[148] With the event of CSP, polymers and ceramics could be sintered at the same time to form a composite in one step below 200 ℃.[148] Guo *et al.* demonstrated this by the combination of lithium molybdate with PTFE (for use as a microwave dielectric) and vanadium oxide with PEDOT:PSS (for use as a semiconductor).[148]

1.5.18 The Theory of Cold Sintering Process

In 2019 Biesuz *et al.* published a theoretical analysis of cold sintering.[160] This separates the cold sintering process into two stages. Stage 1 occurs before the particles are in direct contact with each other; in this stage they are considered to be in a suspension in the solution. The particles experience isostatic pressure due to the presence of the liquid which increases their solubility.[160] Ostwald ripening occurs in which smaller particles dissolve and become deposited onto larger particles which causes grain coursening.[161] During stage 1 the solution

is being slowly evaporated from the unsealed die. Cold sintering processes often include an initial hold at room temperature when pressure is first applied, for anywhere between 1 and 30 minutes, to allow for rearrangement and so that the solvent does not evaporate too quickly.[145,162–165]

In stage 2 particles are in direct contact and pressure gradients exist where the pressure is intensified at contact points, leading to larger rates of mass diffusion, and lowest where voids are present. Material is deposited in low pressure areas, filling voids until the grains form flat interfaces and the pressure gradients are levelled.[160]

When a complex material is dissolved and redeposited it can form an amorphous structure which remains present within the grain boundaries.[159] The transformation of this amorphous structure into a crystalline one is key to achieving highly dense and crystalline materials. Guo *et al.* observed that the boundary between the crystal and the amorphous region is typically arranged in a terrace-ledge manner, Figure 12.[159] The Terrace Ledge Kink model describes the growth of a crystal by incorporating deposited ions with the aid of thermodynamically favourable conditions provided by the ledges and kinks.[166] Impurities can block the surface of the crystal and significantly reduce the rate of crystallisation and so clean interfaces are required for efficient crystal growth.[166]
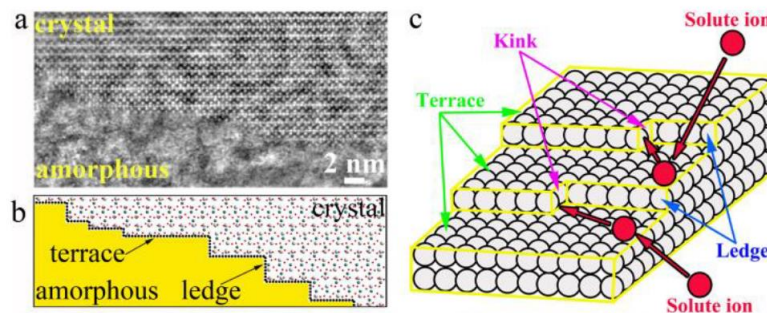
Figure 12 Terrace Ledge Kink at the interface between crystalline and amorphous regions.

Secondly, these mechanisms rely on the congruent dissolution of the particles into solution. This is the case for materials like lithium molybdate and zinc oxide but is not the case for barium titanate ($BaTiO_3$).[167] During the cold sintering of $BaTiO_3$, preferential dissolution of barium ions lead to an amorphous TiO_2 layer at the surface of the particles. This layer passivates the surface and separates the solution from the crystallised grain so that the TLK mechanism is blocked. Preferential dissolution is also seen in other titanates such as $SrTiO_3$ and $CaTiO_3$ and niobates such as $KNbO_3$, $NaNbO_3$. [168,169] Ozmen *et al.* showed that the rate of dissolution of ions from potassium and sodium niobates is inversely proportional to their cation field strength. The larger the cation fields strength the more strongly it is held within the lattice. The cation field strength of ions is as follows: K < Na < Nb, which matched an inverse trend in dissolution rate of these element from potassium, sodium niobate when in solution.[169]

1.5.19 Using The Cold Sintering Process to Sinter Functional Oxides

Ying *et al.* cold sintered MnZn ferrite with the aim of grain refinement in the final product. Using the conventional solid state sintering route ZnMn ferrites are typically sintered ~1380 ºC for up to 9 h.[170] By using the cold sintering process they reduced the sintering temperature to 330 ºC for 2 h. Beginning from powders calcined using the solid state route they added a

transient solvent: ethanol solution acetic acid and pressed using a pressure between 600 and 1400 MPa.[171] Cold sintering was followed by annealing process at 950 ℃ for 6 h to improve the density. By increasing the pressure used in cold sintering the pre annealed densities increased from 75 % to 85% of the theoretical density. A much larger improvement in the density was shown after annealing; this increased the densities to between 95 – 97 %, as shown in Figure 13.

The use of such high pressures (> 1000 MPa) becomes impractical when scaling up the cold sintering process due to the large forces required to exert this pressure over a large surface area. In this case most of the density improvement came from the annealing treatment and so the use of a pressure up to 1400 MPa is debatably not worth the gain. Ying *et al.* also found that the final grain size of the MnZn ferrite increased with increasing pressures used during the cold sintering (Table 1). This shows that the pressure applied drives the coarsening and densifying reactions.
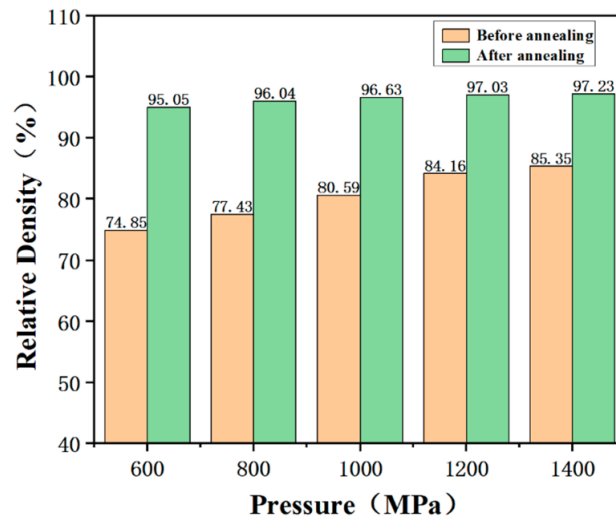
Figure 13 Densities of cold sintered MnZn ferrite before and after annealing at 950 ℃ for 6 h versus the pressure used during cold sintering.[171]

Table 1 Average grain size (D_ave) of cold sintered MnZN ferrite at different cold sintering pressures from Ying et al.[171]

Pressure (MPa)	600	800	1000	1200	1400
D_{ave} (µm)	2.67	2.72	2.80	2.87	2.90

Lan *et al.* employed cold sintering to densify $K_{0.5}Na_{0.5}NbO_3$, a functional oxide which struggles with Na and K volitisation at the temperatures requires for solid state sintering (>1000 ℃) which deteriorates the piezoelectric, dielectric and ferroelectric properties.[172] They cold sintered at 180 ℃ for 1 h using different amounts of their transient solvent (acetic acid) from 0 to 20 wt. % and pressures varying from 400 to 800 MPa. This was following by annealing at 1050 ℃ for 2 h. The bulk densities of pellet before the annealing step are shown in Figure 14, and after annealing in Figure 15. The density was increased by the presence of the acetic acid solvent but not apparently affected by the amount used over 10 wt.%. The

density was once again increased by increasing the pressure used during cold sintering. They found that the optimum cold sintering condition was 15 wt. % of solvent and a pressure of 800 MP. Overall the bulk densities after cold sintering are low (< 80 %) so required the additional annealing step to increase the density. After annealing at 1050 ℃ they achieved a density of 96 %. The fracture surface of a pellet cold sintered under the optimised conditions is shown in Figure 16, which show grains much smaller than 1μm.[172] Grain growth did occur during annealing, Figure 17, though grains remained under ~2 μm.
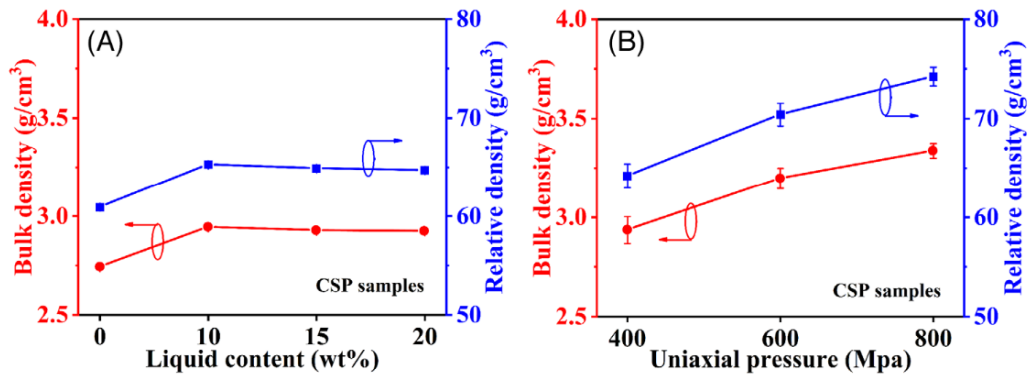
Figure 14 Bulk densities of $K_{0.5}Na_{0.5}NbO_3$ cold sintered, varying transient solvent content and cold sintering pressure by Lan et al.[172]
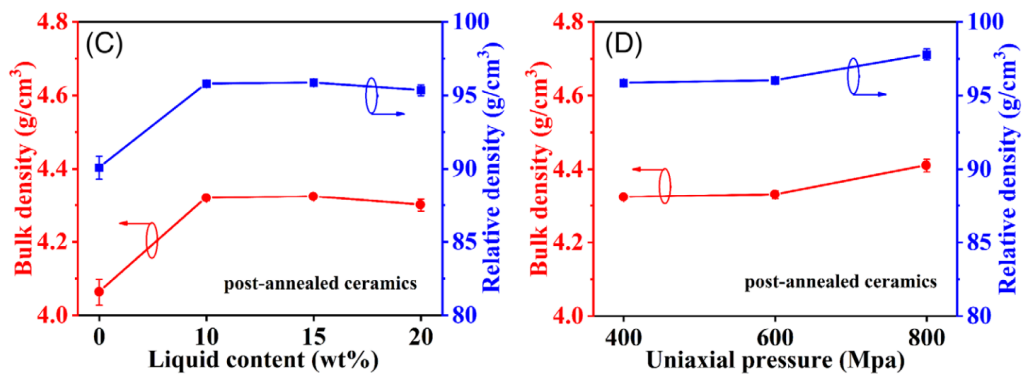
Figure 15 Bulk densities of cold sintered $K_{0.5}Na_{0.5}NbO_3$ after annealing at 1050 ℃ for 2 h.[172]
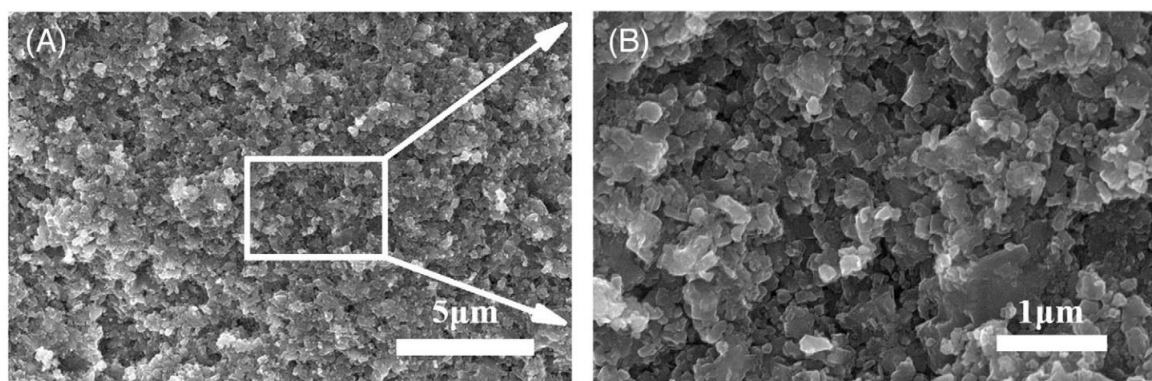
Figure 16 SEM images of fracture surfaces of cold sintered $K_{0.5}Na_{0.5}NbO_3$ using 15 wt. % acetic acid, 180 ℃, 800 MPa for 1 h.[172]
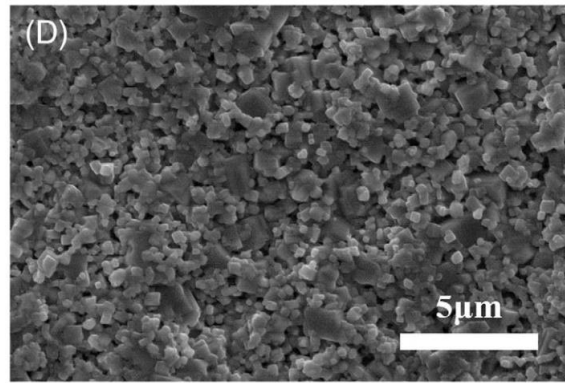
Figure 17 SEM image of fracture surface post annealing at 1050 ºC for 2 h.[172]

1.5.20 Cold Sintering Ceramics with Incongruent Dissolution Rates

To tackle the density issues of incongruent dissolution Guo *et al.* developed an adaptive process to achieve high density in the incongruently soluble $BaTiO_3$ (Figure 18).[158] Instead of dissolving and re-precipitating $BaTiO_3$ starting powder, a suspension of $Ba(OH)_2$, TiO_2 and water was used to wet the starting powder and deposit $BaTiO_3$ on the surface of the power. The super-saturation of Ba in the suspensions largely inhibited the dissolution of Ba from the surface of $BaTiO_3$ powder preventing the formation of the TiO_2 rich passivating layer.[158] Their cold sintering conditions were: 430 MPa at 180 ºC for 30 min. After cold sintering some of the $Ba(OH)_2$ had reacted with TiO_2 and deposited crystalline material onto the starting powder's surfaces, some of the $Ba(OH)_2$ had reacted with CO_2 from the air and formed and impurity of $BaCO_3$, and the rest had formed a carbonate rich glass phase within the voids. This resulted in a density of ~ 93 %. By annealing this material at 900 ºC for 3 h, the purity of the $BaTiO_3$ was improved, as demonstrated by TG in which a mass loss of 1.8 % occurs. Weight loss events are attributed to water evaporation (~100 ºC), decomposition of remaining hydroxide species leading to loss of OH^- (~300 ºC) and decomposition of carbonate species leading to loss of CO_2 (~520 ºC and ~780 ºC).[158] This accompanied the transformation of the as cold sintered grains from rounded surrounded by glass phase (Figure 19 a-c) to angular grain with well crystallised grain boundaries (Figure 19 g-i).[158]

59
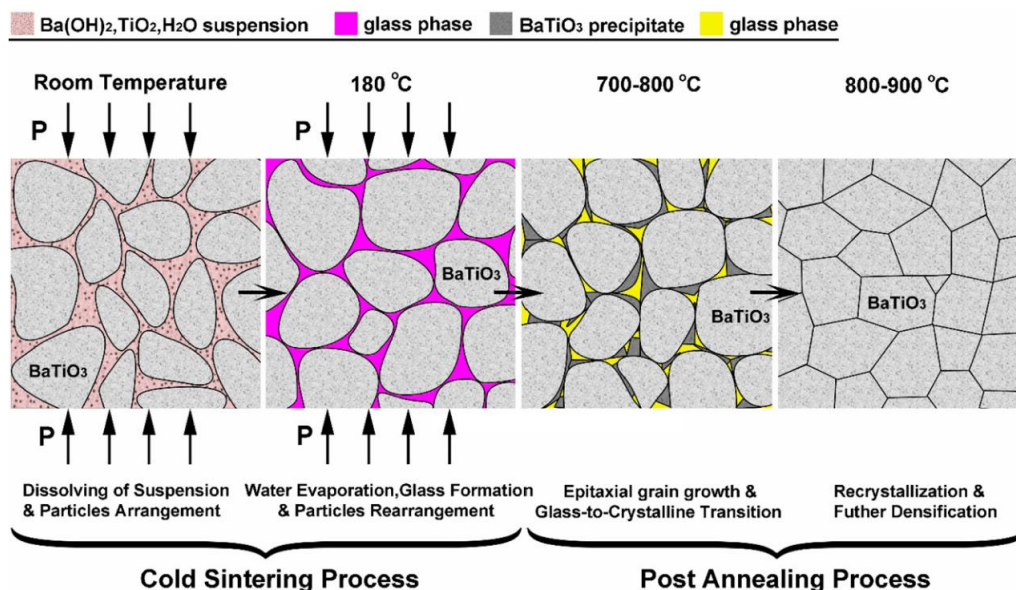
Figure 18 Cold sintering technique for BaTiO₃ by Guo et al.[158]
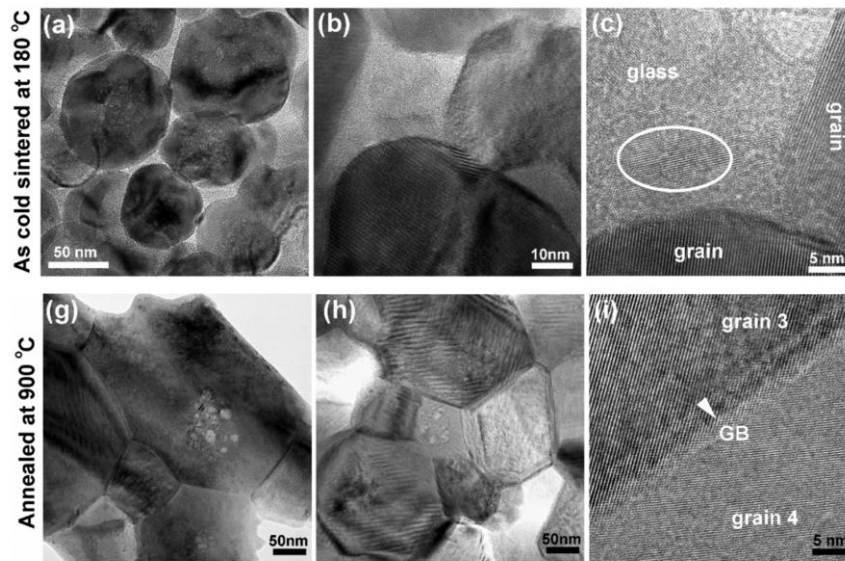
Figure 19 (a-c) TEM Micrographs of grains as cold sintered and, (g-i) and after annealing at 900 ℃ for 3 h.[158]

A highly dense cold sintered BaTiO₃ was achieved in a single step at 300 ℃, without the need of an annealing step, by Tsuji *et al.* who used a molten hydroxide flux to encourage densification.[173] NaOH and KOH when combined have a eutectic point at 170 ℃ so when added to the cold sintering powder, they form a liquid a high temperatures that acts as the transient solvent for cold sintering. The phase diagram is shown in Figure 20, the eutectic point is at 50 mol % and 170 ℃ when β+β' transform directly into a liquid.
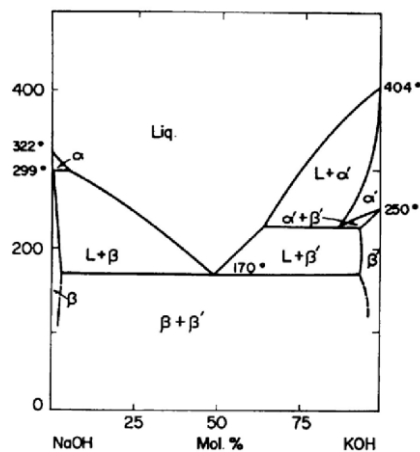
Figure 20 Phase diagram of KOH and NaOH.[174]

Tsuji *et al.* began from BaTiO₃ nanopowder (average size 20 nm) and combined this with 4 and 6 wt.% of the NaOH KOH flux. Nanopowder has a much larger surface area than larger – grained powders and so are more reactive. This was pressed at 520 MPa and heated to 300 ℃ for 12 h. This is a relatively long hold time to the other cold sintering methods, though Tsuji *et al.* state that these conditions are not optimised and the long hold time was used to reduce the porosity, though a dense material could be formed in 3 h. Using this method, they

achieved clean crystalline grain boundaries with no glassy phase which resulted in a density of between 92 – 96 % of the theoretical density pure $BaTiO_3$. Increasing the volume of the flux from 4 to 6 wt.% resulted in the higher density (96 % compared to 92 %) and smaller grain size (75 nm compared to 150 nm). In their report they do not discuss the reasons for this trend though it is clear that the flux improves the cold sintering. Ostwald ripening occurs in the early stages of cold sintering in which the particles coarsen, though the flux in this case is not a liquid at room temperature, so this may be inhibited by the presence of NaOH and KOH between the particles. The increase in density is more obvious as was shown in the work by Lan et al in Figures 13 and 14, more solvent increases density.[172]

Alkali elements from the flux (Na and K) where not detected in TEM EDS, though they suggest that these could have been preferentially removed during TEM sample prep. NaOH and KOH were also not detected in the XRD which showed only the $BaTiO_3$ phase in the cold sintered material. As the temperature remained so low (300 ℃) it is unlikely that the Na and K volatised so may be present in small amounts at the grain boundaries which are below the detection limit of the XRD and /or have low crystallinity after forming the solution then re-solidifying upon cooling. This did not seem to cause a negative effect on the final properties of the $BaTiO_3$ which Tsuji compare to other $BaTiO_3$ of the same grain size. [173]

In some cases, incongruent dissolution is not necessarily a drawback for a material and can be used to alter the composition of the material to enhance properties. Chi et al. used the incongruent dissolution of $K_{0.5}Na_{0.5}NbO_3$ (K dissolution rate > Na dissolution rate > Nb dissolution rate) to create a Na rich surface which improved the electrical properties of the final material.[162] They used an aqueous solution of NaCl as the solvent during cold sintering to saturate the solution in Na^+ ions and allowed the preferential dissolution of K to deplete the surface of potassium. They cold sintered at 120 ℃ for 1 h using a pressure of 420 MPa. The pellet was dried at 120 ℃ for 8 h to remove remaining water and annealed between 900 – 1100 ℃ 3 h. They do not provide the density immediately after cold sintering though their lowest annealing temperature, 900 ℃, gave a density of 87 % of the theoretical. Directly after cold sintering the NaCl was visible in the XRD analysis, though after annealing at 900 ℃ this peak disappeared and the KCl peak appeared. They attributed this to the loss of K^+ from grains which combined with Cl^- ions to become KCl whilst the excess Na^+ was absorbed into the grains. Above 1050 ℃ KCl was no longer visible in the XRD, this was accompanied by an increase in the cell volume, indicating that potassium was being reabsorbed into the grains. The role of the Cl^- ions beyond this point was not determined, perhaps it remained in the grain boundaries or was volatilised. Grain size after annealing at 1050 ℃ was between 1.2 – 1.5 μm and a density of 92 % of the theoretical density (4.18 g/cm^3, theoretical 4.506 g/cm^3).[162,175]

The cold sintering methods so far have aimed to achieve a fully dense ceramic using solvents which partially dissolve and precipitate material such as acetic acid, or solvents which are saturated in one or more of the elements to make up for incongruent dissolution such as an aqueous $Ba(OH)_2$ suspension. These techniques all relied on the Terrace Ledge Kink grain growth model which as previously stated can be negatively impacted by impurities which interfere with the growth mechanisms.[166] In order to avoid this issue Boston et al. proposed a variation of the Cold Sintering Process which introduced reactants into the cold sintering mixture which upon annealing crystallise into the final product, filling the voids in this way rather than dissolution precipitation methods.[149] They called this Reactive Intermediate Phase Cold Sintering or Reactive Cold Sintering (RCS).[149]

Previous to this work a synthesis route had recently been shown to successfully synthesise $BaTiO_3$ at 950 ºC using choline chloride/ malonic acid deep eutectic solvent. This reaction progressed through the formation of barium chloride, which reacted with anatase to give $BaTiO_3$.[176] By taking the intermediates of this reaction which are known to react at 950 ºC to form a perovskite (anatase and a metal chloride i.e. $BaCl_2$) Boston *et al.* incorporated this knowledge into a Cold Sintering technique. To synthesise $SrTiO_3$ Boston *et al.* combined powdered $SrTiO_3$, and aqueous solution of $SrCl_2$ and TiO_2 nano particles.[149] To show the flexibility of the technique they cold sintered using solid state synthesised power and nano powder $SrTiO_3$ as their starting material.
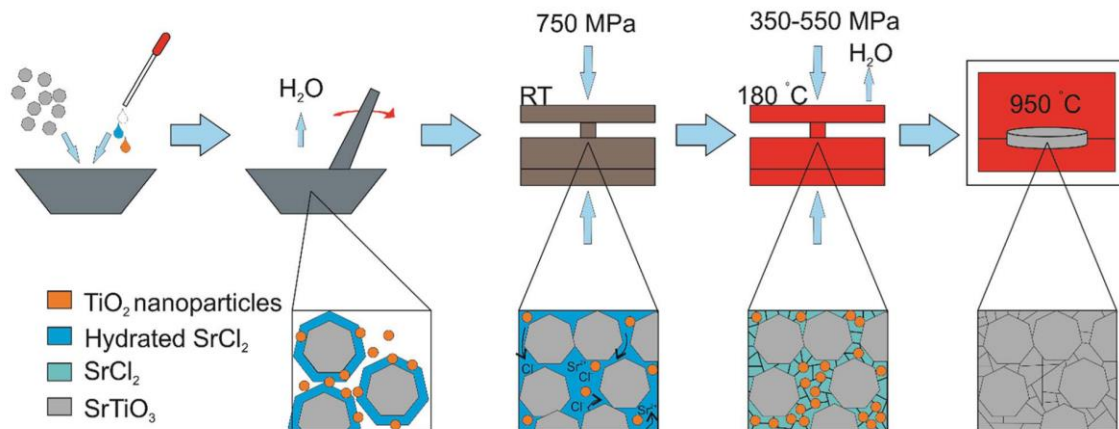
Figure 21 Schematic of Reactive Intermediate Phase Cold Sintering by Boston et al.[149]

This then followed a typical cold sintering procedure at a temperature of 180 ºC, 750 MPa for 1 hr. Figure 21 shows the schematic of this process. Like the work by Guo *et al.* who cold sintered $BaTiO_3$ using a suspension of $Ba(OH)_2$ and TiO_2 nano powder, Figure 18, the saturation of Sr^+ ions in the solution surrounding the powders should prevent the dissolution of Sr from $SrTiO_3$ and prevent the formation of a TiO_2 rich passivating layer.[158] However, unlike the method by Guo *et al.* the intermediate reactants in the method proposed by Boston *et al.* remain unreacted after the cold sintering process. Transformation of the intermediate reactants occurred only after the pellet was heated to 950 ºC for 4 h which induced the reaction of $SrCl_2$ and TiO_2 into $SrTiO_3$ which resulted in a highly dense ceramic; 97.2 ± 0.8 % starting from solid state synthesised $SrTiO_3$ and 96.2 ± 2.2 % starting from $SrTiO_3$ nanopowder.[149] These are both small improvements in density from the Guo *et al.* technique which had a density of 95 % after annealing at 900 ºC for 3 h.

1.5.21 Summary of Cold Sintering Process

The Cold Sintering Process was developed from the knowledge of many other Ultra Low Sintering techniques and still shares many of the same mechanisms with its predecessor Hydrothermal Hot Pressing. The great advantage of the Cold Sintering Process though is the simple equipment used to produce highly dense ceramics. In most cases only a hot press consisting of a steel die and heated platens is required. The first prototypes of this technique emerged in 2014 from Kähäri *et al.* and already since then the works of Randal, Guo, Lan, Chi and Boston *et al.* have developed variations on the technique to densify a wide range of ceramic materials. [149,156,158,162,172]

The optimizable parameters in cold sintering are: surface area of starting materials, temperature, pressure, hold time and the transient solvent. As a new technique each modification on the original process forms an important part in the collection of knowledge used to understand the underlying mechanisms. There is a wide space in this field of research to develop novel adaptions to the Cold Sintering Process to improve energy efficiency and density of the final materials.

1.6 References

1   C. Forman, I. K. Muritala, R. Pardemann and B. Meyer, *Renew. Sustain. Energy Rev.*, 2016, 57, 1568–1579.
2   NASA, Cassini - Radioisotope Thermoelectric Generators, https://science.nasa.gov/mission/cassini/radioisotope-thermoelectric-generator/, (accessed 6 November 2023).
3   Y. Mishima, Y. Kimura and S. Wng Kim, in *Nanomaterials*, 2006, pp. 383–418.
4   H. Ohta, *Mater. Today*, 2007, **10**, 44–49.
5   A. Saini, R. Kumar and R. Kumar, in *Thermoelectricity and Advanced Thermoelectric Materials*, eds. R. Kumar and R. Signh, Elsevier, 2021, pp. 1–21.
6   A. A. Mubarak, *Int. J. Mod. Phys. B*, 2016, **30**, 1650141.
7   N. Espinosa, M. Lazard, L. Aixala and H. Scherrer, *J. Electron. Mater.*, 2010, **39**, 1446–1455.
8   S. S. Shastri and S. K.Pandey, in *Thermoelectricity and Advanced Thermoelectric Materials*, eds. R. Kumar and R. Signh, Elsevier, 2021, pp. 21–55.
9   G. S. Nolas, D. T. Morelli and T. M. Tritt, *Annu. Rev. Mater. Sci.*, 1999, **29**, 89–116.
10   G. A. Slack, in *CRC Handbook of Thermoelectrics*, 1995, pp. 407–441.
11   A. I. Abutaha, S. R. S. Kumar, K. Li, A. M. Dehkordi, T. M. Tritt and H. N. Alshareef, *Chem. Mater.*, 2015, **27**, 2165–2171.
12   H. Alam and S. Ramakrishna, *Nano Energy*, 2013, 2, 190–212.
13   J. He and T. M. Tritt, *Science (80-.).*, 2017, **357**, 1369.
14   L. D. Zhao, V. P. Dravid and M. G. Kanatzidis, *Energy Environ. Sci.*, 2014, **7**, 251–268.
15   A. R. West, in *Solid State Chemistry and Its Applications*, 2014, pp. 125–187.
16   V. E. Alexandrov, E. A. Kotomin, J. Maier and R. A. Evarestov, *Eur. Phys. J. B*, 2009, **72**, 53–57.
17   S. Piskunov, E. Heifets, R. I. Eglitis and G. Borstel, *Comput. Mater. Sci.*, 2004, **29**, 165–178.
18   J. Carrasco, F. Illas, N. Lopez, E. A. Kotomin, Y. F. Zhukovskii, R. A. Evarestov, Y. A. Mastrikov, S. Piskunov and J. Maier, *Phys. Rev. B*, 2006, **73**, 064106.
19   M. K. Yadav and B. Sanyal, in *Thermoelectricity and Advanced Thermoelectric Materials*, eds. R. Kumar and R. Signh, Elsevier, 2021, pp. 105–117.
20   Z. Huang, D. Wang, C. Li, J. Wang, G. Wang and L.-D. Zhao, *J. Mater. Chem. A*, 2020, **8**, 4931–4937.
21   K. Kaur, Enamullah, S. Ahmad Khandy, J. Singh and S. Dhiman, in *Thermoelectricity and Advanced Thermoelectric Materials*, 2021, pp. 145–149.
22   Y. Pei, A. D. Lalonde, N. A. Heinz, X. Shi, S. Iwanaga, H. Wang, L. Chen and G. J. Snyder, *Adv. Mater.*, 2011, **23**, 5674–5678.
23   C. Gayner and K. K. Kar, *Prog. Mater. Sci.*, 2016, **83**, 330–382.
24   J. U. Rahman, W. H. Nam, N. Van Du, G. Rahman, A. U. Rahman, W. H. Shin, W.-S.

Seo, M. H. Kim and S. Lee, *J. Eur. Ceram. Soc.*, 2019, **39**, 358–365.

25   H. Muta, A. Ieda, K. Kurosaki and S. Yamanaka, *Mater. Trans.*, 2005, **46**, 1466–1469.

26   R. Moos and K. H. Härdtl, *J. Appl. Phys.*, 1996, **80**, 393–400.

27   G. J. Snyder and E. S. Toberer, *Nat. Mater.*, 2008, **7**, 105–114.

28   P. C. Wei, C. X. Cai, C. R. Hsing, C. M. Wei, S. H. Yu, H. J. Wu, C. L. Chen, D. H. Wei, D. L. Nguyen, M. M. C. Chou and Y. Y. Chen, *Sci. Rep.*, 2019, **9**, 8616.

29   C. Chang, M. Wu, D. He, Y. Pei, C.-F. Wu, X. Wu, H. Yu, F. Zhu, K. Wang, Y. Chen, L. Huang, J.-F. Li, J. He and L.-D. Zhao, *Science (80-.).*, 2018, **360**, 778–783.

30   X. Shi, J. Yang, J. R. Salvador, M. Chi, J. Y. Cho, H. Wang, S. Bai, J. Yang, W. Zhang and L. Chen, *J. Am. Chem. Soc.*, 2011, **133**, 7837–7846.

31   Warwick, Phonons, https://warwick.ac.uk/fac/sci/physics/current/postgraduate/regs/mpagswarwick/ex5/ph onons/#:~:text=When the unit cell contains,and negative ions swing together, (accessed 14 July 2023).

32   University of Cambridge, Non-metals: Thermal Phonon, https://www.doitpoms.ac.uk/tlplib/thermal_electrical/nonmetal_thermal.php, (accessed 14 July 2023).

33   R. Wang, H. Zobeiri, Y. Xie, X. Wang, X. Zhang and Y. Yue, *Adv. Sci.*, 2020, **7**, 1–14.

34   K. Kuar, Enamullah, S. A. Khandy, J. Singh and S. Dhiman, in *Thermoelectricity and Advanced Thermoelectric Materials*, eds. R. Kumar and R. Signh, Elsevier, 2021, pp. 139–163.

35   L.-D. Zhao, M. G. Kanatzidis, G. Tan and M. G. Kanatzidis, *Chem. Rev.*, 2016, **116**, 12123–12149.

36   G. Guélou, V. Pavan Kumar, V. Carnevali, O. I. Lebedev, B. Raveau, C. Couder, C. Prestipino, P. Lemoine, B. Malaman, J. Juraszek, C. Candolfi, B. Lenoir, R. Al Rahal Al Orabi, M. Fornari and E. Guilmeau, *Chem. Mater.*, 2021, **33**, 9425–9438.

37   B. Xin, *Synthesis of nanoporous Ca3Co4O9 thin films for flexible thermoelectrics*, Linköping University Electronic Press, Linköping, 2020, vol. 1887.

38   I. T. Witting, T. C. Chasapis, F. Ricci, M. Peters, N. A. Heinz, G. Hautier and G. J. Snyder, *Adv. Electron. Mater.*, 2019, **5**, 1–20.

39   H. J. Goldsmid, *Materials (Basel).*, 2014, **7**, 2577–2592.

40   R. T. Delves, A. E. Bowley, D. W. Hazelden and H. J. Goldsmid, *Proc. Phys. Soc.*, 1961, **78**, 838–844.

41   H. S. Kim, N. A. Heinz, Z. M. Gibbs, Y. Tang, S. D. Kang and G. J. Snyder, *Mater. Today*, 2017, **20**, 452–459.

42   Z. Xu, H. Wu, T. Zhu, C. Fu, X. Liu, L. Hu, J. He, J. He and X. Zhao, *NPG Asia Mater.*, 2016, **8**, 302.

43   B. Poudel, Q. Hao, Y. Ma, Y. Lan, A. Minnich, B. Yu, X. Yan, D. Wang, A. Muto, D. Vashaee, X. Chen, J. Liu, M. S. Dresselhaus, G. Chen and Z. Ren, *Science (80-.).*, 2008, **320**, 634–638.

44   S. Il Kim, K. H. Lee, H. A. Mun, H. S. Kim, S. W. Hwang, J. W. Roh, D. J. Yang, W. H. Shin, X. S. Li, Y. H. Lee, G. J. Snyder and S. W. Kim, *Science (80-.).*, 2015, **348**, 109–114.

45   L.-D. Zhao, G. Tan, S. Hao, J. He, Y. Pei, H. Chi, H. Wang, S. Gong, H. Xu, V. P. Dravid, C. Uher, G. J. Snyder, C. Wolverton and M. G. Kanatzidis, *Science (80-.).*, 2016, **351**, 141–144.

46   L.-D. Zhao, S.-H. Lo, Y. Zhang, H. Sun, G. Tan, C. Uher, C. Wolverton, V. P. Dravid and M. G. Kanatzidis, *Nature*, 2014, **508**, 373–377.

47   G. Leibfried and W. Ludwig, *Solid State Phys. - Adv. Res. Appl.*, 1961, **12**, 275–444.

48   S. Sassi, C. Candolfi, J. B. Vaney, V. Ohorodniichuk, P. Masschelein, A. Dauscher

and B. Lenoir, *Appl. Phys. Lett.*, , DOI:10.1063/1.4880817.

49   K. Takahata, Y. Iguchi, D. Tanaka, T. Itoh and I. Terasaki, *Phys. Rev. B - Condens. Matter Mater. Phys.*, 2000, **61**, 12551–12555.

50   I. Terasaki, Y. Sasago and K. Uchinokura, *Phys. Rev. B - Condens. Matter Mater. Phys.*, 1997, **56**, R12685–R12687.

51   Y. Miyazaki, K. Kudo, M. Akoshima, Y. Ono, Y. Koike and T. Kajitani, *Japanese J. Appl. Physics, Part 2 Lett.*, 2000, **39**, 531–533.

52   K. Koumoto, I. Terasaki and R. Funahashi, *MRS Bull.*, 2006, **31**, 206–210.

53   R. Funahashi, I. Matsubara, H. Ikuta, T. Takeuchi, U. Mizutani and S. Sodeoka, *Jpn. J. Appl. Phys.*, 2000, **39**, 1127–1129.

54   K. Fujita, T. Mochida and K. Nakamura, *Int. Conf. Thermoelectr. ICT, Proc.*, 2001, **40**, 168–171.

55   G. E. Lee, A. Y. Eum, K. M. Song, I. H. Kim, Y. S. Lim, W. S. Seo, B. J. Choi and C. W. Hwang, *J. Electron. Mater.*, 2015, **44**, 1579–1584.

56   L. Hu, H. Wu, T. Zhu, C. Fu, J. He, P. Ying and X. Zhao, *Adv. Energy Mater.*, 2015, **5**, 1–13.

57   F. Wu, H. Song, F. Gao, W. Shi, J. Jia and X. Hu, *J. Electron. Mater.*, 2013, **42**, 1140–1145.

58   G. S. Nolas, M. Kaeser, R. T. Littleton IV and T. M. Tritt, *Appl. Phys. Lett.*, 2000, **77**, 1855–1857.

59   J. W. Fergus, *J. Eur. Ceram. Soc.*, 2012, **32**, 525–540.

60   E. Guilmeau, A. Maignan and C. Martin, in *Journal of Electronic Materials*, 2009, vol. 38, pp. 1104–1108.

61   J. P. Wiff, Y. Kinemuchi, H. Kaga, C. Ito and K. Watari, *J. Eur. Ceram. Soc.*, 2009, **29**, 1413–1418.

62   X. Qu, W. Wang, S. Lv and D. Jia, *Solid State Commun.*, 2011, **151**, 332–336.

63   M. Ohtaki, K. Araki and K. Yamamoto, in *Journal of Electronic Materials*, 2009, vol. 38, pp. 1234–1238.

64   H. S. Kim, C. R. Lee, J. H. Im, K. B. Lee, T. Moehl, A. Marchioro, S. J. Moon, R. Humphry-Baker, J. H. Yum, J. E. Moser, M. Grätzel and N. G. Park, *Sci. Rep.*, 2012, **2**, 1–7.

65   C. Pithan, D. Hennings and R. Waser, *Int. J. Appl. Ceram. Technol.*, 2005, **2**, 1–14.

66   M. Kim, G. M. McNally, H. H. Kim, M. Oudah, A. S. Gibbs, P. Manuel, R. J. Green, R. Sutarto, T. Takayama, A. Yaresko, U. Wedig, M. Isobe, R. K. Kremer, D. A. Bonn, B. Keimer and H. Takagi, *Nat. Mater.*, 2022, **21**, 627–633.

67   W. Wunderlich, H. Ohta and K. Koumoto, *Phys. B*, 2009, **404**, 2202–2212.

68   T. Kolodiazhnyi, A. Petric, M. Niewczas, C. Bridges, A. Safa-Sefat and E. Greedan, *Phys. Rev. B - Condens. Matter Mater. Phys.*, 2003, **68**, 1–5.

69   S. Singh, P. A. Jha, S. Varma and P. Singh, *J. Alloys Compd.*, 2017, **704**, 707–716.

70   S. Hui and A. Petric, *J. Electrochem. Soc.*, 2002, **149**, J1–J10.

71   C. Franchini, M. Reticcioli, M. Setvin and U. Diebold, *Nat. Rev. Mater.*, 2021, **6**, 560–586.

72   M. Molinari, D. A. Tompsett, S. C. Parker, F. Azough and R. Freer, *J. Mater. Chem. A*, 2014, **2**, 14109–14117.

73   T. Okuda, K. Nakanishi, S. Miyasaka and Y. Tokura, *Phys. Rev. B*, 2001, **63**, 113104.

74   D. Srivastava, C. Norman, F. Azough, M. C. Schäfer, E. Guilmeau, D. Kepaptsoglou, Q. M. Ramasse, G. Nicotra and R. Freer, *Phys. Chem. Chem. Phys.*, 2016, **18**, 26475–26486.

75   J. Ravichandran, W. Siemons, D.-W. Oh, J. T. Kardel, A. Chari, H. Heijmerikx, M. L. Scullin, A. Majumdar, R. Ramesh and D. G. Cahill, *Phys. Rev. B*, 2010, **82**, 165126.

76   A. Kinaci, C. Sevik and T. Çağın, *Phys. Rev. B*, 2010, **82**, 155114.

77   C. E. Ekuma, M. Jarrell, J. Moreno and D. Bagayoko, *AIP Adv.*, , DOI:10.1063/1.3700433.

78   H. Stöcker, J. Hanzig, M. Zschornak, E. Mehner, S. Jachalke, C. Richter, F. Hanzig, F. Meutzner, T. Leisegang and D. C. Meyer, *Cryst. Res. Technol.*, 2017, **52**, 1600222.

79   H. Yamada and G. R. Miller, *J. Solid State Chem.*, 1973, **6**, 169–177.

80   R. D. Shannon, *Acta Crystallogr. Sect. A*, 1976, **32**, 751–767.

81   D. Burnat, A. Heel, L. Holzer, D. Kata, J. Lis and T. Graule, *J. Power Sources*, 2012, **201**, 26–36.

82   V. R. and V. P. D. M. M. McGibbon, N. D. Browning, M. F. Chisholm, A. J. McGibbon, S. J. Pennycook, *Science (80-.).*, 1994, **266**, 102–104.

83   J. Cao, D. Ekren, Y. Peng, F. Azough, I. A. Kinloch and R. Freer, *ACS Appl. Mater. Interfaces*, 2021, **13**, 11879–11890.

84   R. E. Ward, C. L. Freeman, J. S. Dean, D. C. Sinclair, J. H. Harding, R. E. Ward, C. L. Freeman, J. S. Dean, D. C. Sinclair and H. Harding, *Adv. Funct. Mater.*, 2020, **30**, 1905077.

85   H. Muta, K. Kurosaki and S. Yamanaka, *J. Alloys Compd.*, 2005, **392**, 306–309.

86   C. L. Freeman, J. A. Dawson, H.-R. Chen, J. H. Harding, L.-B. Ben and D. C. Sinclair, *J. Mater. Chem.*, 2011, **21**, 4861–4868.

87   L. U. Hasanah, F. R. Agustina, N. F. S. Puspita, B. Suherman, F. Nurosyid, D. K. Sandi and Y. Iriani, *J. Phys. Conf. Ser.*, 2022, **2392**, 012034.

88   H. Muta, K. Kurosaki and S. Yamanaka, *J. Alloys Compd.*, 2003, **350**, 292–295.

89   F. D. Morrison, A. M. Coats, D. C. Sinclair and A. R. West, *J. Electroceramics*, 2001, **6**, 219–232.

90   Z. Lu, H. Zhang, W. Lei, D. C. Sinclair and I. M. Reaney, *Chem. Mater.*, 2016, **28**, 925–935.

91   F. D. Morrison, D. C. Sinclair and A. R. West, in *International Journal of Inorganic Materials*, Elsevier, 2001, vol. 3, pp. 1205–1210.

92   C. J. Howard, G. R. Lumpkin, R. I. Smith and Z. Zhang, *J. Solid State Chem.*, 2004, **177**, 2726–2732.

93   I. Akin, M. Li, Z. Lu and D. C. Sinclair, *RSC Adv.*, 2014, **4**, 32549–32554.

94   A. V Kovalevsky, A. A. Yaremchenko, S. Populoh, P. Thiel, D. P. Fagg, A. Weidenkaff and J. R. Frade, *Phys. Chem. Chem. Phys.*, 2014, **16**, 26946–26954.

95   N. -H. Chan, R. K. Sharma and D. M. Smyth, *J. Electrochem. Soc.*, 1981, **128**, 1762–1769.

96   J. A. Kilner and R. J. Brook, *Solid State Ionics*, 1982, **6**, 237–252.

97   A. C. Iyasara, W. L. Schmidt, R. Boston, D. C. Sinclair and I. M. Reaney, in *Materials Today: Proceedings*, Elsevier Ltd, 2017, vol. 4, pp. 12360–12367.

98   J.-H. Lin, C.-S. Hwang and F.-R. Sie, *Mater. Res. Bull.*, 2020, **122**, 110650.

99   F. Yang, J. S. Dean, Q. Hu, P. Wu, E. Pradal-Velázquez, L. Li and D. C. Sinclair, *J. Mater. Chem. A*, 2020, **8**, 25120–25130.

100   P. Zhang, Z. Lou, M. Qin, J. Xu, J. Zhu, Z. Shi, Q. Chen, M. J. Reece, H. Yan and F. Gao, *J. Mater. Sci. Technol.*, 2022, **97**, 182–189.

101   A. Walsh, C. R. A. Catlow, A. G. H. Smith, A. A. Sokol and S. M. Woodley, *Phys. Rev. B - Condens. Matter Mater. Phys.*, 2011, **83**, 1–4.

102   R. Ubic, K. Tolman, K. Chan, N. Lundy, S. Letourneau and W. M. Kriven, *J. Alloys Compd.*, 2013, **575**, 239–245.

103   F. Azough, S. S. Jackson, D. Ekren, R. Freer, M. Molinari, S. R. Yeandel, P. M. Panchmatia, S. C. Parker, D. H. Maldonado, D. M. Kepaptsoglou and Q. M. Ramasse, *ACS Appl. Mater. Interfaces*, 2017, **9**, 41988–42000.

104 M. T. Dylla, J. J. Kuo, I. Witting and G. J. Snyder, *Adv. Mater. Interfaces*, 2019, **6**, 1–7.

105 R. Kim and M. S. Lundstrom, *J. Appl. Phys.*, 2012, **111**, 024508.

106 M. Thesberg, H. Kosina and N. Neophytou, *J. Appl. Phys.*, 2016, **120**, 234302.

107 M. T. Buscaglia, F. Maglia, U. Anselmi-Tamburini, D. Marré, I. Pallecchi, A. Ianculescu, G. Canu, M. Viviani, M. Fabrizio and V. Buscaglia, *J. Eur. Ceram. Soc.*, 2014, **34**, 307–316.

108 S. Ohta, H. Ohta and K. Koumoto, *J. Ceram. Soc. Japan*, 2006, **114**, 102–105.

109 Hicks, Harman, Sun and Dresselhaus, *Phys. Rev. B. Condens. Matter*, 1996, **53**, R10493--R10496.

110 H. Ohta, S. Kim, Y. Mune, T. Mizoguchi, K. Nomura, S. Ohta, T. Nomura, Y. Nakanishi, Y. Ikuhara, M. Hirano, H. Hosono and K. Koumoto, *Nat. Mater.*, 2007, **6**, 129–134.

111 Y. Wang, X. Zhang, L. Shen, N. Bao, C. Wan, N. H. Park, K. Koumoto and A. Gupta, *J. Power Sources*, 2013, **241**, 255–258.

112 J. B. Li, J. Wang, J. F. Li, Y. Li, H. Yang, H. Y. Yu, X. B. Ma, X. Yaer, L. Liu and L. Miao, *J. Mater. Chem. C*, 2018, **6**, 7594–7603.

113 D. Bokov, A. Turki Jalil, S. Chupradit, W. Suksatan, M. Javed Ansari, I. H. Shewael, G. H. Valiev and E. Kianfar, *Adv. Mater. Sci. Eng.*, , DOI:10.1155/2021/5102014.

114 S. Yue, Z. Yan, Y. Shi and G. Ran, *Mater. Lett.*, 2013, **98**, 246–249.

115 D. C. Hague and M. J. Mayo, *J. Am. Ceram. Soc.*, 1994, **77**, 1957–1960.

116 S. Doeuff, M. Henry, C. Sanchez and J. Livage, *J. Non. Cryst. Solids*, 1987, **89**, 206–216.

117 B. Li, X. Wang, M. Yan and L. Li, *Key Eng. Mater.*, 2002, **224**–**226**, 577–580.

118 A. M. Huízar-Félix, T. Hernández, S. de la Parra, J. Ibarra and B. Kharisov, *Powder Technol.*, 2012, **229**, 290–293.

119 Y. Liu, Y. Lin, Z. Shi, C. W. Nan and Z. Shen, *J. Am. Ceram. Soc.*, 2005, **88**, 1337–1340.

120 M. Dhiman and S. Singhal, *J. Rare Earths*, 2019, **37**, 1279–1287.

121 G. W. Morey, *J. Am. Ceram. Soc.*, 1953, **36**, 279–285.

122 J. Ćirković, K. Vojisavljević, M. Šćepanović, A. Rečnik, G. Branković, Z. Branković and T. Srećković, *J. Sol-Gel Sci. Technol.*, 2013, **65**, 121–129.

123 D. N. Hikmah, D. K. Sandi, F. Nurosyid and Y. Iriani, *J. Phys. Conf. Ser.*, 2021, **2110**, 012011.

124 T. Xian, H. Yang, L. Di, J. Ma, H. Zhang and J. Dai, *Nanoscale Res. Lett.*, 2014, **9**, 1–9.

125 IR Spectrum Table & Chart, https://www.sigmaaldrich.com/GB/en/technical-documents/technical-article/analytical-chemistry/photometry-and-reflectometry/ir-spectrum-table, (accessed 6 October 2023).

126 J. Richter and M. Ruck, *Molecules*, 2020, **25**, 78.

127 R. D. Seddon, K. R., Plechkova, N. V., & Rogers, in *Ionic liquids further uncoiled : Critical expert overviews.*, 2011, pp. 217–235.

128 D. C. Green, S. Glatzel, A. M. Collins, A. J. Patil and S. R. Hall, *Adv. Mater.*, 2012, **24**, 5767–5772.

129 T. Kühl, M. Chen, K. Teichmann, A. Stark and D. Imhof, *Tetrahedron Lett.*, 2014, **55**, 3658–3662.

130 P. C. Marr and A. C. Marr, *Green Chem.*, 2015, **18**, 105.

131 K. Donato, L. Matějka, R. Mauler and R. Donato, *Colloids and Interfaces*, 2017, **1**, 5.

132 L. Mottram, D. Z. C. Martin, N. Reeves-McLaren and R. Boston, *J. Am. Ceram. Soc.*, 2018, **101**, 4468–4471.

133 A. K. Jha and N. Khare, *Phys. C Supercond.*, 2009, **469**, 810–813.

134 S. Safran, A. Kılıç, E. Kılıçarslan, H. Ozturk, M. Alp, E. Asikuzun and O. Ozturk, *J. Mater. Sci. Mater. Electron.*, 2015, **26**, 2622–2628.

135 H. Choi, Y. J. Kim, R. S. Varma and D. D. Dionysiou, *Chem. Mater.*, 2006, **18**, 5377–5384.

136 S. Hu, H. Wang, J. Cao, J. Liu, B. Fang, M. Zheng, G. Ji, F. Zhang and Z. Yang, *Mater. Lett.*, 2008, **62**, 2954–2956.

137 K. S. Yoo, T. G. Lee and J. Kim, *Microporous Mesoporous Mater.*, 2005, **84**, 211–217.

138 N. Yu, L. Gong, H. Song, Y. Liu and D. Yin, *J. Solid State Chem.*, 2007, **180**, 799–803.

139 P. Voepel and B. M. Smarsly, *Zeitschrift für Anorg. und Allg. Chemie*, 2017, **643**, 3–13.

140 Y. Liu, M. Calcabrini, Y. Yu, A. Genç, C. Chang, T. Costanzo, T. Kleinhanns, S. Lee, J. Llorca, O. Cojocaru-Mirédin and M. Ibáñez, *Adv. Mater.*, 2021, **33**, e2106858-n/a.

141 S. Grasso, M. Biesuz, L. Zoli, G. Taveri, A. I. Duff, D. Ke, A. Jiang and M. J. Reece, *Adv. Appl. Ceram.*, 2020, 119, 115–143.

142 S. S. Faouri, A. Mostaed, J. S. Dean, D. Wang, D. C. Sinclair, S. Zhang, W. G. Whittow, Y. Vardaxoglou and I. M. Reaney, *Acta Mater.*, 2019, **166**, 202–207.

143 US8313802B2, 2012.

144 H. Kähäri, M. Teirikangas, J. Juuti and H. Jantunen, *J. Am. Ceram. Soc.*, 2014, **97**, 3378–3379.

145 D. Wang, H. Guo, C. S. Morandi, C. A. Randall and S. Trolier-McKinstry, *APL Mater.*, , DOI:10.1063/1.5004420.

146 US11001530B2, 2021, 2.

147 C. Vakifahmetoglu, J. F. Anger, V. Atakan, S. Quinn, S. Gupta, Q. Li, L. Tang and R. E. Riman, *J. Am. Ceram. Soc.*, 2016, **99**, 3893–3901.

148 J. Guo, S. S. Berbano, H. Guo, A. L. Baker, M. T. Lanagan and C. A. Randall, *Adv. Funct. Mater.*, 2016, **26**, 7115–7121.

149 R. Boston, J. Guo, S. Funahashi, A. L. Baker, I. M. Reaney and C. A. Randall, *RSC Adv.*, 2018, **8**, 20372–20378.

150 S. Hirano and S. Somiya, *J. Am. Ceram. Soc.*, 1976, **59**, 534–534.

151 E. Y. Gutmanas, A. Rabinkin and M. Roitberg, *Scr. Metall.*, 1979, **13**, 11–15.

152 D. V Wagle and G. A. Baker, *Mater. Horizons*, 2015, **2**, 157–167.

153 N. Yamasaki, K. Yanagisawa, S. Kanahara, M. Nishioka, K. Matsuok and J. Yamazaki, *J. Nucl. Sci. Technol.*, 1984, **21**, 71–73.

154 K. Yanagisawa, S. Kanahara, M. Nishioka and N. Yamasaki, *J. Nucl. Sci. Technol.*, 1984, **21**, 558–560.

155 J. Guo, H. Guo, A. L. Baker, M. T. Lanagan, E. R. Kupp, G. L. Messing and C. A. Randall, *Angew. Chemie - Int. Ed.*, 2016, **55**, 11457–11461.

156 US2021230075, 2021.

157 A. Baker, H. Guo, J. Guo, C. Randall and D. J. Green, *J. Am. Ceram. Soc.*, 2016, **99**, 3202–3204.

158 H. Guo, J. Guo, A. Baker and C. A. Randall, *ACS Appl. Mater. Interfaces*, 2016, **8**, 20909–20915.

159 J. Guo, H. Guo, A. L. Baker, M. T. Lanagan, E. R. Kupp, G. L. Messing and C. A. Randall, *Angew. Chemie*, 2016, **128**, 11629–11633.

160 M. Biesuz, G. Taveri, A. I. Duff, E. Olevsky, D. Zhu, C. Hu and S. Grasso, *Adv. Appl. Ceram.*, 2020, **119**, 75–89.

161 Entegris, Unstable- Ostwald Ripening,

https://www.entegris.com/en/home/resources/technical-information/glossary/unstable.html, (accessed 5 September 2023).

162   M. Chi, W. Ma, J. Guo, J. Wu, T. Li, S. Wang and P. Zhang, *J. Mater. Sci. Mater. Electron.*, 2019, **30**, 21435–21443.

163   H. Huang, J. Tang and J. Liu, *Ceram. Int.*, 2019, **45**, 6753–6758.

164   S. Funahashi, H. Guo, J. Guo, A. L. Baker, K. Wang, K. Shiratsuyu and C. A. Randall, *J. Am. Ceram. Soc.*, 2017, **100**, 3488–3496.

165   J. Cockburn and R. Boston, *RSC Adv.*, 2019, **9**, 40917–40923.

166   D. G. Vlachos and K. F. Jensen, *Surf. Sci.*, 1992, **262**, 359–370.

167   J. Andrews, D. Button and I. M. Reaney, *Tohnson Matthey Technol. Rev.*, 2020, **64**, 219–232.

168   H. W. Nesbitt, G. M. Bancroft, W. S. Fyfe, S. N. Karkhanis, A. Nishijima and S. Shin, *Nature*, 1981, **289**, 358–362.

169   O. Ozmen, C. Ozsoy-Keskinbora and E. Suvaci, *J. Am. Ceram. Soc.*, 2018, **101**, 1074–1086.

170   J. Kalarus, G. Kogias, D. Holz and V. T. Zaspalis, *J. Magn. Magn. Mater.*, 2012, **324**, 2788–2794.

171   Y. Ying, L. Hu, Z. Li, J. Zheng, J. Yu, W. Li, L. Qiao, W. Cai, J. Li, D. Bao and S. Che, *Materials (Basel).*, , DOI:10.3390/ma16093454.

172   J. jun Lan, X. ming Chen, M. dan Liu, L. na Liu and H. li Lian, *J. Am. Ceram. Soc.*, 2023, 6826–6836.

173   K. Tsuji, A. Ndayishimiye, S. Lowum, R. Floyd, K. Wang, M. Wetherington, J. P. Maria and C. A. Randall, *J. Eur. Ceram. Soc.*, 2020, **40**, 1280–1284.

174   S. Devyatkin, *Interaction of Oxides and Molten Alkalis, Products of Reaction and Application*, 2015.

175   C. Jiang, X. Tian and G. Shi, 2016, **136**, 321–327.

176   R. Boston, P. Y. Foeller, D. C. Sinclair and I. M. Reaney, *Inorg. Chem.*, 2017, **56**, 542–547.

2.0 Methodology

2.1 Processing

2.1.1 Ionic Liquid Synthesis

The raw materials listed in Table 2.1 were used during Ionic liquid synthesis. The acetates were used without further purification. The acetates were all assayed to determine the water content using a TA Instruments SDT 650. This was then used in the batch calculations to ensure the correct stoichiometry. Two sources of 1-Ethyl-3-methylimidazolium acetate (emimOAc) were used which differed in purity and price, the Sigma Aldrich emimOAc was used in all the experiments unless specifically specified. These were used without further purification.

Table 2.1 Raw materials used for ionic liquid synthesis.

Name	Chemical Formula	CAS Number	Supplier	Purity
Strontium acetate	$C_4H_6O_4Sr$	543-94-2	Sigma Aldrich	Quality level 200 (~3% water)
Lanthanum acetate	$C_6H_9LaO_6.xH_2O$	100587-90-4	Sigma Aldrich	99.9%
Europium acetate	$C_6H_9EuO_6.xH_2O$	62667-64-5	Alfa Aesar	99.9%
1-Ethyl-3-methylimidazolium acetate (default IL)	$C_8H_{14}N_2O_2$	143314-17-4	Sigma Aldrich	$\geq 95.0\%$
1-Ethyl-3-methylimidazolium acetate (high purity IL)	$C_8H_{14}N_2O_2$	143314-17-4	Alfa Aesar	97%

The ionic liquid method was used to synthesis $Eu_xLa_{0.15-x}Sr0_{.775}TiO_{3,}$ a schematic of this is shown in Figure 2.1. In this method stoichiometric amounts of europium acetate, lanthanum acetate and strontium acetate were combined in accordance with the composition being made. A fixed mass of 1.9912g of strontium acetate was used, then the required masses of Eu and La acetates were calculated based on the desired stoichiometry of the final product. The acetates were combined and dissolved in deionized water under a continuous stirring action. The level of water used to dissolve the acetates was not measured as this would be fully evaporated later, though just enough was used to dissolve the acetates.

16 ml of the ionic liquid, 1-ethyl-3-methylimidazolium acetate (emimOAc) was then added. This was left stirring at 90 ℃ for approximately 3 hours, until all the water had evaporated. 3552 μl of titanium isopropoxide was added drop wise to the mixture, maintaining the stirring action. Once allowed to fully combine for 5 minutes the solution was transferred into a square flat-bottomed crucible and calcined for 2hr at 800 ℃ in a muffle furnace.
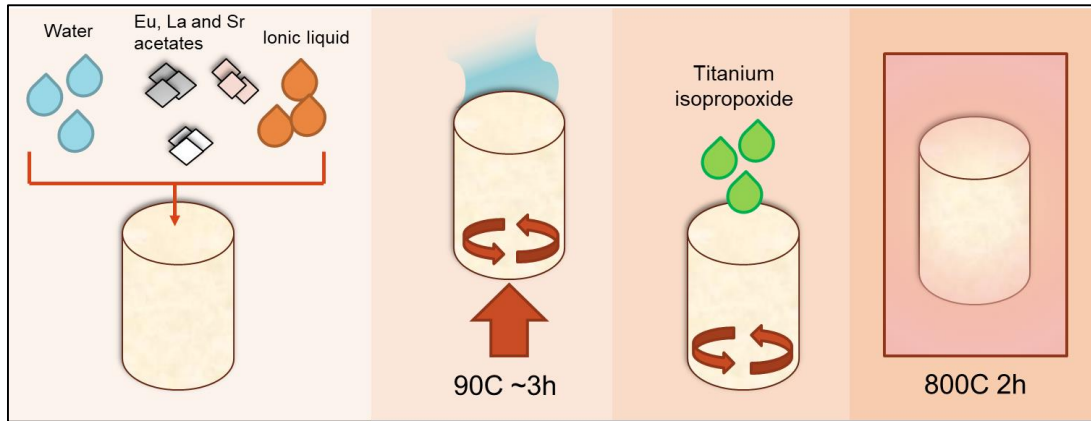
Figure 2.1 Schematic of ionic liquid synthesis technique

2.1.2 Cold Sintering

The cold sintering process involved combining 30 wt. % of the 420 ℃ fired powder (the infill) with the 800 °C calcined powder (matrix) in a batch size of ~ 5g. The large batch size was required to achieve sufficient milling in the ball milling step. Pellets made both with and without this milling step are shown in the results chapter. Once combined the powders were placed in a ball mill with sufficient isopropanol and milled overnight to break up agglomerates and allow for thorough mixing. After removing from the ball mill the isopropanol was evaporated using a Kenwood Induction Heater and the powder then stored in a desiccator.

To make one cold sintered pellet a mass of 0.7g was taken from this batch and combined with 700μl of distilled water. A schematic of the process that followed is shown in Figure 2.2. The combined powder and water were hand ground in a pestle and mortar for approximately 15 minutes until the powder was no longer wet and was free flowing. This was then loaded into a 12.7mm cylindrical die and tapped to encourage the close packing of the powder. Disks of parchment paper cut to the exact size of the die were applied to the top and bottom plungers, separating the powder from direct contact with the metal. This prevented the powder from fusing with the plungers, enabling easier removal from the die.

Uniaxial pressure was applied and the powder allowed to settle for 10 minutes before adding additional pressure to account for any lost in that resettling time. A set temperature was then applied via heated platens on the top and bottom of the die. After 1 hour the temperature was removed and allowed to cool with the assistance of a fan for half an hour. The pressure was slowly released and the pellet removed from the die. An annealing procedure of 800 ℃ for 2 hr in a muffle furnace allowed the infill phase to complete the reaction into the cubic perovskite phase.
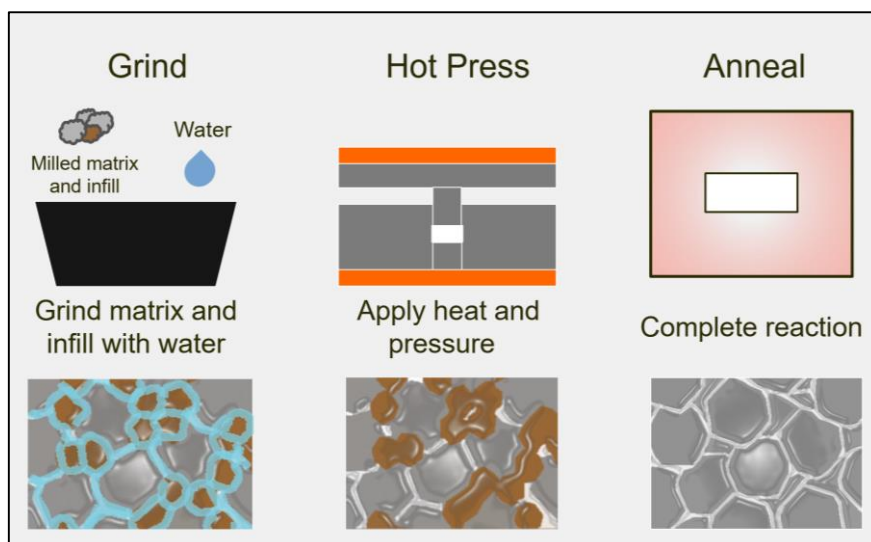
Figure 2.2 Schematic of Cold Sintering Process

2.1.3 Reducing Under Atmosphere

In order to promote oxygen vacancies samples were sintered in a continuously flowing reducing atmosphere of 5% H_2 / 95% N_2 gas. This was done by placing the sample in the centre of a tube furnace which was sealed at both ends. The gas would enter at one end of the tube and flow out through the other side through a bubbler. This allowed rough control of the flow rate for consistency, though the exact flow rate was not measured.

During this procedure the furnace would heat the sample up to the maximum set temperature at a rate of 5 ℃/min then hold for the set dwell time, followed by a ramp back down to room temperature also at 5 ℃/min. The default procedure was 1325 ℃ held for 8 h. The reducing gas would only be turned off once the sample had reached ~60 ℃ or less. At which point the sample was removed from the furnace and stored in a desiccator.

2.1.4 Solid State Sintering

Table 2.2 Raw materials of Solid State Synthesis.

Name	Formula	CAS	Supplier	Purity
Titanium dioxide	TiO_2	13463-67-7	Sigma Aldrich	99.9 %
Strontium carbonate	$SrCO_3$	1633-05-2	Sigma Aldrich	99.9 %
Lanthanum Oxide	La_2O_3	1312-81-8	Sigma Aldrich	99.9 %

$La_{0.15}Sr_{0.775}TiO_3$ was solid state sintered following the protocol of Lu *et al.* in order to produce comparable results.[1] The raw materials used for this are detained in Table 2.2. Raw

materials were dried overnight: La_2O_3 at 180 ° C, $SrCO_3$ at 180 ℃ and TiO_2 at 900 ℃, then stored in a desiccator to cool to room temperature. Stoichiometric quantities were weighed and milled together using isopropanol as a lubricant. After milling overnight, the powder was dried, sieved and calcining in a muffle furnace, ramp rate 5 ℃ / min up to and from, 1100 ℃ for 3 hr in an alumina crucible in air. The resulting powder was hand ground in a pestle and mortar before being pressed into pellets using a uniaxial force of 75 MPa applied foe 1 min.

These pellets were sintered in a tube furnace under flowing 5% H_2 / 95 % N_2 for 6 h at 1500 ℃ for 6 h or 1325 ℃ for 8 h, ramp rates 5 ℃/min. The different temperatures were due to furnace limitations at the time. Lattice parameter of LSTO solid state sintered and reduced at 1500 ℃ was 3.9099 Å.

2.2 Materials Characterisation

2.2.1 X-Ray Diffraction (XRD)

Principles of XRD

In a diffractometer monochromatic x-rays are generated by firing electrons accelerated through a potential difference at a metal target, e.g. Copper. The subsequent ionization of the inner shell electrons and the refilling of those orbitals by higher energy electrons which reduce energy to occupy lower shells, generates characteristic x-rays. This process is illustrated in Figure 2.4. The use of a nickel filter can remove all but the Kα radiation, a narrow and intense range of wavelengths which can be used for XRD. Kα radiation is generated by an electron in the 2p orbital dropping to occupy the now empty 1s orbital. There are two possible spin states of the 2p electron so this produces a doublet; two x-rays which are very close in wavelength. $K\alpha_1$ ($2p_{\frac{1}{2}} \rightarrow 1s_{\frac{1}{2}}$) wavelength is 1.54051 Å, and $K\alpha_2$ ($2p_{\frac{3}{2}} \rightarrow 1s_{\frac{1}{2}}$) wavelength is 1.54433 Å. $K\alpha_2$ is approximately 2/3 of the intensity of the $K\alpha_1$ and can be identified and removed in post data analysis.
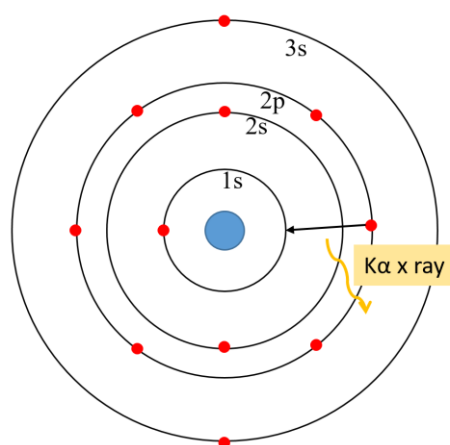
Figure 2.4 Schematic of Cu Characteristic X-ray production

When X-rays are directed at a crystalline material they interact with electronic orbitals of atoms. XRD relies on the elastic scattering of the primary x-rays by pseudo planes formed by the regular arrangement of atoms.

The Bragg Law dictates that when a monochromatic x ray source is directed onto a set of planes, positive interference will occur only when the diffracted beams are in phase with one another, Figure 2.5 shows a schematic of this process. The Bragg equation in shown in Equation 2.1 where λ is the wavelength of the radiation, θ is the angle of incidence, d is the spacing between the planes and n must be an integer.

$$2d \sin \theta = n\lambda \qquad \textit{Eqn. 2.1}$$
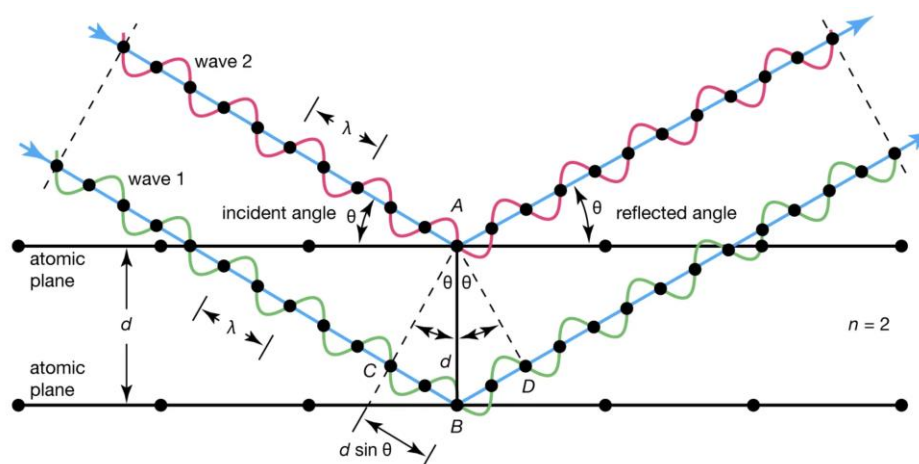
Figure 2.5 Schematic of constructive interference of x-rays diffracted from a set of planes.

Only when this equation is satisfied will diffracted radiation be able to reach the detector and cause an intensity peak. When the Bragg equation is not satisfied, the diffracted beams are out of phase, and destructively interfere with one another. The XRD spectra is typically plotted as the level of intensity from the detector against the angle of incidence multiplied by 2. This can be used against a database of crystal structures to identify the phases present. Each crystal system has a unique symmetry and distancing between planes and so a unique XRD spectra, much like a fingerprint. Furthermore, as the wavelength of the radiation and the angle of incidence are known we can calculate the d spacing for each set of planes, which allows the determination of lattice parameters.

Instrumentation for XRD

A Panalytical Aeris Diffractometer with a copper tube (30kV 40mA) was used in a Bragg-Brentano reflection powder diffraction set-up, ¼° divergence slit, a 0.15mm Ni filter, 0.02 Rad soller slits. All scans covered 10 to 100 °2θ. Phases matching was performed using the PDF4+ software database.

Samples were either measured as powders in which case the powders were hand ground to a fine consistency similar to talcum powder, then mounted in a pack filled XRD holder to ensure a flat surface with no preferred orientation. To perform refinements on bulk samples the samples were smashed and ground to a powder to homogenise the material and allow for

the reference powder to be combined. Bulk samples were on occasion measured to gather an XRD pattern, these were mounted using putty onto a zero background XRD sample holder and pressed flush to the rim of the holder using a glass slide.

2.2.2 Rietveld Refinement

Principles of Rietveld Refinements

Rietveld refinement allows the modelling of a crystal structure whose XRD profile matches most closely that of a measured spectra. From the refinement of this modelled structure key crystal features such as the lattice parameter and relative phase abundance can be inferred about a sample.[2] A Rietveld refinement does this by using a least squares method in which the intensity differences between that of the model profile and the measured profile are minimised to create the most accurate model. The summed square of the differences at each data point is referred to as the residual, S_y, and this is the parameter which the model tries to minimise. S_y is calculated using Equation 2.2 where w_i is $1/y_i$, y_i is the observed intensity at the *i*'th step (from the measured XRD) and y_{ei} is the calculated intensity at the *i*'th step (of the model).[3] The closer the residual is to zero the better the model fits the measured data.

$$S_y = \sum_i w_i (y_i - y_{ei})^2 \qquad \textit{Eqn. 2.2}$$

The intensities of the model, y_i, are calculated using Equation 2.3 where s is the scale factor, K represents the miller indices (hkl) of the Bragg reflection, L_k contains the Lorentz, polarisation and multiplicity factors, ϕ is the reflection profile function, P_k is the preferred orientation function, A is an absorbance factor, F_k is the structural factor and y_{bi} is the intensity of the background.[3]

$$y_{ei} = s \sum_K L_K |F|^2 \phi \, (2\theta_i - 2\theta_K) P_K A + y_{bi} \qquad \textit{Eqn. 2.3}$$

Equation 2.3 is a back end calculation performed by refinement software using the much more physical parameters of the structure inputted by the user such as site occupancy, site species, crystal structure ect. The least square method uses small adjustments in the parameters being refined which should result in an improved model with an overall lower residual.[3] This process is repeated until a good fit is found. A 'good' refinement is judged by the values of the Goodness of Fit (GOF) or the Rwp value which reduce as the residual, S_y, reduces. The GOF is determined by Equation 2.4 where N is the number of data points in the XRD and P is the number of varied parameters.

$$GOF = \left(\frac{S_y}{N-P} \right)^{1/2} \qquad \textit{Eqn. 2.4}$$

Arguably most important is that the model must contain values which are physically possible, and reasonable as the refinement may move towards false minima in GOF which is not an accurate description of the measured data. This is down to the user who must use logic and published literature to keep the values in the realm of possibility.

Process of a Rietveld Refinement

XRD analysis was run on powdered samples with the addition of a 640f or 660c silicon standard at a level of ~ 10 wt.%, which allows corrections to be made for instrumental features and sample height displacement in the XRD pattern. This powder pattern is loaded into GSAS 2, which was used to perform Rietveld Refinement. Parameters of the measurement are selected in the software such as the XRD arrangement: Bragg-Brentano and the X-ray source: Cu Kα. The software asks for an instrument parameter file and in most cases refinements were begun by selecting the generic template for copper source X-ray data or loaded from a previous refinement of a sample analysed on the same instrument.

If using the template, the instrument parameters and background were refined first based only on the silicon standard peaks. These parameters included the sample height displacement, and parameters U, V, W, X, Y, Z and SH/L which control the profile of the peaks. A combination of Gaussian and Lorentzian distributions are used to simulate the measured profiles; U,V and W are parameters in the Gaussian distribution and X,Y,Z are parameters in the Lorentzian distribution. A Gaussian distribution is a classic bell shaped distribution and Lorentzian distribution has a broader base with narrow top.[4] in parameters are used to create the closest match for the peak shapes. The background was fit using a Chebyschev-1 function, typically with 3 coefficients.

These parameters were then carried forward into the fitting of the sample data, at which point no change was made to the sample height displacement and only small adjustments to the instrument parameters were made. The following crystal structure information for the perovskite phase was input into the model: Crystal structure pm-3m, initial lattice parameter of ~ 3.91 Å. The atoms Eu, La, Sr, Ti, and O were input into atomic positions with the relevant fractional occupancy, Figure 2.6 shows an example of how this was done for a refinement for $La_{0.15}Sr_{0.775}TiO_3$. From this point the parameters refined were: unit cell parameter, crystallite size, small changes to the profile parameters and occasionally the fractional occupancies. The order of this was dictated by the difference plot, shown in Figure 2.7. This is visible throughout the refinement and allows the user to see the difference between the modelled pattern and the measured pattern which indicates which parameters need to be adjusted in the model structure.

◀ General	Data	Atoms	Draw Options		Draw Atoms		RB Models	Map peaks	MC/SA	RMC	ISODIS
	Name	Type	refine	x	y	z	frac	site sym	mult	I/A	Uiso
0	Sr1	Sr+2		0.00000	0.00000	0.00000	0.7750	m3m	1	I	0.01000
1	La2	La+3		0.00000	0.00000	0.00000	0.1500	m3m	1	I	0.01000
2	Ti3	Ti+4		0.50000	0.50000	0.50000	1.0000	m3m	1	I	0.01000
3	O4	O-2		0.50000	0.50000	0.00000	1.0000	4/mmm(z)	3	I	0.01000

Figure 2.6 Atoms modelled in the refinement of La$_{0.15}$Sr$_{0.775}$TiO$_3$.
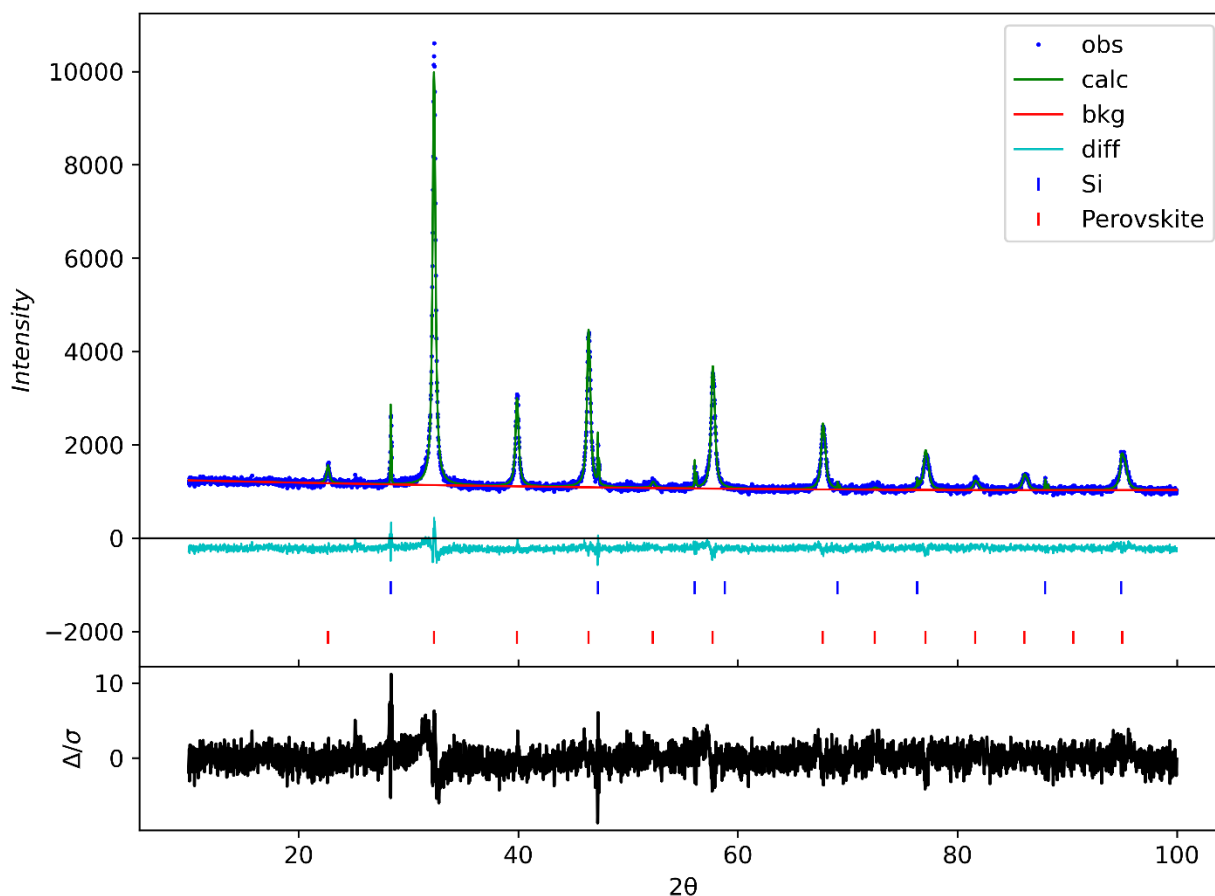
Figure 2.7 The top half of this figure shows the powder XRD pattern overlaid with the calculated profile based on the model structure and the background in a reitveld refinement. The lower half shows the difference plots which shows the difference in intensity between the model and the measured data.

2.2.3 Simultaneous Thermal Analysis (SDT)

Principles of SDT

SDT combines two techniques: Thermogravimetric analysis (TGA) and Differential Scanning Calorimetry (DSC). Firstly, TGA allows the weight of a sample to be measured during a heating cycle and is usually used to monitor weight loss during a reaction. DSC monitors the heat energy required to maintain a specific temperature which is compared to a reference to see how much energy a particular sample is absorbing or emitting. This is particularly useful if an endothermic or exothermic reaction takes place in the material as the temperature the reaction occurs can be found. An example of an endothermic reaction is one in which energy is required for the transition such as the breaking of bonds to form a new phase. An exothermic reaction is one in which heat energy is released such as the burning of a wax in a candle.

Combining these two techniques allows a larger picture to be gathered about the behavior of a sample under specific conditions. You can also control the atmosphere these reactions occur in: under an inert atmosphere such as nitrogen or in a reactive gas such as air. It is important

to know if weight loss occurs at the same time as a change in heat input required as this can indicate that a reaction is taking place and a product is being lost.

These instruments typically work by placing an empty reference pan on one thermobalance, which simultaneously heat and weighs the reference. A small amount of sample is then placed in an identical pan onto the sample thermobalance and the heat energy required to maintain a specific temperature and the weight is compared to the reference.

Instrumentation

A TA Instruments SDT 650 was used for this work with alumina pans. This instrument can be operated in a nitrogen or compressed air flowing atmosphere (100 ml/min as standard). Heating rate of 10 °C/ min from room temperature up to a maximum of 1500 ℃ could be used to heat samples and TRIOS software was used to display and analyse the data.

For oxygen uptake experiments sintered samples were ground using a pestle and mortar to increase surface area and encourage oxygen loss. This also increased surface contact with the pan to ensure that heat was applied evenly to the sample. Using a small depth of powdered sample mitigates the possibility of cold spots. These were then heated from room temperature to 1200 ℃ at 10 ℃ / min in flowing air. The loss of absorbed water caused an initial weight loss and so the 'start weight' was actually taken as the weight at 400 ℃ to observe only oxygen uptake effects. Oxygen uptake is a thermally activated process and according to Moos *et al.* is 'frozen-in' below 400 ℃. [5] The weight was then converted into a percentage of this value, giving a value for wt % oxygen uptake.

2.2.4 Seebeck Analysis

Principles of Seebeck Analysis

Figure 2.8 shows a schematic of the Seebeck Analyser. To determine the Seebeck coefficient and electrical conductivity of a thermoelectric material as a function of temperature, a sample in the shape of a prism is placed vertically between two blocks inside a furnace. An additional heater on one end of the sample creates a temperature gradient whilst the furnace is held at a specific temperature. The Seebeck coefficient is then measured by taking readings of the upper and lower temperatures (T_1 and T_2) using thermocouples that are pressed against the sample's side. A constant current is simultaneously applied to the two end of the sample. The two thermocouple act as a multimeter determine the voltage drop across the sample (dV) and current (I). Resistance is voltage divided by the current, therefore, resistance can be calculated. This is equivalent to the dc four-probe method.[6]

Therefore, the Seebeck coefficient, dV/dT, and electrical conductivity, which is the inverse of electrical resistance, can be determined simultaneously.
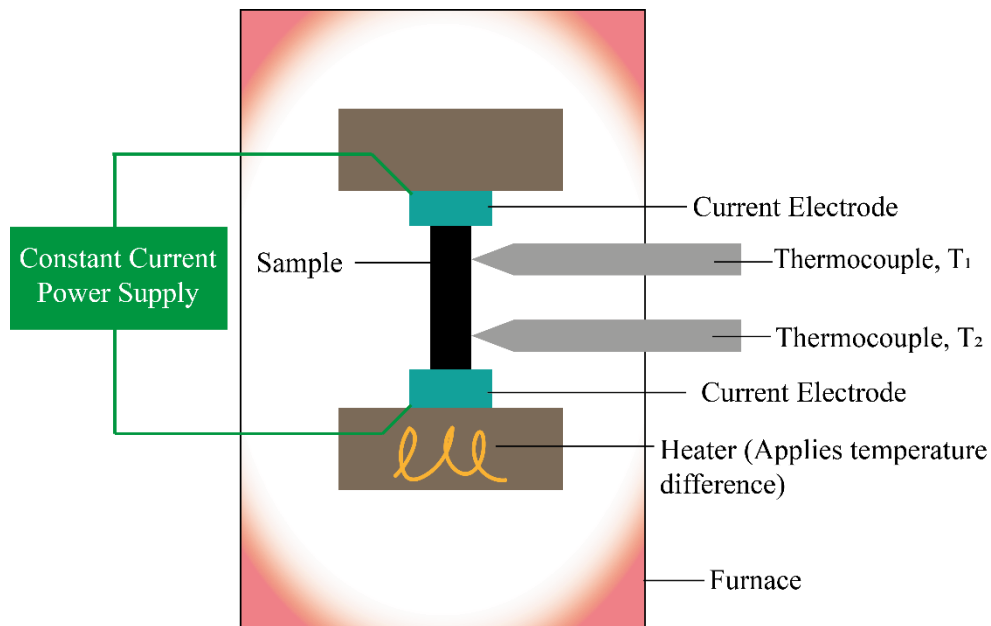
Figure 2.8 Schematic of Seebeck Analyser

Instrumentation

A ZEM-3 Seebeck analyser was used which measures samples in low pressure helium gas up to 600 °C. This instrument belonged to Dr Robert Freer at The University of Manchester and measurements were performed by PhD student Yibing Zhu.

Due to the way in which the Seebeck analyser operates, requiring a temperature differential, the output data is not at round temperature values. For example, input a request to measure between 50 and 100 ºC with two steps, the output data might be at 52.4 ºC and 100.6 ºC. Therefore, to align these values to the same temperatures of the thermal conductivity a spline fit was used to interpolate values in order to calculate the ZT. This was undertaken on Origin using a cubic spline method only between acquired points – no extrapolation of values was performed.

2.2.5 Zeta Potential

Principles of Zeta Potential

A colloidal system is where one state of matter is finely dispersed in another state of matter e.g. a powder finely dispersed in a liquid, an aerosol or an emulsion. The Zeta potential gives an indication of whether this colloidal system is stable – remains a dispersion and does not coagulate.[7]

DVLO theory – Derjaguin, Verwey, Landau and Overbeek developed the theory on the stability of colloidal systems. They found that the stability is determined by Van der Waals attractive force and the electrical double layer repulsive forces between particles. These two opposing forces sum to give a net energy which varies as a function of the particle separation. By increasing the temperature, the repulsive force can be overcome and particles come into

contact. If repulsion is dominant, then the colloidal system is stable but if repulsion can be overcome by attractive force the colloid is unstable and will coagulate.[7]

Surface charge of a particle can be caused by dissociation of acidic groups on the surface, preferential dissolution of ions from the lattice, adsorption of charged species on the surface. When a surface charge is present, in order to form an equilibrium surrounding ions arrange themselves close to the surface creating an 'electrical double layer'. The electrical double layer consists of two parts: the stern layer which is an inner layer of strongly bound ions and a secondary layer where ions are more loosely associated called the diffuse layer. When this particle moves though the liquid the ions within double layer boundary move with the particle but unassociated ions stay with the bulk and hydrodynamically shear past each other. The potential at that boundary is the Zeta potential. A Zetasizer is used to measure the speed of particles moving due to an electric field, the velocity of the particle in a unit electrical field is called the electrophoretic mobility. The Smoluchowski approximation is used to convert the electrophoretic mobility into the zeta potential.

A large negative or a large positive zeta potential means that particles will electrostatically repel each other and the dispersion will be stable. However, a zeta potential between -30 and 30 mV forms an unstable dispersion and will coagulate. A Zeta potential of anything other than 0 indicates that there is surface charge present.

PH has a strong influence on the zeta potential of a solution, when the pH changes the concentration of hydrogen ions changes which may protonate or deprotonate groups on the surface. This in turn changes the surface charge. By increasing the basicity (reducing the concentration of H^+) you can drive the zeta potential to more negative values through deprotonation. Alternatively, in an acidic solution you can make the zeta potential more positive through protonation. The pH at which the zeta potential is zero is called the isoelectric point.[7] Figure 2.9 shows the zeta potential of three polymers varying with pH with an isoelectric point at pH 4.[8]
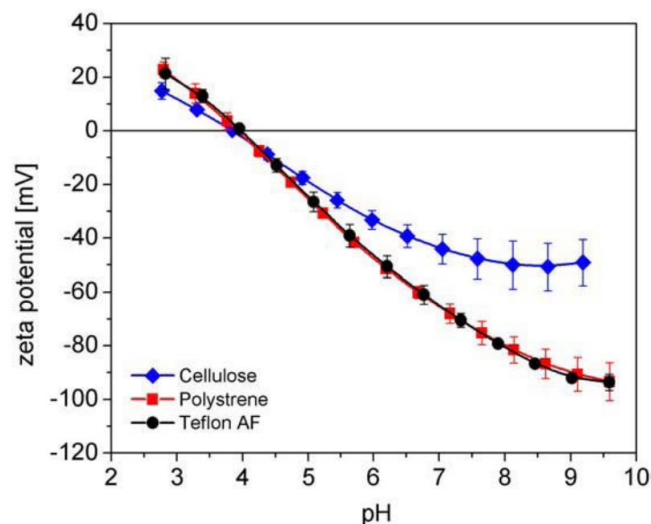
Figure 2.9 A typical Zeta potential dependence on pH for three plastic thin films.[8]

Instrumentation

Malvern Zetasizer Nano ZS instrument equipped with a 4 mW He-Ne laser (lambda= 633 nm) operating at a fixed scattering angle of 173 °. The potentials were calculated from the Henry equation using the Smoluchowski approximation. Samples were diluted in 1mM KCl at 0.1 % w/w.

2.2.6 Grain Size Determination

Grain size measurements were undertaken from SEM SE images using the software ImageJ. By measuring the longest distance across at least 500 grains the average grain size was determined.

2.2.7 Density Measurements

2.2.7.1 Archimedes Method

The density of the ionic liquid synthesised then regular sintered pellets and the solid state synthesised pellets was determined using the Archimedes method in water. Archimedes principle relies on the difference in weight recorded for the pellet in air, the actual weight, and when submerged, submerged weight. This weight difference is generated by the buoyancy force F_b, created by the displacement of water equal to the volume of the pellet. Using the density of the submerging liquid, ρ_f, in this case water, and acceleration due to gravity, g, the volume of the pellet, V, can be determined. The weight of the dry pellet in air divided by this volume is equal to its density.

$$Submerged\ weight = Actual\ weight - F_b \qquad \text{Eqn. 5}$$

$$F_b = -\rho_f gV \qquad \text{Eqn.6}$$

$$V = \frac{F_b}{-\rho_f g} \qquad \text{Eqn. 7}$$

$$Density = \frac{Actual\ weight}{V} \qquad \text{Eqn.8}$$

2.2.7.2 Geometric Method

Cold sintered pellet densities were determined using the geometric density method as these were expected to be high in porosity. The Archimedes method is not recommended for highly porous materials. Geometric density is determined by measuring the thickness, t, and diameter, d, of the pellets (each measured three times then averaged). This is then used to calculate the volume which is divided by the mass, m, measured by a balance.

$$Density = \frac{\pi(\frac{d}{2})^2 t}{m} \qquad \text{Eqn.9}$$

2.2.8 Scanning Electron Microscopy (SEM)

SEM is a technique in which electrons emitted from an electron gun are focussed and accelerated towards a sample, where they scan across the surface interacting with the atoms within that sample. The penetration depth and interaction volume of the incident electrons can be controlled by altering the accelerating voltage, typically between 5-50 keV, and the spot size. The result of this interaction can be one of three mechanisms, whose products can be focused back into a detector to form an image.[9]

First, elastic scattering (or diffraction) can occur where electrons interact with the atoms without losing a significant amount of energy, these are Back Scattered Electrons (BSE). Contrast is caused by variation in the atomic mass of atoms and density of the sample.[9]

Secondly, inelastic scattering is when electrons lose some of their energy during the interaction. Electrons impart their energy to the atoms and are re-emitted as Secondary Electrons (SE). This type of scattering provides information from much closer to the surface compared to BSE as these lower energy electrons cannot escape from as large a depth within the sample as BSE. In this case contrast is caused by variations in sample height.[9] Charging can also occur if the sample is not a conductive material, insulating materials accumulate charge at the surface which can interfere with the image acquisition. To avoid this, resistive materials are coated with carbon or gold atoms using low pressure deposition.

Finally, when atoms are excited by the incoming electrons they may re- emit energy in the form of characteristic X-rays. These are unique to the shell spacings within a particular element and so can be used to identify chemical composition, which is the basis of Energy-dispersive X-ray Spectroscopy (EDS).[9] This technique can be used to observe featured within the range of 0.1 to 10 μm.[9]

Instrumentation

SEM was conducted using two instruments: Inspect F and Inspect F 50 Field Emission SEM. For SE imaging accelerating voltage of 5 eV and spot size 2.5-3.5 was used. For EDS an accelerating voltage of 20 keV was used with spot size 3.5 was used.

Samples were mounted on aluminium stubs with carbon stickers in the form of pellets or powers. And coated with carbon or gold. In the case of solid pellets, silver paint was used to provide greater electrical connection between the sample and the stub to avoid charging.

2.2.9 Transmission Electron Microscopy (TEM)

Similar to SEM, in which a beam of electrons is generated from an electron gun and accelerated towards the sample, in the case of TEM the electron beam penetrates through the sample rather than reflecting or diffracting from the near surface. For this reason, the specimen thickness must be much less than in SEM, usually thinner than 2000 Å and much higher accelerated voltage can be used. The much smaller resolutions can be seen using TEM, in the range of 1 – 100nm. [9]

There are three transmission signals generated by TEM, these are: inelastic scattering (used for Electron Energy Loss Spectroscopy), coherent elastic scattering (used for Selected Area Diffraction) and the undiffracted beam (used for imaging). [9]

In TEM imaging the detector below the sample collects the undiffrated beam and in simple imaging the contrast originates from sample thickness and/or atomic mass. [10]

2.2.10 Electrospray Ionisation Mass Spectroscopy

Electrospray Ionisation is used to generate ions from a solution in order to pass into a mass spectrometer. The sample solution is passed through a capillary tube which is maintained at a voltage, when they exit the electrospray tip they generate highly charged droplets which forms a mist. Using a pressure and potential gradient the droplets are guided towards the mass spectrometer and are reduced in size by the evaporation of the solvent (aided by an application of temperature or a drying gas e.g. nitrogen) until ions from the surface of the droplets can be ejected into the gaseous phase.[11] This process is illustrated in Figure 2.10.[11] Ions are protonated or de-protonated forms of the molecules within the sample or fragments of them. The resulting ions are accelerated into a mass analyser.
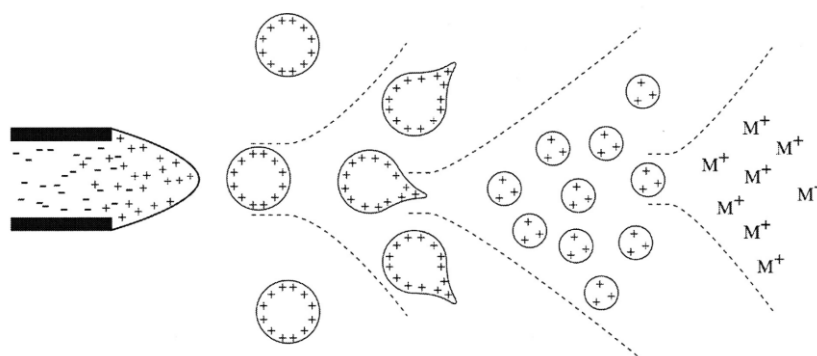
Figure 2.10 Schematic of the electrospray ionisation.[11]

A mass spectrometer is able to separate ions by their mass to charge ratio (m/z). This is done using a magnetic or electrical field. The Waters LCT Classic uses a Time of Flight mass analyser which separates ions based on the time it takes to travel through a flight tube. The ions response to a pulsed accelerating voltage is determined by their m/z ratio.[12] Ions with lower m/z travel fastest and arrive at the detector before ions with larger m/z.[12] A mass spectrum is outputted which plots the intensity vs. m/z with the largest intensity set as 100 %, to which the other intensity peaks are scaled.

Instrumentation

MS instrument – Waters LCT Classic. The sample was diluted 1:1 in HPLC grade Acetonitrile and infused into the mass spectrometer (Flow rate 20uL min^{-1})

Instrument parameters, +ve mode

Mode:	ESI +ve ion
Range:	60-1700 m/z
Source temperature	120°C
Desolvation temperature:	150°C

Cone gas flow:	10L hr^{-1}
Desolvation gas flow:	524L hr^{-1}
Capillary voltage	3300v
Sample cone voltage	25v
RF Lens	150v

Instrument parameters, -ve mode

Mode:	ESI -ve ion
Range:	60-1700 m/z
Source temperature	120ºC
Desolvation temperature:	150ºC
Cone gas flow:	18L hr^{-1}
Desolvation gas flow:	522L hr^{-1}
Capillary voltage	2896v
Sample cone voltage	25v
RF Lens	150v

2.2.11 Laser Flash Analysis

Laser Flash Analysis (LFA) can be used to determine the diffusivity and heat capacity of a material to determine its thermal conductivity according ASTM standard E1461-13.[13] The lower surface of a sample is heated by a short energy pulse whilst the top side of the sample is monitored by an infrared detector which records the temperature change versus time curve, Figure 2.11.[14] Figure 2.12 shows an example of this curve which can be used to determine the diffusivity of the sample from the diffusivity ,a, the sample thickness, d, and the time value at half the maximum temperature change, $t_{1/2}$ (Equation 2.10). The diffusivity can be measured at different temperatures to determine the diffusivity as a function of temperature. The furnace heats the sample to a set temperature before applying the pulse, which is repeated three times, allowing the sample to return to the set temperature between pulses. The diffusivity is averaged from the result of the three pulses.

$$a = 0.1388 \; \frac{d^2}{t_{1/2}} \qquad \qquad Eqn. \; 2.10$$

By using a standard sample alongside the sample with a known specific heat capacity the heat capacity of the sample can be determined. This is because the maximum temperature change experienced by the sample is proportional to the heat capacity of the material, thereby the heat change experienced by the standard material can be compared to the sample to determine its specific heat capacity when taking into account the mass of the material. Finally, the thermal conductivity, λ, can be calculated from the specific heat capacity, c_p, density, ρ, and diffusivity, a (Equation 2.11).

$$\lambda = \; c_p . \rho . a \qquad \qquad Eqn. \; 2.11$$
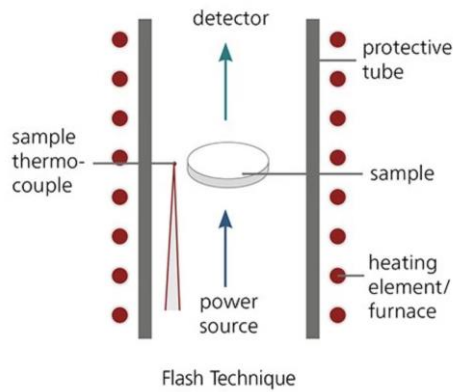
Figure 2.11 Schematic of laser flash analyser.[15]
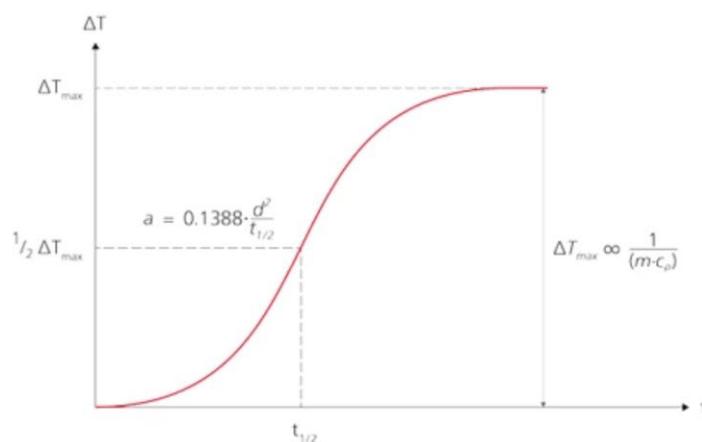
Figure 2.12 Graphical determination of the thermal diffusivity from laser flash analysis

Instrumentation

In this work a Netzsch LFA 467 HT HyperFlash was used to determine diffusivity between 50 and 700 ºC where three measurements were taken at 50 ºC intervals and averaged to find the diffusivity value. Samples were 12.7 diameter disks typically between 0.9 and 1.5 mm thick and coated in a thin graphite layer applied via an aerosol. Samples were measures using nitrogen as purge and protective gas, set at a flow rate of 50 ml/min. The detector was a InSb high temperature infrared detector with a spot size of 2.8.

2.2.12 X-Ray Photo Electron Spectroscopy (XPS)

XPS is a technique in which the energy of electrons ejected from a sample stimulated by X-rays is analysed and used to determine the element and oxidation state of atoms within a sample.[16] This technique has been used in previous works to differentiate and quantify the relative content of Ti^{3+} and Ti^{4+} ions in titanates, such as in the work by Jana *et al.* shown in Figure 2.13.[17–20]
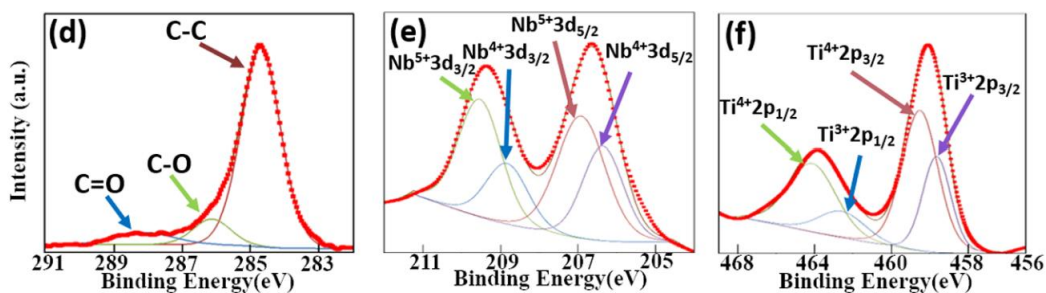
Figure 2.13 XPS spectra generated from a composite of $La_{0.07}Sr_{0.93}Ti_{0.93}Nb_{0.07}O_3$ and graphite by Jana et al. [17]

In this technique, a focused beam of X-rays is directed at a samples surface and electrons who absorb energy above their binding energy are ejected from the sample and detected by an Electron Energy Analyser. [16] The kinetic energy of the electrons is measured by the detector and equal to the photon energy of the incoming X-rays, E_{photon} minus the binding energy of the electron, $E_{binding}$, and the work function, ϕ (a correction factor equal to the minimum energy to eject an electron from an atom), according to Equation 2.12.

$$E_{kinetic} = E_{photon} - E_{binding} - \phi \qquad \textit{Eqn. 2.12}$$

The kinetic energy, the work function and the photon energies are known variables and so the binging energy of the electron can be calculated. The resulting binding energies are plotted vs. intensity in the XPS spectra, as shown by an example in Figure 2.14. Each electron in the orbital shells of an atom has a unique binding energy and so the intensity peaks can be assigned to a specific shell from a specific element and the oxidation state of that element. The higher the intensity peak the more electrons with this binding energy there are, and so the relative abundance of elements and oxidation states can be quantified using this technique.

An important note about this technique is that the photons only have a penetration depth of between 1-10nm in a solid material and so this technique can only provide information about the composition at the surface of a material.[21]
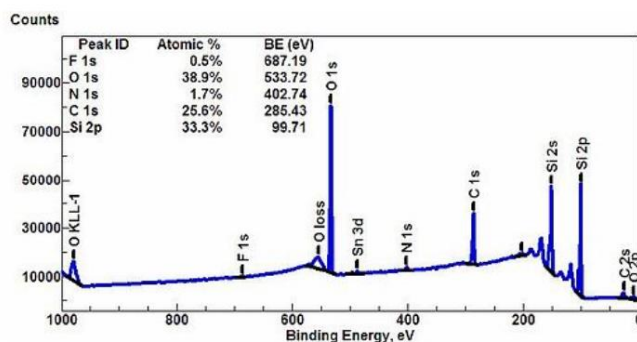
Figure 2.14 Example of an XPS spectra from good et al.[16]

Instrumentation

In this work the XPS data was collected and analysed by Dr Debbie Hammond, Experimental Officer at Sheffield Surface Analysis Centre at Sheffield University. The Fitting and

quantification of elements was performed by Dr Hammond who provided reports on the analysis. The reports are provided in full in section 7.Appendix.

The analyses were carried out using a Kratos Supra instrument with a monochromated aluminium source, and two analysis points per sample, of area 700 μm by 300 μm. Survey scans were collected between 1200 to 0 eV binding energy, at 160 eV pass energy, 1 eV intervals, and 300 seconds/sweep with one sweep being collected. High-resolution O 1s, C 1s, La 3d, La 4p, Sr 3d, and Ti 2p spectra were also collected at 20 eV pass energy and 0.1 eV intervals for each analysis point over an appropriate energy range, with one 300 second sweep for all spectra except the La 3d which two sweeps were collected due to the extended eV range necessary.

The data collected was calibrated in intensity using a transmission function characteristic of the instrument to make the values instrument independent. The data can then be quantified using theoretical Schofield relative sensitivity factors modified to account for instrument geometry, variation in penetration depth with energy and the angular distribution of the photoelectrons. The high resolution spectra were all calibrated in eV by fixing the main C 1s peak to be 285.0 eV.

The Kratos Supra Instrument is equipped with a Minibeam 4, Ar^+ ion gun, which is used to clean the sample surface before the measurements are conducted.

2.2.13 Fourier Transform Infrared (FTIR) Spectroscopy

In FTIR, infrared is the type of spectroscopy and the Fourier Transform is a mathematical function applied to the detector data to generate an interpretable spectrum. First the spectroscopy technique is covered.

When infrared radiation is directed at a sample the molecules within the material can absorb this radiation at specific frequencies determined by the mass of the atoms, the strength of the bonds between atoms and the environment around the atoms. This energy when at the right frequency can make the bonds vibrate or stretch. The frequency of this energy absorbed by the sample is recorded by the detector.

In order to be able to absorb infrared radiation, and be infrared active, the bond must undergo a change in the dipole moment as it bends or stretches. This means that if the bond is symmetrical at both ends there is no change in dipole moment as the bond stretches or bends and so it is not infrared active. This is the case for N_2 and so it is used as the purge gas during the spectroscopy and KBr which is used to collect the background spectrum before the sample is measured as it is infrared inactive. [22]

The Fourier Transform converts the data from a function of time to a function of frequency which makes a spectrum of the intensity versus the frequency, this can then be converted into % transmittance (%T) by comparing the background measurement with the sample measurement using Equation 2.13 where I is the intensity measured by the detector when infrared is shone onto the sample and I_0 is the intensity measured by the detector when infrared radiation is shone through a KBr reference material (the background).

$$\%T = \frac{I}{I_0} \times 100 \qquad\qquad Eqn.\ 2.13$$

This gives the classic FTIR spectrum which is often plotted as % transmittance vs. wavenumber or wavelength which is 1 over the frequency in cm. An example of a spectrum gathered from fluorapatite nanoparticles made using deep eutectic solvents by Karimi *et al.* is shown in Figure 2.15 where they have identified the bonds causing each absorption.[23]
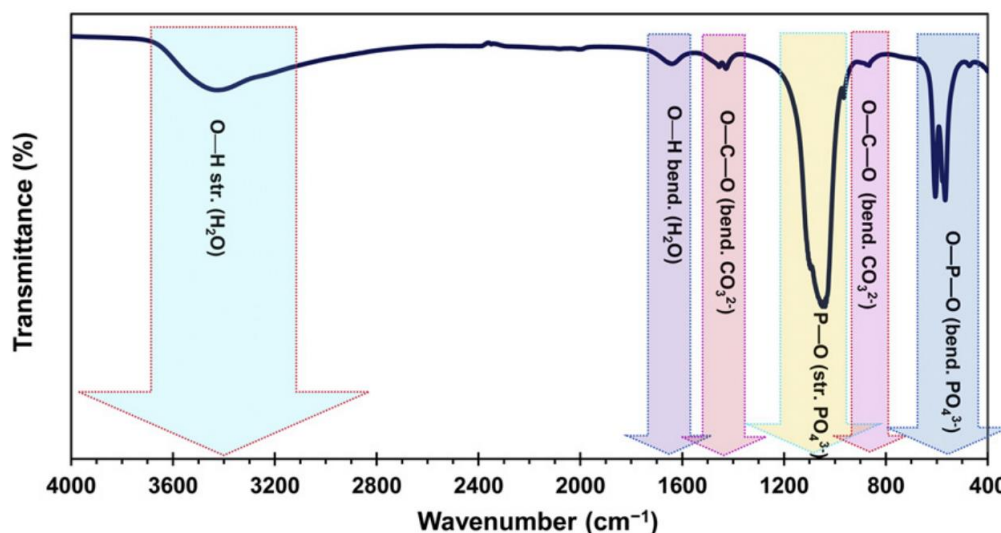
Figure 2.15 FTIR spectrum of fluorapatite nanoparticles made using deep eutectic solvents by Karimi et al.[23]

Instrumentation

In this work a Perkin Elmer Frontier FTIR Spectrometer was used to collect data, operated by Dr Oday Hussein of Sheffield university. Spectra were gathered between 400 and 4000 cm^{-1} using a data interval of 0.125 cm^{-1} and 16 accumulation scans. The background was collected using a tablet made from potassium bromide (Thermo Scientific, 99+ %).

2.2.14 References

1   Z. Lu, H. Zhang, W. Lei, D. C. Sinclair and I. M. Reaney, *Chem. Mater.*, 2016, **28**, 925–935.

2   H. M. Rietveld, *J. Appl. Crystallogr.*, 1969, **2**, 65–71.

3   R. A. Young, *The Rietveld Method*, 1993.

4   V. Jain, M. C. Biesinger and M. R. Linford, *Appl. Surf. Sci.*, 2018, **447**, 548–553.

5   R. Moos and K. H. Härdtl, *J. Appl. Phys.*, 1996, **80**, 393–400.

6   ULVAC, ZEM-3 series Seebeck Coefficient / Electric Resistance Measurement System, https://showcase.ulvac.co.jp/en/products/heat-treatment-and-thermal-properties/thermoelectric-evaluation-device/thermoelectric-properties/zem-3series.html, (accessed 10 May 2023).

7   Malvern Instruments Limited, *Zetasizer Nano Serles Tech. Note. MRK654-01*, 2015.

8   R. Zimmermann, U. Freudenberg, R. Schweiß, D. Küttner and C. Werner, *Curr. Opin. Colloid Interface Sci.*, 2010, **15**, 196–202.

9   A. R. West, in *Solid State Chemistry and Its Applications*, 2014, pp. 271–325.

10   D. B. Williams and C. B. Carter, *Transmission Electron Microscopy : A Textbook for Materials Science*, Springer, New York, NY, UNITED STATES, 1996.

11   C. Ho, C. Lam, M. Chan, R. Cheung, L. Law, L. Lit, K. Ng, M. Suen and H. Ta, *Clin. Biochem. Rev.*, 2003, **24**, 3–12.

12   R. Faller, in *UCD: Biophysics 241 : Membrane Biology*, University California Davis, 2023, p. 14604.

13   A. International, 2022.

14   Netzsch, *Technical Specifications LFA 467 HT HyperFlash*, .

15   Netzsch, Laser Flash Analyzer, https://analyzing-testing.netzsch.com/en/products/thermal-diffusivity-and-conductivity.

16   C. Good and H. Facey, X-ray Photoelectron Spectroscopy (XPS), https://chem.libretexts.org/@go/page/142906, (accessed 21 January 2022).

17   S. S. Jana and T. Maiti, *ACS Appl. Mater. Interfaces*, 2022, **14**, 14174–14181.

18   A. V. Kovalevsky, K. V. Zakharchuk, M. H. Aguirre, W. Xie, S. G. Patrício, N. M. Ferreira, D. Lopes, S. A. Sergiienko, G. Constantinescu, S. M. Mikhalev, A. Weidenkaff and J. R. Frade, *J. Mater. Chem. A*, 2020, **8**, 7317–7330.

19   A. V Kovalevsky, M. H. Aguirre, S. Populoh, S. G. Patrício, N. M. Ferreira, S. M. Mikhalev, D. P. Fagg, A. Weidenkaff and J. R. Frade, *J. Mater. Chem. A*, 2017, **5**, 3909–3922.

20   A. A. Yaremchenko, S. Populoh, S. G. Patrício, J. Macías, P. Thiel, D. P. Fagg, A. Weidenkaff, J. R. Frade and A. V. Kovalevsky, *Chem. Mater.*, 2015, **27**, 4995–5006.

21   J. F.Moulder, W. F.Stickle, P. E. Sobol and K. D. Bomben, *Handbook of X-ray Photoelectron Spectroscopy*, Wiley, 1992.

22   Thermofisher Scientific, Thermo Scientific FTIR spectrometer and microscope resources, https://www.thermofisher.com/uk/en/home/industrial/spectroscopy-elemental-isotope-analysis/molecular-spectroscopy/fourier-transform-infrared-spectroscopy/resources/ftir-spectroscopy-academy, (accessed 12 October 2023).

23   M. Karimi, M. R. Ramsheh, S. M. Ahmadi, M. R. Madani, M. Shamsi, R. Reshadi and F. Lotfi, *Mater. Sci. Eng. C*, 2017, **77**, 121–128.

24   Z. Y. Li, W. M. Lam, C. Yang, B. Xu, G. X. Ni, S. A. Abbah, K. M. C. Cheung, K. D. K. Luk and W. W. Lu, *Biomaterials*, 2007, **28**, 1452–1460.

2.3 Determining the Specific Heat Capacity

The specific heat capacity, c_p, is required to calculate the thermal conductivity, κ, of a sample according to Equation 2.3.1 where D is the diffusivity and ρ is the density. The thermal conductivity is then used to calculate the ZT of this material.

$$\kappa = \rho.D.c_p \quad Eqn.\ 2.3.1$$

Specific heat capacity describes the energy required to raise 1 mol of a substance by 1 ℃ (or K) and as such is given in the unit $Jmol^{-1}K^{-1}$. The aim of this section of work was to determine the specific heat capacity of the LST and LEST samples in-house. The determination of c_p is a none trivial task and it typically done using Differential Scanning Calorimetry (DSC). This technique compares the heat energy applied to a sample to raise the temperature in a linear fashion, compared to the heat energy required to raise the temperature of sapphire, which has a known specific heat capacity. This requires three measurements taken in identical conditions: 1) two empty crucibles, 2) a sapphire reference and an empty crucible, and 3) the sample material and an empty crucible. This data is then used to calculate c_p using Equation 2.3.2 where Q_0, Q_{sap} and Q_s are the heat flows from the three runs respectively, m_{sap} and m_s are the sapphire weight and mass weight, $c_{p,sap}$ is the specific heat capacity of the sapphire. Figure 2.3.1 shows the specific heat vs. temperature for $SrTiO_3$ and $EuTiO_3$ measured using DSC by Muta *et al.* corroborated with data from The SGTE Pure Substance and Solution Databases.[1,2]

$$c_p = \frac{Q_s - Q_0}{Q_{sap} - Q_0} \times \frac{m_{sap}}{m_s} \times c_{p,sap} \qquad Eqn.\ 2.3.2$$

This technique is time consuming and requires skilled data handling to generate c_p values though does give reliable results as shown in Figure 2.3.1. Other research groups have sent samples away to be analysed at significant cost. Attempts to replicate the c_p of STO using DSC in house were unsuccessful due to the difficulty of gathering the required heat flows and applying this to the c_p equation; the result gave illogical values a factor of ten from the expected values. Other methods were explored which could provide a most cost effective and user friendly method to determine the c_p.
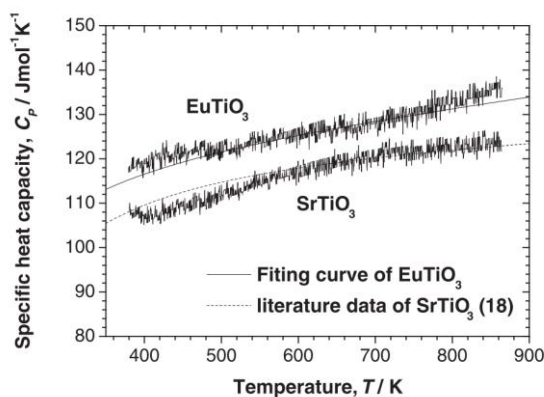
Figure 2.3.1 Specific heat capacity vs temperature data from Muta et al.[1]

2.3.1 Modulated DSC

A second use of DSC is to measure c_p through a technique called Modulated DSC. This is a more recent adaption of the conventional DSC method and differs in the heating profile applied to the sample. Not all DSC machines have this feature but the Discovery SDT 650 is able to perform this technique. In Modulated DSC, rather than a linear heating profile, e.g. 50 °C / min, a sinusoidal heating profile is superimposed on top of the linear profile so that the sample experiences a modulated heating profile. An example of this is shown in Figure 2.3.2, where the sinusoidal dotted line is the modulated heating profile which is superimposed on to the dotted linear heating profile to give the solid line. The modulation period, amplitude and the underlying linear heating rate must be optimised to create a non-distorted sinusoidal profile. Depending on whether the machine has active cooling, the period must be great enough to allow the system to achieve the temperature modulation. In this work the Discovery SDT 650 had no active cooling and so the parameters recommended by TA Instruments technicians were: period = 200s, amplitude ± 3°C, ramp rate 5 °C/min.
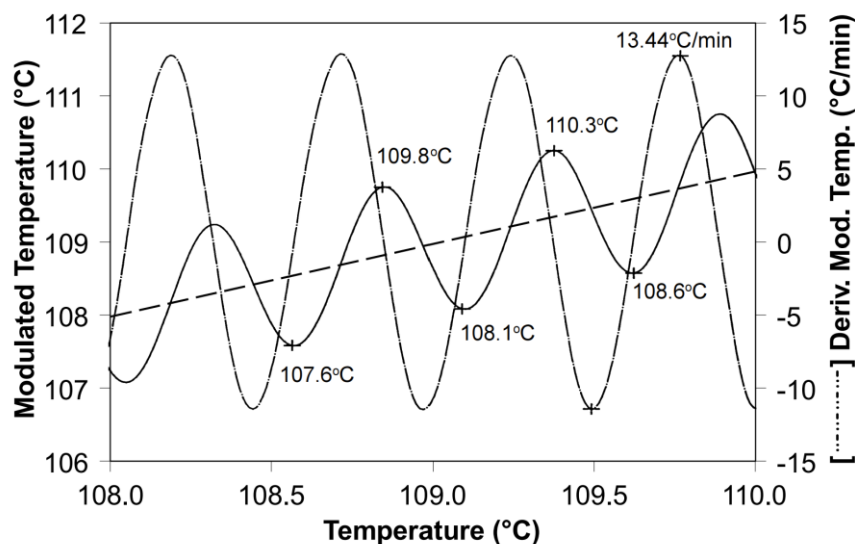
Figure 2.3.2 modulated DSC heating profile from TA Instruments.[3]

The machine is calibrated using a sapphire sample and an empty pan from which the heat flow difference between that and the reference can be used to calculate the heat capacity directly by the SDT 650. Importantly this required one measurement from the user (excluding the calibration) and the machine calculates the heat capacity (J/gK) directly which can be converted into the specific heat capacity (J/molK) by multiplying by the molar mass. Figure 2.3.3 shows the results of Modulated DSC on a sample of $SrTiO_3$ which shows the heating profile and the specific heat capacity.
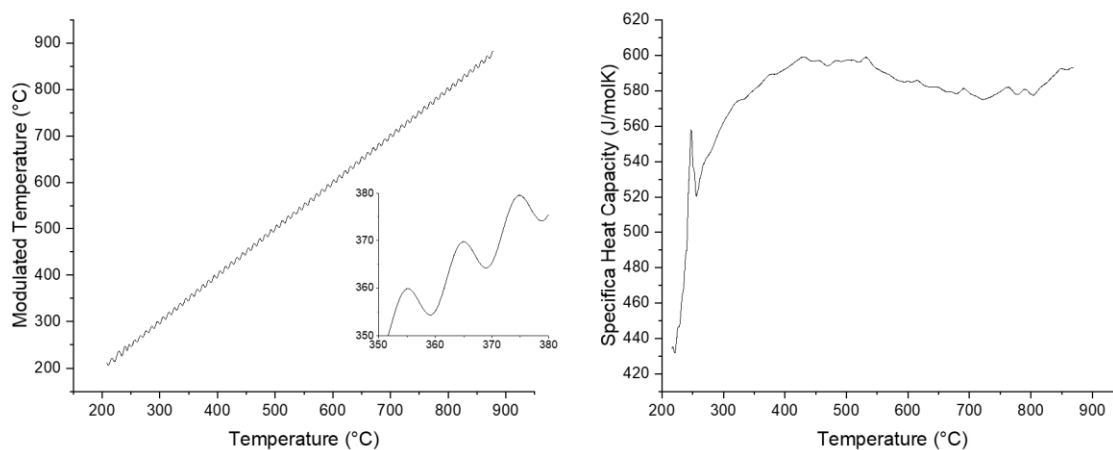
Figure 2.3.3 Modulated Heat Capacity Results.

The value of the c_p does not compare to that in Figure 2.3.1 and was also unrepeatable. Figure 2.3.4 shows the repeats of the same material. This data is not intentionally stacked; the data is shown at the correct y value. The data profile appears to the be same in all four result but at very different values, none of which match the result shown in Figure 2.3.1 of standard DSC of STO. It is unclear why these values are so different but it may because of the difference in the ambient conditions. The similar profile indicated that the sample is reacting in the same way but the consistent offset may be to do with a difference in the ambient conditions when taking the measurement. In summary this technique is quick and relies very little on the user for data processing though it did not produce accurate or reliable results.
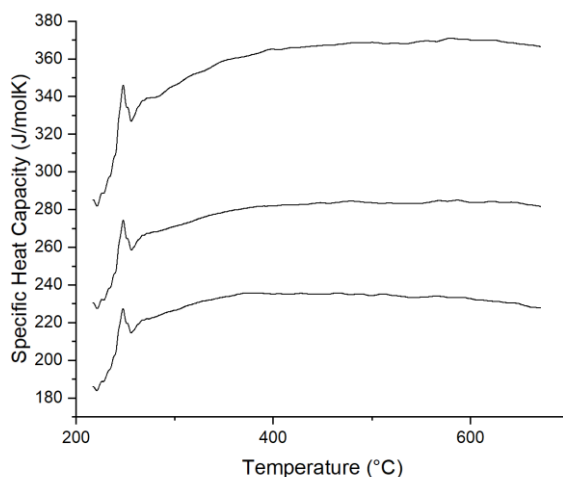
Figure 2.3.4 Modulated DSC repeats of STO.

2.3.2 Laser Flash Analysis

The laser flash method in combination with a reference material of known specific heat capacity can be used to determine specific heat capacity at the same time as diffusivity. This method involves firing a pulse of energy to one side of the sample and measuring the energy detected through to the other side as a function of time. Measurements are taken whilst held in atmosphere of certain temperature to determine how the specific heat capacity varies with temperature. As the same conditions are applied to a reference material with known c_p, the energy applied can be calculated from the references temperature change and assuming the same energy is applied to the unknown sample, the temperature change is measured and the c_p calculated by the machine. Lu *et al*. use this technique in their paper on $La_{0.15}Sr_{0.775}TiO_{3-\delta}$.[4]

Figure 2.3.5 shows the specific heat capacity determined from a set of samples using the laser flash. The results were close to the $SrTiO_3$ literature but with some major deviations. Excluding the obvious outlying results there is still a large variation in the results as shown in Figure 2.3.6 which masks any trend between samples. For the three samples of x = 0.10 the error between values at different temperatures was as large as 15% in some cases. There is a large error associated with this heat capacity data, which when used in the calculation for the thermal conductivity increases the error associated with this value in turn.

This method is by far the quickest of the experimental techniques as it is performed at the same time as the diffusivity measurement, therefore, the thermal conductivity can be determined in one measurement. However, the apparent low accuracy of the c_p is a disadvantage of this technique.
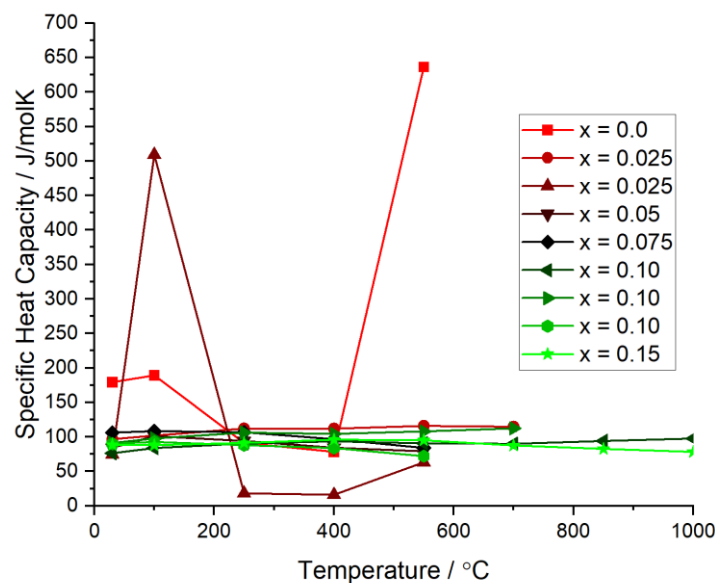
Figure 2.3.5 Specific heat capacity produced by Laser Flash Analyser calculated based on a reference comparison method.
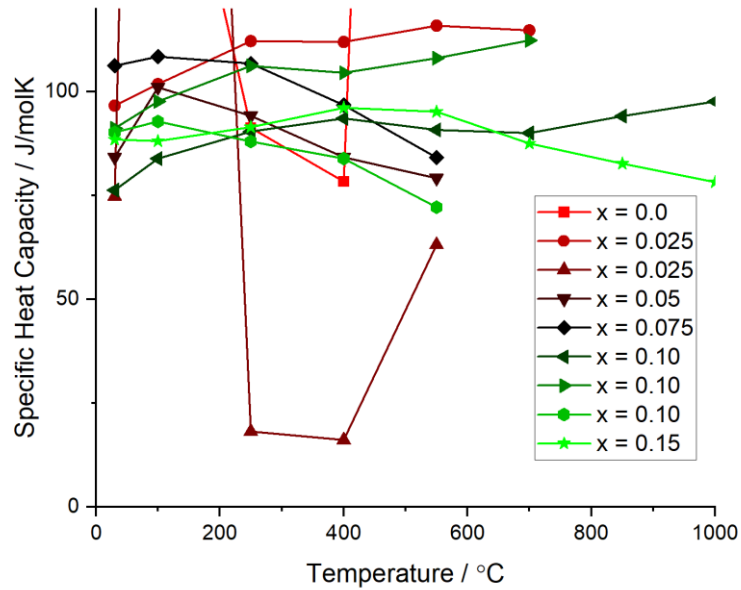
Figure 2.3.6 Enlarged y-axis from Figure 2.3.5, Specific heat capacity produced by Laser Flash Analyser.

2.3.3 Neumann-Kopp Model

Finally, the specific heat capacity can be determined using theoretical models based on the experimental data of other known compounds which make up the samples composition. One of these models is The Neumann Kopp method, which was used by Leitner *et al.* for the determination of specific heat capacity of mixed oxides: $SrZrO_3$, $BaZrO_3$.[5] This uses the known specific heat capacity of the comprising oxides to predict the properties of related compounds. This is done using simple addition, such that the specific heat capacity, c_p, of a solid compound with the formula $A_aB_bX_x$ formed from solid elements A, B and X is summed using Equation 2.3.3 to determine the heat capacity of the compound.[5]

$$c_p(A_aB_bX_x) = a.c_p(A) + bc_p(B) + xc_p(X) \qquad Eqn.\ 2.3.3$$

For example, Leitner *et al.* used ZrO_2 and SrO to determine the c_p of $SrZrO_3$.[5] Oxygen is not classed as a solid reactant, and oxygen content is considered as a small influence compared to the other constituents, so the oxygen stoichiometry need not be maintained in the equation. For this work data for SrO, La_2O_3, Eu_2O_3, TiO_3 were combined in accordance with the stoichiometry of the heavy elements. The source of this data was O. Knacke's Thermochemical Properties of Inorganic Substances and is shown in Figure 2.3.6.[6] The resulting c_p calculated for each composition is shown in Figure 2.3.7. This prediction lies in the same region as the data shown in Figure 2.3.1 for $SrTiO_3$ and $EuTiO_3$, between 100 and 120 J/molK.
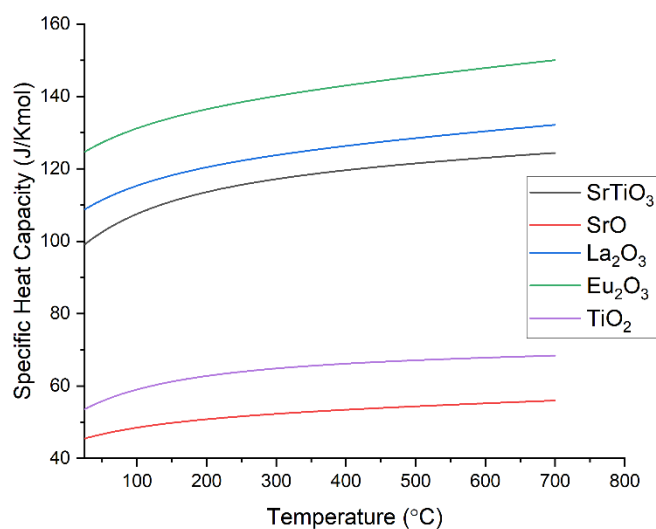
Figure 2.3.6 Neumann Kopp predicted oxides and calculated compositional specific heat capacities using stoichiometric addition.
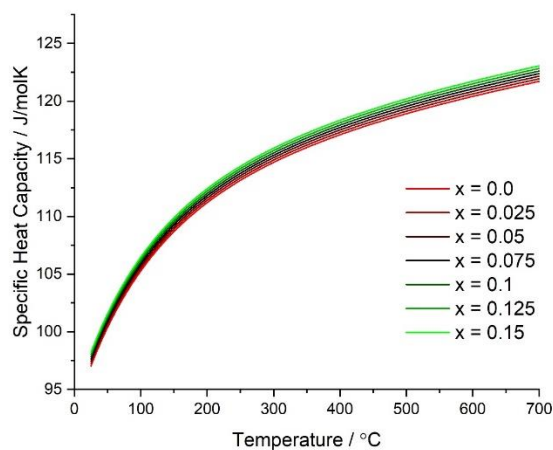
Figure 2.3.7 Specific heat capacity calculated from the Neumann Kopp method.

2.3.4 Summary

The laser flash, standard DSC and modulated DSC use the comparison of heat flow between a sample and a reference material to determine the heat capacity. The modulated DSC and standard DSC both use a sapphire reference material. The modulated route relies on a calibration with the sapphire that can be run at any time before the sample, days or even weeks. This relies on the condition of the ambient and machine conditions to remain consistent over time. This saves time over the standard DSC method where three runs are performed by the user one after another, but does not promote accuracy or reliability in the result.

The laser flash runs a reference sample alongside the sample. The user can choose from a variety of reference materials which most closely match the sample species. Running both samples at the same time saves time for the use and ensures the ambient and machine conditions remain the same. However, this technique showed large errors associated with the result. This is likely because, unlike in DSC the heat flow from the furnace is not directly measured, instead the maximum temperature changes between the reference and the sample is compared once the laser pulse travels through the material. This could be more affected by the morphology of the sample and possible pore networks that exist in the sample which has an influence on how the heat is absorbed by the material as well as the materials intrinsic heat capacity.

Finally, the Neumann Kopp method is a theoretical prediction of a compositions specific heat capacity based on the properties of other oxide materials. This technique removes experimental error and allows a reliable prediction to be made which limits the errors taken forward into the thermal conductivity and the ZT value. What's more, this value is readily calculated so can be removed from the thermal conductivity value in place of more accurate experimental data if this is required. This method would be less appropriate if samples were made with very different compositions where the heat capacity can vary largely between the samples. However, in this work, small increments were made in the composition so values should be very similar.

2.3.5 Conclusion

The following chapters in this thesis require reliable heat capacity values to calculate the thermal conductivity of the europium doped strontium titanate. DSC gives a highly accurate and reliable result which may be necessary for some works but may not be necessary in this work. Looking at the data in Figure 2.3.1 the heat capacity values of $EuTiO_3$ and $SrTiO_3$ are not vastly different. The addition of Eu to a Lanthanum doped $SrTiO_3$ would not be expected to change the heat capacity dramatically, especially when added in such low quantities as this work (up to 15%). Determining the heat capacity using DSC is a none trivial technique that could not be performed in house so would come at a high cost and possible delay. The heat capacity could be confirmed later in further work and used to recalculate the thermal conductivity if required as the values used from Neumann Kopp are consistent.

The laser flash produced some unexplained deviation from the expected results and the modulated DSC produced some clearly illogical results. The advantage of the Neumann Kopp method was that this technique produced a reliable result which demonstrated the small increment of heat capacity associated with the addition of Eu. The lack of variation in this result would allow the fine details from other affects such as the diffusivity to and density to be observed in the thermal conductivity and importantly result the error carried into the thermal conductivity value which ultimately affects the ZT value. The Neumann Kopp method has been verified in the literature and provides reliable and logical results.[5,7] For these reasons the Neumann Kopp method was used to calculate the specific heat capacity in this work.

2.3.6 References

1   H. Muta, A. Ieda, K. Kurosaki and S. Yamanaka, *Mater. Trans.*, 2005, **46**, 1466–1469.

2   The Scientific Group Thermodata Europe, The SGTE Pure Substance and Solution Databases, https://www.sgte.net/en/sgte-molten-salt-database-salt, (accessed 15 August 2023).

3   TA Instruments, *TA Instruments*, 2012, 12.

4   Z. Lu, H. Zhang, W. Lei, D. C. Sinclair and I. M. Reaney, *Chem. Mater.*, 2016, **28**, 925–935.

5   J. Leitner, P. Voňka, D. Sedmidubský and P. Svoboda, *Thermochim. Acta*, 2010, **497**, 7–13.

6   O. Knacke, O. Kubaschewski and K. Hesselmann, *Thermochemical Porperties of Inorganic Substances*, 1991.

7   S. K. Sahu, M. Sahu, R. S. Srinivasa and T. Gnanasekaran, *Monatshefte für Chemie - Chem. Mon.*, 2012, **143**, 1207–1214.

3.0 Ionic Liquid Synthesis of Lanthanum-Doped Strontium Titanate

3.1 Aims and objectives

The aim of this chapter was to interrogate the physical properties of ionic liquid synthesised $La_{0.15}Sr_{0.775}TiO_3$ (LST). Though the feasibility of this method has been proven by Mottram *et al.*, the characterisation of the product was limited. This study shows a larger scale characterisation of the purity, structural properties and size of the synthesised powder.[1] This is important as this synthesises method was used to create the starting powders for the other experimental chapters and so anything found in this study gives a history of the powders and could be used to explain abnormalities in the measured properties.

Ionic liquid synthesis clearly has the advantage of energy saving over the conventional solid state technique, as the temperature of calcination can be reduced from 1100 ℃ for 3 h to 600 °C or 800℃ for 2 h, therefore also allowing the synthesis of much smaller grain sizes.[1,2] However, the vast difference in the synthesis protocol compared to solid state synthesis are likely to create variations in the product which may affect the handling and purity of the product, and need to be understood in order to get the best out of the material. There is precedent for this in thermoelectric materials, as shown by Liu *et al.* in the characterisation of solution processed SnSe, impurities can have a large effect on the measured properties.[3]

3.2 Introduction

Ceramics are conventionally made using the solid state process, which usually begins from metal carbonates or oxides which are milled and heated together to promote solid state diffusion. In many cases, several milling and heating steps at high temperatures are required to encourage solid state diffusion and achieve a homogenous product. The calcination protocol used by Lu *et al.* in the solid state synthesis of $La_{0.15}Sr_{0.775}TiO_3$ is typical of such a process: strontium carbonate, lanthanum oxide and titania were milled for 60 minutes before drying and firing at 1100 ℃ for 3 hr.[2] A single phases homogenous product was not achieved at this stage and required sintering at 1500 °C for 6hr to produce the final product.

Whereas, ionic liquid synthesis is a liquid phase method, so mass diffusion occurs on much shorter time scales. Therefore, the demand for external energy input to encourage homogenisation is much decreased. Mottram *et al* studied this process for the synthesis of $La_{0.15}Sr_{0.775}TiO_3$ and found that the metal ions (Sr^{2+}, La^{3+}, Ti^{4+}) begin in solution which are chelated by the ionic liquid. The ionic liquid begins to decompose at 250 ℃, small amounts of nano-scale titanium dioxide (anatase) form first, followed by mixed strontium and lanthanum carbonates. The final conversion to the cubic perovskite phase occurs at 600 ℃.[1] They report a lattice parameter of 3.9076 ± 0.0009 Å for $La_{0.15}Sr_{0.775}TiO_3$ - larger than that reported by Lu et al. with a cell volume of 59.3 Å^3 which equates to a lattice parameter of 3.8995 Å.[1,2] The larger lattice parameter found by Mottram *et al.* was attributed to combustion techniques, which have previously been shown to inducing larger lattice parameters than the equivalent composition made via solid state synthesis; the reason for this is not fully understood.[1,4–6]

In this work LST was calcined using the ionic liquid method fired up to 800 ℃. This increased temperature was an arbitrary value greater than 600 ℃, chosen to ensure that the product was fully calcined and accounted for the increased temperature additional dopants might require. The ionic liquid (IL) used in this work was 1-ethyl-3-methylimidaziolium acetate, in line with the ionic liquid shown by Mottram *et al,* in their synthesis of LST.[1] A key reason why ILs are used a solvent for the synthesis of titanates is that they can chelate titanium ions. [7,8] Not many liquids can do this, for example in water titanium ions readily form titanium dioxide. Titanium dioxide is difficult to break down once formed (as demonstrated by the high temperatures required by solid state synthesis where titania is present) and often remains present as a secondary phase in the final product so its creation should be avoided as much as possible for the benefit of a single phase product.[5,9] Furthermore, this particular ionic liquid being an acetate is key because the anion of the ionic liquid and the metal salt precursors must match for good mixing and there are readily available acetate forms of the metal ions required for LST: lanthanum acetate and strontium acetate.

Due to their synthesis route, halide impurities are common in ionic liquids.[10–12] Specifically in the synthesis of imidazolium based ILs, a reaction between N,N'-dialkylimidazolium salt and alkyl halide occurs, followed by an ion exchange of the halide with the desired anion.[11] If this reaction is incomplete halide anions, such as Cl^- or Br^-, and alkali cations such as Li^+, Na^+ or K^+ remain.[11] The low melting point and non-volatility make them difficult to purify,[10] and so they often persist into the final IL. Already a relatively expensive solvent, their price is heavily dependent on the purity level: water and halide content.[10]

Work by Lui *et al.* stressed the importance of surface adsorbents in solution synthesised materials due to the presence of other molecules and ions present in the precursors.[3] Their solution synthesised SnSe had a zeta potential of -22 ± 5 mV which induced Na^+ ions to adsorb to the surface. It is yet to be seen whether the same properties will be seen in ionic liquid-synthesised materials which are known to contain alkali cations such as Na^+.

Therefore, with these previous works in mind the lattice parameter, purity and morphology of the ionic liquid synthesised product are observed closely to determine if these effects repeat themselves in this work, and postulate their consequence during later processing and use as thermoelectric materials. The ionic liquid synthesise technique was used as the synthesis method for all the powders in this work and so this chapter provides the thermal and chemical history of this material which can provide a better understanding and provide context for the following experimental chapters.

3.3 Results and Discussion

Using the ionic liquid synthesis method with 1-ethly-3-methyl imidazolium acetate (emim OAc), Sr acetate, La acetate and titanium isopropoxide, a cubic perovskite phase was calcined at 800 ℃, as shown by XRD analysis in Figure 3.1. The peak widths are consistent with broadening caused by small crystallites, which is in agreement with the findings from SEM images of the ionic liquid synthesised powder in Figure 3.2. The average particle size determined by measurements from SEM micrographs was 97 ± 33 nm.
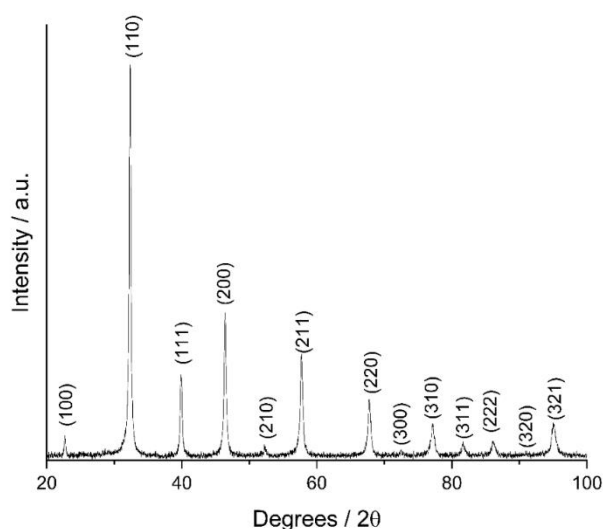
Figure 3.3 XRD of ionic liquid synthesised La$_{0.15}$Sr$_{0.775}$TiO$_3$ using Sigma Aldrich >95% emim OAc.
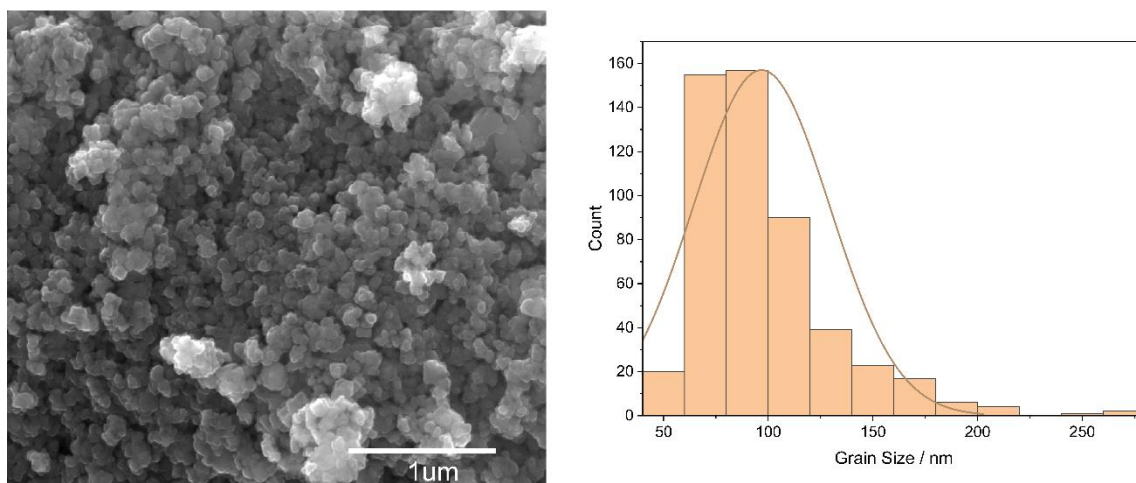
Figure 3.2 SEM of ionic liquid synthesised La$_{0.15}$Sr$_{0.775}$TiO$_3$ using Sigma Aldrich >95% emimOAc (left) and size distribution generated from grain size measurements from SEM images (right).

As could be predicted, in Figure 3.2, the grains of the ionic liquid synthesised powder are slightly larger than those which were shown by Mottram *et al.* (36 ± 12 nm), as a higher calcination temperature of 800 °C was used *vs* 600 °C in their original work. In previous work by Yang *et al.* a large grain size distribution of 2-10 μm, was shown in sodium doped bismuth titanate due to non-homogenous mixing in solid state synthesis.[13] Not only did this make generally large grains but dopant rich areas caused much greater degrees of grain growth due to the increased mobility in some areas. [13] In contrast the particles in this work and that of Mottram *et al.* showed not only a smaller average size but also a small distribution in size (50-200 nm) indicating that the dopants were evenly distributed when using the ionic liquid synthesis method.

The lattice parameter of the LST perovskite, determined by Rietveld refinement, was 3.9079 ± 0.0002 Å, the fitting data is shown in Figure 3.3 and Table 3.1. This was consistent with findings from Mottram *et al*. who found a lattice parameter of 3.9076 ± 0.0009 Å. This too was larger than that reported for the same composition by Lu et *al*. (3.8995 Å) who synthesised the composition using solid state synthesis in air.[2] The possible explanations for this will be explored in later in this section.
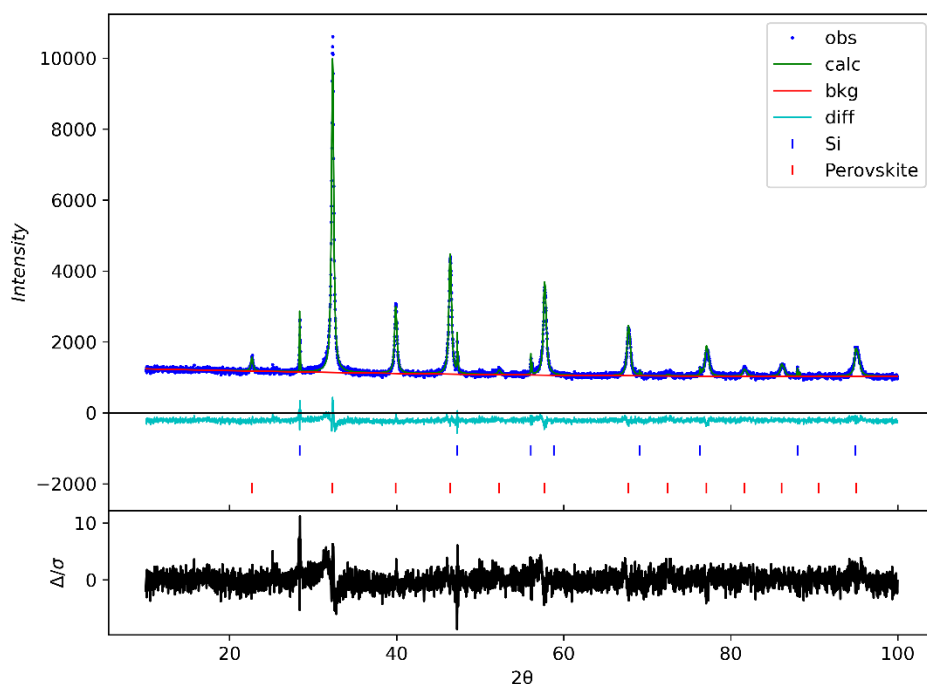
Figure 3.3 Reitveld refinement of ionic liquid synthesised La$_{0.15}$Sr$_{0.775}$TiO$_3$.

Table 3.1 Reitveld refinement parameters of ionic liquid synthesised La$_{0.15}$Sr$_{0.775}$TiO$_3$ which accompany Figure 3.3.

Space group:	P m -3 m	GOF	1.63				
a (Å)	b (Å)	c (Å)	alpha	beta	gamma		
3.907892	3.907892	3.907892	90º	90º	90º		
label	element	multiplicity	x	y	z	fraction	Uiso
Sr1	Sr+2	1	0	0	0	0.775	0.0247
La1	La+3	1	0	0	0	0.15	0.0247
Ti1	Ti+4	1	0.5	0.5	0.5	1	0.0122
O1	O-2	3	0.5	0.5	0	1	0.0227

Solid state sintered samples were fabricated, following the procedure given by Lu *et al.,* for the purpose of direct comparisons of the two techniques. Figure 3.4 shows the XRD of calcined and sintered powders. When using the solid state synthesis method, a single phase product was not achieved after the calcination step, despite attempts to induce a single phase with further heating at the same temperature, 1100 ºC. The additional peaks in the calcined

LST XRD indicate the presence of rutile and lanthanum rich titanate. A single phase cubic perovskite was only achieved after sintering at 1500 °C, indicating that higher temperature was what was needed to encourage the transformation into a single phase cubic perovskite, rather than extended time. Unlike in the ionic liquid synthesis method where full calcination was achieved at a much lower temperature of 800 ºC.

Furthermore, the peaks in Figures 3.4 appear much less broad than those in the IL synthesised LST (Figure 3.1), indicative of significantly larger grain sizes in the solid state synthesised powder. This is due to the fact that in the ionic liquid process, the cubic perovskite forms from an atomically mixed precursor. Grain growth is limited by the use of low temperatures and so grains remain very small. On the other hand, solid state synthesis relies on solid state diffusion from raw materials with grain sizes on the scale of microns, limited by interfacial contact between grains. The demand for high temperatures to encourage solid state diffusion also causes significant grain growth.
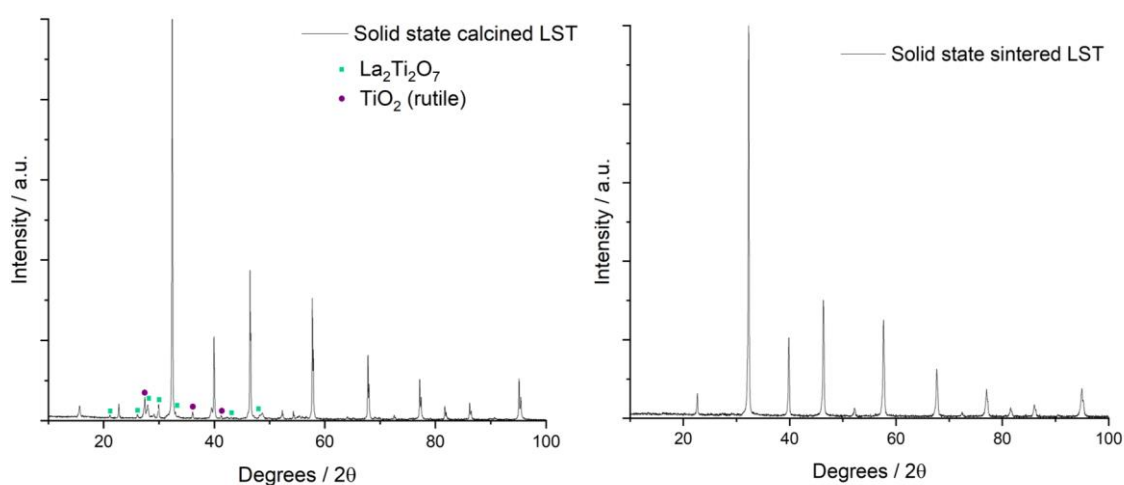
Figure 3.4 XRD analysis of solid state calcined LST at 1100 ºC and sintered at 1500 ºC.

3.3.1 Potential Causes of the Larger Lattice Parameter

There are three potential causes for the larger lattice parameter observed in the ionic liquid synthesised LST. Firstly, the ionic liquid is acting as a template which expands the lattice. Long chain organic molecules have been used as templates during synthesis previously, such as sodium alginate used to grow nanowires of $BaTiO_3$ and dextran used to make a YBCO foam. [14,15] These organic molecules were shown to direct the morphology of the material as it grew. It is unclear if the template effect could extend to changes in the lattice parameter. The dimensions of a unit cell are usually dictated by the size of the ions which occupy it, and their respective attractive and repulsive forces.

The second possibility is a degree of oxygen loss resulting in the reduction of Ti^{4+} to Ti^{3+}, which expands the lattice. The combustion of the ionic liquid could reduce the oxygen levels in the furnace, flooding the surrounding air with CO_2, leaving less oxygen available to form the fully stoichiometric LST. The resulting powder appeared white, so the Ti^{3+} content must be low enough as to not to exhibit the classic colour change in the powder from white to

black (as Ti^{3+} is black).[16,17] This will be further investigated along with the third possibility through Reitveld refinement.

The third possibility is that an additional dopant has entered the cubic perovskite and caused lattice expansion. The source of this unintentional dopant could be the known impurities of the ionic liquid: K, Na and Cl. Sodium and potassium doped titanates have been demonstrated in prior work, these atoms sit on the A site of cubic perovskites due to their ionic radii most closely matching the A-site ion (Sr^{2+}).[13,18]

There is limited body of evidence which suggests that chlorine can be "incorporated" into LST and other perovskites by replacing oxygen.[19,20] Dogu *et al.* demonstrated chlorine incorporation into LST (specifically not referring to this as doping and did not provide the compensation mechanisms), which gave the composition $La_xSr_{1-x}TiO_{3\pm\delta}Cl_\sigma$. This was made via a modified-Pechini method where $LaCl_3.7H_2O$ was the source of Cl.[19] They suggested that chloride distorted the perovskite lattice due to the larger size of Cl compared to O. This could explain the slight increase in the lattice parameter seen in ionic liquid synthesised LST.

To interrogate the possibility of oxygen loss and unintentional dopants, a new Rietveld refinement was conducted on the calcined ionic liquid synthesised powder in which the site occupancies were refined. During an XRD analysis X-rays are scattered by the electrons within atom and the detected peaks are an average result of multiple atoms within that bulk hit by the x-ray source at that lattice position. By applying a single element *i.e.* Sr^{2+} with a defined number of electrons to the A-site and allowing the occupancy to vary, what a refinement can show is whether more or less than the anticipated number of electrons from Sr^{2+} are in fact scattering the X-rays in that site. Therefore, to simplify the refinement only Sr was placed on the A-site rather than Na, K and Cl as this would form a complex simultaneous equation. In reality what is causing the scattering may be multiple different species: Sr, La, K, Na or a vacancy, but these subtleties cannot be quantified using XRD alone. Figure 3.5 and Table 3.2 show the results of this refinement.
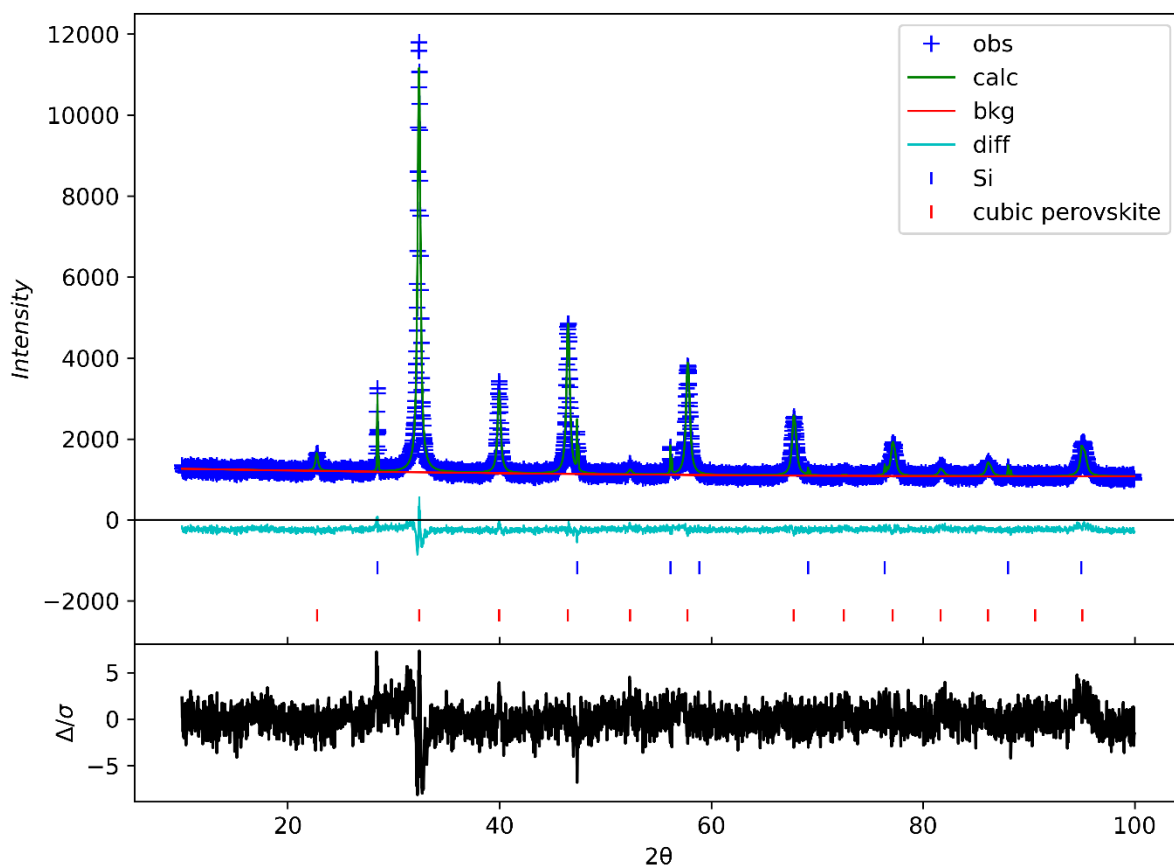
Figure 3.5 Rietveld refinement generated occupancies and lattice parameter values of ionic liquid synthesised LST.

Table 3.2 Rietveld refinement parameters of ionic liquid synthesised LST where site occupancies were refined, this data accompanies Figure 3.5.

Space group:	P m -3 m	GOF	1.43				
a (Å)	b (Å)	c (Å)	alpha	beta	gamma		
3.90841	3.90841	3.90841	90º	90º	90º		
label	element	multiplicity	x	y	z	fraction	Uiso
Sr1	Sr+2	1	0	0	0	1.026	0.0336
Ti3	Ti+4	1	0.5	0.5	0.5	1.007	0.012
O4	O-2	3	0.5	0.5	0	0.982	0.0208

This refinement has a reasonable GOF value of 1.43 (the lower the better and below 2 is generally accepted as a good refinement), and the lattice parameter is similar to the previous refinement performed on an ionic liquid synthesised LST, 3.9084 Å compared to 3.9079 Å, so this is believed to be a good representation of the measured data.

On the A-site of this structure, the average number of electrons surrounding a nucleus can be calculated using the electrons in Sr^{2+} multiplied by the fractional occupancy predicted by the refinement. There are 36 electrons in Sr^{2+}, multiplied by the occupancy predicted by the model, 1.026 gives 36.9. La^{3+} has 54 electrons so from the batched stoichiometry of pure

$La_{0.15}Sr_{0.775}TiO_3$ the electrons present at the A-site on average should also be 36 ((0.775 x 36) + (0.15 x 54). The value predicted by the model is very close the value predicted by the stoichiometry, and so if any other elements are acting to increase the electron density on the A-site then this is in very small quantities.

To assess if K^+ or Na^+ are doping into the structure on the A-site, the method of compensation and effect this would have on the crystal structure was considered. Being singly charged species Na^+ or K^+ would require charge compensation to replace Sr^{2+} on the A-site. They could be self-compensated by the La^{3+}; rather than La being compensated by half an A site vacancy. This could look like $(K, Na)_{0.1125}La_{0.1125}Sr_{0.775}TiO_3$. K^+ has 18 electrons and Na^+ has 10, so the electron occupation on the A site would average between ((y x 0.1125) + (54 x 0.1125) + (36 x 0.775) where y is 18 or 10) 36 and 35.1. This shows that if K is occupying the A-site then this would be indistinguishable through reitveld refinement, though Na would reduce the fractional occupancy seen below 1, which was not seen. Therefore, from the refinement the most that can be determined is that Na is not doping onto the A-site though it is unclear if K is.

The refinement does predict an O^{2-} occupancy of < 1, which could indicate that a small amount of oxygen loss has occurred. Coupled with a Ti^{4+} occupancy >1, indicating that more electrons than Ti^{4+} are causing scattering on the B-site, this could indicate the presence of Ti^{3+} which is known to accompany oxygen loss in strontium titanates. Cl^- has much more electrons than O^{2-} and so if Cl^- occupied this site then there would be a predicted fractional occupancy above 1.

Reitveld refinements is a modelling technique based on experimental data and the output can in some cases be influenced by the user giving false predictions. Though the GOF gave a good value there is the possibility that this is a false minimum in the refinement. For this reason, the information gathered from the refinements must be considered against logic and other techniques before declaring a definitive result. There is currently no conclusive answer to which of the effects is causing the lattice expansion. What can be said is that from modelling of the site occupancy it is unclear if K occupies the A-site of the cubic perovskite, there may be oxygen deficiency and Cl in the lattice appears unlikely.

3.3.2 Purity Analysis

Though the most abundant phase in the ionic liquid synthesised powder was the cubic perovskite, small amounts of impurities were shown in some of the XRD analysis of ionic liquid synthesised powders. The presence of impurities was small and inconsistent between samples. Impurities identified were KCl, $SrCO_3$, TiO_2 (anatase), NaCl and LaOCl. Figure 3.6 shows an example of an XRD analysis where all these impurities could be identified.
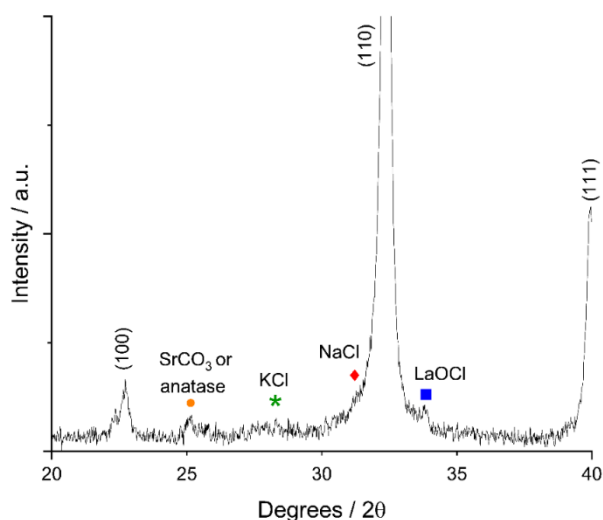
Figure 3.6 XRD of Ionic Liquid synthesised LSTO with impurities of KCl, NaCl, SrCO$_3$ and LaOCl

It is believed that K, Cl and Na impurities originate from the ionic liquid, as halide contaminants are a common impurity associated with their synthesis route.[11] The remaining impurities, (anatase and/or strontium carbonate) likely occurred due to incomplete calcination reactions. From the work by Mottram *et al.* it was shown that the ionic liquid synthesis occurred as thus: initially small particles of intermediate compounds are formed, anatase and mixed lanthanum, strontium carbonate species, which act as reaction sites for the formation of the cubic perovksite.[1] Therefore, it is not unsurprising that strontium carbonate and anatase could occasionally be found in the calcined product as these are known intermediates.

STEM EDS in Figure 3.7 confirms the presence and even distribution of the potassium and chlorine impurities in the ionic liquid synthesised powder. Spot spectra were also gathered and can be found in the section 3.6 Appendix. The intensity of each element correlates to the grey scale intensity of optical the TEM (top left) caused by the thickness of sample, therefore, it appears that all elements are evenly distributed, including the impurities K, Na and Cl. The small amount of elements detected apparently in empty space around the powder itself can be disregarded as background noise.
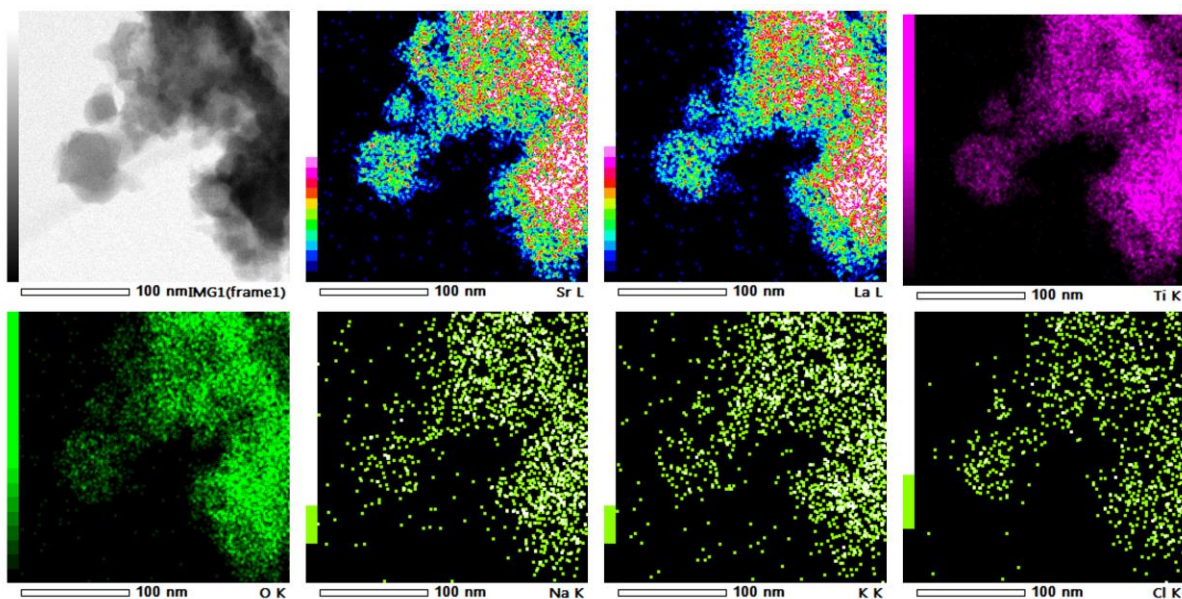
Figure 3.7 STEM EDS of Ionic Liquid synthesised powder elemental maps as calcined

The colour maps show a much larger intensity of strontium, lanthanum, titanium and oxygen compared to the potassium, chlorine and sodium, agreeing with their relative intensities from XRD. It is interesting to note that Cl appears to be less abundant than either the K or the Na in these maps, this may suggest that not all the Na and K are present in stoichiometric KCl and NaCl and could be forming other compounds. However, the spot spectra do not show the same trend and so this could be the effect of noise. It was not possible to quantify the relative abundance of elements from these TEM images without calibration standards, which were not available at the time of this work.

Further experiments were conducted to observe the effect of variations within the synthesis on the final product. In the usual synthesis route the solution of ionic liquid and metal acetates was fully dehydrated before the titanium isopropoxide is added. This is because if water remained, large amounts of anatase would be expected to be present in the final product, due to the reaction of titanium isopropoxide with water.[21] Figure 3.8 shows the XRD of the final powder in the case where water was intentionally left present at the point titanium isopropoxide was added, and also where isopropanol was used, rather than water, to dissolve the metal acetates. These experiments were designed to observe the effect that any accidental presence of water may have in the standard ionic liquid synthesis method.

Interestingly these two conditions produced the same five phases: a cubic perovskite, titania, potassium chloride, sodium chloride and strontium chloride hexahydrate. Titania is formed as predicted on contact with water but also unexpectedly formed when isopropanol was used rather than water. The water source in this case was likely either from a small amount of water in the isopropanol or from the hydrated acetates which were not evaporated before the titanium isopropoxide was added.

As a large number of the titanium ions are being used to form the titania impurity, this disrupts the stoichiometry of the mixture resulting in an excess of strontium. This excess strontium combined with chlorine and water to form a chloride hydrate. The impurities in these two examples are different from those seen in Figure 3.6 of a powder synthesised using

the standard ionic liquid synthesis route, when water is the used to dissolve acetates then evaporated. There is less anatase and none of the strontium chloride in the normal synthesis route. The presence of the strontium chloride appears to be a symptom of a water saturated solution.
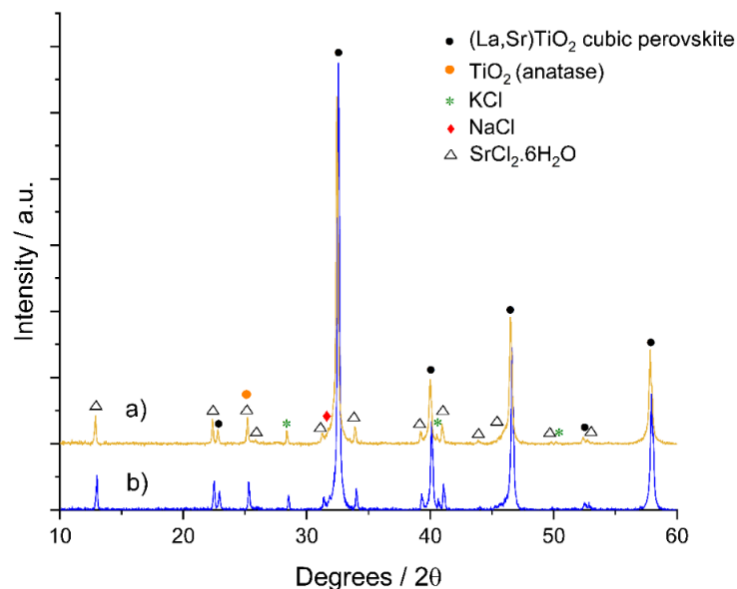
Figure 3.8 XRD of Ionic Liquid synthesised LSTO a) acetated dissolved in isopropanol rather than water, not dried on hot plate b) acetates dissolved in water but not evaporated before adding titanium isopropoxide.

3.3.3 Purification

As potassium and sodium chlorides are soluble in water and $(La,Sr)TiO_3$ is not, it was hypothesised that water filtration could be used to remove these impurities. XRD and SEM EDS of the calcined powders before and after water filtering are shown in Figure 3.9a-c.
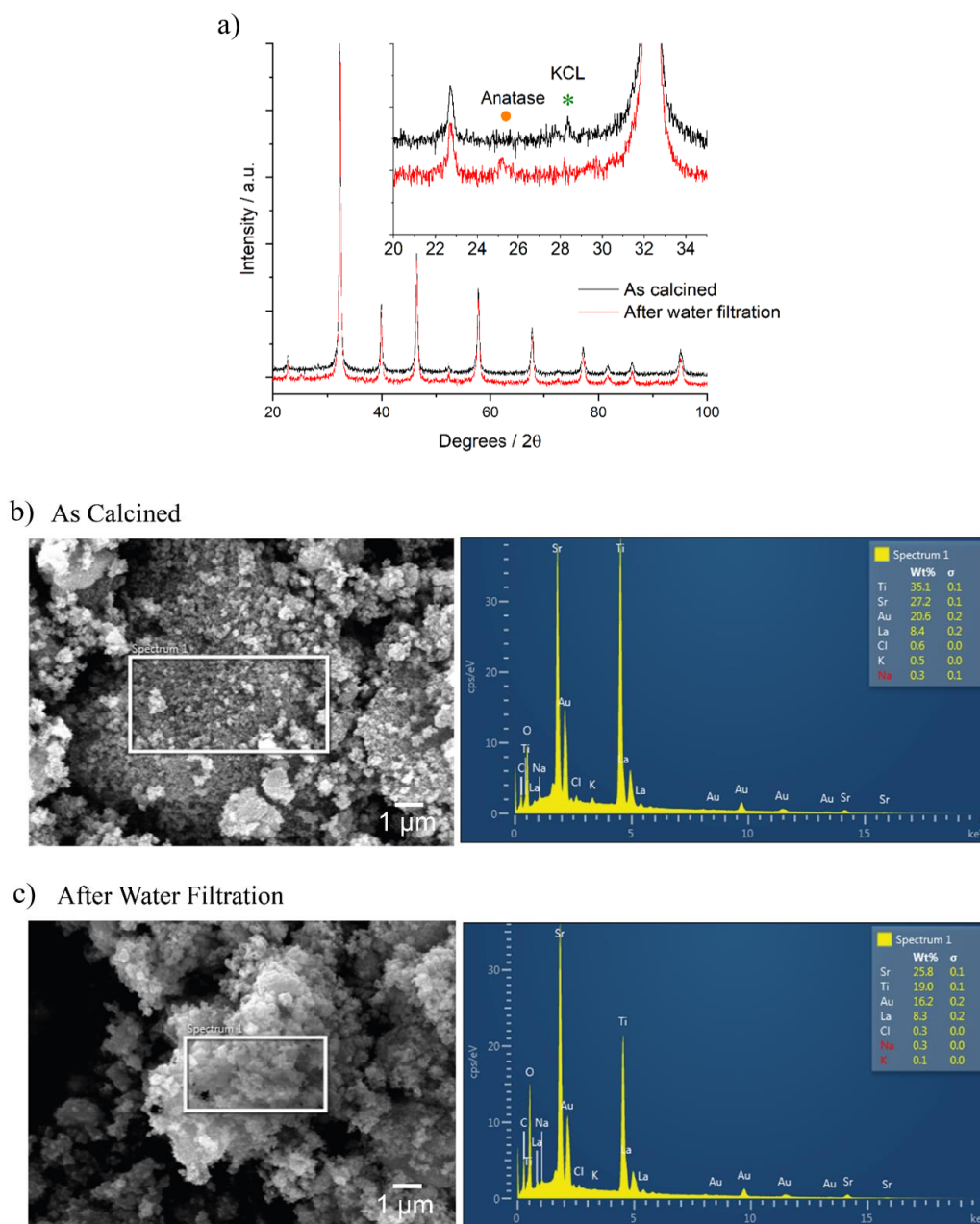
Figure 3.9 a) XRD analysis of ionic liquid synthesised LST before and after water filtration and c-c) SEM, EDS

The XRD in Figure 3.9a shows that the KCl present in the as calcined product was no longer detected in the post water filtration, meaning that KCl had at least reduced to below the detection limit of XRD after water filtration. However, a new peak from anatase was now visible in the filtered sample. This was unexpected as no additional reaction was expected to occur during filtration. This could be due to the preferential dissolution of some of the strontium from the cubic perovskite leaving an Ti rich layer at the surface of the material. This has been known to occur in perovskites such as $BaTiO_3$.[22] This layer may have in turn react with the water to form titania.

EDS has a lower detection limit than XRD and looks for elements rather than crystalline materials, and so can be used to detect trace amounts of elements within a sample even if they are none crystalline. This technique was conducted on pre and post water filtered samples of the powders to probe further into the effect of the water filtration. These results are shown in Figures 3.9b and 3.9c. The wt.% values still cannot be taken as quantification because the EDS is not calibrated with standards, however, the elemental content relative to Au is a useful observation, as Au was sputter coated onto the samples as a charge diffusive coating, so likely present in approximately even distribution over the surface. In the unwashed powder the relative content of Sr and Ti are approximately equal and Na, K and Cl are present in trace amounts, which agree with the previous TEM EDS observations (Figure 3.7).

After water filtration the relative contents of K and Cl are reduced, Na appears unaffected. However, K, Cl and Na are all are still detectable, so not fully removed through water filtration. Since NaCl and KCl are not shown in the post washing XRD but they are visible in EDS, this presents two options: either the K, Na and Cl are present but no longer crystalline or are crystalline and present in amounts below the detection limit of XRD. This will be explored in further detail later in this section.

TEM EDS mapping offers a higher resolution measurement of the distribution of the elements within the sample. This is useful in this case as the particle size is much less than 100 nm and so resolution of individual grains is improved compared to SEM. Figure 3.10 shows a full scope of the elemental distribution which can be directly compared with Figure 3.7, which shows the same technique on a sample before water purification. Once again Na, K and Cl are still present.
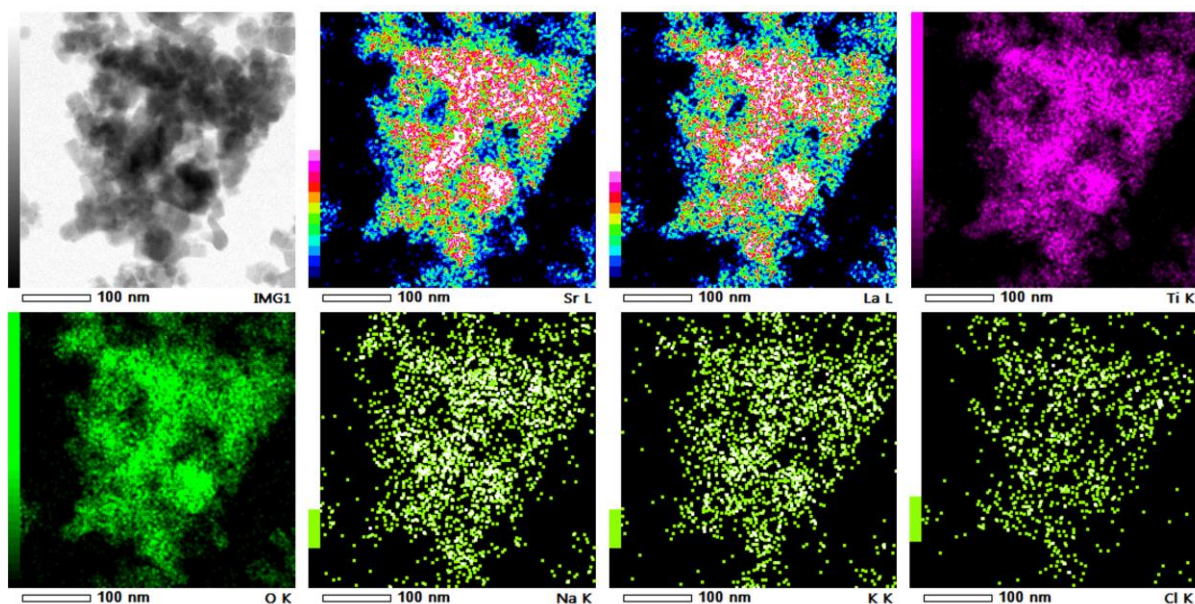
Figure 3.10 STEM EDS of ionic liquid synthesised powder after water filtering.

The density maps of K, Na and Cl look to match the variation in density of the other elements, rather than being present in distinct areas which would suggest that they are not present in distinct particles of a second phase. It appears as though K, Na and Cl are either within the cubic perovskite lattice or coated all over the surface of the perovskite particles.

This is explored in the next section which looks at the surface charge of the powders made via ionic liquid synthesis.

3.3.4 Surface Charge

This section explores the idea that charged ions such as Na, K and Cl may be bonded to the surface of the LST particles due to an inherent surface charge. The Zeta potential can be used to assess the surface charge of a particle. A non-zero zeta potential can be caused by: dissociation of acidic groups on the surface, preferential dissolution of ions from the lattice or adsorption of charged species on to the surface. Lui *et al.* stressed the possibility of surface adsorbates when using liquid synthesis techniques, due to the additional molecules and ions used in the synthesis which can undergo side reactions and adsorb to the surface.[3] In their case SnSe developed a negative surface potential due to partial oxidation of the surfaces, forming polyselanides (Se_x^{2-}), according to their speculation.[3] This resulted in the bonding of Na^+ ions from the precursors to the surface.[3] Zimmermann *et al.* also state that a negative zeta potential is a commonly observed phenomenon in otherwise designated inert surfaces. In their case for several polymer films tested this was due to OH^- group adsorption at surfaces.[23]

Figure 3.11 shows the results of zeta potential measurements of a number of the ionic liquid synthesised powders (red circles and black squares). A zeta potential of around -20 mV at pH 8 was detected when dissolved in 1 mM of KCl. KCl is a standard solute used in Zeta potential measurements, this solution put the pH at around 8. By adding HCl to the solution the pH was decreased, resulting in a positive zeta potential. Roughly interpolating the zeta potential measurements give an isoelectric point of around 6. At this point surface charge is neutralised.
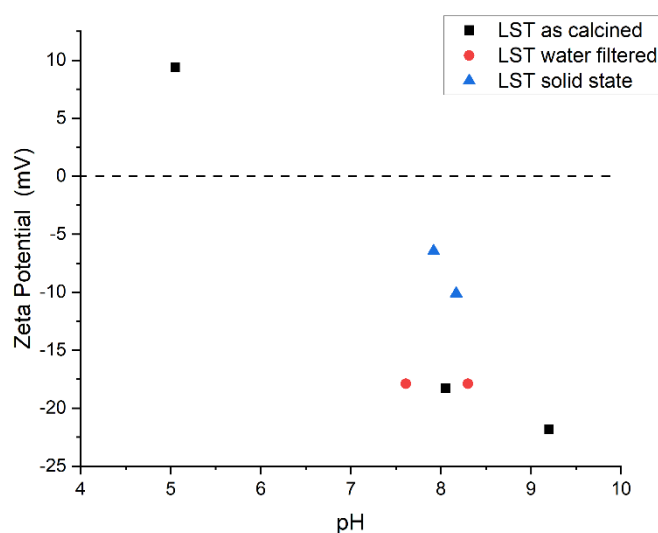
Figure 3.11 Zeta potential measurements of synthesised cubic perovskites.

The cause of the negative surface charge in LST could be preferential dissolution of Sr^{2+} or La^{3+} at the surface, as these are held less strongly in the perovskite structure with ionic bonds, compared to Ti which is covalently bonded.[22,24] Alternatively, this could be due to adsorption of OH- groups or Cl- at the surface. Interestingly, solid state sintered LST showed a much smaller zeta potential between -10 and -5 mV at pH 8, therefore whatever is causing this surface charge is not present in solid state synthesised LST. This is a key finding and confirms the theory presented by Lui *et al.* that surface charges become particularly significant in liquid synthesised thermoelectric materials. The surface properties of the calcined powders become particularly important for low temperature sintering processes such as Cold Sintering.

Fourier Transform Infrared (FTIR) spectroscopy confirmed the presence of OH- groups in the ionic liquid synthesised LST after water filtration, Figure 3.12.[25,26] Additional absorptions corresponding to C=H bonds were found in FTIR, which were also shown in other sol-gel and co-precipitation synthesised samples.[26,27] This is indicative of organic impurities from side reactions with the ionic liquid which is a long chain organic material.
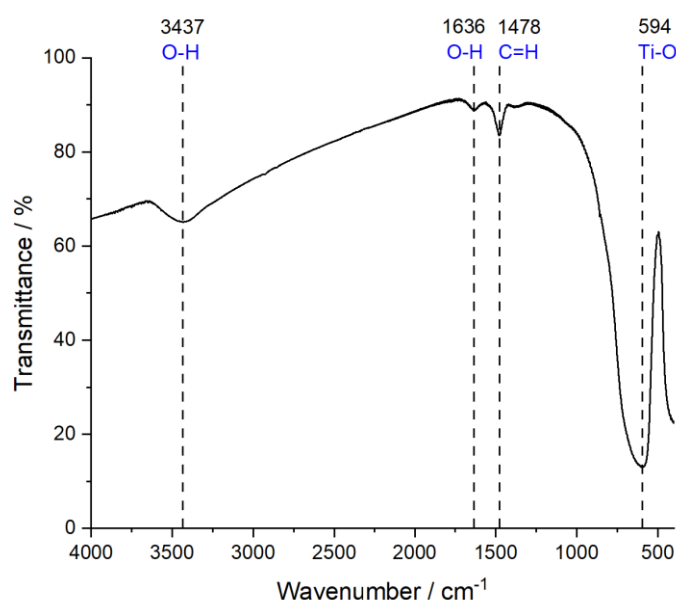
Figure 3.12 FTIR of ionic liquid synthesised La$_{0.15}$Sr$_{0.775}$TiO$_3$ post water filtration.

No peaks could be specifically linked to Cl bonds in the FTIR. Cl would likely form bonds with Sr, Ti, Na or K so the FTIR spectra of compounds containing this bond were studied for comparison. The absorbance peaks of compounds $TiCl_4$ (dissolved in HCl), NaCl and KCl overlapped with those of O-H and Ti-O so would not be distinguishable in the data from Figure 3.12.[28,29] This was largely the case for $SrCl_2.6H_2O$, the FTIR is shown in Figure 3.13, which has the same peaks at ~3440 cm^{-1} and 1640 cm^{-1} which correspond to O-H bonds. It could be argued that there is a common absorbance just below 1500 cm^{-1} in both Figure 3.12 and 13 though the equal intensity absorbance just above 2000 cm^{-1} is not seen in Figure 3.12, this could be masked by the slope of the transmittance curve between 3500-2000 cm^{-1}.
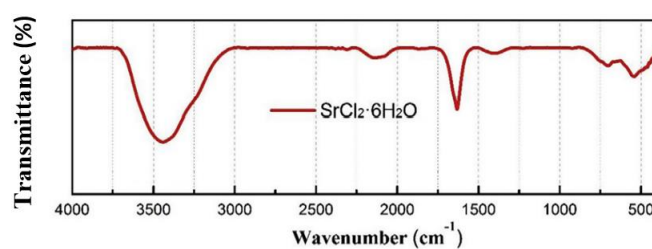
Figure 3.13 FTIR spectra of SrCl₂.6H₂O by Xie et al.[30]

3.3.5 Summary

The negative surface charge determined by Zeta potential measurements, indicates that, as with the work by Liu *et al.*, there are likely to be electrostatically bonded positively charged ions attracted to the negatively charged surface.[3] The origin of this charge is difficult to determine from the current data. OH and Cl appear to be present at the surface which may be adsorbed, though the dissolution of Sr^{2+}/La^{3+} from the surface cannot be ruled out. Whatever is causing the negative surface charge is not as abundant in solid state synthesised LST, evidenced by a smaller surface charge. Therefore, this is not a global characteristic of LST and is likely due to the wet chemical processing route. The presence of the negative surface charge explains the results from EDS showing the presence of K^+ and Na^+ ions, and also explains why these remain even after water filtration – they are electrostatically bonded to the surface so they are harder to remove.

3.3.6 Effect of Impurities on Sintering

The surface charge resulting from the ionic liquid process appears to be resulting in different surface termination. Washing the samples with water had little effect because of the electrostatic attractive forces. The questions that then present themselves are: does the adsorbed material remain in the final sintered product or are they removed by heating, and secondly what effect are they having on the sintering process and final properties.

To address the first question, a simultaneous differential scanning calorimetry and thermogravimetric analysis (DSC/TGA) was conducted to look at the weight loss from the powders when heated. La, Sr and Ti are not known to be volatile elements and so are not likely to leave the structure under heating, though oxygen loss does occur at high temperatures. Conventional solid state sintering would involve firing the powders at a temperature somewhere between 1200 and 1500 ºC, so the ionic liquid synthesised samples were heated up to 1400 ºC (maximum temperature of the instrument used) to observe what material might be lost in this process.

Figure 3.14 shows a significant mass loss between room temperature and 1400 ºC for both samples of LST as calcined and post washed samples which were 4.8 % and 3.4 % respectively. The heat flow results below 200 ºC can be ignored because this machine is meant for high temperature measurements, so results at low temperatures are less reliable. With this in mind, beyond 200 ºC there were no significant peaks or troughs in the heat flow curves. A peak or trough accompanied by weight loss would indicate a degradation of the

LST into other species had taken place, this was not seen. The LST was expected to be stable up to high temperatures.
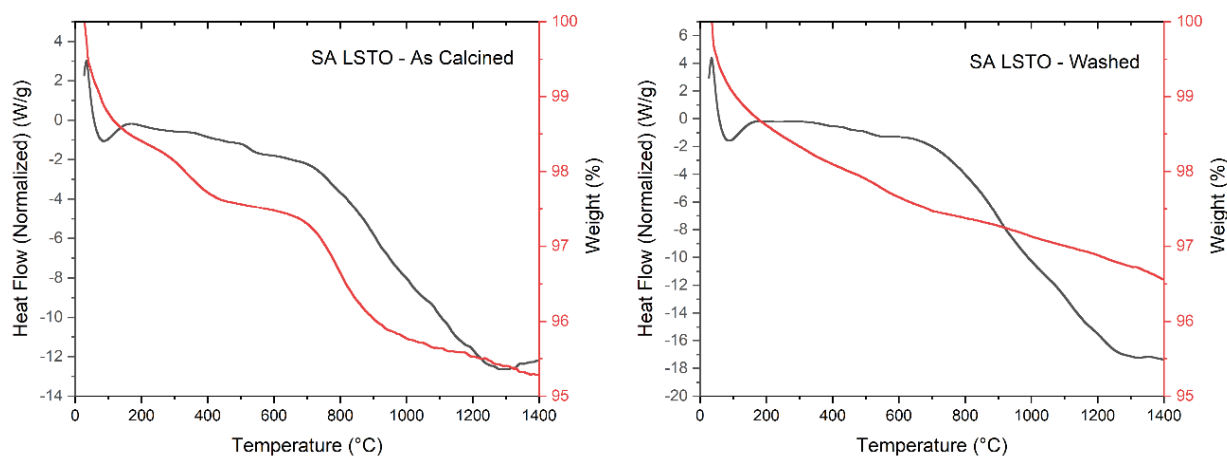
Figure 3.14 SDT of the ionic liquid synthesised LST before and after water filtration.

Concentrating on the weight loss curves (red lines in Figure 3.14) only assumptions about material loss can be made - a mass spectrometer attached to the TG furnace would be able to identify the evolved elements, though this equipment was not available. For the LST 'as calcined' there are two visible features in the weight loss curve: one at ~ 400 ℃ and a larger one at ~ 800 ℃. In the LST 'washed' there was a more continuous decrease in weight percentage over the whole temperature range, and an overall 1.4 % lower weight loss.

The gradual weight loss of the 'washed' sample was likely due to evaporation of surface water at low temperatures, and perhaps some oxygen loss at high temperatures though this is likely background. It was covered in the section 'Strategies to Improve the Figure of Merit in Strontium Titanate: Oxygen Vacancies' that high temperatures lead to oxygen loss in strontium titanates. This is accentuated by low oxygen partial pressures; these samples were run in nitrogen which would not have been actively reducing (scavenging oxygen) but the oxygen partial pressure would have been low.

The two steps in the 'as calcined' sample are harder to define. These accrue to a 1.4 % higher weight loss than in the washed sample. This weight loss occurs mostly below the temperature which the material had been calcined, 800 ℃. This suggests that weight is likely materials absorbed from the atmosphere, such as water of CO_2, between the time it was synthesised and when the test was run.

It was shown in the previous section 'Purification' that the K and Cl contents are reduced through washing, though not totally removed. The evaporation of KCl would be the natural assumption to account for this weight loss, though the boiling points of KCl or in fact NaCl are much too high to account for the steps seen - KCl boils at 1420 ℃ and NaCl boils at 1465 ℃. However, KCl and NaCl are known to be hygroscopic – meaning they absorb moisture from the air.[31,32] If more KCl and NaCl are present in the as calcined material then this material may absorb more moisture from the air meaning that a greater degree of weight loss will occur when heating as this is removed. Though this would suggest a very high salt

content to account for this degree of weight loss, which was not found from XRD or EDS, so this is unlikely to be the sole cause of the weight loss.

The key point of this data is that for the 'as calcined' sample there are clearly additional elements being potentially melted and evolved within the sintering window which could affect the sintering process. Washing the sample makes a more weight stable material whose sintering characteristics should be easier to predict. Furthermore, if using a cold sintering technique, where sintering temperatures are in the range of 120 – 300 ℃, then these impurities will remain present in the final product if not pre-treated before sintering.

Tsuji *et al.* showed a cold sintering technique where they intentionally added KOH and NaOH to barium titanate nanoparticles which acted as flux to aid the sintering.[33] KOH and NaOH form a eutectic which melts at 170 ℃ so when they were sintering at 300 ℃ this molten hydroxide phase acted as a high temperature solvent and induced pressure-solution creep. Just 4 wt.% flux was an effective addition leading to 98 % dense sample.[33]

Is it possible that the K and Na impurities could perform in a similar way in this case? There is OH present as surface adsorbates as shown in Figure 3.12. It is somewhat possible that the OH could combine with the Na and K to form the NaOH-KOH eutectic, though it is difficult to quantify the level of OH on the surface and say whether this would be enough to form the hydroxide. Furthermore, the presence of the Cl⁻ could interfere with the formation of the hydroxide, though there was not a large quantity of the Cl compared to Na and K in Figures 3.7 and 3.10. NaOH and KOH have a boiling point of 1388 ℃ and 1320 ℃ respectively and no features are visible that can be attributed to them in any significant quantities. This theory will be explored in greater detail in a later experimental chapter on Cold Sintering.

To explore the effects of the water filtration on the samples changes in lattice parameter during sintering, Reitveld refinements were conducted on pre and post washed ionic liquid synthesised LST and solid state synthesised LST which underwent a reducing process in 5% H_2/95% N_2. A good indication for the level of reduction (oxygen loss) undergone in the sintering process is the lattice parameter increase, which accounts for Ti^{3+} creation which expands the lattice.[34] Figure 3.15 shows the lattice parameters determined from Reitveld refinements before and after sintering. The details of the individual refinements can be found in section 3.6 Appendix. The lattice parameters determined in the solid state synthesised LST were in agreement to work by Lu *et al.*[2]
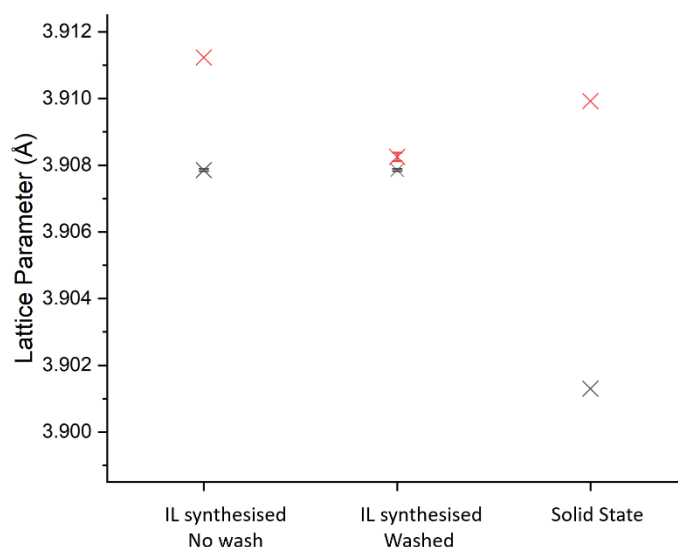
Figure 3.15 Lattice parameters of the LST from reitveld refinements after calcining (black crosses) and after sintering (red crosses) at 1325 ºC for 8 h in 5 % H₂/ 95 % N₂. Some values have error bars denoted by two horizontal lines.

As already highlighted, the calcined lattice parameter of the air sintered ionic liquid-derived LST is much higher than air sintered solid state LST. A degree of oxygen loss in the calcined ionic liquid product has already been proposed to explain the larger lattice parameter in ionic liquid synthesised powders, though considering the lattice parameter of the reduced solid state sintered LST which appears black in colour (3.90992 Å) and IL synthesised LST after calcination (3.90786 Å) which was pure white this seems unlikely. As the parameter for the calcined IL powder is closer to the parameter for the sintered solid state sample the powder would be expected to be at least grey in colour, not pure white. This was not observed.

Assuming that the change in lattice parameter represents the degree of reduction, after washing the calcined powder the observed level of reduction was almost zero. This was supported by XPS which showed the atomic percentage of each Ti oxidation state in the samples, Table 3.3. These results where average from two measurements, the raw data can be found in section 3.6 Appendix. This shows the net gain in at. % of Ti^{3+} was much smaller in the washed ionic liquid synthesised sample than in the solid state sample. Unfortunately, XPS was not conducted on a sample with has not been washed before reduce sintering. The presence of Ti^0 was an unexpected feature in the reduced LST, as this represents titanium in its metallic form which is highly unlikely to be the case. Very strong reducing conditions are required to produce Ti metal from $Ti^{3/4+}$ ions. This is likely a consequence of the fitting parameters used.

Table 3.3 XPS determined atomic % of Ti species in LST samples.

Sample	Ti^{4+} (at.%)	Ti^{3+} (at.%)	Ti^0 (at. %)
Solid state calcined	93.2	6.9	0

Solid state reduce sintered	84.8	14.5	0.7
Net change	-8.4	+7.6	+0.7
Ionic Liquid synthesised	92.7	7.3	0
Ionic Liquid synthesised, washed then reduce sintered.	91.95	8.0	0.05
Net change	-0.75	+0.7	+0.05

3.3.7 Alternative Ionic Liquid

A more expensive version of the same ionic liquid species would be expected to have less impurities. Additional purification steps are costly and so raise the price of the product. Therefore, the ionic liquid synthesis was also repeated with a more expensive emimOAc products from Alpha Aesar with purity 97%. From FTIR the two ionic liquids appear very similar and in line with previously published emimOAc FTIR, Figure 3.16.[35]
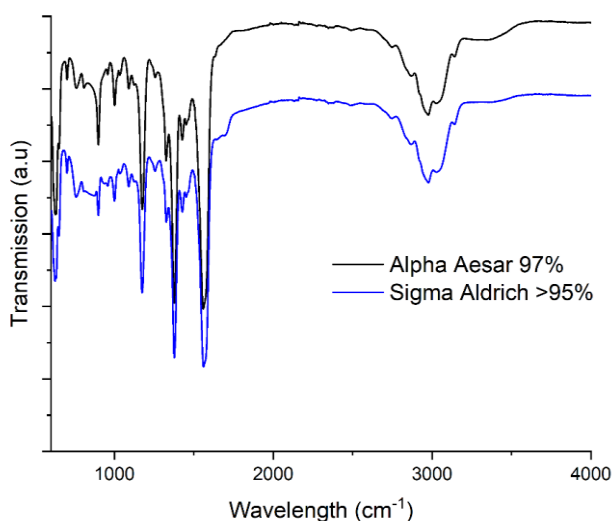
Figure 3.16 FTIR of two the sources of the ionic liquid emimOAc.

Using this IL, a cubic perovskite with lattice parameter 3.9075 Å was also achieved, which also contained small amounts of the impurities seen with the Sigma Aldrich IL in XRD: anatase and KCl, Figure 3.17. Figure 3.18 shows the elemental spectrum of the Alpha Aesar emimOAc synthesised LST from SEM EDS. There was a significant peak of C which was due to the carbon coating. There was also a lack of potassium detected, unlike in the Sigma

Aldrich emimOAc synthesised powder in Figures 3.7, 3.9 and 3.10. There were small Cl and Na peaks, however, indicating the present of some impurities. A similar zeta potential of -21.4 mV at pH 8.15 was recorded which also lined up with the powder synthesised from Sigma Aldrich IL.
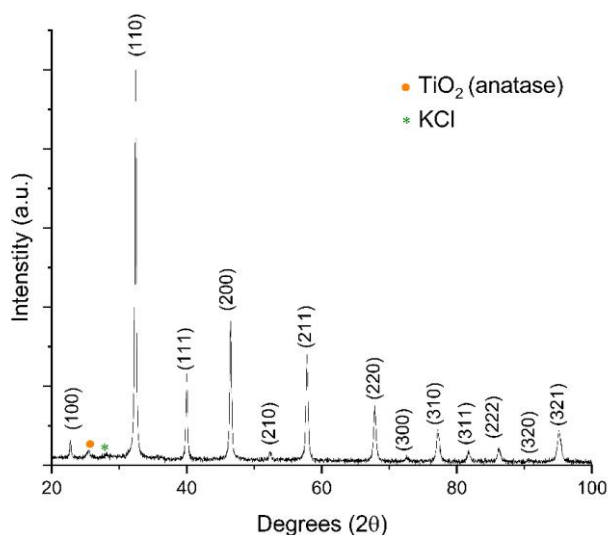
Figure 3.17 XRD of the Alpha Aesar synthesised LST powder with impurities: anatase and KCl.
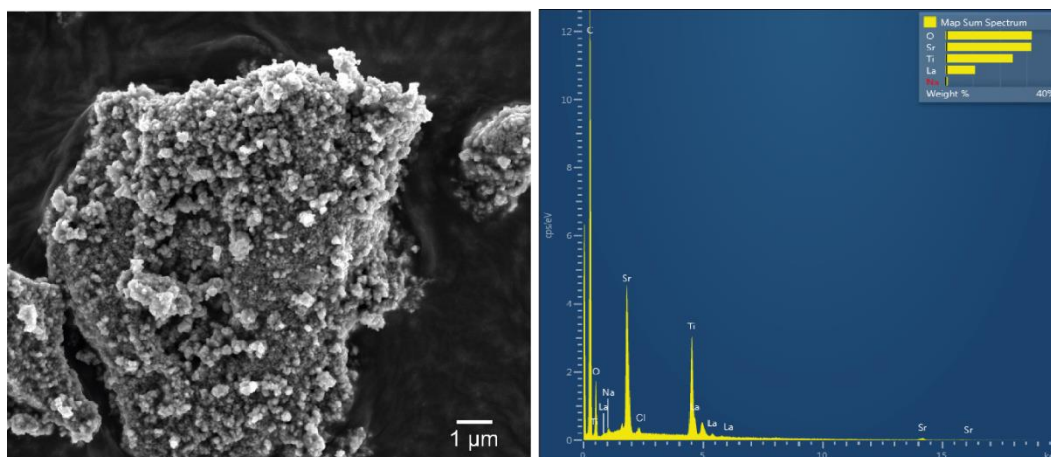
Figure 3.18 SEM secondary electron image of Alpha Aesar emimOAc synthesised LST (left) and the SEM EDS elemental spectrum of the same area.

When observing the weight loss properties in SDT (Figure 3.19) the Alpha Aesar synthesised powder seemed to show the same behaviour as the 'washed' Sigma Aldrich synthesised powder. Once again the results below 200 ºC can be attributed to water loss and low instrument sensitivity in this region, as stated previously. The steady rate of decrease in the mass loss was also likely caused by the loss of oxygen caused by heating at elevated temperatures. The overall mass loss was 2.1 wt.%, this was lower than both the 'as calcined'

(4.8 wt.%) and 'washed' (3.4 wt.%) Sigma Aldrich samples. Figure 3.20 shows a direct comparison of all three samples percentage weight loss by TGA. This either indicates that the powder is purer and has less to burn off at elevated temperatures or the rate of oxygen loss is lower.
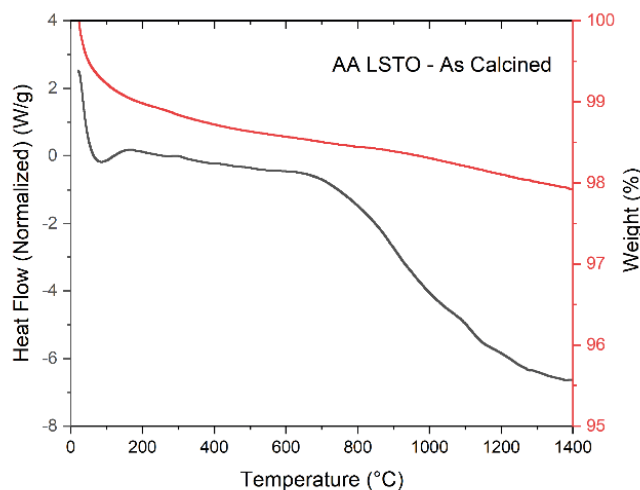
Figure 3.19 SDT of the Alpha Aesar emimOAc synthesised powder as calcined.
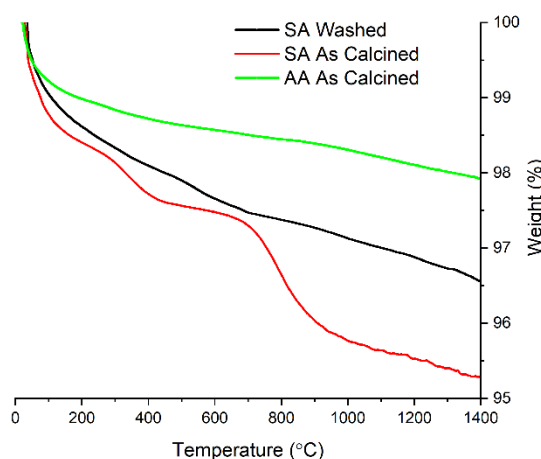
Figure 3.20 Percentage weight loss of LST synthesised with Sigma Aldrich >95% emimOAc, before and after washing, and LST synthesised with Alpha Aesar emimOAc as calcined.

To confirm the level of oxygen loss, a Reitveld analysis was conducted from the XRD of samples made from each ionic liquid. The Sigma Aldrich sample was water filtered before sintering. The results of which can be seen in Tables 3.4 and 3.5, the fitting data can be found in section 3.6 Appendix. The lattice parameter is expected to increase with oxygen loss as this effect is compensated for by reduction of the T^{4+} to the larger Ti^{3+}. In both cases after sintering in a reducing atmosphere the modelled oxygen content reduces and the lattice parameter increases. For the Alpha Aesar LST, when sintered, there is a much larger decrease in oxygen content and degree of lattice expansion. This indicates that in fact the Alpha Aesar

synthesised material loses oxygen more readily than the Sigma Aldrich synthesised and washed LST under the same conditions. This was also confirmed by XPS results in Table 3.6.

What is shown by the reitveld refinement rules out the possibility that the lower weight loss in SDT is caused by less oxygen loss, and is likely due to the high purity of the powder. To go along with this data, the EDS under SEM can give an indication of the elements present, though yet again this cannot be quantified as calibration standards were not available.

Table 3.4 The reitveld refinement results from LST synthesised with Sigma Aldrich >95% emimOAc after calcination and sintering at 1325 ºC for 8h in 5% H2 / 95% N2

Sigma Aldrich Calcined 800ºC		
Element	Occupancy	Electrons
Sr^{2+}	1.026	
Ti^{4+}	1.007	
O^{2-}	0.982	
Lattice parameter (Å)		3.908410
Sigma Aldrich Sintered 1325 ºC, 5% H_2		
Element	Occupancy	
Sr^{2+}	1.018	
Ti^{4+}	0.978	
O^{2-}	0.978	
Lattice parameter (Å)		3.908426

Table 3.5 The reitveld refinement results from LST synthesised with Alpha Aesar 97% emimOAc after calcination and sintering at 1325 ºC for 8h in 5% H_2 / 95% N_2

Alpha Aesar Calcined 800ºC		
Element	Occupancy	
Sr^{2+}	1.033	
Ti^{4+}	1.021	
O^{2-}	0.962	
Lattice parameter (Å)		3.907471
Alpha Aesar Sintered 1325 ºC, 5% H_2		
Element	Occupancy	
Sr^{2+}	1.045	
Ti^{4+}	1.000	
O^{2-}	0.926	
Lattice parameter (Å)		3.910427

Table 3.6 XPS data on calcined and sintered LST synthesises using Alpha Aesar IL.

Sample	Ti^{4+} (at.%)	Ti^{3+} (at.%)	Ti^0 (at.%)

Alpha Aesar IL powder a	93.2	6.8	
Alpha Aesar IL reduce sintered	84.3	12.9	2.8
Net change	-8.9	+6.1	+2.8

3.4 Conclusions

The ionic liquid synthesis of $La_{0.15}Sr_{0.775}TiO_3$ produced a cubic perovskite phase with particle size 97 ± 33 nm after calcining at 800 ℃. This was much smaller than that could be achieved through solid state sintering.[2] Using the ionic liquid emimOAc from Sigma Aldrich with a purity >95% resulted in impurities of NaCl and KCl visible in XRD analysis and K, Na and Cl detected in EDS. These impurities likely originate from the synthesis process of the ionic liquid itself.[11] The study to determine if the impurities enter the perovskite lattice was inconclusive.

Due to the presence of a negative surface charge of ~ 20 mV at pH 8, positively charged impurity ions (Na^+ and K^+) may also be strongly attracted to the surface by electrostatic potential and thus not easily removed. The level of impurities could be reduced, but not entirely removed using water filtration, and this also caused the emergence of small amounts of TiO_2. Filtering with ethanol may have a greater effect as titanium ions are known to form titanium dioxide on contact with water. Ethanol was not available for this work and so this theory was not tested.

LST made using a higher purity emimOAc ionic liquid was compared to an LSt made using lower purity emimOAc. These were EmimOAc 97% from Alpha Aesar and emimOAc >95% from Sigma Aldrich > 95%. Although the two sources of emimOAc appeared identical under FTIR, the pure IL yielded powders with lower impurity levels. This was confirmed by lower mass loss under SDT for the powder synthesis with purer emimOAc. This is of course accompanied by a large increase in cost, as additional purification process for the ionic liquid are required by the manufacturer.

The upgrade to more expensive ionic liquid, however, somewhat hinders the benefits of strontium titanates which are being proposed as a cheaper alternative to other n-type thermoelectric materials i.e. bismuth telluride. The issue of cost and purity should to be considered to reach a trade-off.

For this particular composition and application, the need to induce oxygen vacancies is vital to achieve the electrical conductivity desired in LST. The preparation of the material seemed to play a vital role in the materials propensity to lose oxygen, which can be quantified by an increase in the lattice parameter. Larger increases in the lattice parameter were shown in solid state sintered LST, compared to ionic liquid synthesised LST using the same reduction process. Particularly after water filtration the level of lattice parameter increase was almost zero which was supported by a low level of Ti^{3+} conversion from XPS data. The reason for this is unknown.

3.5 Future Work

Future work should look at alternative ways the purify the ionic liquid synthesised powders. High temperatures could volatise impurities which would somewhat nullify the purity issues for solid state sintering, though the intention of this low temperature synthesis route was to prepare powder for low temperature sintering methods i.e. The Cold Sintering Process, and reduce temperatures/energy required in the synthesis in general. Impurities may be more effectively removed by using stronger solvents rather than distilled water, such as ethanol. Alternatively altering the pH of the solution used to wash the powder could be explored as water is shown to preferentially leach A-site ions, though Pourbaix diagrams show that this effect can be reduced in the case of $BaTiO_3$ by using a solution close to pH 10. [36]

As for ions which may be electrostatically attracted to the surface by the surface charge, previous work has looked at replacing the adsorbed ions with matter that can be combusted with an additional heating step.[3] Liu *et al.* showed that by using tetramethylammonium ($[C_4H_{12}N]^+$) based salts as precursors in the fabrication of SeSn rather than sodium (Na^+) based salts, they were able to purify the final product by combusting the tetramethylammonium adsorbed to the surface. In the case of the ionic liquid synthesis the K^+ and Na^+ are unintentionally present in the IL and so cannot so easily be replaced, however perhaps an additional species could be added to compete with the Na^+ and K^+ to preferentially bond to the surface which can then be combusted.

The potential of K^+ and Na^+ doping into the perovskite should be further investigated, this could be done by intentionally adding potassium and sodium acetates as precursors and examining the XRD for secondary phases and changes to the lattice parameter.

Of course other, purer, sources of the ionic liquid emimOAc could be considered for use in the synthesis, though this would come with a significant cost consideration which must be weighed against the benefits of a purer ceramic powder that can be made in one step, compared to the purity gains that could be achieved through additional purification steps, such as washing of the final powders.

Performing a Hall Effect measurement on theses samples could also quantify the electron concentration within the samples, to confirm that the 3+ charged dopants (La and Eu) are compensated for by A-site vacancies and not electronic compensation. These values would also be useful in forming a baseline with which to compare the electron concentration of samples in later chapters where the electrical conductivity is increased by reducing the material.

3.6 References

1   L. Mottram, D. Z. C. Martin, N. Reeves-McLaren and R. Boston, *J. Am. Ceram. Soc.*, 2018, **101**, 4468–4471.

2   Z. Lu, H. Zhang, W. Lei, D. C. Sinclair and I. M. Reaney, *Chem. Mater.*, 2016, **28**, 925–935.

3   Y. Liu, M. Calcabrini, Y. Yu, A. Genç, C. Chang, T. Costanzo, T. Kleinhanns, S. Lee,

J. Llorca, O. Cojocaru-Mirédin and M. Ibáñez, *Adv. Mater.*, 2021, **33**, e2106858-n/a.

4   D. Burnat, A. Heel, L. Holzer, D. Kata, J. Lis and T. Graule, *J. Power Sources*, 2012, **201**, 26–36.

5   L. Wannasen and E. Swatsitang, *Jpn. J. Appl. Phys.*, 2013, **52**, 06GG11.

6   N. G. Eror and U. Balachandran, *J. Solid State Chem.*, 1981, **40**, 85–91.

7   K. S. Yoo, T. G. Lee and J. Kim, *Microporous Mesoporous Mater.*, 2005, **84**, 211–217.

8   K. Yoo, H. Choi and D. D. Dionysiou, 2004, **4**, 18.

9   A. J. Ahmed, S. M. K. Nazrul Islam, R. Hossain, J. Kim, M. Kim, M. Billah, M. S. A. Hossain, Y. Yamauchi and X. Wang, *R. Soc. Open Sci.*, 2019, **6**, 190870.

10   C. S. G. P. Queirós, X. Paredes, T. F. S. Avelino, D. E. N. Bastos, M. Ferreira, F. J. V. Santos, A. F. Santos, M. L. M. Lopes, M. J. V. Lourenço, H. Pereira and C. A. Nieto de Castro, *J. Mol. Liq.*, 2020, **297**, 111925.

11   D. Berthier, A. Varenne, P. Gareil, M. Digne, C. P. Lienemann, L. Magna and H. Olivier-Bourbigou, *Analyst*, 2004, **129**, 1257–1261.

12   R. Ge, R. W. K. Allen, L. Aldous, M. R. Bown, N. Doy, C. Hardacre, J. M. MacInnes, G. McHale and M. I. Newton, *Anal. Chem.*, 2009, **81**, 1628–1637.

13   F. Yang, J. S. Dean, Q. Hu, P. Wu, E. Pradal-Velázquez, L. Li and D. C. Sinclair, *J. Mater. Chem. A*, 2020, **8**, 25120–25130.

14   Z. Schnepp, S. C. Wimbush, S. Mann and S. R. Hall, *CrystEngComm*, 2010, **12**, 1410–1415.

15   D. Walsh, S. C. Wimbush and S. R. Hall, *Chem. Mater.*, 2007, **19**, 2702.

16   S. Hui and A. Petric, *J. Electrochem. Soc.*, 2002, **149**, J1–J10.

17   S. A. Prosandeev, I. P. Raevski and M. A. Bunin, *Phys. Rev. B - Condens. Matter Mater. Phys.*, 2004, **70**, 2–3.

18   J. X. Liao, X. B. Wei, Z. Q. Xu and P. Wang, *Vacuum*, 2014, **107**, 291–296.

19   D. Dogu, K. E. Meyer, A. Fuller, S. Gunduz, D. J. Deka, N. Kramer, A. C. Co and U. S. Ozkan, *Appl. Catal. B Environ.*, 2018, **227**, 90–101.

20   H. X. Dai, C. F. Ng and C. T. Au, *J. Catal.*, 2000, **189**, 52–62.

21   M. Reinke, Y. Kuzminykh and P. Hoffmann, *J. Phys. Chem. C*, 2016, **120**, 4337–4344.

22   S. Grasso, M. Biesuz, L. Zoli, G. Taveri, A. I. Duff, D. Ke, A. Jiang and M. J. Reece, *Adv. Appl. Ceram.*, 2020, 119, 115–143.

23   R. Zimmermann, U. Freudenberg, R. Schweiß, D. Küttner and C. Werner, *Curr. Opin. Colloid Interface Sci.*, 2010, **15**, 196–202.

24   O. Ozmen, C. Ozsoy-Keskinbora and E. Suvaci, *J. Am. Ceram. Soc.*, 2018, **101**, 1074–1086.

25   T. Xian, H. Yang, L. Di, J. Ma, H. Zhang and J. Dai, *Nanoscale Res. Lett.*, 2014, **9**, 1–

9.

26   L. U. Hasanah, F. R. Agustina, N. F. S. Puspita, B. Suherman, F. Nurosyid, D. K. Sandi and Y. Iriani, *J. Phys. Conf. Ser.*, 2022, **2392**, 012034.

27   T. Xie, Y. Wang, C. Liu and L. Xu, *Materials (Basel).*, 2018, **11**, 646.

28   and T. O. D. Timothy J. Johnson, Tanya L. Myers, Yin-Fong Su, Russell G. Tonkyn, Molly Rose K. Kelly-Gorham, *NIST Chem. Webb.*, , DOI:10.18434/T4D303.

29   D. Lim, S. D. Kim, H. Kong, D. Nam, S. E. Shim and S. H. Baeck, *Int. J. Anal. Chem.*, , DOI:10.1155/2018/6470196.

30   N. Xie, J. Niu, T. Wu, X. Gao, Y. Fang and Z. Zhang, *Sol. Energy Mater. Sol. Cells*, 2019, **200**, 110034.

31   B. Jing, C. Peng, Y. Wang, Q. Liu, S. Tong, Y. Zhang and M. Ge, *Sci. Rep.*, 2017, **7**, 1–11.

32   X. Wang, H. Lei, R. Berger, Y. Zhang, H. Su and Y. Cheng, *Phys. Chem. Chem. Phys.*, 2020, **22**, 9967–9973.

33   K. Tsuji, A. Ndayishimiye, S. Lowum, R. Floyd, K. Wang, M. Wetherington, J. P. Maria and C. A. Randall, *J. Eur. Ceram. Soc.*, 2020, **40**, 1280–1284.

34   J. Cao, D. Ekren, Y. Peng, F. Azough, I. A. Kinloch and R. Freer, *ACS Appl. Mater. Interfaces*, 2021, **13**, 11879–11890.

35   G. Severa, E. Bruffey, P. Q. H. Nguyen, A. Gigante, N. Leick, C. Kelly, G. J. Finkelstein, H. Hagemann, T. Gennett, R. E. Rocheleau and P. Dera, *ACS Omega*, 2021, **6**, 31907–31918.

36   J. H. Adair, J. Crampo, M. M. Mandanas and E. Suvaci, *J. Am. Ceram. Soc.*, 2006, **89**, 1853–1860.

3.7 Appendix
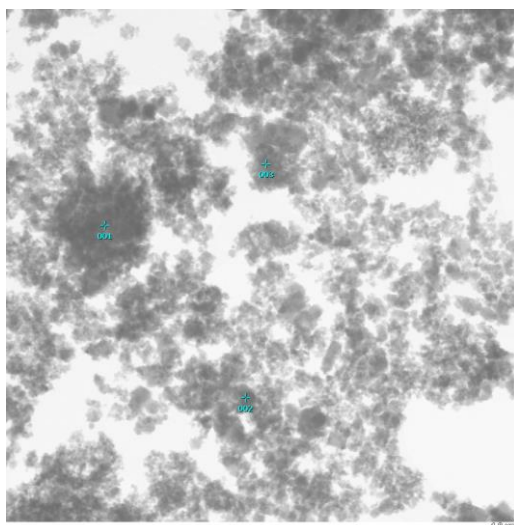
STEM of unwashed ionic liquid synthesised LST, numbered dots correspond to areas were EDS spot spectra were taken.

STEM EDS of IL synthesised LST unwashed spot 001

STEM EDS of IL synthesised LST unwashed spot 001
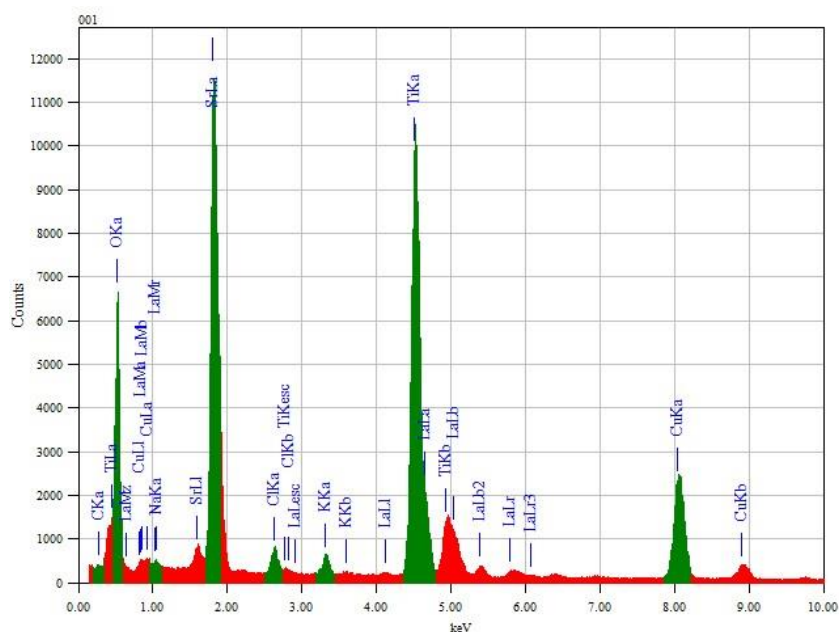
STEM EDS of IL synthesised LST unwashed spot 001
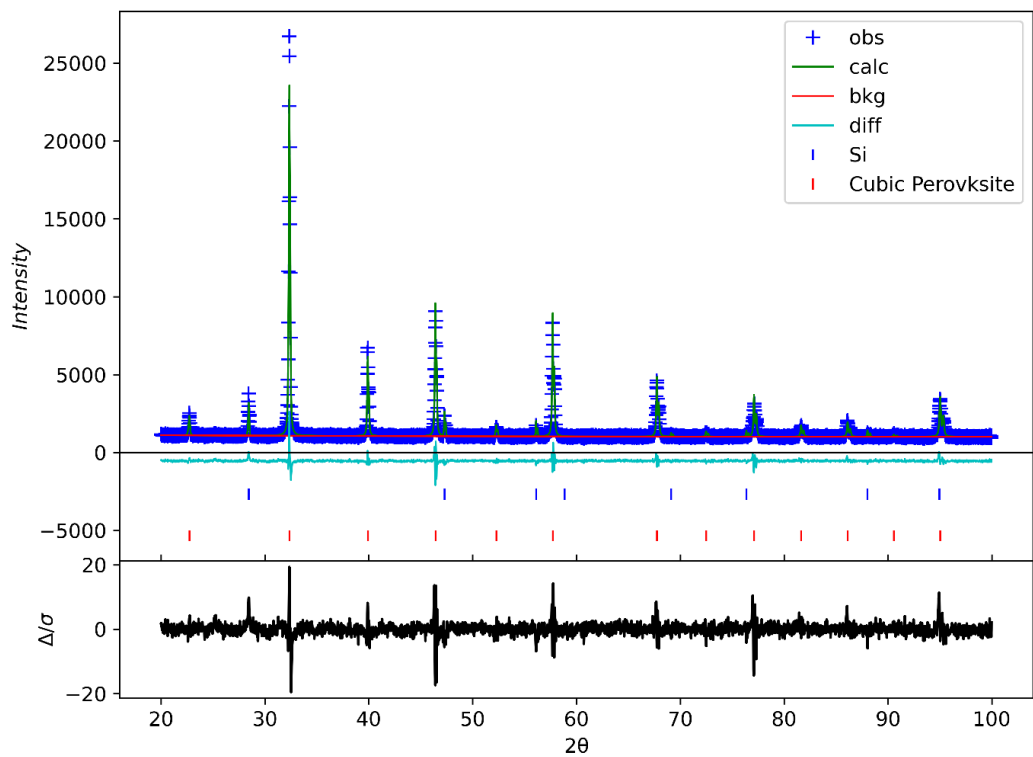
Space group:	P m -3 m	GOF		1.95				
a	b	c	alpha	beta	gamma	volume	
3.908426	3.908426	3.908426	90	90	90	59.704	
label	element	multiplicity	x	y	z	fraction	Uiso
Sr1	Sr+2	1	0	0	0	1.018	0.0158
Ti1	Ti+4	1	0.5	0.5	0.5	0.978	0.0149
O1	O-2	3	0.5	0.5	0	0.978	0.0319

Retiveld refinement data of the Sigma Aldrich LST sintered at 1325 ℃
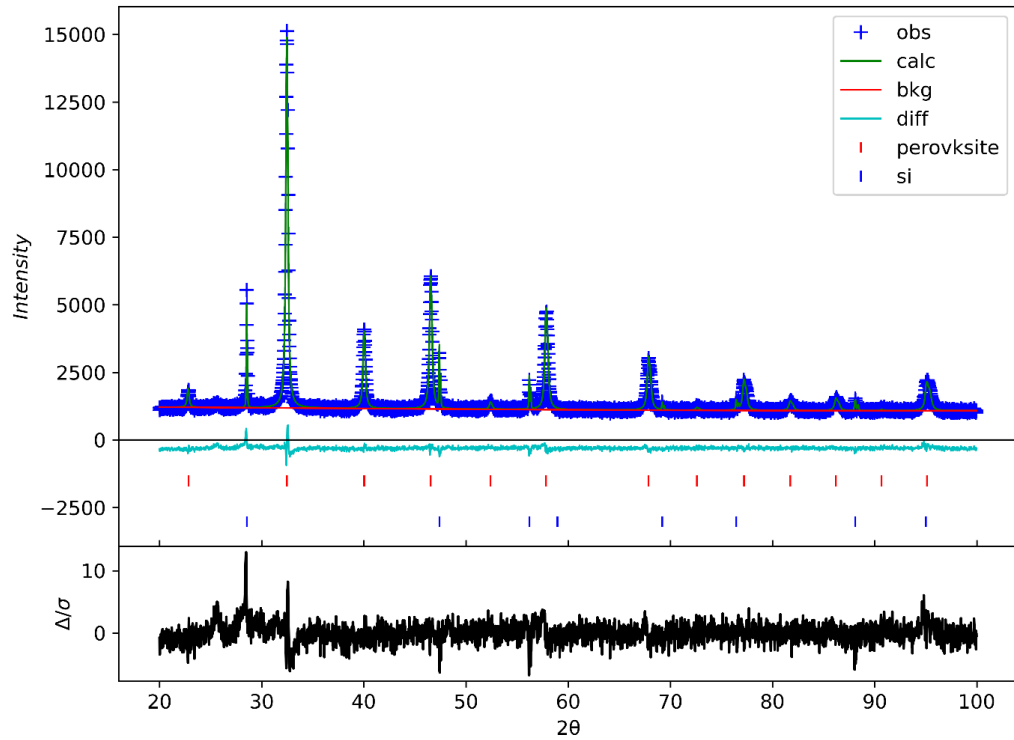
Space group:	P m -3 m	GOF	1.54				
a	b	c	alpha	beta	gamma	volume	
3.907471	3.907471	3.907471	90	90	90	59.661	
label	element	multiplicity	x	y	z	fraction	Uiso
Sr1	Sr+2	1	0	0	0	1.033	0.0241
Ti2	Ti+4	1	0.5	0.5	0.5	1.021	0.0182
O3	O-2	3	0.5	0.5	0	0.962	0.0162

Reitveld refinement results of Alpha Aesar LST calcined at 800 ºC
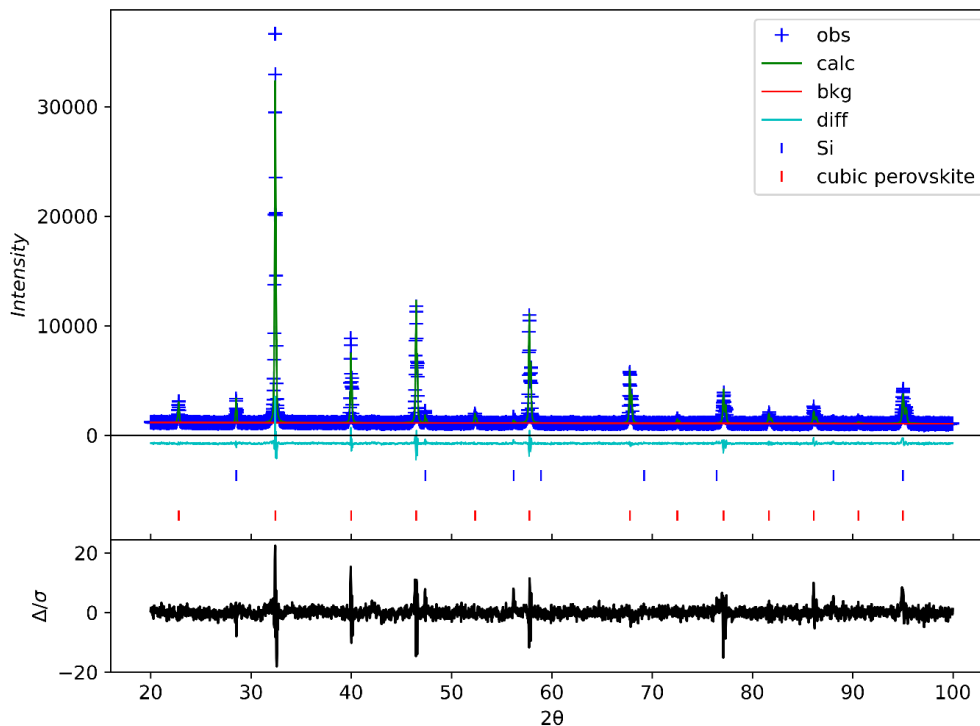
Space group:	P m -3 m	GOF	1.84				
a	b	c	alpha	beta	gamma	volume	
3.910427	3.910427	3.910427	90	90	90	59.796	
label	elem	mult	x	y	z	frac	Uiso
Sr	Sr+2	1	0	0	0	1.045	0.0169
Ti 4+	Ti+4	1	0.5	0.5	0.5	1	0.0145
O	O-2	3	0.5	0.5	0	0.926	0.0216

Reitveld refinement results of Alpha Aesar LST reduce sintered at 1325ºC.

Raw XPS data produced by Deborah Hammond before and after reduce sintering.

	Ti(IV)	Ti2p (III)	Ti2p (metal)
Sample	(at.%)	(at.%)	(at.%)
Solid state powder a	93.6	6.5	
Solid state powder b	92.8	7.3	
Sigma Aldrich IL powder a	92.7	7.3	
Sigma Aldrich IL powder b	92.7	7.3	
Alpha Aesar IL powder a	93.2	6.8	
Alpha Aesar IL powder b	93.2	6.8	
Solid state reduce sintered a	84.7	14.6	0.7

Solid state reduce sintered b	84.9	14.4	0.7
Sigma Aldrich IL reduce sintered a	91.1	8.8	0.1
Sigma Aldrich IL reduce sintered b	92.8	7.2	0.0
Alpha Aesar IL reduce sintered a	83.9	13.5	2.5
Alpha Aesar IL reduce sintered b	84.7	12.3	3.1

4.0 Europium Doping of $La_{0.15}Sr_{0.775}TiO_3$

4.1 Aims and Objectives

Lu *et al.* optimised the La content in series $La_xSr_{1-3/2x}TiO_{3-\delta}$ and found that $La_{0.15}Sr_{0.775}TiO_3$ had the highest ZT of 0.41 at 700ºC. [1] The aim of this study was to further improve the thermoelectric properties of this composition by reducing its thermal conductivity whilst maintaining the electrical conductivity and absolute Seebeck coefficients to overall give a higher figure of merit ZT.

The proposed method to achieve this was to introduce further atomic mass fluctuation onto the A-site by doping with Europium. Europium is a heavy rare earth element with a suitable ionic radius to occupy the A-site. The aim of this was to increase the degree of phonon scattering and thus reduce the thermal conductivity of the material. [2] Rare earths have previously been shown to reduce the thermal conductivity when doped into strontium titanate, though this specific composition had not yet been reported. [3] In order to report this combination of dopants for the first time and optimise the europium content, a whole compositional series with the formula $La_{0.15-x}Eu_xSr_{0.775}TiO_3$ was synthesised. The lattice parameters, electrical, thermal and Seebeck coefficient values of the series were studied in order to assess the suitability of the material as a high performance thermoelectric material.

4.2 Introduction

Efficient *p*- and *n*-type materials are required in cooperation for a successful TEG. To date, high efficiency *p*-type oxides such as $Na_{0.89}CoO_2$ have been identified, [4] whereas successful *n*-type materials are holding back the performance of newly developing devices.

Much work concerning the doping of $SrTiO_3$ perovskites exists, and some promising n-type materials have been found. [5–8] The drawback of most metal oxides is that the strong covalent bonds between oxygen and metal atoms lead to high thermal conductivity, and so there is a focus to drive down the thermal conductivity to help improve ZT.

One of highest ZT *n*-type oxide performances published to date is that of $Sr_{0.775}La_{0.15}TiO_{3-\delta}$ by Lu *et al.* with a value of 0.41 at 973 K. [1] This is an outstanding value for an *n*-type oxide however, this still lags behind the *p*-type counterparts. The high tolerance factor of perovskites allows a high degree of doping which can be used to refine properties, and therefore make it an attractive structural starting point.

Several doping strategies have been implemented using rare earths do to their large masses affording a large degree phonon scattering due to lattice distortion. Y, La Sm, Gd, Dy have all been shown to reduce the thermal conductivity of $SrTiO_3$. [3] A study which has not yet been shown is the doping of LST with europium. Eu^{3+} is a smaller, heavier ion which will replace the Sr^{2+} ion and create mass fluctuation to induce phonon scattering and reduce the thermal conductivity. The europium should also act as a donor dopant, like the La^{3+} ion, which is compensated by A-site vacancies which make oxygen loss easier during the reduction stage, according to Akin *et al.*. [9]

4.3 Results and Discussion

4.3.1 Calcination

Seven compositions of the series $La_{0.15-x}Eu_xSr_{0.775}TiO_3$ (LEST) were synthesised using the ionic liquid method. The composition x = 0.0 was identical to that made by Lu *et al.,* save for the synthesis method, which allowed for the direct comparison between this work and their published works. Increasing amounts of europium were added until the lanthanum was fully replaced by europium. The compensation mechanism for La^{3+} is given in Equation 4.1, and it was predicted that Eu^{3+} would also occupy the A-site and undergo the same compensation mechanism as shown by Muta *et al.*[10] The compositions synthesised are listed in the Table 4.1 and hereafter referred to by their identifying *x* value.

$$Sr_{Sr}^x \ \rightarrow \ La_{Sr}^{\bullet} + \ e' \quad Eqn. \ 4.1$$
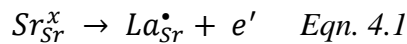
Table 4.1 List of LEST compositions synthesised

Identifier	Composition
x = 0.0	$La_{0.15}Sr_{0.775}TiO_3$
x = 0.025	$La_{0.125}Eu_{0.025}Sr_{0.775}TiO_3$
x = 0.05	$La_{0.10}Eu_{0.05}Sr_{0.775}TiO_3$
x = 0.075	$La_{0.075}Eu_{0.075}Sr_{0.775}TiO_3$
x = 0.10	$La_{0.05}Eu_{0.1}Sr_{0.775}TiO_3$
x = 0.125	$La_{0.025}Eu_{0.125}Sr_{0.775}TiO_3$
x = 0.15	$Eu_{0.15}Sr_{0.775}TiO_3$

Figure 4.1 shows the XRD analysis of the calcined powders. All of the synthesised compositions, except for x = 0.125 and 0.15, readily formed a pure cubic perovskite phase after calcining at 800 °C for 2 hr.
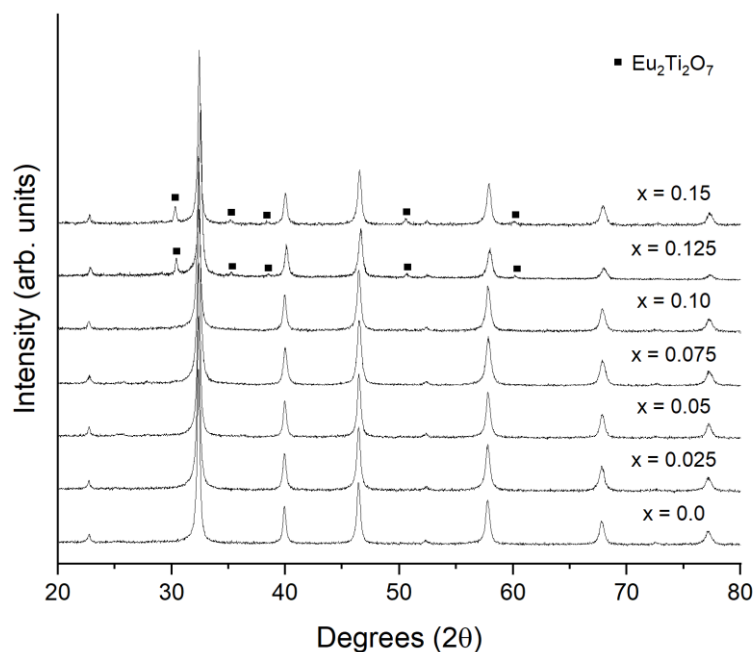
Figure 4.1 XRD of calcined powders from ionic liquid synthesis.

Figure 4.2 shows the lattice parameter of the calcined powders determined using Rietveld refinements from XRD analysis. For the sake of experimental efficiency, refinements of the composition x = 0.075 were not undertaken, as the trends were already becoming clear from the other compositions. Figure 4.2 shows a decrease in lattice parameter with increasing europium content for the first four compositions. Eu^{3+} is a smaller ion (ionic radii 1.12 Å CN9, CN in this structure is 12 but not available in the Shannon tables) than La^{3+} (ionic radii 1.216 Å CN9, 1.36 Å CN12) so this is in line with Vegard's Law.[11,12]
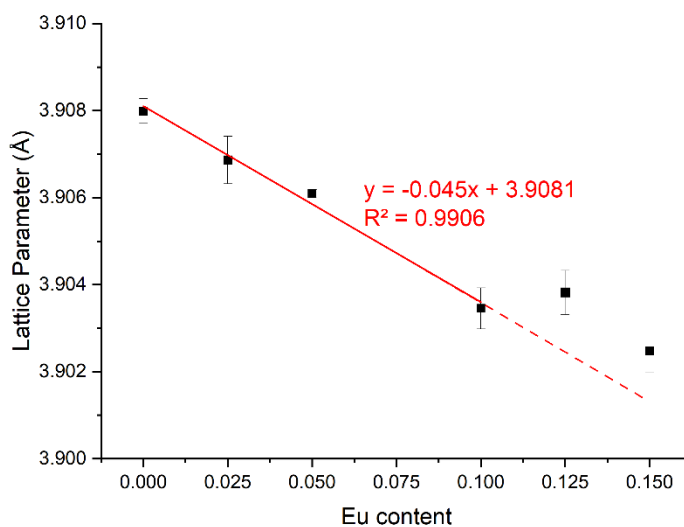
A trend line was inserted in Figure 4.2 which was calculated from the average lattice parameters of compositions x = 0 - 0.1, excluding x = 0.125 and 0.15 as these appeared to deviate from the trend set by the other four samples and contained a second pyrochlore phase. The R^2 value of the line was 0.99 - this gives an indication of the trend lines fit to the data, and in this case shows that the line fits the data reasonably well though does not fully express the variability of the data, in which case the R^2 would be 1.

4.3.1.1 Impurities in Eu Rich Compositions

The perovskite phases in compositions x = 0.125 and 0.15 showed larger lattice parameters than predicted by the trend shown for the rest of the samples and contained an additional pyrochlore phase ($Eu_2Ti_2O_7$), which is a common impurity found when synthesising titanates where large amounts of 3+ ions (such as La^{3+}) replace the Sr^{2+}.[8,13] The cause of this will be discussed in this section.

The tolerance factor is a representation of the stability of the cubic perovskite. $SrTiO_3$ is an ideal cubic perovskite and the tolerance factor is 1, indicating that there is not distortion in the octahedra because atoms fit well into their designated positions on the A and B site.

$$t = \frac{r_A + r_O}{\sqrt{2}(r_B + r_O)} \qquad \text{Eqn. 4.2}$$

The equation for the tolerance factor, *t*, is given in Equation 4.2 for a perovskite with formula ABO_3 where r is the ionic radii of the constituent elements.[14] The relevant ionic radii are given in Table 4.2 which were used to calculate the tolerance factors in Table 4.3 which are shown graphically in Figure 4.3. Adding La $SrTiO_3$ to form the x = 0.0 compositions reduced the tolerance factor to 0.9593. This composition still forms the cubic perovskite phase as shown in by XRD in Figure 4.1 so this amount of strain can be accommodated in the cubic perovskite.

Table 4.2 Ionic radii of elements in Dy doped BaTiO₃ and Eu doped SrTiO₃.[11]

Element	Ionic Radii / Å
Ti^{4+}	0.605
Sr^{2+}	1.44
Eu^{3+}	1.12
La^{3+}	1.36
O^{2-}	1.40

Table 4.3 Tolerance factors for each composition calculated using Equation 4.2
and ionic radii from Table 4.2.

Identifier	Tolerance Factor
x = 0.0	0.9593
x = 0.025	0.9572
x = 0.05	0.9550
x = 0.075	0.9529
x = 0.10	0.9508
x = 0.125	0.9487
x = 0.15	0.9466
$SrTiO_3$	1.0016

As more Eu is added the tolerance factor decreases further away from 1 until x = 0.15 which has a tolerance factor of 0.9466. This could be the reason why the Eu rich compositions x = 0.125 and 0.15 do not form a single phase cubic perovskite and instead a pyrochlore appears as a second phase to accommodate the large strain.
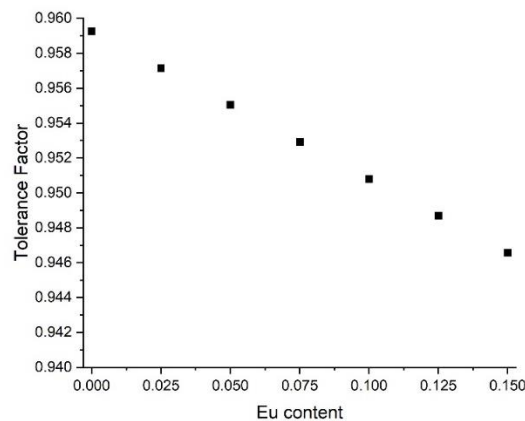
Figure 4.3 Tolerance factors from Table 4.2 calculated from equation 4.2 using
the ionic radii in Table 4.2.

According to the trend line in Figure 4.2, the lattice parameter of the calcined x = 0.15 matches that of something closer to x = 0.1251 (calculated using the slope and intercept given on the graph) leaving 0.0249 Eu to occupy the pyrochlore. This could be the solubility limit at that temperature, though is contradicted by the increased lattice parameter also seen in composition 6. If this was a solubility limit then then the lattice parameter would level off at the maximum saturation of Eu and increasing quantities of the perovskite would be seen in compositions x = 0.125 and 0.15. The data in Figure 4.2 could be seen in two ways.

First, the error bars of x = 0.10, 0.125 and 0.15 do overlap and so this could be a levelling off of the lattice parameter indicating of a solution limit of Eu in the LST somewhere in the

vicinity of x = 0.11. Alternatively, the compositions x = 0.125 and 0.15 could be viewed as showing a systematic upshift in the lattice parameters compared to the trend line calculated from the other samples. This could be due to the formation of a consistent level of pyrochlore, confirmed by the intensities in the XRD and Rietveld which calculate this to be between 0.08 and 0.26 %. Once again the the lattice parameter of x = 0.125 was used to calculate the Eu content (apparent x value) of the perovskite using the equation from the trend line. This gave a value of 0.0951 meaning that 0.0299 of Eu remained to occupy some other space, possibly pyrochlore. This is a very similar value to the Eu remaining to form the pyrochlore in x = 0.15 (0.0249) which seems to confirm the consistent upshift idea. The reason for this consistent level of pyrochlore formation is unknown, perhaps the solubility limit is around x = 0.11 and it is more thermodynamically stable to form more of the pyrochlore and create a lower strain perovskite (one were the tolerance factor is closer to 1).

4.3.1.2 Eu Occupancy Debate

Freeman *et al*. published work on rare earth doped $BaTiO_{3-\delta}$ for MLCCs in which they showed that mid-size rare earths such as Dy dope onto both the A-site and the B-site in $BaTiO_3$.[15] Eu is close to Dy in the periodic table, so their ionic radii are similar and comparisons can be made between that of Freeman *et al.* and this work. It is possible that Eu could be occupying the A and B sites in $SrTiO_3$ like in $BaTiO_3$. This comes down to the relative size of the dopant ion and the ions in the parent structure.

Table 4.4 shows the ionic radii of the elements in both these structures. In $BaTiO_3$ the ionic radii of Dy is much more evenly situated between the ionic radii of Ba and Ti and so is likely to be able to occupy both, though does not fit well into either site. Whereas, in $SrTiO_3$ the ionic radius of Eu is similar in size to the size of Sr, and so most likely to occupy the A-site. If the Eu did occupy both sites, then this would lead to self-compensation rather than A-site defect formation. Eu on the B-site would also expand the lattice parameter as it is much larger than Ti^{4+}. The lattice parameter in fact decreased as the Eu content increases for x = 0.0, 0.025, 0.05 and 0.1. The lattice parameter, however, does increase for x = 0.125 and 0.15 but the Eu is atleast in part accounted for by the presence of pyrcholore.

Table 4.4 Ionic Radii of atoms present in Dy doped BaTiO₃ and Eu doped SrTiO₃.

Element	Ionic Radii
Ba^{2+}	1.61
Dy^{3+}	1.083
Ti^{4+}	0.605
Sr^{2+}	1.44
Eu^{3+}	1.12

4.3.2 Sintering

Before sintering all powders were water filtered as described in the chapter 'Characterisation of LSTO' before sintering. This decision was taken to remove what impurities could be removed in order to reduce any influence this impurity may have on the sintering and focus on the composition itself. The pyrochlore and perovskites are not water soluble so would not be dissolved. The effect of the water filtration is shown and discussed in section 'Characterisation of Ionic Liquid Synthesised LST'.

After ionic liquid synthesis, powders were pressed into pellets and sintered in a reducing atmosphere to increase electrical conductivity, generated by oxygen loss, demonstrated for simplicity in SrTiO in Equation 4.3. The electrons from Equation 4.3 reduce the Ti^{4+} to Ti^{3+} according to Equation 4.4.

$$SrCO_3 + TiO_2 \rightarrow Sr_{Sr}^x + Ti_{Ti}^x + (3-\delta)O_O^x + \frac{\delta}{2} O_2(g) + \delta V_O^{\bullet\bullet} + 2\delta e' + CO_2(g) \quad Eqn.\ 4.3\ [16,17]$$

$$Ti^{4+} + e' \rightarrow Ti^{3+} \quad Eqn.\ 4.4$$
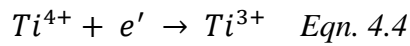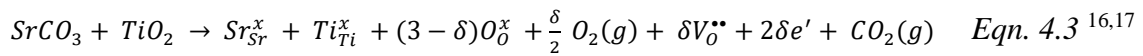
In other works, studying the reduction of rare earth doped strontium titantates several different reduction conditions have been used; Lu *et al.* sintered at 1500 °C for 6 h in 5% H_2-N_2, Kovalevsky *et al.* sintered at 1500 °C for 10 h in 10% H_2/N_2, Liu *et al.* sintered 1450 °C for 6 h in 5% H_2/Ar and Azough *et al.* used 1460 °C for 4 h in 5% H_2/Ar. [1,5,8,18]

In this study, 1325 °C for 8 h in 5% H_2/N_2 was used as this was the highest temperature available to sinter the required dimension of sample and the available hydrogen nitrogen mixed gas. Higher temperatures would likely result in a larger degree of reduction as oxygen loss is a thermally activated process however, for the purpose of observing the behaviour of this compositional series, importance was put on consistency in the sintering conditions used.[9,19] Figure 4.4 shows the XRD spectra of the reduce sintered compositional series.
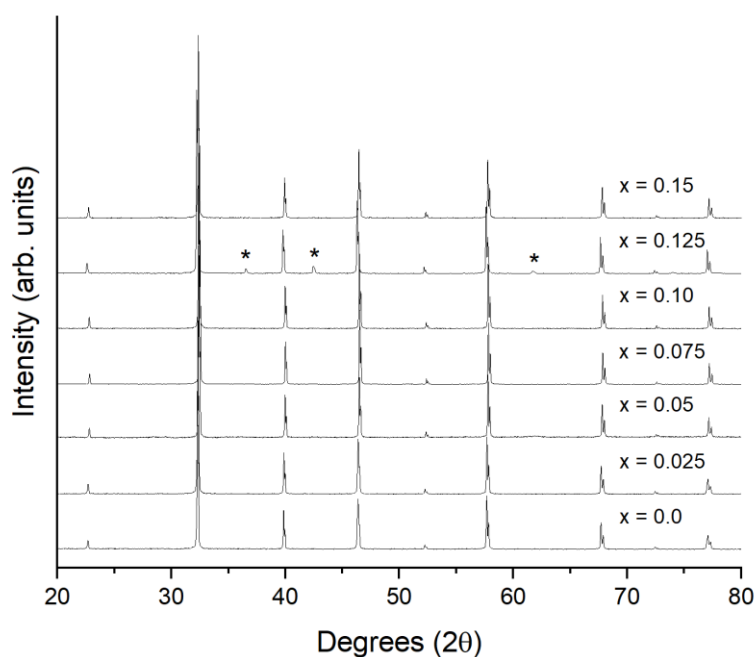
Figure 4.4 XRD of pellets after sintering at 1325 ºC for 8h in 5%H$_2$/95%N$_2$.

The x = 0.15 composition was converted to a single phase cubic perovskite after sintering at 1325 °C but x = 0.125 was not. This indicates that composition x = 0.125 may be above the solute limit up to 1325 °C. In order to form a single phase x = 0.15 may convert Eu^{3+} to Eu^{2+}, in which case A-site vacancies do not form. A large amount of energy would be required to reduce the Eu species which could be provided during the 1325 °C sintering stage. Future work could prove or disprove this with XPS.

After sintering in a reducing atmosphere all XRD peaks were noticeably narrower, indicating an increase in grain size (Figure 4.4). This is also confirmed by SEM images in Figure 4.5. The lattice parameters of each composition are shown in Figure 4.6 and generally increased after sintering, coinciding with the reduction of Ti^{4+} (0.745 Å CN6) to the larger Ti^{3+} species (0.81 Å CN6).[11] This increase did not appear to be systematic like the effect of increasing Eu content, indicating that there was inconsistency in the conversion of Ti^{4+} to Ti^{3+}.
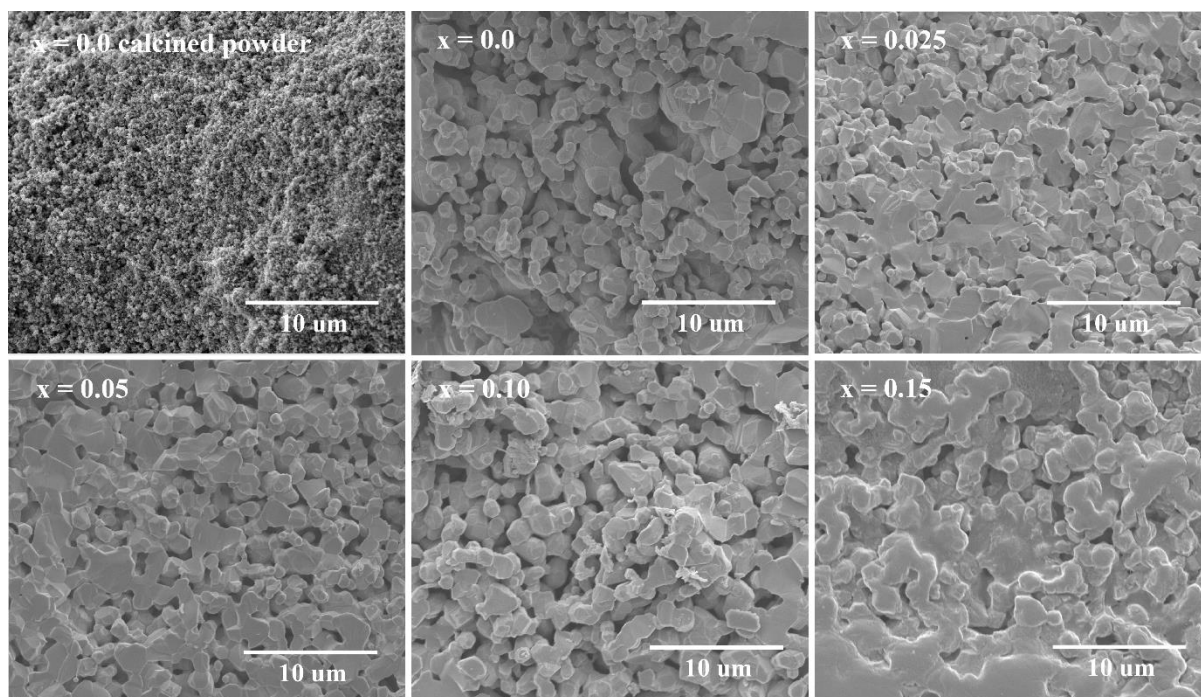
Figure 4.5 SEM of compositions x = 0.0, 0.025, 0.05, 0.1 and 0.15 after reduce sintering at 1325 ºc for 8 h compared to an SEM of x = 0.0 calcined powder.
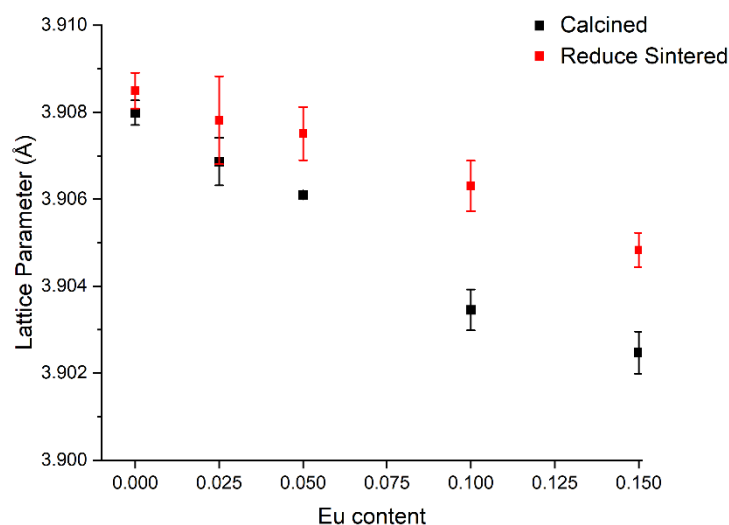
Figure 4.6 Lattice parameters determined using reitveld refinement on the calcined powders and reduce sintered pellets.

A widening in the gap between calcined and reduced lattice parameters emerged for the Eu rich samples, indicating that the compositions may have different propensity to become reduced. In work published by Akin *et al.* they proposed that oxygen loss was aided by A-site vacancies which allowed space for the oxygen to move and escape from the lattice.[9] In the case of this work the A-site vacancy level should remain consistent therefore, it is unlikely that more A-site vacancies are causing this increase in oxygen loss. The exception for this would be the case of x = 0.15 where it was postulated that the Eu species may be in the 2+ oxidation state and therefore not induce any A-site vacancies. This would go against the

theory proposed by Akin *et al.* and wouldn't explain the same effect seen in the x = 0.125 composition.

It was also shown by Yang *et al.* that inhomogeneity in the sodium content of bismuth titanate led to areas of large grain size where sodium was rich and much smaller grains of sodium low sodium content, indicating that the acceptor dopant, sodium, affected the rate of diffusion.[20] Looking at SEM images of the compositions in Figure 4.4, there does not seem to be an obvious increase in grain size with Eu content, which would be seen if the Eu content was having a large effect on the diffusion rate within the material. So the idea of increased diffusion caused by Eu can be ruled out.

To understand how oxygen loss can be encouraged, consider the crystal structure shown in Figure 4.7. Within the cubic perovskite there is mixed bonding, the titanium and oxygen form a covalently bonded octahedral with Ti in the centre coordinated to A-site ions with ionic bonds. The oxygen atoms are coordinated by four ionic bonds to the A-site atoms (Sr^{2+}, Eu^{3+} or La^{3+}) and two covalent bonds with B site atoms (Ti^{4+}). Changing the A-site ion changes the local bonding environment of the oxygen atoms.
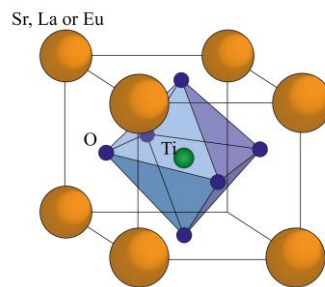
Figure 4.7 Schematic of (Sr,Eu,La)TiO₃ cubic perovskite.

Strong ionic bonds are formed between species which have a large difference in electronegativity. If a comparatively more electronegative ion, such as Eu^{3+} compared to La^{3+}, occupies the A-site, this would reduce the strength of the ionic bond with oxygen. Assuming this has no effect on the Ti-O bond strength, then this could mean that the oxygen can more easily break its bonds to A-site ions and slip out of the structure. Therefore, increasing Eu content could make reduction easier.

There are certainly complex mechanisms occurring in this compositional series which intensify as Eu content increases. Speculations have been made about the compensation and site occupancy of the materials though none can be confirmed without other techniques. The thermal and electrical properties may give weight to some the postulated theories.

4.3.3 Thermoelectric Properties

4.3.3.1 Thermal Conductivity

Thermal conductivity measurements were made using the Laser Flash technique to determine the diffusivity, D, combined with the density, ρ, using the Archimedes method and specific

heat capacity, c_p, derived suing the Neumann-Kopp method. These were combine according to Equation 4.5.

$$\kappa = D.c_p.\rho \quad Eqn.\ 4.5$$

Demonstrated in Figure 4.8 the thermal conductivity of the parent phase, $La_{0.15}Sr_{0.775}TiO_3$, showed the same general trend of decreasing thermal conductivity with increasing temperature as was shown by Lu et al., though the gradient was less severe.[1] The thermal conductivity decreases as the level of lattice vibrations increase which cause scattering of phonons. The less severe gradient could be due to the method in which the specific heat capacity was determined: because Lu et al. used the laser flash reference comparison method rather than the Neumann-Kopp model used in this work.[1]
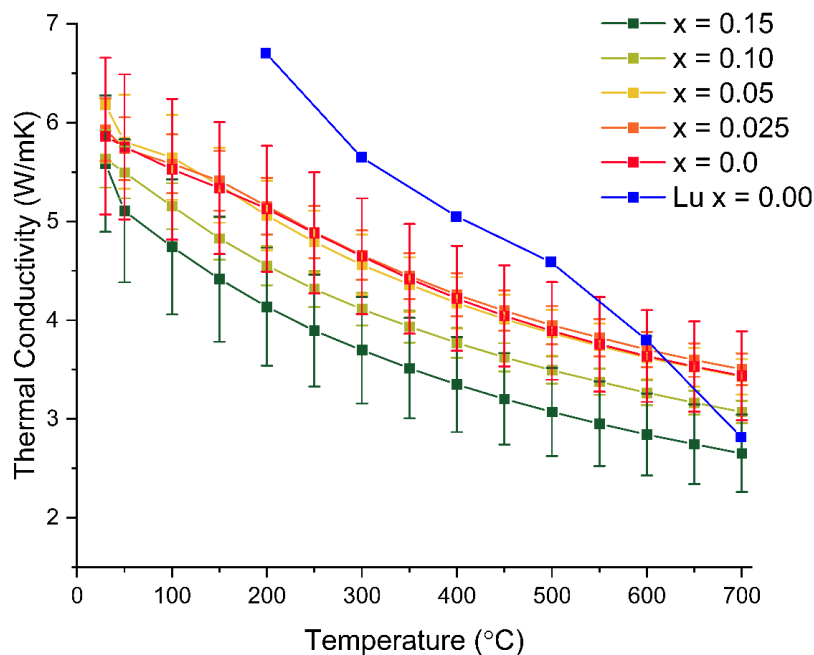
Figure 4.8 Thermal conductivity vs. temperature of reduced sintered pellets from this work and that of $La_{0.15}Sr_{0.775}TiO_{3-\delta}$ from Lu et al. (Lu x =0.00).[1]

Over all of the compositions made, x = 0.0 showed the largest thermal conductivity between 25 – 700 ºC. Small additions of Eu, up to x= 0.05, did little to affect the thermal conductivity, as can be seen by the clustering of the x = 0.0 to 0.05 samples. When the Eu content reached 0.10, the thermal conductivity reduced. Figure 4.9 shows the thermal conductivity of each composition at 700 °C which makes this trend clearer - 700ºC was chosen as it is the

temperature Lu *et al.* quoted their values and found the highest ZT and within the expected operating temperature range for this material.[1]
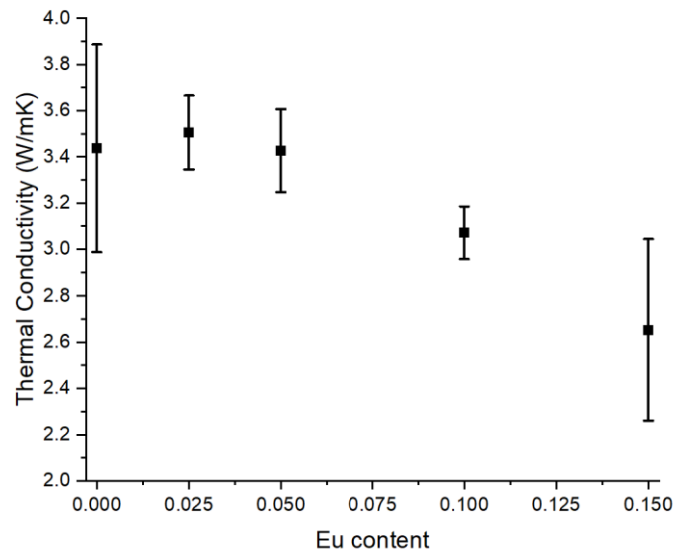
Figure 4.9 Thermal conductivity of x = 0.0, 0.025, 0.05, 0.1 and 0.15 at 700 ºC.

It is clear from Figure 4.9 that there is little statistical difference between the thermal conductivity of compositions x = 0.0, 0.025 and 0.05 as their error bars largely overlap. Large error bars are not an unexpected feature of this data as Boston *et al.* showed that thermal conductivity contains a significant amount of error compounded from diffusivity and density measurements. In their study the diffusivity alone showed a 17 % scatter between laboratories.[21]

Despite the large errors, it can be seen that the addition of Eu did reduced the thermal conductivity when present at $\geq$ 10 at. %. The thermal conductivity was lowest when the Eu had fully replaced the La. Importantly, the thermal conductivity was not minimised when all three elements La, Sr and Eu were present, which was what was postulated to induce a low thermal conductivity in the first instance. To understand this, consider the relative ionic sizes and atomic weights given in Table 4.5.

Table 4.5 Ionic mass and radii of A-site atoms in (La,Eu,Sr)TiO₃.[11]

Element	Ionic Radii	Atomic Mass
Sr	1.31	87.62
La	1.216	138.91
Eu	1.12	151.96

From this information it can be seen that Eu has the greatest size and mass difference between itself and the Sr, so any effect that the lanthanum creates in terms of atomic mass/ size fluctuations will be accentuated for Eu, therefore having a greater effect at reducing the

thermal conductivity than the La - so in fact is more effective at reducing the thermal conductivity than La.

The thermal conductivity is an important contributor to the ZT but the material must also be an excellent conductor of electricity and possess a high Seebeck coefficient. This can be quantified by the Power Factor. Adding Eu reduced the thermal conductivity but what are the effects on the Power Factor of the material. These properties are explored in the next section.

4.3.3.2 Electronic Properties

Figure 4.10 shows the electrical conductivity (σ) and the Seebeck coefficient (S) which combine to make the power factor according to Equation 4.6.

$$\text{Power factor} = S^2\sigma \qquad \textit{Eqn. 4.6}$$
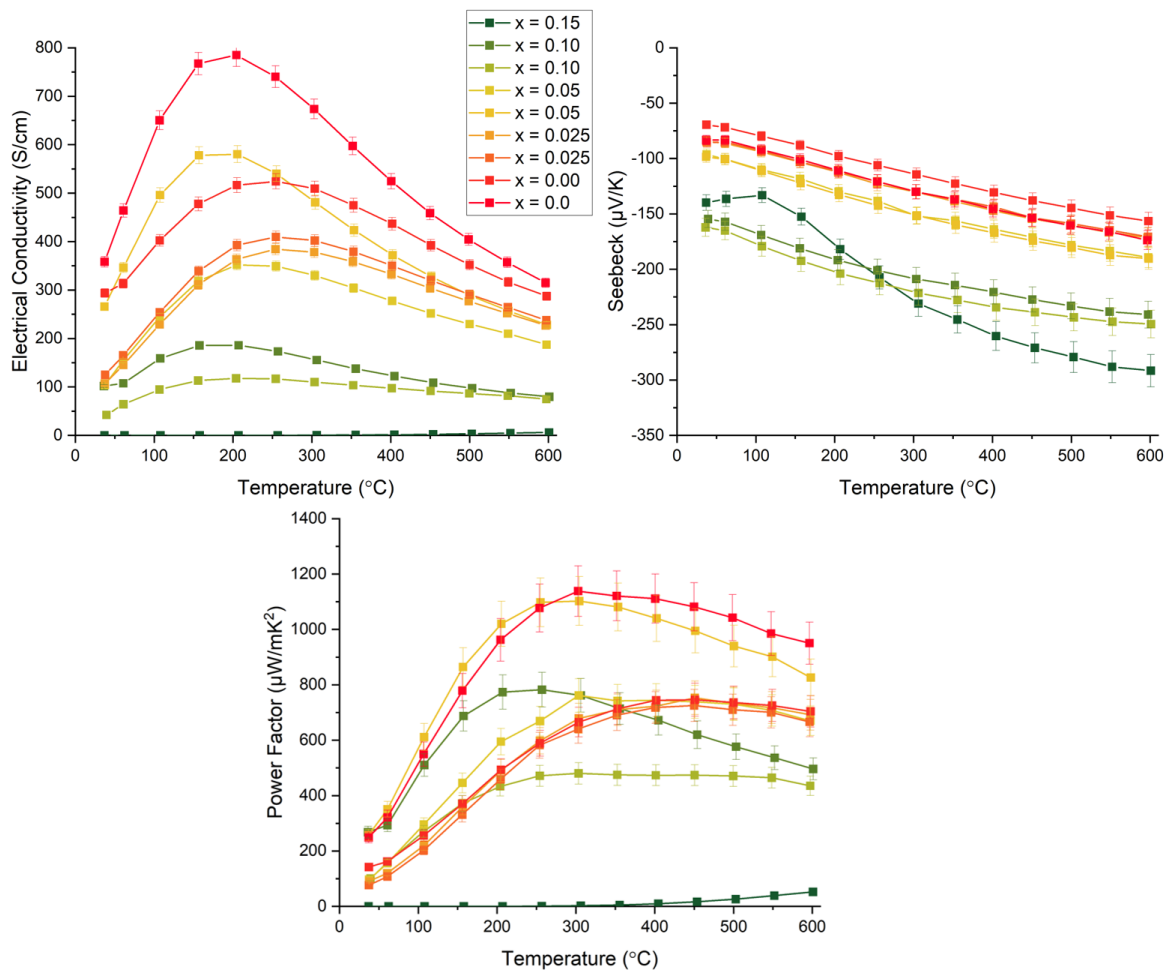
Figure 4.10 Electric conductivity, Seebeck coefficient and power factor of individual samples of x = 0 - 0.15. Individual sample data is shown to demonstrate the large variations between samples. Error bars shown are those of the instrument.

In these graphs the data from individual samples is shown as there was a large variation in some of the measured electrical conductivity of samples with the same composition, and so an average would not be an accurate representation of this data. This effect was particularly prominent for samples of x = 0.0 and x = 0.05. Ideally a third measurement would be taken to determine an outlier but this was not possible due to time limitations. Because of this, for these two compositions only, one of the samples whose lattice parameter most closely matched the average lattice parameter of the reduced composition, shown in Figure 4.6, was used as a representative measurement. The other compositions electrical conductivities were averaged. This data is shown in Figure 4.11. Figure 4.12 shows which data for x = 0.0 and 0.05 was not selected (blue stars) and which sample was selected (red triangle).
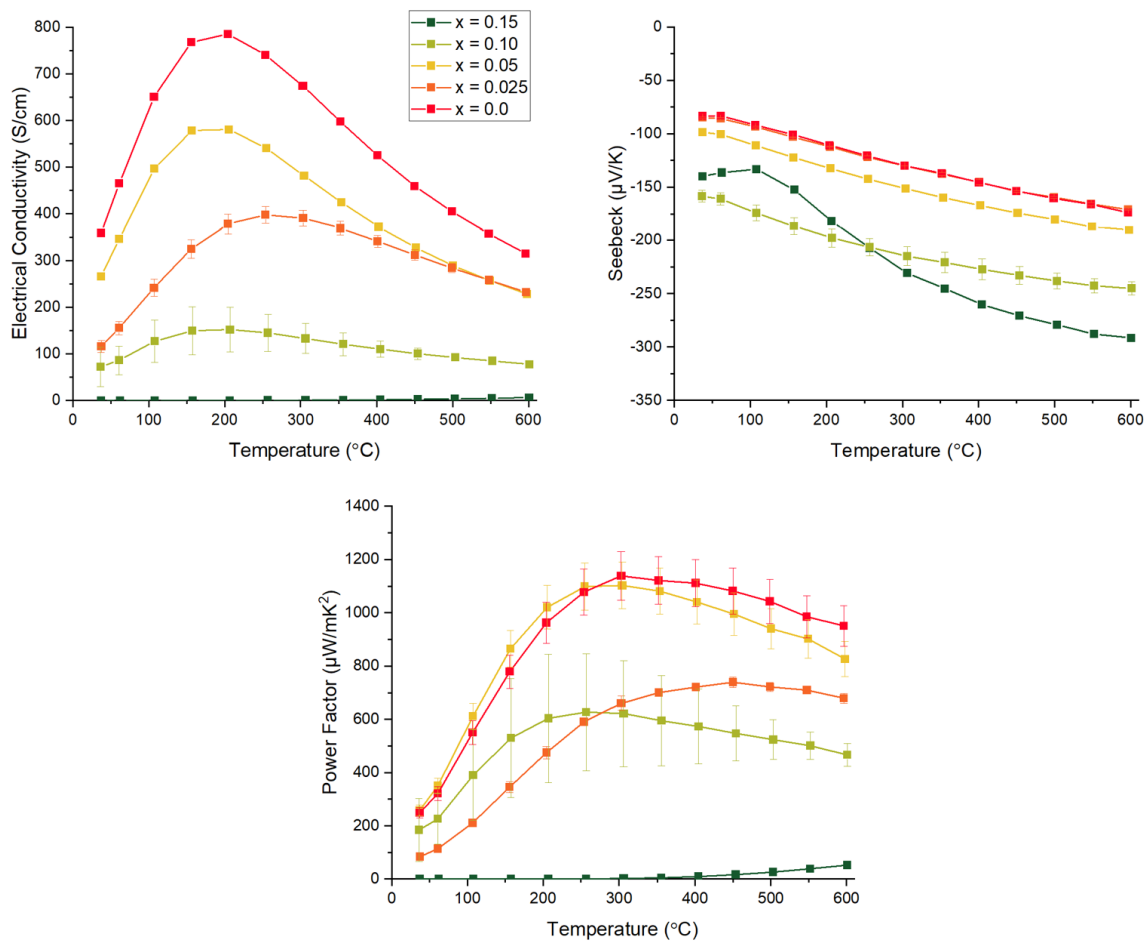
Figure 4.11 Electrical conductivity, Seebeck coefficient and power factor of representative sample or averaged values.
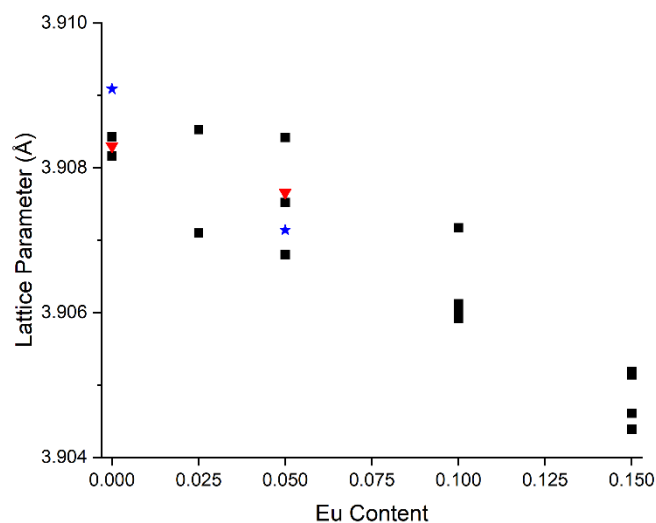
Figure 4.12 Lattice parameters measured for all sintered compositions. For x = 0.0 and 0.025 the blue stars are the lattice parameters for the electrical data disregarded and the red triangles are the carried forward data in Figure 4.11.

4.3.3.2.1 General Trend in Electrical Conductivity as a Function of Temperature

In general, the electrical conductivities across the series showed an initial increasing from room temperature to a point around 200 ℃, before reducing with temperature up to 600 ℃. The largest electrical conductivity was shown in x = 0.0, which peaked at 800 S/cm at 200 ℃. This was much lower than the maximum value observed by Lu *et al.* who reported an electrical conductivity of ~ 2500 S/cm at 200 ℃ for $La_{0.15}Sr_{0.775}TiO_{3-\delta}$.[1] Muta *et al.* also reported a much larger maximum value of 1420 S/cm at 200 ℃ for a similar composition, $Sr_{0.9}La_{0.1}TiO_{3-\delta}$.[10]

In the case of Lu *et al.,* data below 200 ℃ was not reported so it is not possible to see the trend below 200 ℃. In the work of Muta *et al.* the electrical conductivity below 200 ℃ was reported and, unlike in this work, the electrical conductivity decreased from a maximum at 25 ℃ as the temperature increased up to 700 ℃. [10] This data did not show the same rise and fall in the electrical conductivity as is shown in the ionic liquid synthesised compositions in this work. At higher temperatures (> 400 ℃) the electrical conductivity of ionic liquid

synthesised LST became more in line with the work of Muta *et al., as* shown in Figure 4.13, though still remains lower than that reported by Lu *et al.* [1,10]
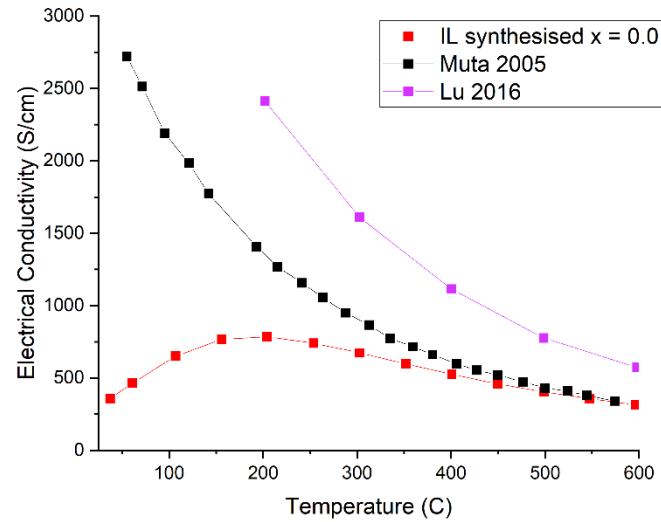
Figure 4.13 Comparing the electrical conductivity of x = 0.0 in this work with that published by Muta et al. for $Sr_{0.9}La_{0.1}TiO_{3-\delta}$ and Lu et al. for $La_{0.15}Sr_{0.775}TiO_{3-\delta}$.

This data looks very similar to that modelled by Cao *et al.* of oxygen deficient strontium titanate grains with resistive grain boundaries, Figure 4.14.[22] Cao *et al.* modelled five cases of STO with different levels of band offset (ΔE_0) between grain and grain boundaries, which correspond to a potential barrier at grain boundaries caused by a lesser concentration of oxygen vacancies at grain boundaries. In this work the electrical conductivity of the ionic liquid synthesised LST matches most closely the trend of the largest band offset of 80 meV. This suggests that the ionic liquid synthesised material has highly resistive grain boundaries which is reducing the electrical conductivity at low temperatures.
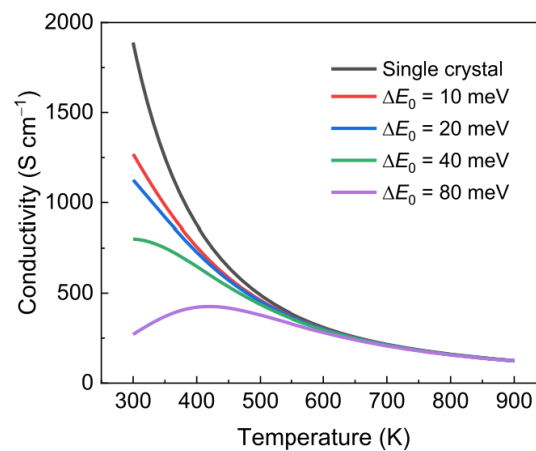
Figure 4.14 Modelled electrical conductivity temperature dependence of $SrTiO_3$ using a two phase model (grain and grain boundary) with different band offset values (ΔE_0).[22]
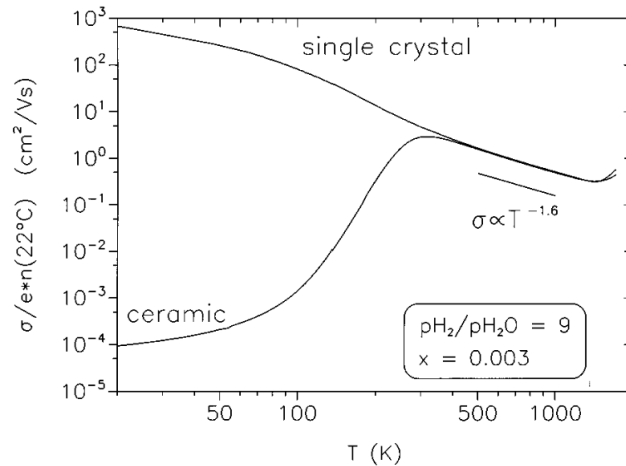
Figure 4.15 Electrical conductivity behaviour with temperature for single crystal and polycrystalline La$_{0.003}$Sr$_{0.997}$TiO$_{3-\delta}$ normalised for charge carrier density, n, and elementary charge, e.[19]

This behaviour in the electrical conductivity as a function of temperature was also confirmed by Moos *et al.* who found for a polycrystalline Sr$_{0.997}$La$_{0.003}$TiO$_3$ the electrical conductivity below 127 °C increased in temperature, peaked, then began to reduce with temperature up to 727 °C. On the other hand, the electrical conductivity of a single crystal of the same composition with a constant number of charge carrier was much higher at low temperatures and consistently decreased with temperature. They stated that this was due to acceptor states at grain boundaries which 'trap' conduction electrons and reduce the electrical conductivity of polycrystalline material at low temperatures.[19]

This effect likely explains the electrical conductivity of the ionic liquid synthesised LST, indicating that grain boundaries are highly resistive and reduce the electrical conductivity. Two distinctly resistive regions, bulk and grain boundary, would likely be detectable using impedance measurements, this was not performed in this work but would be an interesting study for future work. This effect was not observed in the data by Muta *et al.* and Lu *et al.* likely because the grain boundaries were not significantly resistive in these materials and so show more similar trends to the single crystals.

The presence of resistive grain boundaries in ionic liquid synthesised LST was likely due to impurities shown in the section 'Characterising ionic Liquid Synthesised LST'- K, Cl, Na, OH which likely reside in grain boundaries. It is difficult to identify how these elements come together within the grain boundaries but what is clear is that they are having an effect on the electrical conductivity. The structure of the grain boundary could be further investigated in future work using high resolution TEM which would show the level of crystallinity and dispersion of elements at and near to grain boundaries.

In some cases, grain boundaries can cause an energy filtering effect which prevent low energy electrons from taking part in conduction, enhancing the Seebeck coefficient.[23,24] This does not seem to be the case in this work as the Seebeck co-efficient remains comparable to that reported by Lu *et al.* over the entire temperature range.[1] This is likely because the grain

size is too large, filtering effects are said to become most apparent in grain sizes below 50 nm.[23]

4.3.3.2.2 Electrical Conductivity and Europium Content

With the addition of europium to the bulk composition, the electrical conductivities decreased further. The lowest electrical conductivity was observed in the sample with most europium, x = 0.15. Several other samples of the x = 0.15 composition where in fact too resistive to measure on the Seebeck Analyser and so are not plotted in Figure 4.10. According to the lattice parameter shown in Figure 4.6, the x = 0.15 composition should have the largest degree of Ti^{4+} to Ti^{3+} conversion which produces the conduction electrons. This would suggest that the electrical conductivity would be higher than the other compositions, though in fact the opposite effect is observed. This could be explained by a large degree of electron scattering by Eu^{3+} as this is a heavier ion than La^{3+} and Sr^{2+} (see Table 4.5 for exact values), which also lead to the low thermal conductivity observed in Figures 4.8 and 4.9 for x = 0.15.

Between the x values of 0.0 and 0.15 the electrical conductivity maximum gradually decreases, with the exception of 0.05 where a higher electrical conductivity was observed than the x = 0.025 composition - though x = 0.05 and 0.025 become almost indistinguishable at 600 ºC (Figure 4.10). Figure 4.16 shows the trend of electrical conductivity and Seebeck coefficient with Eu content at 600 ºC for all samples measured on the left and the selected data presented in Figure 4.10 on the right. There is a systematic decrease in the value of Seebeck coefficient (becoming more negative) with increasing Eu content coupled with a decrease in electrical conductivity, with the exception of x = 0.05 in the right hand side graph. As already stated this sample was chosen as a representative sample because the lattice parameter was closest to the average value but was not repeated. In this sample there was a relatively large electrical conductivity, which broke the trend of the series and was not coupled with a reduction in absolute Seebeck coefficient. This could be an outlying result, or a decoupling of the electrical conductivity and the Seebeck coefficient. This effect was not observed in the other sample of the same composition, so was most likely a small anomaly.
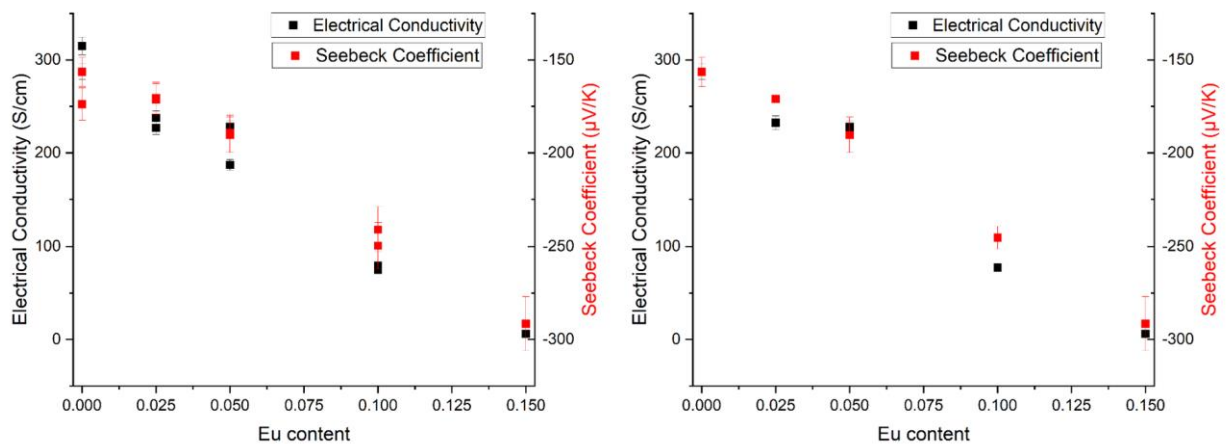
The highest power factor found was 1138 μW/mK^2 for x = 0.0 at 300 ºC closely followed by 1103 μW/mK^2 for x = 0.05 at 300 ºC though the x = 0.05 result may be an anomaly. These values were still not competitive with other rare earth doped STO such as $Sr_{0.9}Nd_{0.1}TiO_{3\pm\delta}$ whose power factor was 1.55 W/mK^2- three orders of magnitude higher than found in this work.[8] This was due to the highly resistive grain boundaries already discussed.

The overall figure of merit takes the power factor and divides this by the thermal conductivity and so these results need to be combined with the previously shown thermal conductivity data to assess their overall efficiency as thermoelectric materials.

4.3.3 Thermoelectric Figure of Merit

Figure 4.17 shows the figure of merit, ZT, for each composition calculated using the electronic data, combined with the average thermal conductivity of each composition using Equation 4.8. In this equation *S* is the Seebeck coefficient (V/K), σ is the electrical conductivity (S/m), *T* is the absolute temperature (K) and κ is the thermal conductivity (W/mK).

$$ZT = \frac{S^2 \sigma T}{\kappa} \qquad Eqn.\ 4.8$$
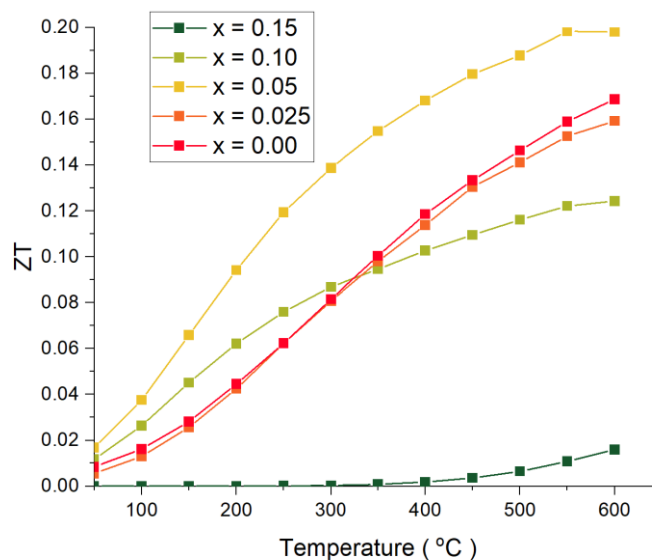
Figure 4.17 Figure of merit, ZT, for compositions x = 0.0, 0.025, 0.05, 0.1, 0.15 from 50-600 ºC.

The ZT increased with temperature due to the T component of Equation 4.8. Figure 4.18 shows the ZT values at the maximum determined temperature: 600 ºC. The Seebeck coefficient in the ZT equation is squared and so this can have a great effect on the overall ZT.

Due to the increase in the absolute value of the Seebeck coefficient in x = 0.05, combined with an equally low thermal conductivity compared to x = 0.0, the composition x = 0.05 showed the largest ZT despite having a slightly lower electrical conductivity than x = 0.0. This is a perfect illustration of the trade-off required to achieve a high ZT. This result comes with a large caveat that the electronic data from x = 0.05 was based on one measured value that did not correspond to the other measured x = 0.05 sample. For comparison the ZT calculated with the other electronic data measurement is shown in Figure 4.18 by a red star. This data point falls more in line with the general trend which would suggest it is the most accurate though this should be confirmed with further measurements.
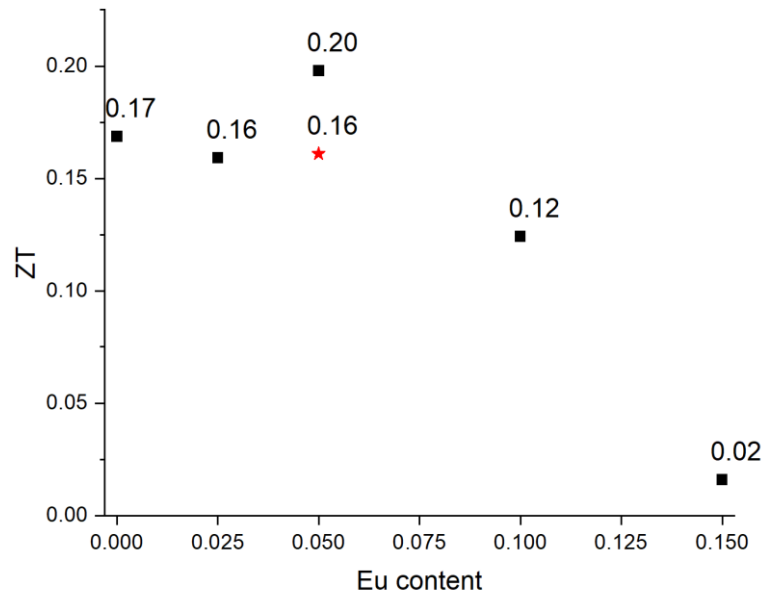
Figure 4.18 ZT of each composition at 600 ºC.

In all the samples the ZT does not reach the maximum value reported by Lu *et al.,* 0.41 at 700 ºC. Despite the data only being measured up to 600 ºC it appeared to be forming a plateau, indicating that the highest value would not reach 0.41 at 700 ºC. These results were on the other hand, comparable to that found by Muta *et al.* and Kovalevsky *et al.* for La doped STO, shown in Table 4.6.

Table 4.6 Published data of La doped STO and this projects data.

Composition	ZT	Temp. / ºC	Electrical conductivity / S/cm	Thermal Conductivity / $Wm^{-1}K^{-1}$	Seebeck coefficient / μVK^{-1}	Source
$Sr_{0.775}La_{0.15}TiO_{3-\delta}$	0.41	700	416	2.7	-163	Lu, 2016[1]
$Sr_{0.5}La_{0.33}TiO_{3-\delta}$	0.27	797	200	3.5	-180	Azough, 2017[5]
$Sr_{0.9}La_{0.1}TiO_{3-\delta}$	0.20	570	350	4.7	-180	Muta, 2005[10]
$Sr_{0.9}La_{0.1}TiO_{3\pm\delta}$	0.19	800	102	3.5	-246	Kovalevsky, 2014[8]

$Sr_{0.775}La_{0.15}TiO_{3-\delta}$	0.17	600	287	3.4	-157	This work
$Sr_{0.775}La_{0.1}Eu_{0.05}TiO_{3-\delta}$	0.20	600	228	3.4	-190	This work
$Sr_{0.775}Eu_{0.15}TiO_{3-\delta}$	0.02	600	6	2.8	-291	This work

4.4 Conclusion

Ionic liquid synthesised LST showed lower electrical conductivity, particularly at low temperatures, than previously published solid state synthesised LST. This is thought to be due to impurities detected in the chapter 'Charactering IL synthesised LST' which remain at the grain boundaries increasing the resistivity.

Overall the issues caused by the resistive grain boundaries in ionic liquid synthesised LST and LEST should not cause a significant issue for this material, as thermoelectric oxides are designed to operate at higher temperatures (~500- 700 ºC). One of their key advantages is thermal stability and the ZT is maximised at high temperatures due to the thermal conductivity which decreased as temperature is increased. At these temperatures the effect of the resistive grain boundaries is no longer apparent in the electrical conductivity measurements and therefore, does not impact maximum ZT. The electrical data collected showed comparable values to previously reported STO based materials without the resistive grain boundaries by ~ 400 ºC by Muta *et al.* but not so high as that reported by Lu *et al.*(whose data is yet to be shown to be repeatable). [1,10]

In 'Characterising IL synthesised LST' impurities were shown to be less abundant in samples made with a more expensive ionic liquid, where further purification steps are undertaken by manufacturers, so the grain boundary resistivity could be reduced by making the samples with the more expensive ionic liquid. However, if the thermoelectric material is to be used near to 600 ºC, then the resistivity of these grain boundaries is overcome by that point, making the increased investment in a purer IL redundant.

The addition of europium reduced the lattice parameter in calcined and reduced materials. Adding Eu appeared to reduce the thermal conductivity only when x exceeded a value of 0.05. This also led to reduction of electrical conductivity and an increase in the absolute value of the Seebeck coefficient. These effects are believed to be caused by increased scattering due to the large mass of Eu compared to Sr and La.

An improvement in the ZT was shown for x = 0.05 due to an enhanced Seebeck coefficient. Conclusions are made with the caveat that this is based on one sample which was not repeated in this work and therefore requires confirmation.

4.5 Future Work

Future work should look to confirm the properties of samples in the range of x = 0 and 0.075; this region seems to show the most potential in terms of improving the ZT of the *n*-type thermoelectric material. At least three electronic property measurements should be performed

to confirm the inherent properties of the composition, which was not possible in this work due to time and equipment limitations. A greater study could be conducted with smaller increments of Eu additions in this smaller window to look for a potential ZT maximum.

The specific heat capacity needs to be confirmed using differential scanning calorimetry for each composition as the values here have been calculated using the Neumann-Kopp model. This would be expected to make little difference to the overall ZT but the data must be gathered to confirm this.

4.5 References

1   Z. Lu, H. Zhang, W. Lei, D. C. Sinclair and I. M. Reaney, *Chem. Mater.*, 2016, **28**, 925–935.

2   C. Gayner and K. K. Kar, *Prog. Mater. Sci.*, 2016, **83**, 330–382.

3   H. Muta, K. Kurosaki and S. Yamanaka, *J. Alloys Compd.*, 2003, **350**, 292–295.

4   N. S. Krasutskaya, A. I. Klyndyuk, L. E. Evseeva and S. A. Tanaeva, *Inorg. Mater.*, 2016, **52**, 393–399.

5   F. Azough, S. S. Jackson, D. Ekren, R. Freer, M. Molinari, S. R. Yeandel, P. M. Panchmatia, S. C. Parker, D. H. Maldonado, D. M. Kepaptsoglou and Q. M. Ramasse, *ACS Appl. Mater. Interfaces*, 2017, **9**, 41988–42000.

6   B. H. F. Kay and P. C. Bailey, *Acta Crystallogr.*, 1957, **10**, 219–226.

7   A. C. Iyasara, W. L. Schmidt, R. Boston, D. C. Sinclair and I. M. Reaney, in *Materials Today: Proceedings*, Elsevier Ltd, 2017, vol. 4, pp. 12360–12367.

8   A. V Kovalevsky, A. A. Yaremchenko, S. Populoh, P. Thiel, D. P. Fagg, A. Weidenkaff and J. R. Frade, *Phys. Chem. Chem. Phys.*, 2014, **16**, 26946–26954.

9   I. Akin, M. Li, Z. Lu and D. C. Sinclair, *RSC Adv.*, 2014, **4**, 32549–32554.

10   H. Muta, A. Ieda, K. Kurosaki and S. Yamanaka, *Mater. Trans.*, 2005, **46**, 1466–1469.

11   R. D. Shannon, *Acta Crystallogr. Sect. A*, 1976, **32**, 751–767.

12   A. R. Denton and N. W. Ashcroft, *Phys. Rev. A*, 1991, **43**, 3161–3164.

13   D. Burnat, A. Heel, L. Holzer, D. Kata, J. Lis and T. Graule, *J. Power Sources*, 2012, **201**, 26–36.

14   R. Ubic, K. Tolman, K. Chan, N. Lundy, S. Letourneau and W. M. Kriven, *J. Alloys Compd.*, 2013, **575**, 239–245.

15   R. E. Ward, C. L. Freeman, J. S. Dean, D. C. Sinclair, J. H. Harding, R. E. Ward, C. L. Freeman, J. S. Dean, D. C. Sinclair and H. Harding, *Adv. Funct. Mater.*, 2020, **30**, 1905077.

16   S. Hui and A. Petric, *J. Electrochem. Soc.*, 2002, **149**, J1–J10.

17   H. Yamada and G. R. Miller, *J. Solid State Chem.*, 1973, **6**, 169–177.

18   J. Liu, C. L. Wang, ; Y Li, Y. Li, W. B. Su, Y. H. Zhu, J. C. Li and L. M. Mei, $-\delta$ *J. Appl. Phys.*, 2013, **114**, 223714.

19   R. Moos and K. H. Härdtl, *J. Appl. Phys.*, 1996, **80**, 393–400.

20   F. Yang, J. S. Dean, Q. Hu, P. Wu, E. Pradal-Velázquez, L. Li and D. C. Sinclair, *J. Mater. Chem. A*, 2020, **8**, 25120–25130.

21   R. Boston, W. L. Schmidt, G. D. Lewin, A. C. Iyasara, Z. Lu, H. Zhang, D. C. Sinclair and I. M. Reaney, *Chem. Mater.*, 2017, **29**, 265–280.

22   J. Cao, D. Ekren, Y. Peng, F. Azough, I. A. Kinloch and R. Freer, *ACS Appl. Mater. Interfaces*, 2021, **13**, 11879–11890.

23   R. Kim and M. S. Lundstrom, *J. Appl. Phys.*, 2012, **111**, 024508.

24   M. Thesberg, H. Kosina and N. Neophytou, *J. Appl. Phys.*, 2016, **120**, 234302.

5.0 Cold Sintering

5.1 Aims and Objective

This work shows the foundations of the novel method development which aims to provide a low temperature sintering solution to incongruently dissolving complex stoichiometry materials such as La doped, A site deficient $SrTiO_3$. The objective of this work was to develop a technique in which the small grain size, created by the ionic liquid synthesis method, could be retained in a dense ceramic after sintering. The advantage of small grain size being that a large density of grain boundaries should reduce the thermal conductivity and improve the ZT of the thermoelectric material.[1,2] A high density is required to retain high electrical conductivity as pores filled with air are poor electrical conductors. As this is a completely novel method the microstructure of the bulk would be examined to determine the exact mechanisms of densification, if this could be achieved.

5.2 Introduction

The microstructure of dense ceramics has been shown in section 1.5.2 'Applying Grain Boundary Engineering', to have a substantial effect on the measured bulk properties, such as thermal conductivity. The control of microstructure in sintered ceramics is therefore a critical step in fabricating materials, and which until recently has been limited by the use of high (>1000 °C) temperatures for solid state sintering.[3] Sintering in this way relies on minimisation of the number of grain boundaries, necessarily resulting in grain growth; this is however at odds with the goal of creating nanostructured but dense ceramics. In 2016, sintering technologies took a significant step forward with the development of the cold sintering process.[4]

Cold sintering is an emergent technique which uses transient solvent phases to supply ions which can fill voids between grains. These ions are either dissolved from the bulk phase powder, or can be introduced in the solvent itself. The process requires a small amount of applied heat and pressure which aids grain compaction and deposition of ions through terrace ledge kink deposition. In some cases, the reduction in overall sintering temperature can be as much as 1000 °C, which means that cold sintering is providing a transformative route to sinter ceramic materials.[5]

While highly effective for soluble materials, the technique is incompatible for either sparingly or incongruently soluble materials such as $SrTiO_3$. Adapted routes using more complex physicochemical routes are therefore now highly sought-after, and are being investigated on a material-by-material basis. One notable example was reported by Tsuji *et al.* who sintered $BaTiO_3$ at 300 ℃ from a nanoparticles of the ceramic and a molten hydroxide flux consisting of NaOH and KOH. A second example is the Reactive Cold Sintering process where reactive intermediate phases (strontium chloride and titania nanopowder) filled the voids between $SrTiO_3$ powders which were then reacted to form the target phase in a secondary heating step.[6] A schematic of this process is shown in Figure 5.1.[6]
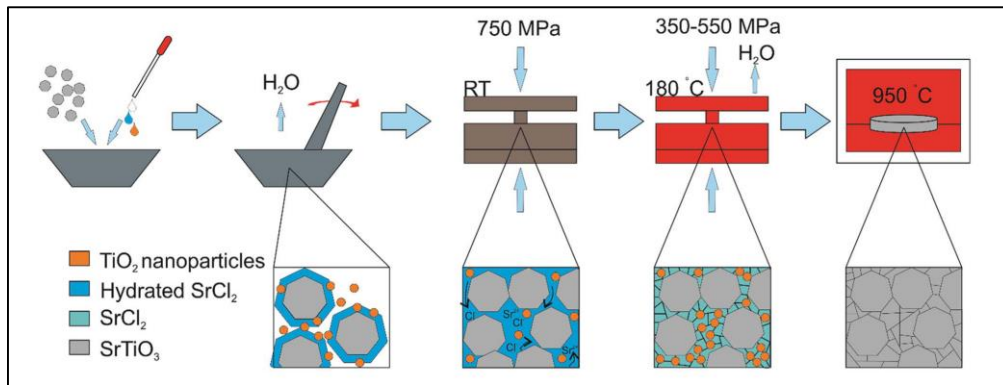
Figure 5.1 Reactive Cold Sintering Process by Boston et al.[6]

Reactive cold sintering of $SrTiO_3$ used an existing low temperature synthesis route to inspire the choice of infill phase, however the use of highly specific precursor materials e.g. chlorides is not always possible; as such a more general route was sought to create reactive in-fill phases which can be used in the reactive cold sintering process.[7] This inspired the novel cold sintering technique in which an intermediate of the ionic liquid synthesis method (demonstrated in Chapter 3) was used to fill voids between the final product of the ionic liquid synthesis method.

The reaction mechanism of the ionic liquid synthesis of $La_{0.15}Sr_{0.775}TiO_3$ was shown by Mottram et al. in which the perovskite forms from a largely amorphous intermediate mixture of precursor ions.[8] This provides an opportunity to create an amorphous infill which surrounds the crystalline matrix which can be transformed into a dense ceramics body upon annealing at ~600 ℃. Unlike the crystalline matrix, which is a brittle ceramic, an amorphous infill should be able to deform to fit around the matrix powder to create a dense body when pressure and temperature are applied. A schematic of how this process should work is shown in Figure 5.2. This chapter focusses on the development of this method to create a dense ceramic body at low temperatures (<1000 ℃). Though the larger goal would be to increase the electrical conductivity by reducing the materials oxygen content, this aspect was excluded from the beginning of the method development to simplify the process and focus on achieving a dense ceramic using this novel cold sintering technique.
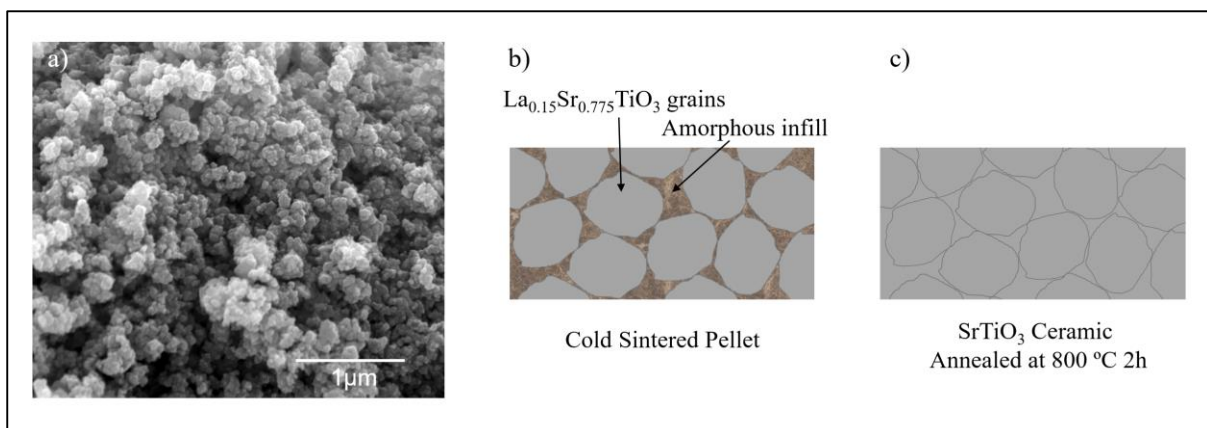
Figure 5.2 a) SEM micrograph of the fully calcined LSTO from the ionic liquid process, b) cold sintered LSTO powder (matrix) with amorphous powder from ionic liquid process (infill) c) infill transformed into crystalline LSTO by annealing at 800 ºC.

5.3 Results and Discussion

5.3.1 Creating the Infill

To create a dense ceramic body at low temperatures the infill needs to fill the gaps between grains and aid mass transport as much as possible. This is because the high temperatures which promote mass transport and grain growth used in the conventional solid state sintering process, are not available in the cold sintering process.

In this work the infill used was a partially calcined product of the ionic liquid synthesis. This was formed by firing the ionic liquid and precursor mix in air at a temperature below the point at which the cubic perovskite phase fully forms. The point at which the cubic perovskite forms in the ionic liquid synthesis route was previously identified from Simultaneous Differential Scanning Calorimetry and Thermal Gravimetric Analysis (SDT) and XRD undertaken by Mottram *et al.* The temperature difference vs. temperature graph produced by Mottram *et al.* was replicated in this study, Figure 5.3.[8] The peaks indicated by the black box in Figure 5.3 shows the transformation from intermediate phases into the cubic perovskite, which begins ~ 500 ºC and is complete by ~ 600 ºC, agreeing with the work by Mottram *et al.*[8]

The aim was to create an amorphous infill powder which would crystallise into LST upon annealing, like in the case of the Reactive Cold Sintering, therefore the infill had to be fired to below the onset of the LST transformation. To select the infill firing temperature, several points were chosen just below onset of the cubic perovskite formation peak (~500 ºC). A secondary reason for choosing firing temperatures just below the onset of the LST peak, was that the SDT showed a large degree of mass loss (~ 80%) occurred between room temperature and 300 ºC. If the infill was fired below 300 ºC, a large amount of mass loss would occur in the annealing stage, likely resulting in a low density pellet as most of the volume contraction was expected to occur during the cold sintering stage, therefore mass loss would decrease the density. To avoid this a lower limit of 300 ºC was considered to fire the infill. The yellow band in Figure 5.3 shows the selected firing window, and six infill samples were prepared by firing between these temperatures: 300, 350, 375, 400, 420 and 450 ºC.
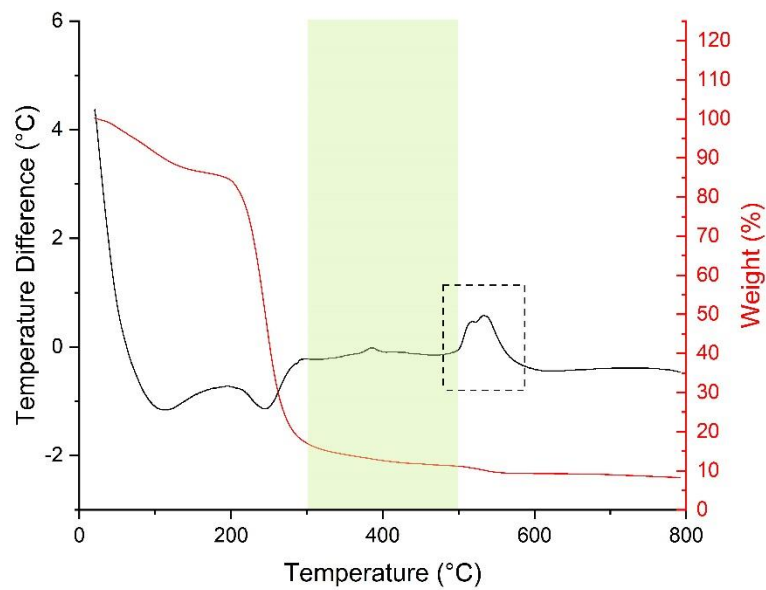
Figure 5.3 SDT of the ionic liquid with metallic precursors strontium acetate, lanthanum acetate and titanium isopropoxide.

Figure 5.4 shows the XRD analysis of these infills, in which all the XRD patterns have been normalised to the same value. The XRD describes powders whose crystallinity are all relatively low, evidenced by the ratio of background variation to peak heights. XRD is only able to diffract from crystalline substances, so if a sample of powder is of low crystallinity the peak intensities will be low, the background noise is a consistent and unavoidable characteristic from the machine which is normally very small compared to the peaks in a crystalline substance.
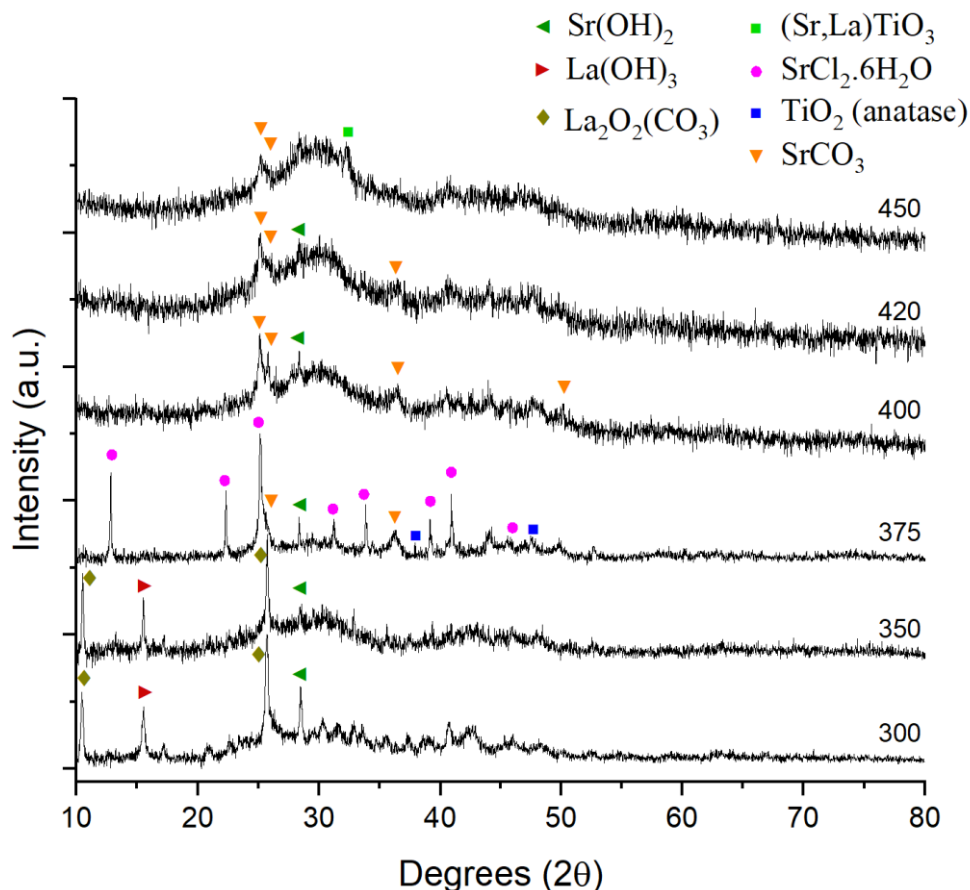
Figure 5.4 XRD analysis of infills fired between 300 and 450 ºC for 2 hr.

At the lowest temperature, 300 ℃, $La_2O_2(CO_3)$, La and Sr hydroxides are present. Small quantities of La and Sr form chlorides, carbonates and hydroxides and a small amount of anatase is detectable at 375 ℃. At an increased temperature of 375 ℃, these phases reduce in intensity, giving way to a majority of $SrCl_2.6H_2O$ which is formed from Sr ions of Sr acetate and the Cl impurity from the ionic liquid. By 400 ℃ the chloride hydrate phase is no longer detectable and is replaced by $SrCO_3$ as well as the emergence of a broad hump at ~ 30 °, which is a feature in amorphous materials such as glass.[9] At 450 ℃ the (110) peak of the LST phase begins to emerge. The background noise in the XRD patterns seems to increase steadily as the firing temperature increases with the exception of the 375 ℃ sample, this indicated a decrease in the crystallinity of the samples, except for the 375 ℃ sample. This could be an outlying result and would need to be repeated to confirm this. Alternatively, this temperature could provide the ideal conditions to crystallise a large amount of $SrCl_2.6H_2O$ which is not seen in the other samples.

XRD analysis of the powder at different stages of the ionic liquid synthesis was also performed by Mottram *et al.*, and is shown in Figure 5.5 (black lines). These were taken at much larger temperature steps than in this work, though where equivalent temperatures were used this works XRD patterns have been overlaid in Figure 5.5 (red lines). The spectra generally agree at 400 ℃, both are dominated by $SrCO_3$, though Mottram *et al.* also detected anatase. The lower temperature, 300℃, tells a different story; Mottram *et al.* observe a

significant amount of anatase which is not visible in the XRD of this work, instead there is a $La_2O_3(CO_3)$ phase.
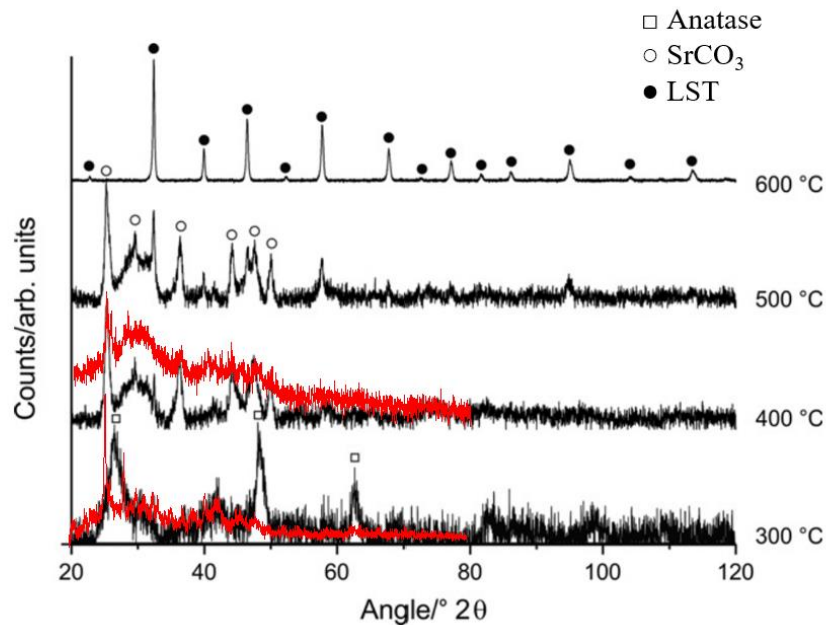
Figure 5.5 XRD analysis of powders at different stages of the ionic liquid synthesis of LST by Mottram et al.[8] The red lines are XRD patterns taken from Figure 5.4 which are overlaid in cases where the firing temperatures in both studies where examined: 300 ºC and 400 ºC.

From the information provided by the XRD, the 420 ºC sample appeared to be the leading choice of infill firing temperature as this fulfilled the previously set out criteria: remaining below the point of the LST phase formation and had been taken to a high enough temperature to lose the majority of mass associated with the calcination. To confirm this SEM was undertaken on the infills fired at and around this temperature, which are shown in Figure 5.6. Figures 5.6a and 5.6b present a very similar appearance under SEM with particle sizes of ~1µm, though their XRD analysis (Figure 5.4) show that significant reduction in the intensity of $SrCl_2.6H_2O$ peaks between these two temperatures. Whatever is occurring in the chemical reaction does not appear to be affecting the microstructure.

The difference between samples fired at 400 and 420 ºC in SEM is much more apparent. The 1µm diameter particles in the sample fired at 400 ºC give way to clusters of much smaller diameter particles. The only change in the XRD patterns was the reduction in intensity of $SrCO_3$ and $SrCl_2.6H_2O$ peaks – there is no emergence of new peaks which could be attributed to these smaller particles. This would suggest that these new particles are something amorphous which does not appear under XRD analysis. Increasing the firing temperature to 450 ºC shows minimal microstructural changes, though some coagulation between the particle clusters appears which makes their outlines less apparent. The XRD patterns (Figure 5.4) showed the emergence of LST peaks at this temperature.

Through the combination of XRD and SEM analysis the firing temperature 420 ºC was chosen. At this temperature very small particles of an amorphous phase are present; the large

159

surface area increases the reactivity of the particles. Furthermore, the amorphous nature should decrease the mechanical strength of the infill and allow it to be broken down and fit between the gaps of the matrix particles.
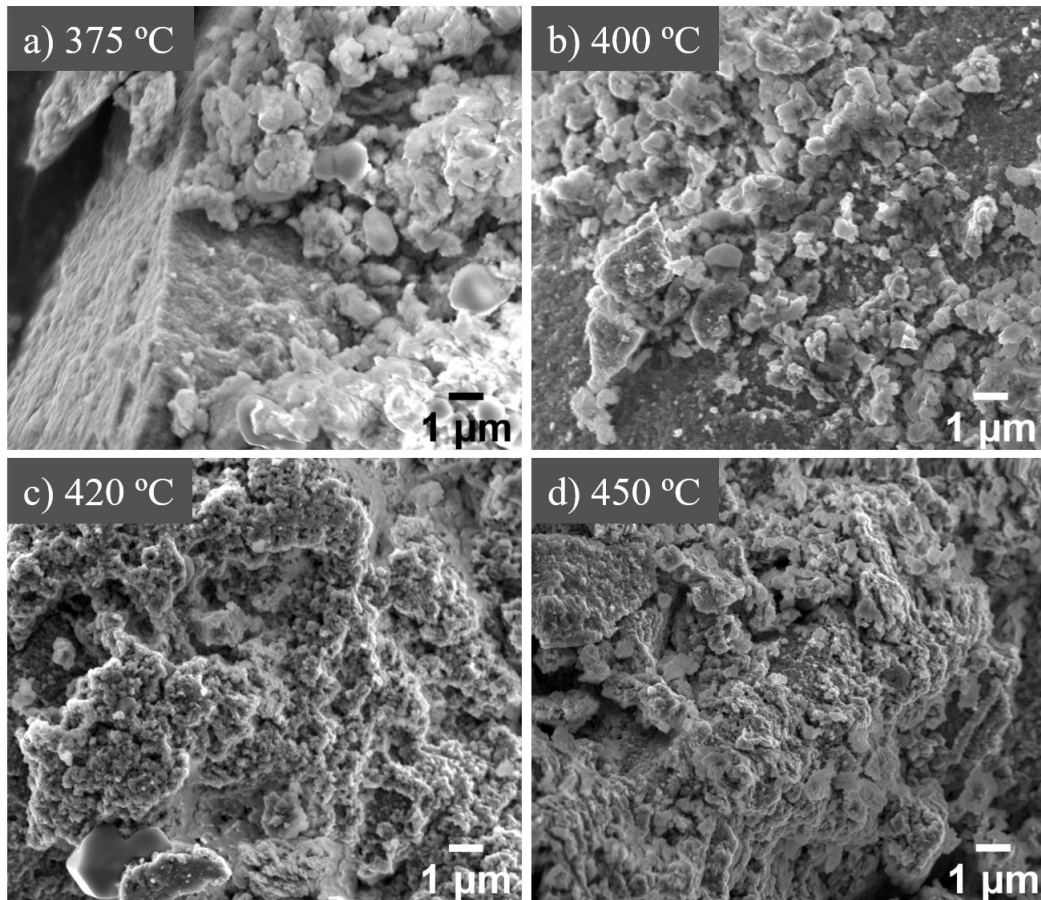
Figure 5.6 SE SEM micrographs of infills fired at a)375 ºC, b) 400 ºC, c) 420 ºC and d) 450 ºC for 2 h in air.

5.3.2 Combining Matrix and Infill

Figures 5.7a and 5.7b show the SE SEM micrographs of the matrix and the infill powders respectively which had both been hand ground using a pestle and mortar. The matrix forms large agglomerates ~70 μm made up of small grains in the region of 200 nm diameter (Figure 5.8a and c). The infill did not appear to form agglomerates but clumped together in one body, Figure 5.7b, though the particle size was very similar to the matrix, Figure 5.8b and d. Without seeing their macrostructure, the infill and the matrix appear very similar. The only real difference between them would be their level of crystallinity, which is not distinguishable in SEM.
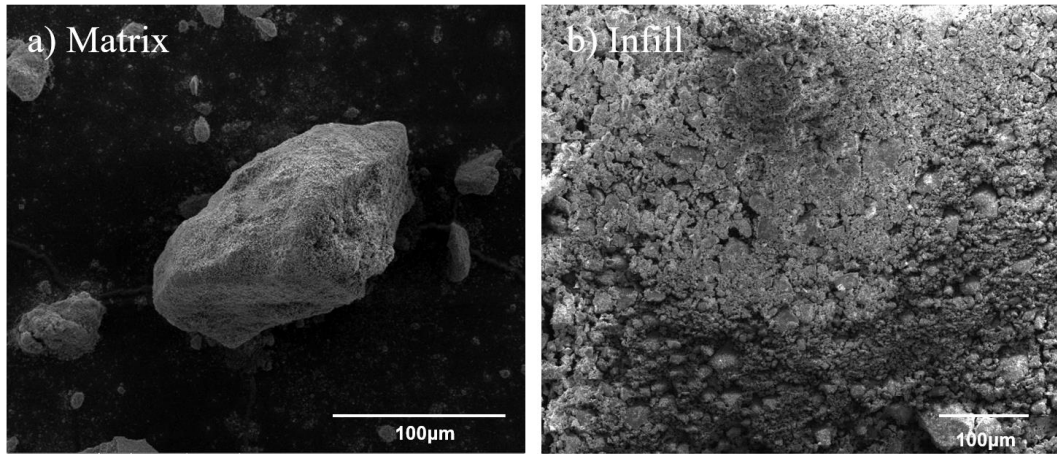
Figure 5.7 SE SEM Micrographs of a) LSTO matrix calcined at 800 ºC, b) infill fired at 420 ºC.
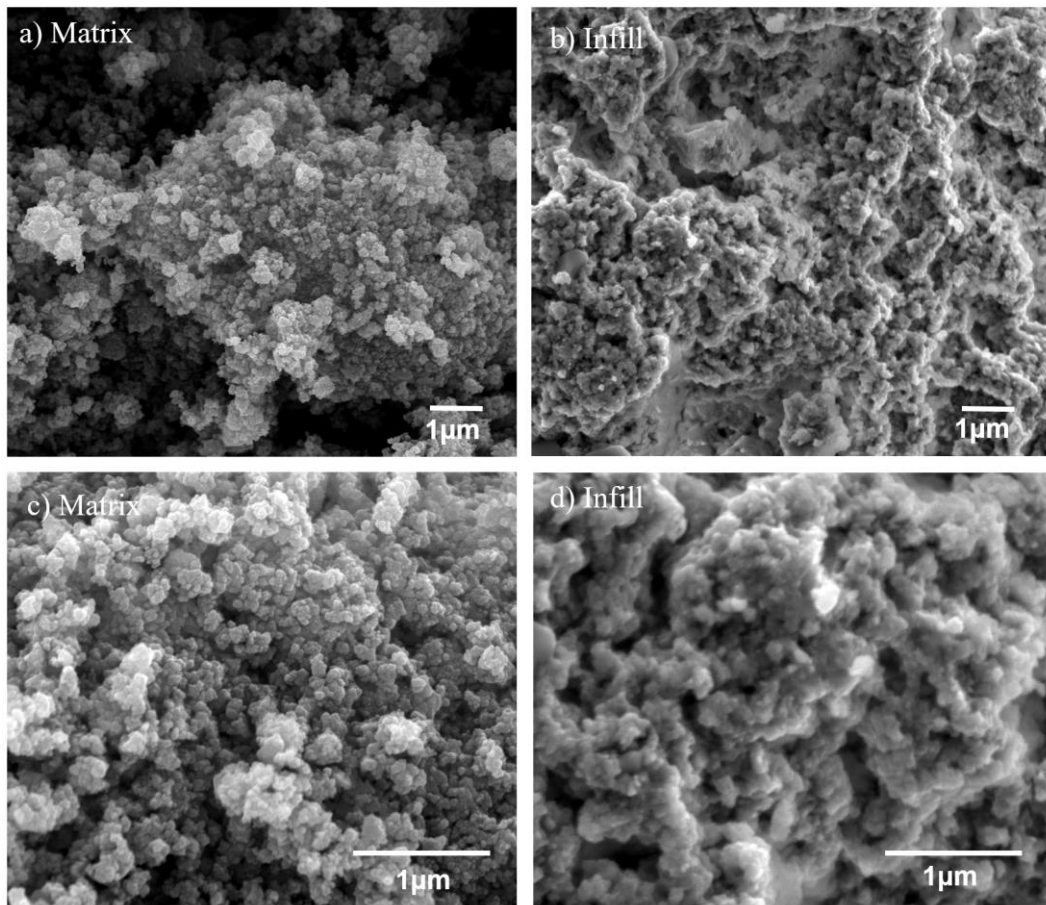
Figure 5.8 SEM micrographs of the matrix and the infill at greater magnifications.

Figure 5.9a and 5.9b show the combination of 30% infill with 70% matrix phase which had been hand ground together with water. The larger particles of the matrix are surrounded by the infill phase; this is particularly prominent in Figure 5.9b where the infill appears to be gluing the large matrix particles together.
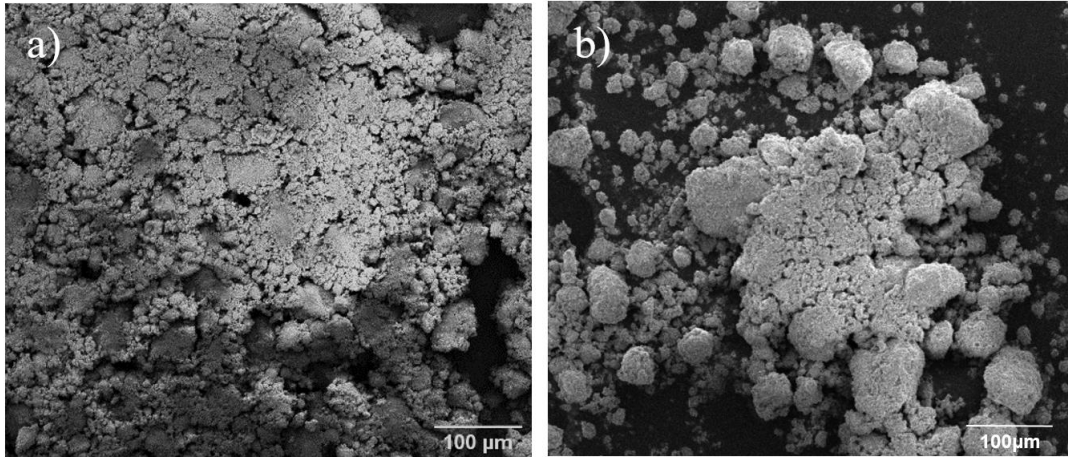
Figure 5.9 30 wt.% infill combined with 70 wt.% matrix which has been hand ground with water.

5.3.3 Pressed and Annealed Control Pellet

In order to decouple effects occurring during Cold Sintering Process (which is defined by the local hydrothermal conditions introduced by the transient solvent) dry matrix and infill powders were combined and subjected to pressing and annealing. This was done to observe the density of the pellet without any of the Cold Sintering Process densifications mechanisms, which come with adding a solvent and applying temperatures between RT and 300℃ and to see if adding the solvent was in fact needed. The mixture was hand ground and pressed at 355 MPa, without the use of a solvent or applied temperature. This pellet was annealed at 800 ℃ for 2 h to complete the transformation of the infill into the cubic perovskite LST. The SEM micrographs of a ground and polished surface are shown in Figure 5.10 and the measured density was 46 % of the theoretical density, though was mechanically stable.
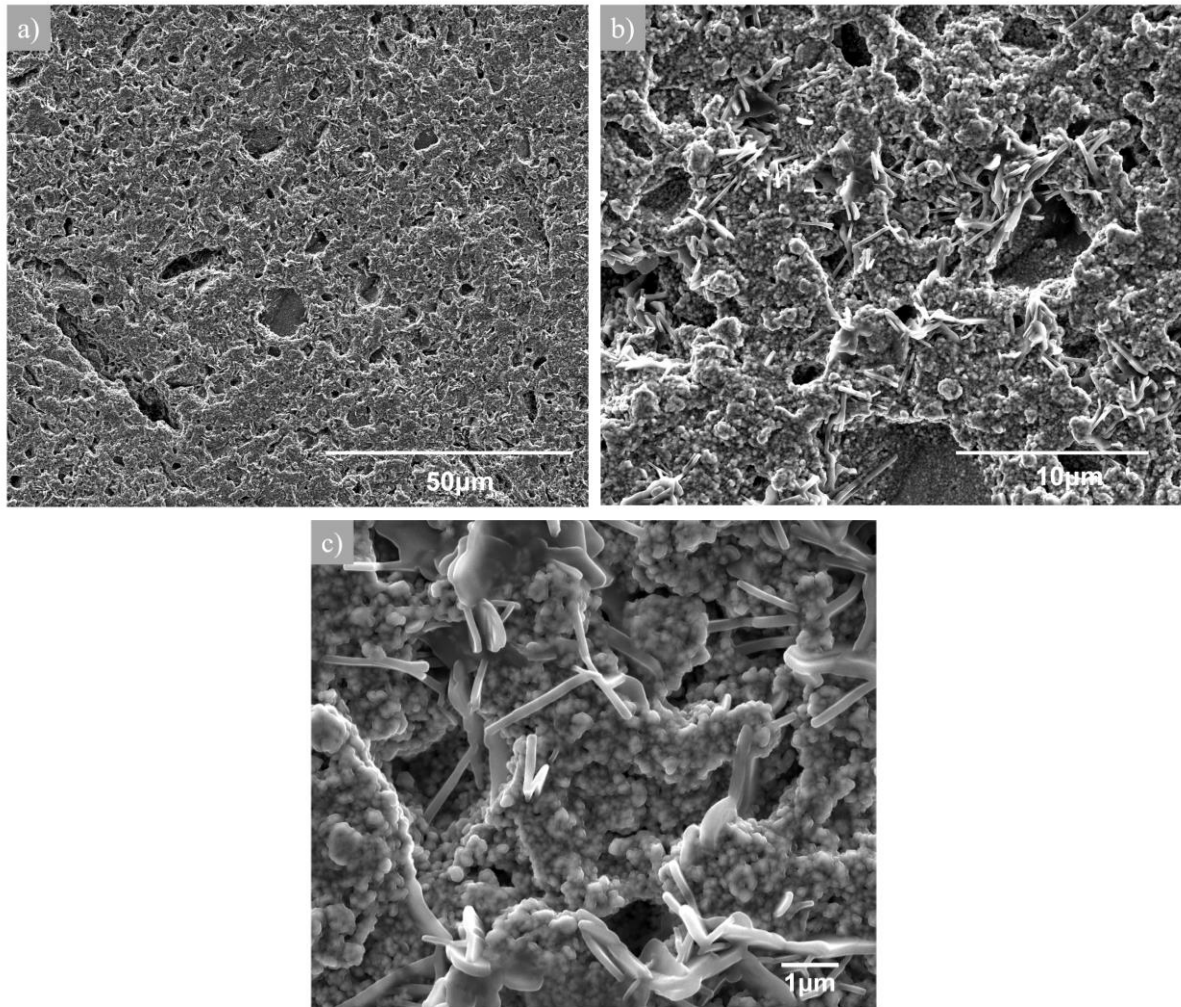
Figure 5.10 SE SEM micrographs of pellet pressed at 355 MPa, using no solvent or temperature, then removed from the die and annealed at 800 ºC for 2 h.

The high degree of porosity shown in the samples surface agrees with the low density (46%) measured. Figure 5.10b shows the pores which ranged between 1 and 10 μm. Figure 5.10c shows small (~200 nm) rounded particles and longer rod-like particles, the rounded particles are LST and the rod-like particles are an impurity phase believed to be caused by the polishing process, as these do not feature in un touched fracture surface samples (Figure 5.11). The rod-like features will be discussed in further detail within the section 'Surface Impurities'. This experiment shows that by using only the infill and pressure, a high density pellet is not achieved. The next step is to add temperature and a solvent to induce local hydrothermal conditions and observe their effect on densification.
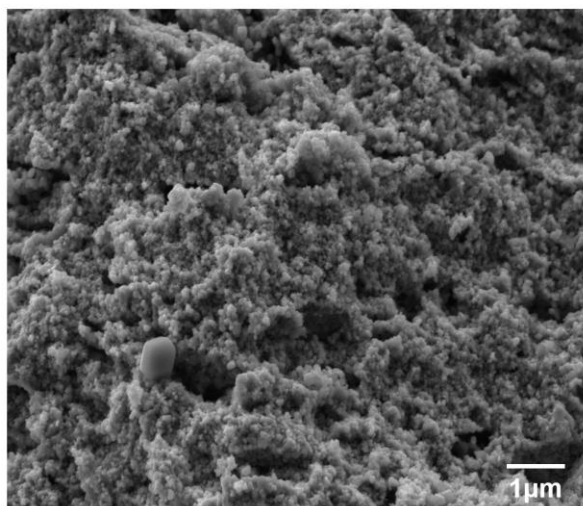
Figure 5.11 fracture surface SE SEM of cold sintered annealed pellet which does not contain rod-like particles in contrast to Figure 5.10.

5.3.4 Cold Sintering

As this was a novel method, the parameters with which to cold sinter had to be determined. The initial cold sintering parameters were based on those used by Boston *et al.* (750 MPa, held for ten minutes at RT then 180 ℃ for 1 h) who performed reactive cold sintering of $SrTiO_3$ and Guo *et al.* (430 MPa held for 10 minutes at RT then 180 ℃ for 1-3 h) who performed hydrothermally assisted cold sintering technique for $BaTiO_3$.[6,10] These parameters achieved high densities in $SrTiO_3$ and $BaTiO_3$, which are chemically and structurally similar to the composition $La_{0.15}Sr_{0.775}TiO_3$ used in this work, though it was unclear how similar the underlying mechanisms of this novel approach were to these other methods initially. [6,10] Furthermore, an overarching goal of this work is to keep the temperature and applied pressure as low as possible, to reduce the embodied energy of the ceramic, this meant that the initial parameters aired on the lower side of Boston and Guo *et al.*

The initial protocol was as follows: 30 wt.% infill was combined with 70 wt.% matrix to form a total of 0.7g of powder. The total mass of powder was roughly the amount which would fit in the cylindrical die used for cold sintering. 30 wt.% was chosen because the green body density of a well pressed ceramic pellet is around 60 % and so the aim was to sparingly fill these gaps with the infill.[11] 700 μl of water was added to this mixture and hand ground for ~15 minutes until the powder was free flowing. This was placed into a cylindrical die (12.7 mm diameter), using pre-cut parchment disk to line the bottom and top plungers, which reduced adhesion to the die itself, aiding removal from the die. This was pressed at 355 MPa (4.5 T) for ten minutes at room temperature to allow for particle rearrangement which caused the pressure to drop. Additional load was then applied to increase the pressure back to 355 MPa before the temperature was increased to 160 ℃. This temperature was held for 1 h, then cooled with the assistance of a fan for half an hour before the pressure was released. The typical temperature of the die when the pellet was removed from the die was < 50 ℃. The pellet was then annealed in air at 800 ℃ for 2 h, as per the calcination protocol of matrix powder. The parchment was left on for the annealing process as it became fused to the pellet

after cold sintering and was impossible to remove. The parchment combusted in the annealing step and could be brushed off the surface afterwards.

Figure 5.12 shows the XRD of the mixed powders before annealing, and of the pellet after cold sintering and annealing. When combined with the matrix, the 30 % infill is virtually undetectable in the XRD analysis due to the lack of crystallinity, leading to low intensity peaks. The only way to confirm the reaction to form LST had taken place was the change in colour of the pellet from a grey/brown colour to a pure white after annealing.
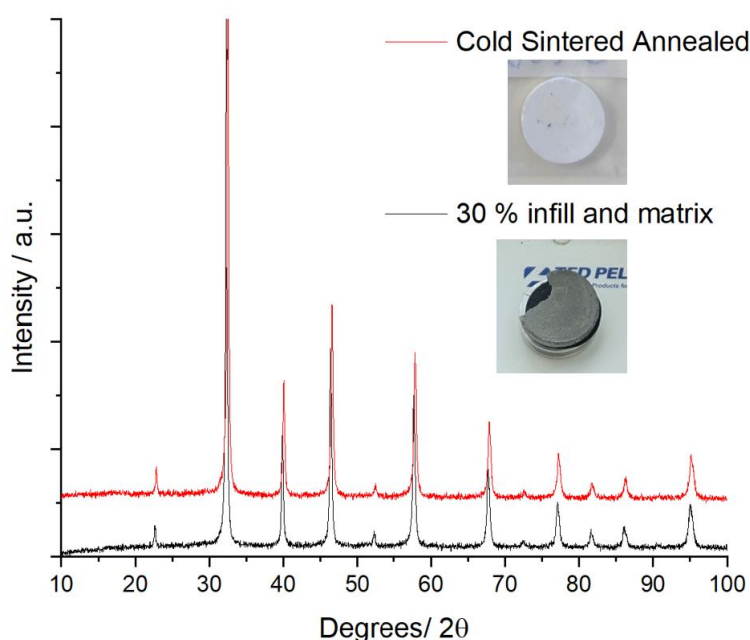
Figure 5.12 XRD analysis of cold sintered pellet (30% infill) before annealing and the cold sintered pellet post annealing at 800 ºC for 2h.

The Full Width Half Maxima (FWHM) of seven peaks from the pre annealed and annealed XRD patterns were calculated to observe any evidence of crystallite growth, these are shown in Table 5.1 and plotted in Figure 5.13. The graphical determination of these values can be found in Chapter 5 Appendix Figures 5.A1 and 5.A2. Peak broadening in XRD is an effect caused by increasing degree of scattering from a decrease in crystallite size. Table 5.1 shows the results of the Scherer analysis, there is no statistical difference between the two crystallite sizes as both averages are within the standard deviations of each other. This indicates no significant level of crystallite growth.

Table 5.1 Results from Scherer analysis

Sample	Bragg angle (2θ)	Bragg Angle (Radians)	FWHM (degrees)	FWHM (radians)	Crystallite size /nm
Annealed Pellet	32.5	0.284	0.267	0.00466	31.0
	40.1	0.350	0.280	0.00489	30.2
	46.5	0.406	0.323	0.00563	26.8
	57.8	0.504	0.376	0.00657	24.1
	67.9	0.593	0.443	0.00774	21.6

	77.2	0.674	0.490	0.00855	20.8
	95.1	0.830	0.650	0.01134	18.1
				Average	_29.3_
				Standard dev.	_1.8_
Pre annealed pellet	32.3	0.282	0.251	0.00438	33.0
	39.7	0.346	0.283	0.00494	29.9
	46.2	0.403	0.318	0.00555	27.2
	57.7	0.504	0.360	0.00628	25.2
	67.7	0.591	0.445	0.00777	21.5
	77.0	0.672	0.494	0.00863	20.6
	95.1	0.830	0.657	0.01147	17.9
				Average	_30.0_
				Standard dev.	_2.4_
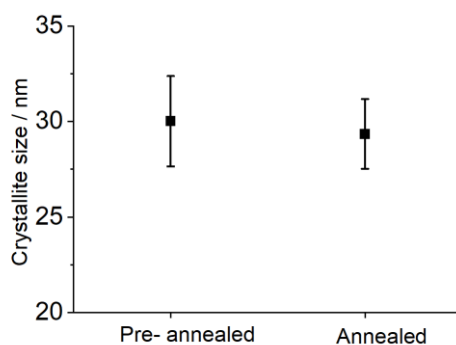
Figure 5.13 Full Width Half Maximum results from Scherer analysis of from XRD patterns of cold sintered pre annealed pellets and cold sintered annealed pellets.

Back scattered electron (BSE) micrographs of the polished surface are shown in Figure 5.14. The contrast in BSE micrographs, Z contrast, is caused by the variation in atomic mass of a particular region (large atomic mass appears brighter than low atomic mass) and so are useful to observe the density of the material. Low density areas have a lower concentration of the atomic mass and so appear as dark regions. In Figure 5.14 dark boundaries surround large (50 -70 μm) irregular shaped regions, the size and shape of which match those observed in Figure 5.9a of the matrix powder. In the bottom right corner of Figure 5.14a, an intersection of one of these particles can be seen which shows an inconsistent Z contrast, indicating low density. A higher magnification of this particle is shown in Figure 5.15a, alongside a secondary electron micrograph of a similar region. Secondary electron images show variations in topology and charging often occurs at edges which cause them to show up brighter. These micrographs both show clusters of small particles surrounded by dark boundary areas which indicate low density or empty space. This shows that there is poor adhesion between the matrix particles and the infill.
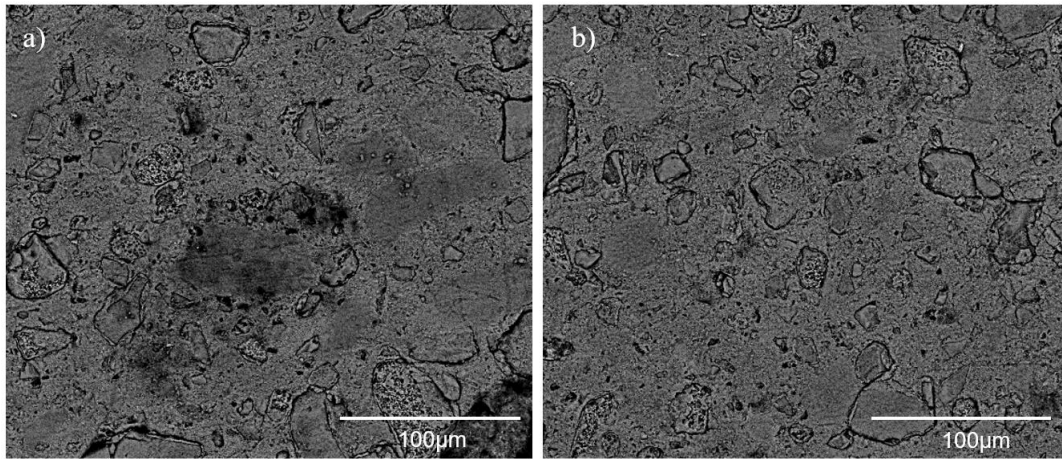
Figure 5.14 a,b) BSE SEM micrographs of cold sintered and annealed pellet.
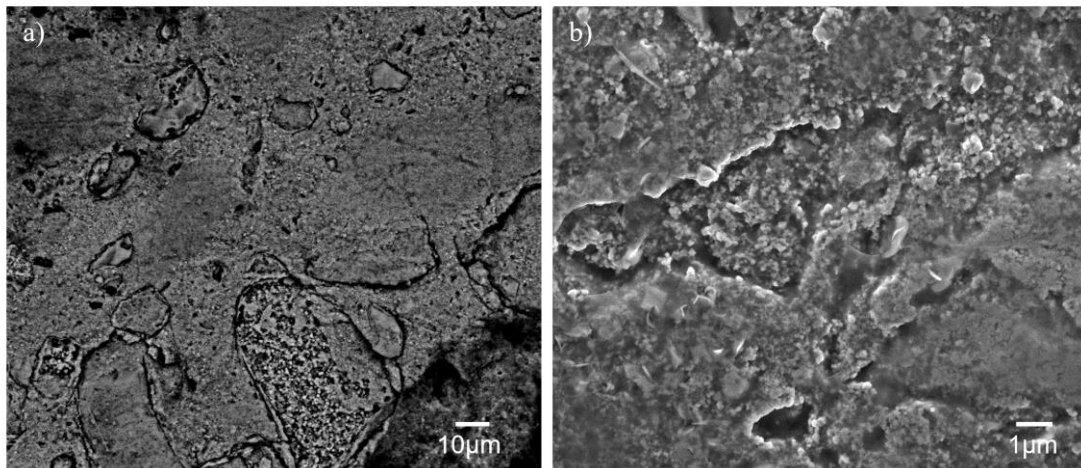
Figure 5.15 a) BSE micrograph b) SE micrograph of cold sintered and annealed pellet.

In order to improve the homogeneity of the cold sintered pellet, a milling step was introduced in which a batch of matrix and infill (still with 30 wt.% infill) was milled overnight on a ball mill in isopropanol, which was then dried before being cold sintered using the same conditions. Figure 5.16 shows BSE micrographs comparing the polished surfaces of pellets with (16a) and without (16b) the milling step. The large particles are no longer present in 16a and so the milling step has successfully broken down the matrix which improves the homogeneity of the pellet. Figure 5.17 shows SE SEM micrographs of the milled pellet under greater magnifications which still showed a large degree of porosity. The next step to attempt to improve the density of the pellet was to optimise the cold sintering parameters.
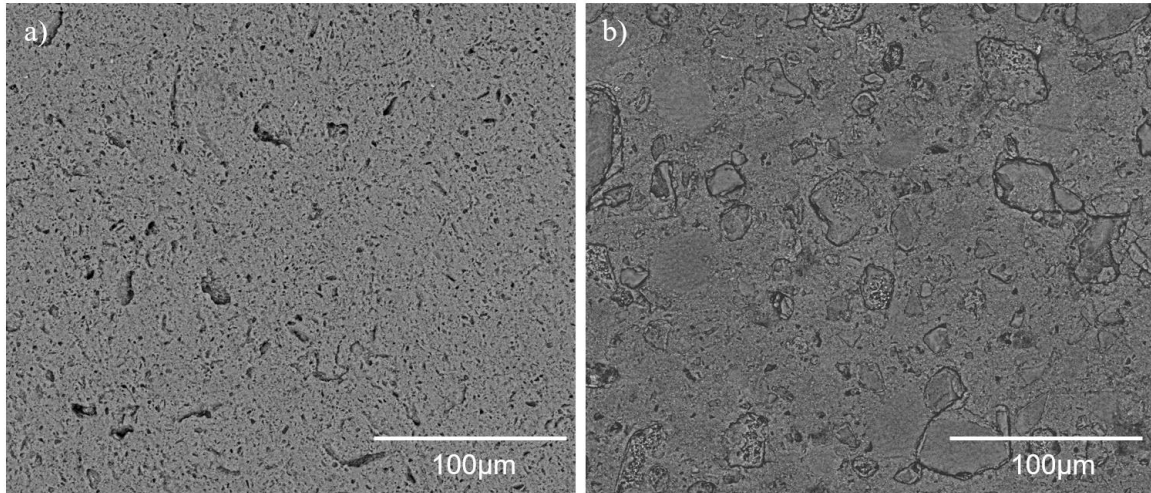
Figure 5.16 BSE micrographs of a) milled b) non-milled cold sintered pellet polished surfaces.
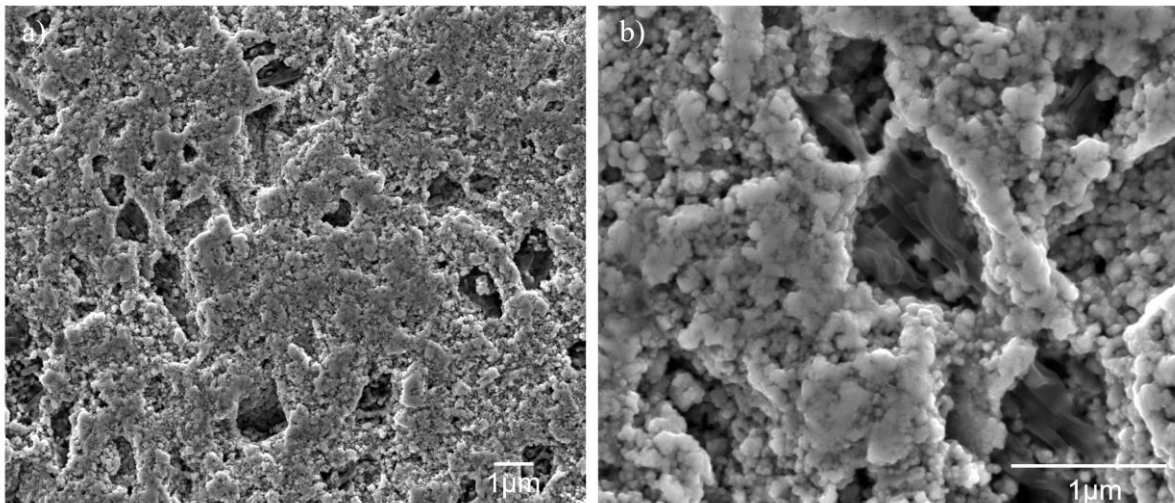
Figure 5.17 SE SEM micrographs of milled pellet surface.

5.3.5 Optimising Cold Sintering Process Parameters

Despite the improvement in homogeneity from introducing a milling step, issues with porosity and low density remained, remaining between 40 -50 % of the theoretical density. With the aim of improving the density the process parameters of the cold sintering where optimised. There are many variable parameters within cold sintering, such as: amount of the solvent, pressure, temperature and hold time, annealing temperature and time. For the purpose of a compact study, two parameters were selected which were: pressure and temperature. The pressure applied to the die was varied above and below the initial pressure of 355 MPa by 118 MPa, which corresponded to a change in the force applied of 1.5 Tonnes. This gave three pressure variations: 237, 355 and 474 MPa. The temperature was also varied

above and below the initially selected temperature of 160 ºC by 50 ºC giving three temperatures variations: 110, 160 and 210 ºC. The water added during grinding was fixed at 700 μl for 0.7g of powder. The infill level was fixed at 30 wt.% and the hold time remained 1 h with a 10-minute settling time. The resulting geometrically measured densities after annealing at 800 ºC for 2 hr are shown in Figures 5.18 and 5.19. Each experiment was repeated three times and are all represented on the graphs. Values were the density is zero, equate to pellets which were mechanically unstable and broke after minor handling
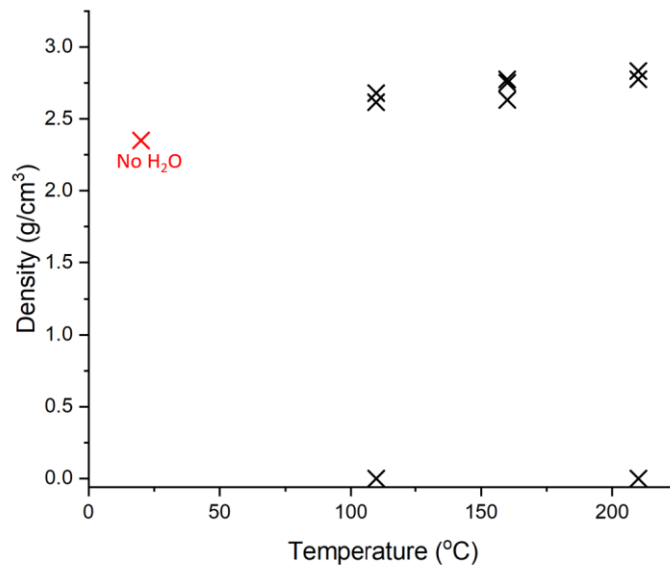
Figure 5.18 Density of cold sintered and annealed pellets versus cold sintering temperature when pressed at 355 MPa.
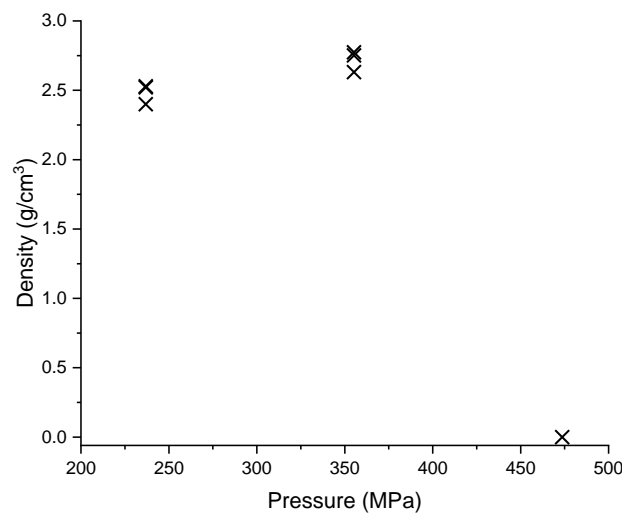
Figure 5.19 Density of cold sintered and annealed pellets versus cold sintering pressure using 160 ºC.

Firstly, in Figure 5.18 the density value of the pellet which was just pressed, without the use of solvent or added temperature, is indicated by the red cross at 20 ºC (RT), to compare to the

cold sintered pellet densities. Despite two of the samples breaking, there is a clear trend is in the density which increased as the cold sintering temperature increased. The increase in density is small with each increment of temperature and reaches a maximum of 2.83 g/cm^3 which equates to 55% of the theoretical density. The positive correlation between the density temperature was expected, as higher temperatures allow the increased rate of mass diffusion which is key to densification. The maximum density in this study is still very low and so further optimisation of the pressure is needed.

Figure 5.19 shows the pressure versus density study in which the density is increased by moving from a pressure of 237 MPa to 355 MPa, reaching a maximum of 2.77 g/cm^3 (54 % density). However, all the samples cold sintered using a pressure of 474 MPa were mechanically unstable. The nature of the pellet fractures was most often through-thickness fractures, shown in Figure 5.20. Increasing the pressure was expected to increase the density by compacting the powders and squeezing out pores. The largest pressure seems to have reached a point where the brittle material could no longer accommodate the compression and formed fractures which made the pellet mechanically unstable. The maximum density achieved in this study was still very low at ~54 %. To explain this apparent density maxima, SDT measurements were conducted which showed the behaviour of the material at high temperatures.

Figure 5.20 Cold sintered and annealed pellet through-thickness split.

5.3.6 SDT Analysis

Figure 5.21a shows the SDT of the 420 ℃ infill between room temperature and 800 ℃, which simulates the weight loss the infill would undergo during the annealing process. Though most of the mass loss in the ionic liquid synthesis process was shown to occur below ~300 ℃ (Figure 5.3), still the material loses 18% of its starting weight between room temperature and 800 ℃. The use of the partly calcined infill introduces a new theoretical density maximum, because there is an unavoidable mass loss when the infill is converted to LST when it is annealed. The majority of the mass loss (~ 14 %) in Figure 5.21a appears to be below 420 ℃, the infill firing temperature, which indicates that the infill has adsorbed

mass from the atmosphere in the time between firing and SDT analysis. This is likely in the form of water and/or carbon dioxide and is represented by the blue are in Figure 5.21a.

Beyond 450 ℃ there is a sharp drop in mass, this is just above the firing temperature of the infill, marked by the orange square in Figure 5.21a. Considering the $SrCO_3$ found in the XRD of the 420 and 450 ℃ infills (Figure 5.22) which reduces in intensity, this mass loss is likely associated with the breakdown of $SrCO_3$, evolving CO_2.

Figure 5.21b shows the mass loss from the matrix powder in SDT. There is a 3.6 % mass lass from between room temperature and 800 ℃. When heating up to 1500 ℃, further mass loss occurs giving a total of 5%. The heat-cool-heat process applied to the sample shows that this is a mostly irreversible mass loss, though the small change in mass is likely oxygen loss and reabsorption. This mass loss is associated with removal of material adsorbed from the air in the form of water and CO_2.
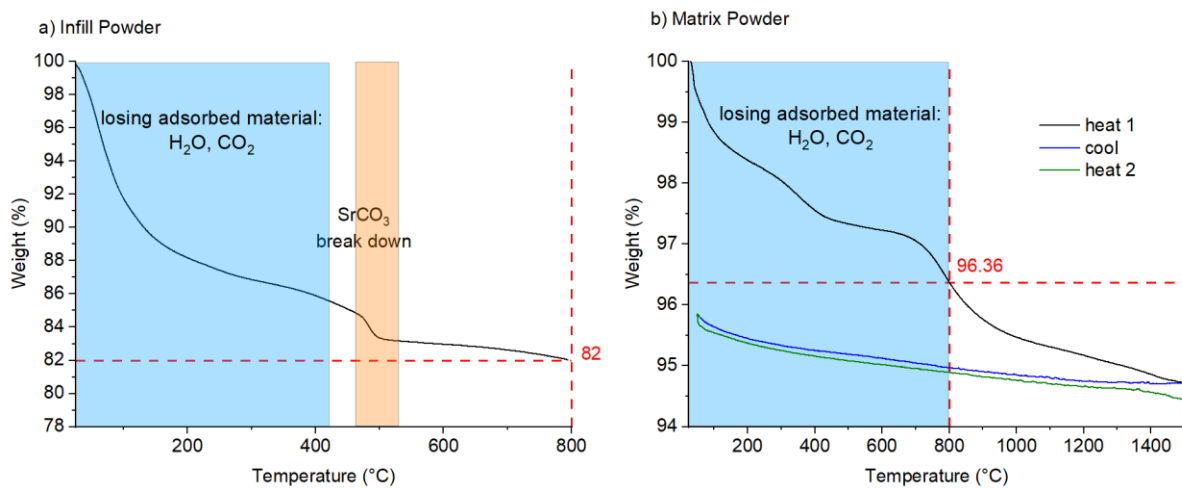
Figure 5.21 SDT of a) the 420 ℃ infill and b) heat cool heat of the matrix powder
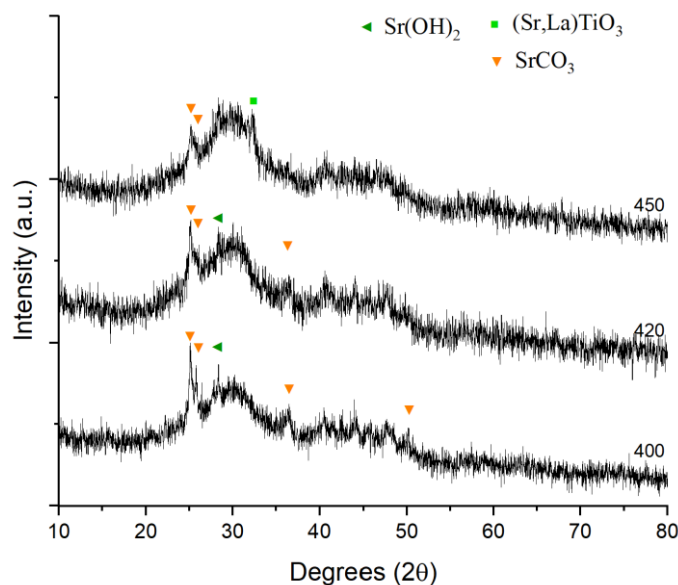
Figure 5.22 XRD of infills fired at 400, 420 and 450 ℃.

For a cold sintered pellet containing 30 wt.% infill this would equate to a mass loss of 8.2 % (0.3 * 18 % + 0.7 * 4 %) during the annealing process. As no external dimension change was observed in the annealing process, the external dimensions are fixed. Therefore, if the dimensions do not change but there is an inevitable mass loss, then the maximum theoretical density of a cold sintered pellet with 30 % infill would be 91.8%. This mass loss still by no means accounts for the low densities ~54 % observed- there must be also a reduction in volume of the infill (without a reduction in the pellet external surface) which leads to such low densities. To investigate this the cold sintered and annealed pellets interior was observed under SEM.

5.3.7 SEM Observation of Porosity

The SEM micrographs of the internal fracture surface of the cold sintered and annealed pellets are shown in Figure 5.23. In these micrographs the red boxes highlight clusters of the LST grains, surrounded by empty space. This is believed to be caused by particle clusters originating from the matrix phase, which during cold sintering, are surrounded by infill phase. When the infill converts from an amorphous structure to crystalline LST during annealing, a significant volume reduction occurs do to the ordering of atoms and mass loss. The volume reduction of the amorphous infill to the crystalline LST causes empty space to form in the space where the infill previously occupied. In this case the new LST appears to shrink back from the particles unlike in the work of Guo *et al.* where precipitation led to $BaTiO_3$ forming on the surface of $BaTiO_3$ grains.[10] A perquisite to the formation of new material directly on to the particle surface is pristine surfaces. In this work, Cl has been shown to be electrostatically bonded to the surface of particles leading to a surface charge (see section 'Processing of $(La,Sr)TiO_3$). The impurities attached to the particle surfaces could be causing a barrier to the formation of LST on the surface of pre-existing particles.
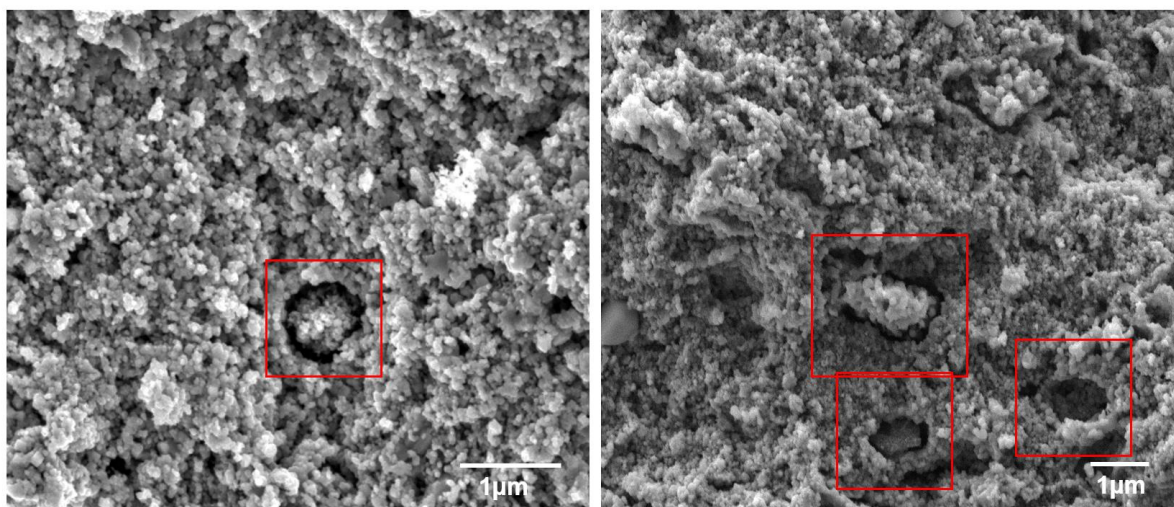
Figure 5.23 SE SEM micrographs of a fracture surface cold sintered at 160 ºC using 355 MPa and annealed at 800 ºC for 2 h.

In summary SDT measurements and SEM have shown that the mass loss and volume reduction associated with the transformation of the amorphous infill into crystalline LST could be the cause of the low density. Though without the infill the cold sintered pellet was completely mechanically unstable. Figure 5.24 which shows the result of a pellet following the same cold sintering and annealing process except with no infill phase. Impurities potentially cause a barrier to the deposition of new LST onto pre-existing LST particles. The presence of impurities in the cold sintered pellets became highly apparent when preparing the specimens for SEM analysis. By grinding and polishing the surfaces, additional phases appeared on the surface of the pellets as they dried. The next section looks into these phases in more detail.

Figure 5.24 Image of cold sintered and annealed pellet with no filler which was mechanically unstable.

5.3.8 Surface Impurities

When the cold sintered pellets were ground and polished for SEM, their surfaces were exposed to water and isopropanol, then cleaned with isopropanol to remove debris. When left to dry a new phase developed on the surface which was observable under SEM. This was most prevalent on the polished surfaces in pre-annealed pellets, as shown in Figure 5.25. The contrast of the BSE micrographs, originating from atomic number, shows brighter material on top of a darker background. The lighter areas were revealed by SEM EDX (Figure 5.26) to be rich in K, Cl and Na which is likely crystalline KCl and NaCl. There appears to be much more KCl than NaCl. The darker areas are LST, which forms the bulk of the pellet. In Figure 5.26 the EDS maps show that Sr, La and Ti are visible through the chlorides which indicates that they are thinly dispersed on the surface. Figure 5.27 compares point spectra from the darker area (solid yellow) and one of the lighter crystals (red line) which confirms a much higher Cl and K content- it would be reasonable to assume that this is KCl. This is of interest as it confirms the presence of impurities retained in the sintered pellets, KCl is present despite this not being visible in the XRD - likely because this is below the detection limit of the XRD analysis threshold.
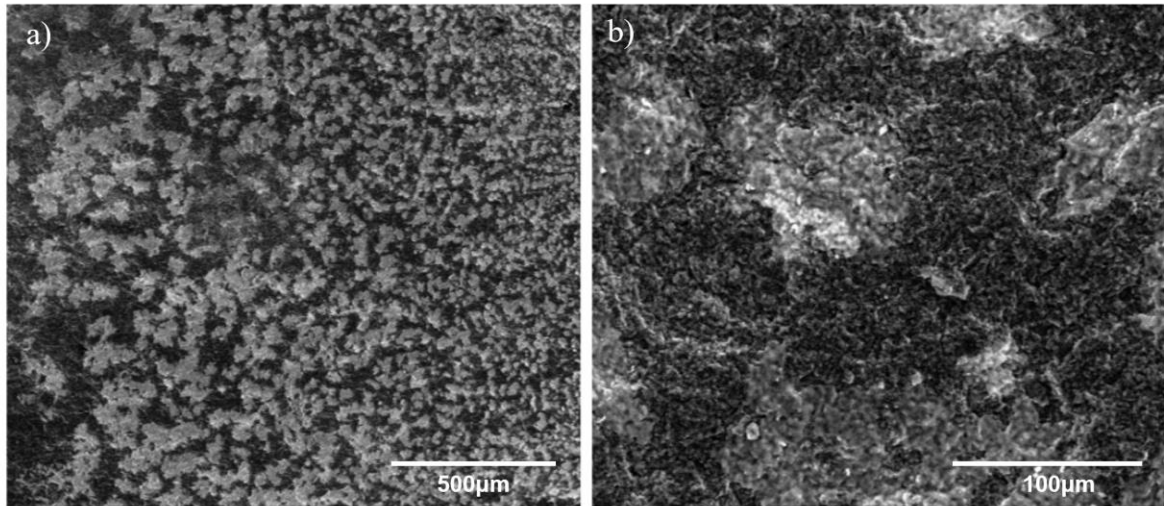
Figure 5.25 BSE SEM micrograph of showing the polished surface of a pre anneal cold sintered pellet.
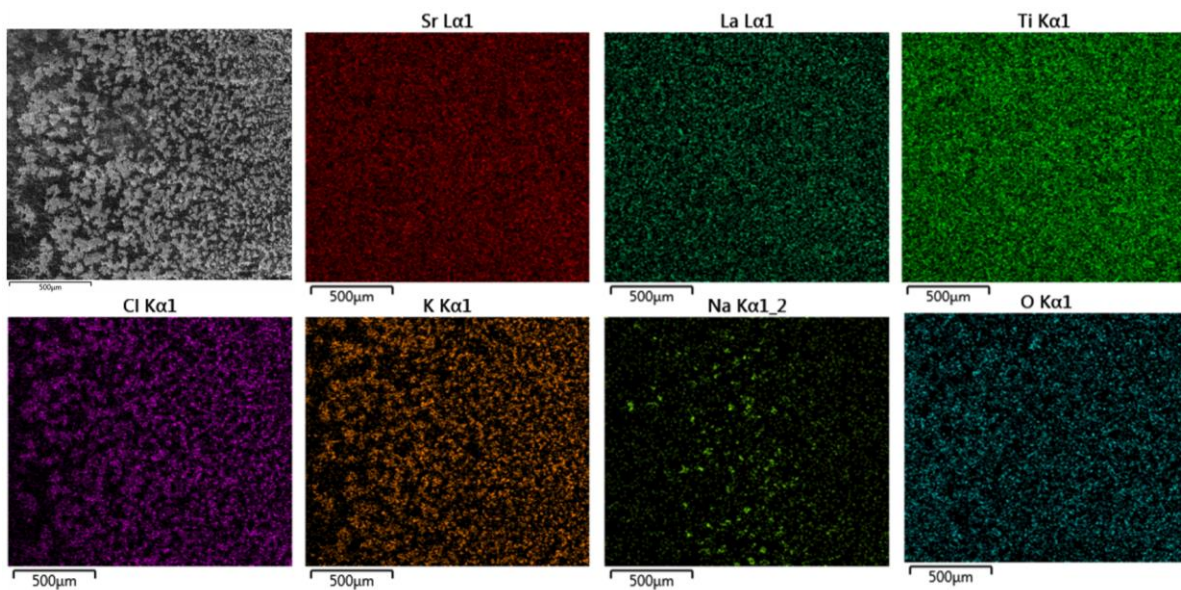
Figure 5.26 SEM EDS maps of the BSE micrographs from Figure 5.24.
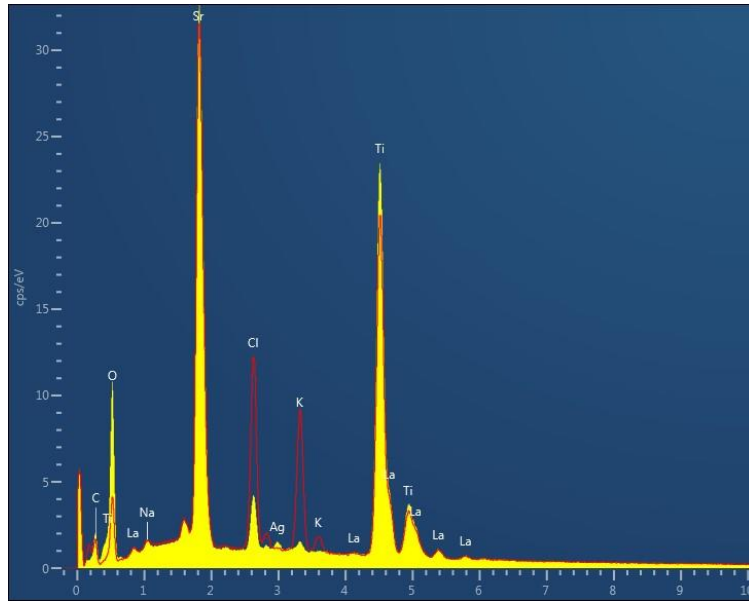
Figure 5.27 SEM EDS point spectrum of the bulk (solid yellow) overlaid with a point spectrum from the lighter crystals (red line).

After different samples had been subject to an annealing step at 800 °C for 2 hr and polished, a wire like phase emerged from the surface as shown in Figure 5.28a-d. The composition of this phase was once again confirmed to be KCl and NaCl by SEM EDS spectra (Figure 5.29) and EDS mapping (Figure 5.30). Figure 5.28a is an SE SEM micrograph and the chloride wires appear bright for two likely reasons: firstly, they are at a greater elevation to the surface and so appear much brighter in accordance with the SE SEM method, and secondly because they are in poor contact with the surface due to their 3D spiral shape and so charge gathers within them which cannot be adequately dispersed across the surface.

The cause of the different morphology of chlorides between Figures 5.25 and 5.28 is unclear though it appears as though in the annealed pellets the KCl wires have been extruded through small pores in the surface, whereas, in pre-annealed pellets the KCl lies flatter on the surface. This could because as the pellets anneal the infill becomes mechanically stronger due to the conversation from amorphous material to a crystallised LST material. In order for the KCl to crystallise from the water and isopropanol, it is squeezed out from the near surface by rigid pores rather than a softer infill. The base of the wires all seem to originate from darker areas in the BSE micrographs which are pores, confirming this theory. Figure 5.28d shows an abnormally shaped chloride on the surface of the pellet which appears comb shaped. This does not appear to be extruded like the rest of the particles and lies on a pore free surface. This particle likely broke off from one of the wires early in the drying process and continued to grow. To the right of the comb is a NaCl particle (confirmed by Figure 5.30) which does appear to be extruded out from a crack in the surface.
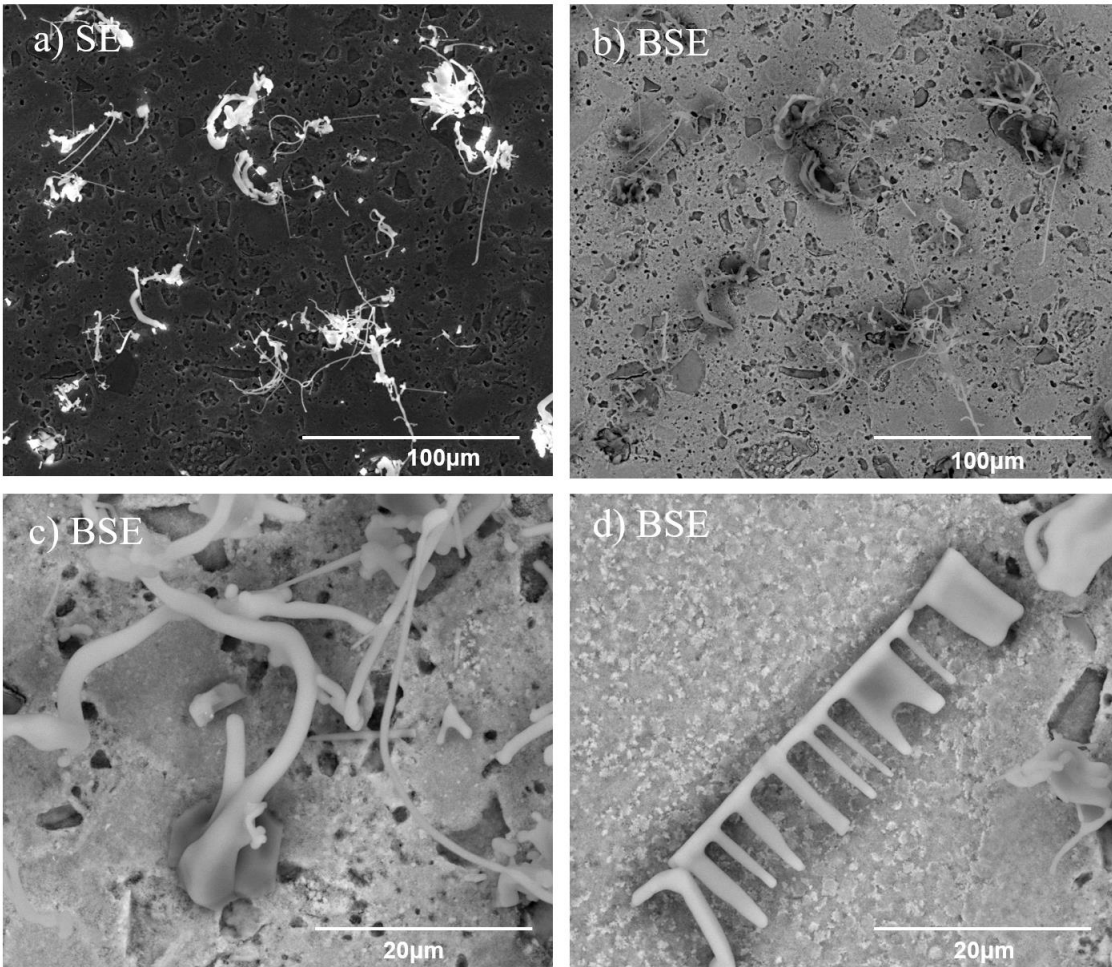
Figure 5.28 SEM micrographs of annealed cold sintered pellet.
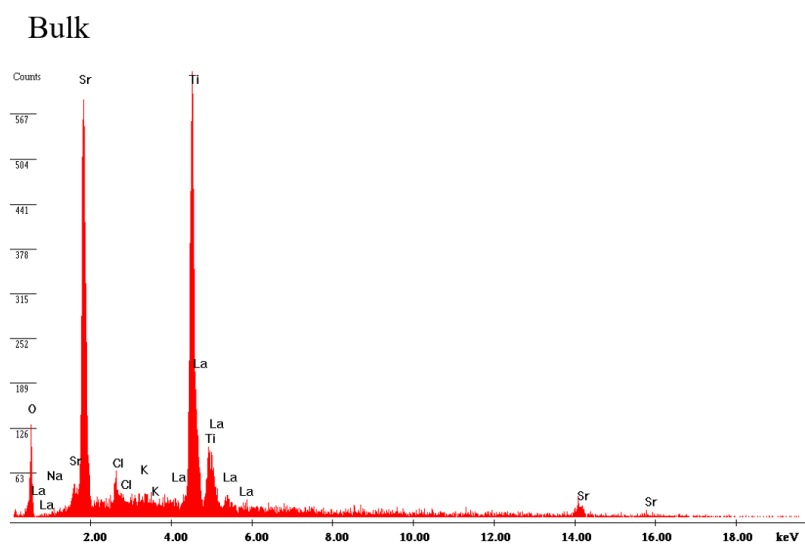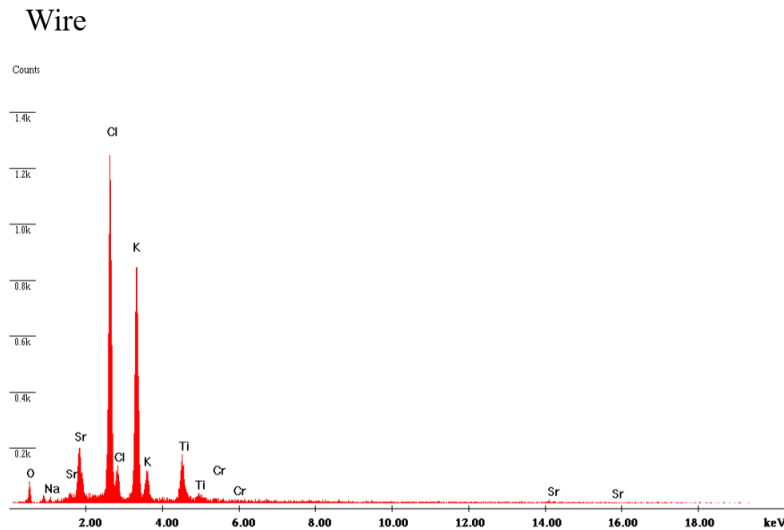
Bulk

Wire

Figure 5.29 SEM EDS spectra from the bulk and wires formed on the surface of annealed cold sintered pellets.
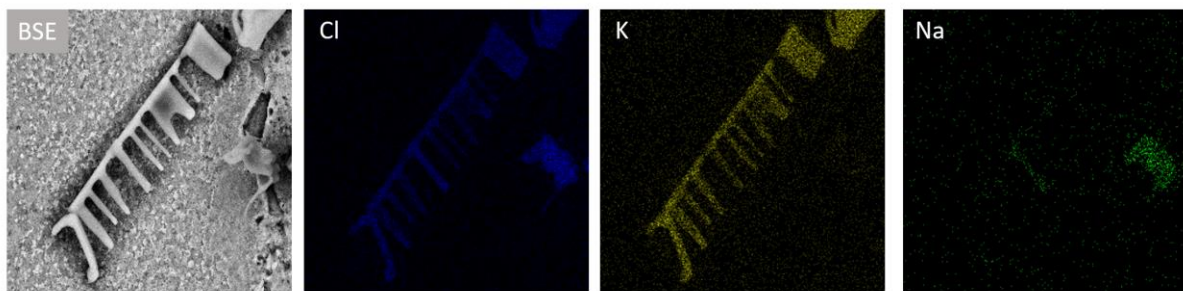
Figure 5.30 SEM EDS of particle on the surface of the pellet from Figure 5.28d.

5.3.9 The Role of Potassium and Sodium Impurities

The emergence of KCl and NaCl particles in the pre and post annealed pellets makes clear that K, Na and Cl impurities are present throughout the cold sintering and annealing processes in significant quantities. Previously in this chapter it was hypothesised that the Cl impurities were interfering with the pristine surfaces required for LST to deposit onto the pre-existing grains in the cold sintering process. Tsuji *et al.* intentionally added Na and K hydroxides which acted as a fluxing agent and aided the sintering of $BaTiO_3$ at 300 ºC which reached a density of 96 % of the theoretical density after 12 h under a pressure of 520 MPa.[12] If Tsuji *et al.* achieved high density by adding additional potassium and sodium hydroxides then why isn't K and Na performing the same role in this work?

XPS analysis in Table 5.2 confirms and quantifies the presence of Na, K and Cl impurities within the surface of an annealed pellet, which had not been previously exposed to water or isopropanol. Unlike EDS which examines the bulk composition and has a penetration depth of up to 5 μm, XPS can only provide information from the first 10nm of the surface, so this must be considered when using XPS to determine composition. However, this technique was

calibrated and can provide a quantification of the composition unlike the EDS. According to XPS Cl is present at 2.6 at. %, Na at 1.7 at. % and K at 0.9 at. %. The Na and K contents add up to the same quantity as the Cl and so it is reasonable to assume that there is 1.7 at. % NaCl and 0.9 at. % KCl present.

Table 5.2 XPS of Pellet Cold Sintered and Annealed at 800 ºC for 2 h.

	Na	K	Cl	Sr	La	Ti	O	C
At. %	1.7	0.9	2.6	12.7	3.6	14.4	48.0	16.2

Firstly, Tsuji *et al.* added the hydroxides in a much greater quantity, in a 50:50 ratio, at 4-6 wt.% when combined (equivalent to 10-14 at. % NaOH and 7-10 at . % KOH). They added no water so that the NaOH and KOH were not dissolved but formed a melt at 170 ºC which acted as the solvent (Figure 5.30). In this work, much less of the Na and K are present and water was added during cold sintering so the ions are likely to have been dissolved. As the water was evaporated at temperatures above 100 ºC the Na and K could have formed NaOH and KOH via reactions with water, though EDS shows that they are forming KCl and NaCl preferentially.

Unlike NaOH and KOH which have a eutectic at 170 ºC (Figure 5.31) which allows them to form a liquid which acts as a solvent which aids densification, NaCl and KCl can form melt but at much higher temperature, which makes this a less desirable flux for cold sintering. Figure 5.32 shows that depending on the ratio of Na to K the chlorides could melt between 657 ºC and 801 ºC. This melt could occur during the annealing stage, though without the addition of pressure the hydrothermal conditions are not created and so significant densification was not seen. In any case the NaCl-KCl quantities would likely need to be increased to see a significant impact. In summary the present of potassium and sodium chlorides does not have the same impact as potassium and sodium hydroxides during cold sintering. Their presence in this case is interfering with the deposition of LST onto existing grains which inhibits a dense microstructure in the cold sintered pellets.
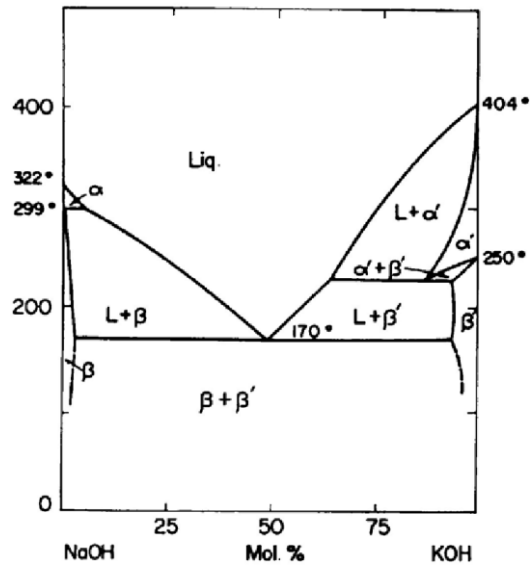
Figure 5.31 Phase diagram of NaOH and KOH.[13]
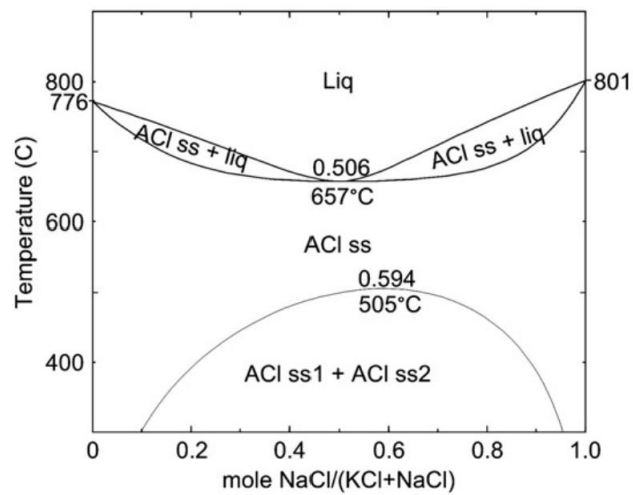
Figure 5.32 Phase diagram of NaCl and KCl.[14]

5.3.10 Surface Composition from XPS

Table 5.3 Ratio of elements to Ti from Table 5.2 XPS data in cold sintered pellet annealed in air at 800 ºC.

	Na	K	Cl	Sr	La	Ti	O	C
Ratio to Ti	0.12	0.06	0.18	0.88	0.25	1.00	3.33	1.13
Excess from $La_{0.15}Sr_{0.775}TiO_3$	0.12	0.06	0.18	0.105	0.1	0	0.33	1.13

179

Table 5.3 shows the ratio of each element in comparison to Ti content which were calculated by dividing the atomic percentages from Table 5.2 by the at. % of Ti. The expected composition of the LST phase was $La_{0.15}Sr_{0.775}TiO_3$. The values of Sr, and La are above the expected values, this could be due to local fluctuations at the surface of the pellet or the presence of other compounds. A finding of particular interest is the large amount of carbon detected as this should not be present in pure LST- this could just be surface reacting with the air to form carbonates ect. though this excess carbon is not accompanied by an equal excess of oxygen which would be expected if the carbon originated from adsorbed CO_2 or carbonates.

In the ionic liquid synthesised powders carbon is also detected, but this is accompanied by an equal excess of oxygen, Table 5.4. This agrees with the findings from SDT in Figure 5.21b showing some degree of mass loss from the LST powder which was attributed to surface adsorbents such as CO_2 and H_2O. There is a much higher carbon content in the cold sintered pellet than the powder which indicated that the addition of the infill phase brings more carbon which is not expelled in the annealing process.

A high carbon content is also found on the surface of solid state synthesised powders, which is accompanied by an equal oxygen excess, Table 5.5. This carbon and oxygen excess is retained in the sintered pellet. This body of evidence suggests that, unlike in solid state pellets, the carbon found in the cold sintered pellet plays a more complicated role than forming carbonates, likely existing in the form of Sr and La carbides (as Sr and La were shown to be in excess), pure carbon or carbides. This is introduced from the carbon rich infill phase and not completely removed in the annealing process. XPS was also used to look at the Ti^{3+}/Ti ratio of the cold sintered pellets and how this changed when subjected to reducing conditions. It was hypothesised that the carbon in the infill could aid the reduction of the Ti species and reduce the temperature required to induce high electrical conductivity in LST.

Table 5.4 Atomic percentages of elements on the surface of ionic liquid synthesised LST powder determined from XPS.

Samples	Sr	La	Ti	O	C
IL synthesised powder (at. %)	15.9	5.3	16.6	55.8	6.3
	15.7	5.3	16.3	55.5	7.3
Average (at. %)	15.8	5.3	16.5	55.7	6.8
Ratio to Ti	0.96	0.32	1.00	3.38	0.41

Table 5.5 Atomic percentages of elements on the surface of solid state synthesised LST powder determined from XPS.

Samples	Sr	La	Ti	O	C
Solid state synthesised powder	12.4	7.2	13.8	54.4	12.2
	11.9	7.4	13.6	54.1	12.9
Average (at.%)	12.15	7.3	13.7	54.25	12.55
Ratio to Ti	0.89	0.53	1.00	3.96	0.92
Solid State Sintered Pellet 1350 ℃	14.3	2.6	12.8	53.5	16.8
	15.3	3	13.8	56.6	11.4
Average (at.%)	14.8	2.8	13.3	55.05	14.1
Ratio to Ti	1.11	0.21	1.00	4.14	1.06

5.3.11 Ti^{3+} Content in Cold Sintered Reduced LST

The electrical conductivity of LST is increased for thermoelectric applications by creating oxygen deficiency, which is compensated for by the reduction Ti^{4+} into Ti^{3+}.[15–17] Cao *et al.* showed that by sintering LST in direct contact with a sacrificial bed of carbon, rather than adjacent to the carbon the level of electrical conductivity was increased from 492 S/cm to 1288 S/cm at 57 ℃ after both had been sintered at 1427 ℃ for 24 h in 5% H_2/Ar .[16] Their XPS showed that by sintering the LST on the sacrificial carbon bed the Ti^{3+}/Ti percentage was 4.4 % compared to a Ti^{3+}/ Ti percentage of 3.2 % in the sample sintered without a carbon bed. This led to the hypothesis that the carbon retained within the cold sintered sample could aid the reduction process and produce the same Ti^{3+}/Ti percentage at a lower temperate than a solid state sintered counterpart.

When assessing XPS data some caveats must be made; XPS data can be sensitive to the fitting parameters used and so it is most reliable when comparing trends within a dataset rather than comparing values with other studies. XPS also only shows the Ti oxidation states at the surface of the pellets and does not represent the bulk's oxidation states. With this in mind Table 5.6 shows the percentage content of Ti^{3+} and Ti^{4+} in samples of LST which had been cold sintered then annealed in air at 800 ℃ for 2h, before a 6 h reducing step (ex situ reduced) or simultaneously annealed and reduced for 6 h (in situ reduced). These percentages are an average of at least two measurements, the raw data can be found in the Appendix (Table 5.A1).

The sample cold sintered and annealed in air, without a reducing step, forms a baseline to compare the rest of the samples with. This treatment resulted in pellets which appeared

completely white after annealing and so can be assumed to contain negligible level of Ti^{3+} and very low electrical conductivity, Figure 5.33. Whereas a high proportion of Ti^{3+} results in a black colouration of the material, such as in Figure 5.34. The solid state sintered pellet was produced to act as an "ideal" Ti^{3+} content reference point as this sintering procedure was modelled on that by Lu *et al.* who used a similar procedure to reduce LST and achieved a high electrical conductivity which gave the outstanding ZT of 0.41 at 700 ℃. Lu *et al.* sintered at 1500 ℃ for 6 h, though due to the dimension of the pellets the only available furnace went to 1350 and do the sintering time was extended to somewhat compensate for this. The aim of this study was to try to achieve the same level of Ti^{3+} by reducing the material in as low a temperature as possible in order to preserve the fine grained structure. It was anticipated that the retained carbon may help in reducing the required temperature to reduce the Ti species.

Table 5.6 XPS determined oxidation states of Ti in LST samples which have been cold sintered annealed then reduced (Ex-situ) or cold sintered and annealed whilst simultaneously reduced (In-situ)

Sample	Ti Oxidation State (%)	
	4+	3+
Cold Sintered, Annealed in air at 800 ℃	96.2	3.8
Cold Sintered, Annealed in Air at 800 ℃, Reduced at 800 ℃ (Ex-Situ)	94.8	5.2
Cold Sintered, Annealed in Air at 800 ℃, reduced at 1000 ℃ (Ex-Situ)	93.8	6.3
Cold Sintered, Annealed in reducing atmosphere 800 ℃ (In-Situ)	94.6	5.4
Cold Sintered, Annealed in reducing atmosphere 1000 ℃ (In-Situ)	94.3	5.8
Matrix and infill just pressed and reduced at 800 ℃ (In-Situ)	93.0	7.1
Solid State Sintered, Calcined 1100 ℃ 3h, Reduced 1350 ℃ 8h	92.3	7.7
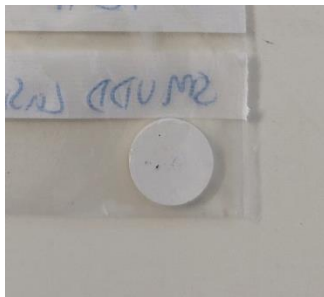
Figure 5.33 Image of Cold sintered LST pellet annealed in air at 800 ºC for 2h.

Figure 5.34 Oxygen deficient LST after reducing in 5% H_2/N_2 gas.

Observing the Ex-situ reduced samples the Ti^{3+} content is increased in both cases from the non-reduced sample and shows an increase in Ti^{3+} content with increasing temperature which is expected as oxygen loss is a thermally driven process. Moving to the in situ samples were the infill is converting to LST within a reducing atmosphere so oxygen content is low and likely further scavenged by the carbon present in the infill. A small increase in the 3+ content is seen in the sample reduced in situ at 800 ºC compared to the sample reduced ex-situ at 800 ºC, which would suggest the infill is having a positive effect on the strength of reducing conditions. However, there is a decrease in the 3+ content of the sample in-situ reduced at 1000 ºC compared with the sample ex-situ reduced at 1000 ºC, which contradicts the previous statement.

There is a much greater improvement in 3+ content in the sample which contained the infill and matrix but had not undergone cold sintering, and was just pressed then in-situ sintered. This has the closest Ti^{3+} content to that of the solid state sintered LST despite being reduced at a much lower temperature. All of the cold sintered samples and the just pressed sample were relatively low density (50-60 %) compared to the solid state sintered sample which rules out the idea that the just pressed sample may have had greater surface areas exposed by pores for oxygen to escape from compared to the cold sintered samples. The addition of water during cold sintering, in which the powders are ground together before pressing, may dissolve impurities such as chlorides which coat the powders' surfaces and provide a barrier though which it is more difficult for oxygen to escape from. The powder which formed the

just pressed sample had been milled in isopropanol then dried, so this likely would have had some coating effect also unless the impurities were less solvent or insoluble in isopropanol.

Due to the low density of the cold sintered pellets at this stage the electrical conductivity and the thermal conductivity measurements would not represent the bulk material and be dominated by the pores which reduce thermal conductivity and electrical conductivity. Therefore, further work is required to improve the density if reliable data of this kind is to be collected. Figure 5.35 shows the low thermal conductivity of the cold sintered pellets (IL-RCS) compared to ionic liquid synthesised powder sintered at 1325 °C (IL-HT) and solid state sintered pellets sintered at 1350 °C (S-HT).
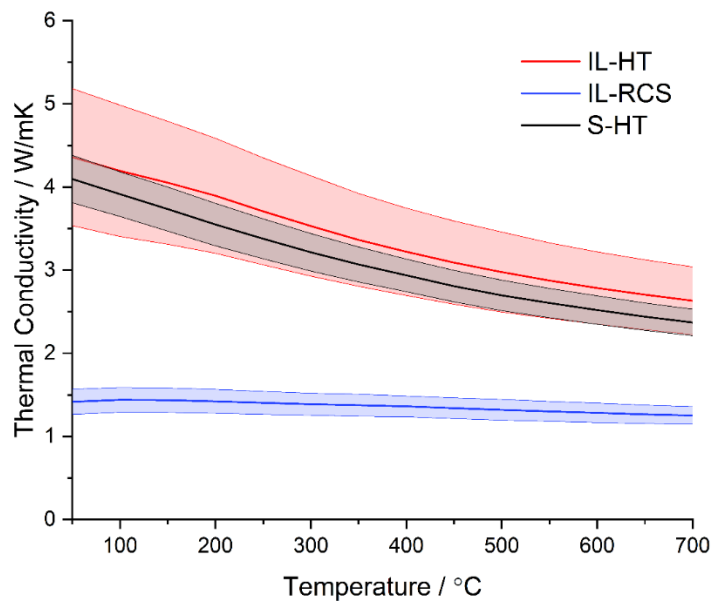
Figure 5.35 Thermal conductivity of pellets ionic liquid derived and cold sintered (IL-RCS), ionic liquid derived then 1325 º C sintered (IL-HT) and conventional solid state sintered (S-HT)

5.4 Conclusions

The initial development of a novel cold sintering technique, inspired by the reactive intermediate cold sintering method of Boston *et al.*, has been explored in this work.[6] Like reactive cold sintering an infill was used in the cold sintering which would transform into the desired phase upon annealing. In this novel method the reactive infill phase was a part calcined product the ionic liquid synthesis of LST.

An infill was chosen which had been fired past the point of the majority of mass loss in the ionic liquid process associated with the ionic liquid decomposition and combustion though just before the formation of the LST crystallisation in order to create an amorphous in fill phase that could fit between the gaps in the matrix phase and glue the material together without the need to sinter at high temperature. This led to the selection of a firing temperature of 420 ºC for the infill.

This was combined with the fully calcined LST matrix and water, which acted as a transient solvent in a cold sintering process. This was annealed at 800 ºC for 2 h in air to react the infill

into LST. This reaction was confirmed mostly through a visual colour change from grey to white as the infill was indistinguishable in XRD, being so amorphous.

An optimisation study of the pressure and temperature used in cold sintering found that a pressure of 355 MPa and a temperature of 210 ℃ gave the best results. Further increasing the pressure caused through thickness cracks in the cold sintered pellets leading to mechanical failure. Despite optimisation the final densities after annealing only reached ~55 % of the theoretical density of LST when calculated using the geometric method. This is far too low to be suitable for application in thermoelectric materials and low density reduced the electrical conductivity. It was determined that the Archimedes method, though gave much larger density values, was not suitable for this type of specimen due to the mix of open and closed porosity expected within this type of sample and so could not provide accurate results. This cold sintering method clearly requires further development to achieve higher densities. Without the addition of solvent or temperature applied whilst pressing a density of 46 % was achieved which showed that the cold sintering did improve the density somewhat compared to just pressing.

It was hypothesised that the low density was likely due to the mass and volume reduction of the infill upon annealing, which left pores in the cold sintered pellet. The mass loss from the infill was 18 wt.%. The volume change was not quantified but observed from SEM pores in the annealed pellet and the rational that an amorphous material is much less dense than a crystalline material. There was no contraction in the external dimensions of the pellet during annealing to account a reduction in material volume which meant that no matter the density achieved in the cold sintering stage this was reduced significantly after annealing.

The exact mechanisms of this cold sintering technique are not yet fully understood though it is thought that impurities on the surface of the powders (originating from the ionic liquid synthesis) played a role in preventing the growth of new LST grains from the infill onto existing LST grains. This came from observation of empty space surrounding agglomerates of particles which were likely matrix agglomerates which were surrounded by the infill after cold sintering and became empty space when the LST formed and was not able to stick to the surface of the existing LST.

NaCl and KCl were not observed in the matrix or powder XRD but appeared as a secondary phase on the surface of the pellets when exposed to water and isopropanol. Na, Cl and K are known to originate from the ionic liquid synthesis and so are likely present even when undetected in the XRD, which only shows crystalline phases present above a threshold of ~4 wt. %.

In other studies, NaOH and KOH have been shown to act as a flux which aids densification in $BaTiO_3$ during cold sintering.[12] This is because NaOH and KOH have a eutectic at 170 ℃ so molten hydroxides act as the transient solvent in cold sintering. Though Na an K are present which could react with water to form the hydroxides, the presence of chlorine prevents this and KCl and NaCl are formed. NaCl and KCl do form a liquid eutectic but at much higher temperature, between 567 and 776 ℃ depending on their ratio. This could act as a flux in the annealing step which is at 800 ℃ but the application of pressure is required and the current equipment used would not allow for such a high temperature to be applied while pressing. This could be explored in future work.

The carbon content detected in the ionic liquid powder, which is likely even more abundant in the infill, shows a promising opportunity to lower the reducing temperature required to increase the electrical conductivity in the LST for thermoelectric applications. Lowering this temperature further reduces the embodied energy of the material and preserves the small grains. However, the cold sintering process appeared to interfere with the Ti species reduction, possibly due to the present of the impurities which when ground together with water, evenly coat the particles which provides a barrier for oxygen to escape.

5.5 Future Work

The immediate next steps of this project should be as follows:

Firstly, remove impurities (K, Na, Cl) from the starting material. This could be done by washing the matrix with ethanol (the infill cannot be washed as it is likely this contains soluble mobile ions which would be removed also) or synthesising the material with a purer starting Ionic Liquid. By removing impurities from the matrix powder the mechanisms of this sintering technique can be more easily observed. There is a possibility that the impurities are helping the densification, perhaps by acting as a flux, in which case this would reveal more about the mechanisms and provide a path for improvement.

Currently the main issue with this method is the low density which appears to be caused by loss of mass and volume during the annealing process where no external shrinkage occurs to fill these voids. The mass loss is already quantified though the volume is not, therefore, a study should be conducted to quantify this by making a pellet purely from the infill and observing the volume change when taken to high temperatures e.g. 1500 ℃ and perhaps additionally a mercury impregnation study when sintered to 800 ℃.

If this does indeed reveal that the infill loses significant volume during crystallisation to the LST phase, then three things should be considered: either using an infill which does not lose volume, encouraging compaction during the annealing process by additional heat (the aim of cold sintering is to keep the temperature as low as possible and so if this becomes >1000 ℃ then this largely negates the benefit of the method), or using less infill to reduce the volume loss.

The final suggestion for future work would be to encourage the recrystallization to occur during the cold sintering step rather than in the anneal. This would mean that pressure is applied as the volume is reducing, hopefully helping the densification. Mottram *et al.* showed that the crystallisation of LST in the ionic liquid method begins ~400 ℃ and is complete by 600 ℃. If at least some of this occurred during the cold sintering stage, then this would reduce the volume loss in the annealing step which creates pores. This may require more specialised equipment to reach such temperatures in the hot press set-up, which was certainly not available in this work.

Finally, water is known to preferentially leach A-site ions from the surface of strontium oxide leaving an amorphous titania layer on the surface. In order to avoid this, other solvents should be considered which congruently dissolve the surface. This could be achieved by altering the

pH. It is known that a pH 10 passivates the dissolution of Ba in $BaTiO_3$ and so a similar tactic could be employed to control the dissolution rates of A-site ions in the doped $SrTiO_3$.[18]

5.6 References

1. Buscaglia, M. T. *et al.* Effect of nanostructure on the thermal conductivity of La-doped SrTiO 3 ceramics. *J. Eur. Ceram. Soc.* **34**, 307–316 (2014).

2. Ohta, S., Ohta, H. & Koumoto, K. Grain Size Dependence of Thermoelectric Performance of Nb-Doped SrTiO3 Polycrysals. *J. Ceram. Soc. Japan* **114**, 102–105 (2006).

3. Lu, Z., Zhang, H., Lei, W., Sinclair, D. C. & Reaney, I. M. High-Figure-of-Merit Thermoelectric La-Doped A-Site-Deficient SrTiO 3 Ceramics. *Chem. Mater.* **28**, 925–935 (2016).

4. Guo, J. *et al.* Cold Sintering: A Paradigm Shift for Processing and Integration of Ceramics. *Angew. Chemie* **128**, 11629–11633 (2016).

5. Faouri, S. S. *et al.* High quality factor cold sintered Li2MoO4BaFe12O19 composites for microwave applications. *Acta Mater.* **166**, 202–207 (2019).

6. Boston, R. *et al.* Reactive intermediate phase cold sintering in strontium titanate. *RSC Adv.* **8**, 20372–20378 (2018).

7. Boston, R., Foeller, P. Y., Sinclair, D. C. & Reaney, I. M. Synthesis of Barium Titanate Using Deep Eutectic Solvents. *Inorg. Chem.* **56**, 542–547 (2017).

8. Mottram, L., Martin, D. Z. C., Reeves-McLaren, N. & Boston, R. Low-temperature crystallization of La 0.15 Sr 0.775 TiO 3 using ionic liquids. *J. Am. Ceram. Soc.* **101**, 4468–4471 (2018).

9. Karczewski, J., Miruszewski, T., Bochentyn, B. & Kusz, B. Determination of ionic conductivity in the Bi-Si-O and Pb-Si-O glasses. *Mater. Sci.* **35**, 681–686 (2017).

10. Guo, H., Guo, J., Baker, A. & Randall, C. A. Hydrothermal-Assisted Cold Sintering Process: A New Guidance for Low-Temperature Ceramic Sintering. *ACS Appl. Mater. Interfaces* **8**, 20909–20915 (2016).

11. Francis, L. F. Powder Processes. in *Materials Processing* (ed. Francis, L. F. B. T.-M. P.) 343–414 (Elsevier, 2016). doi:10.1016/B978-0-12-385132-1.00005-7.

12. Tsuji, K. *et al.* Single step densification of high permittivity BaTiO3 ceramics at 300 ºC. *J. Eur. Ceram. Soc.* **40**, 1280–1284 (2020).

13. Devyatkin, S. *Interaction of Oxides and Molten Alkalis, Products of Reaction and Application.* (2015).

14. Broström, M., Enestam, S., Backman, R. & Mäkelä, K. Condensation in the KCl–NaCl system. *Fuel Process. Technol.* **105**, 142–148 (2013).

15. Rahman, J. U. *et al.* Oxygen vacancy revived phonon-glass electron-crystal in SrTiO3. *J. Eur. Ceram. Soc.* **39**, 358–365 (2019).

16. Cao, J. *et al.* Modulation of Charge Transport at Grain Boundaries in SrTiO 3 : Toward a High Thermoelectric Power Factor at Room Temperature. *ACS Appl. Mater. Interfaces* **13**, 11879–11890 (2021).

17. Akin, I., Li, M., Lu, Z. & Sinclair, D. C. Oxygen-loss in A-site deficient Sr 0.85 La 0.10 TiO 3 perovskite. *RSC Adv.* **4**, 32549–32554 (2014).

18. Adair, J. H., Crampo, J., Mandanas, M. M. & Suvaci, E. The role of material chemistry in processing BaTiO 3 in aqueous suspensions. *J. Am. Ceram. Soc.* **89**, 1853–1860 (2006).

5.7 Appendix

Table 5.A1 XPS Data

Sample	Treatment	Ti Oxidation State (%)	
		4+	3+
Baseline i	Cold Sintered, Annealed in air at 800 °C	96.4	3.6
Baseline ii		96.0	4.0
CSES800a i	Cold Sintered, Annealed in Air, Reduced at 800 °C	95.5	4.5
CSES800a ii		95.3	4.8
CSES800b i		94.1	5.9
CSES800b ii		94.4	5.6
CSES1000a i	Cold Sintered, Annealed in Air, reduced at 1000 °C	93.9	6.1
CSES1000a ii		94.3	5.7
CSES1000b i		93.1	6.9
CSES1000b ii		93.7	6.3
CSIS800a i	Cold Sintered, Annealed in reducing atmosphere 800 °C	94.3	5.7
CSIS800 a ii		95.7	4.3
CSIS 800a iii		94.4	5.6
CSIS 800a iv		95.2	4.8
CSIS800 b i		93.6	6.4
CSIS800 b ii		94.6	5.4
CSIS1000a i	Cold Sintered, Annealed in reducing atmosphere 1000 °C	94.1	5.9
CSIS1000a ii		94.5	5.6

NCSIS800a i	Matrix and infill just pressed and annealed at 800 ℃	94.0	6.0
NCSIS800a ii		92.7	7.4
SSI350 i	Solid State Sintered, Calcined 1100 ℃ 3h, Reduced 1350 ℃ 8h	92.1	7.9
SSI350 ii		92.5	7.5

Pre- annealed pellet
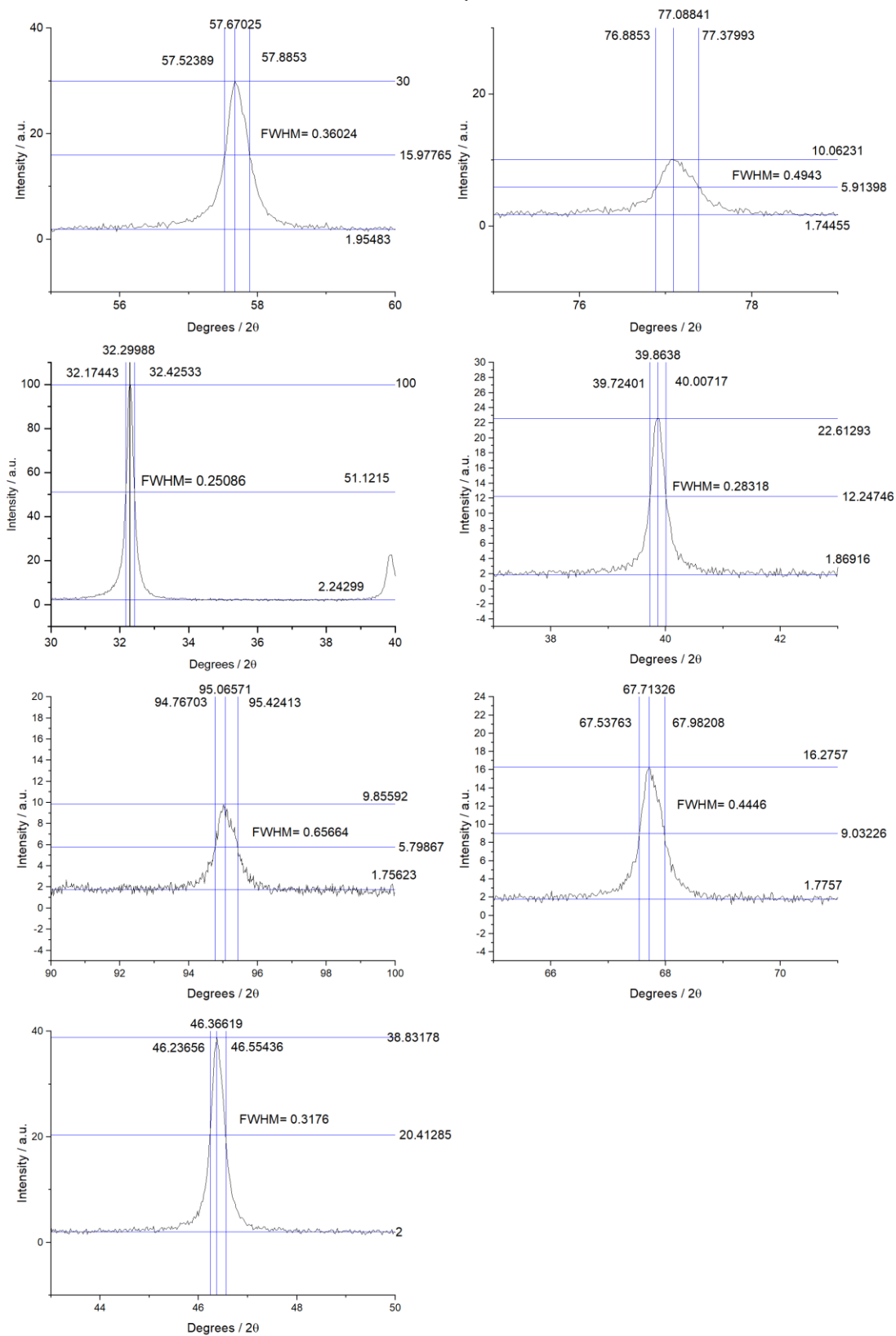
Figure 5.A1 Values input into the Scherer equation for non-annealed col sintered pellets
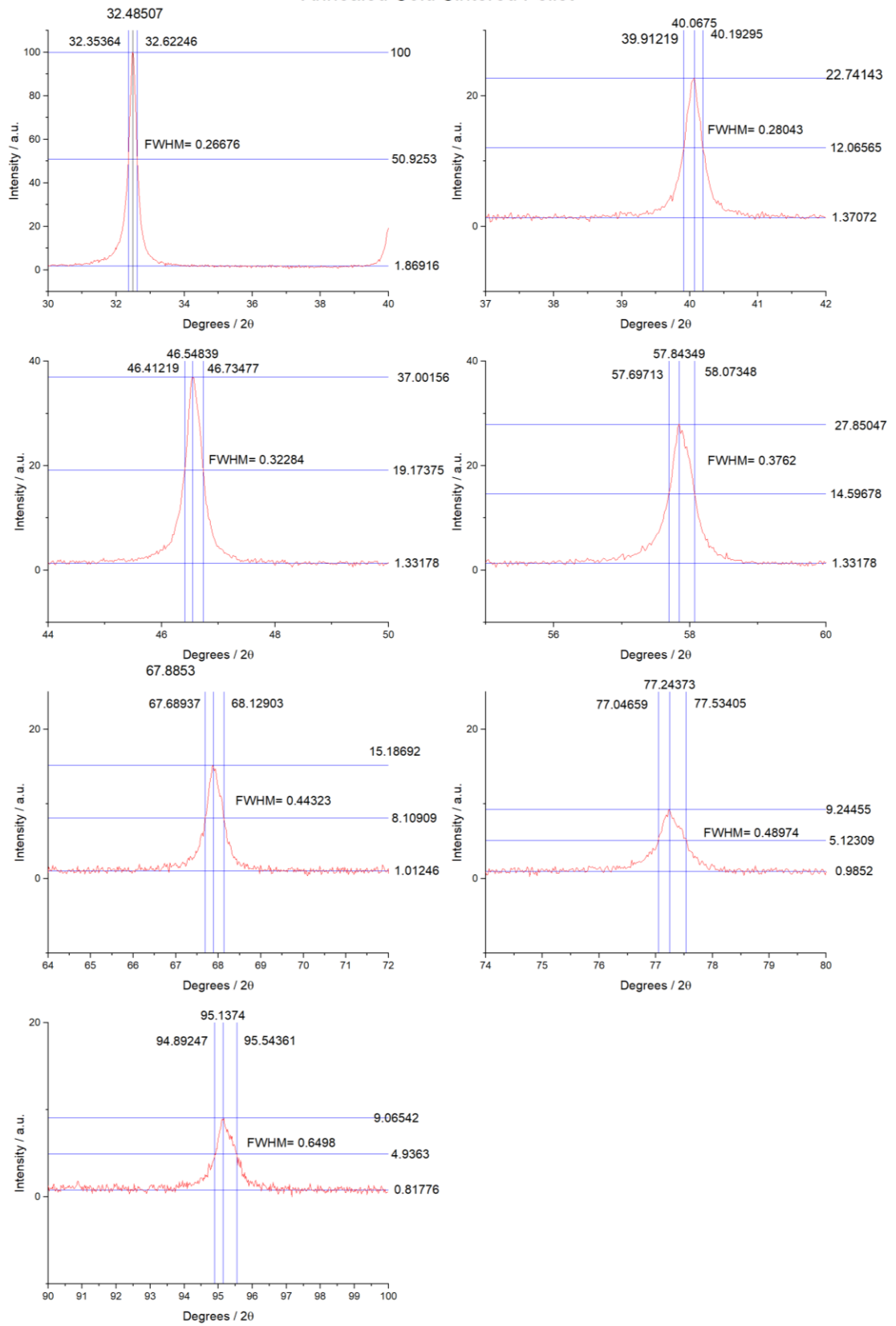
Figure 5.A2 Values input into the Scherer equation for annealed cold sintered pellets

6.0 Overall Conclusions

The ionic liquid synthesis of $La_{0.15}Sr_{0.775}TiO_3$ (LST) produced a cubic perovskite phase with particle size 97 ± 33 nm after calcining at 800 ℃. This was much smaller than that could be achieved through solid state sintering.[1] Using the ionic liquid emimOAc from Sigma Aldrich with a purity >95% resulted in impurities of NaCl and KCl visible in XRD analysis and K, Na and Cl detected in EDS. These impurities likely originate from the synthesis process of the ionic liquid itself.[2] Ionic liquid synthesis of ceramic material was applied to two branches of research: complex doping and a novel cold sintering method.

First, this method was successfully used to synthesise the complex stoichiometry of $La_{0.15-x}Eu_xSr_{0.775}TiO_{3-\delta}$ at 800 ℃ which also produced nanoscale particles. The addition of europium reduced the lattice parameter in calcined and reduced materials. Adding Eu appeared to reduce the thermal conductivity only when x exceeded a value of 0.05. This also led to reduction of electrical conductivity and an increase in the absolute value of the Seebeck coefficient. These effects are believed to be caused by increased scattering due to the large mass of Eu compared to Sr and La. There may be a promising increase in ZT of the composition x = 0.05, though this needs to be confirmed by a repeat of the electronic measurement.

The electrical conductivities observed as a function of temperature revealed the symptoms of a material with restive grain boundaries in all of the samples with and without europium. This is thought to be due to impurities originating from the ionic liquid. This lead to a reduction of the electrical conductivity at low temperatures. At higher temperatures ~ 400 ℃ the effect of resistive grain boundaries was overcome and electrical conductivity of the LST returned to comparable values with Muta *et al.* but not so high as that reported by Lu *et al.* [1,3]

Secondly, a novel cold sintering technique has been proposed in this work, inspired by the reactive intermediate cold sintering method of Boston *et al.*[4] This was aimed to provide a new solution for the cold sintering of complex stoichiometry materials with incongruent dissolution rates. Like Reactive Cold Sintering, an infill was used in the cold sintering which would transform into the desired phase upon annealing. In this novel method the reactive infill phase was a part calcined product the ionic liquid synthesis of LST.

Despite optimisation the final densities after annealing only reached ~55 % of the theoretical density of LST. It was hypothesised that the low density was likely due to the mass and volume reduction of the infill upon annealing, which left pores in the cold sintered pellet. The mass loss from the infill was 18 wt.%. The volume change was not quantified but observed from SEM pores in the annealed pellet and the rational that an amorphous material is much less dense than a crystalline material. There was no contraction in the external dimensions of the pellet during annealing to account a reduction in material volume which meant that no matter the density achieved in the cold sintering stage this was reduced significantly after annealing.

The exact mechanisms of this cold sintering technique are not yet fully understood and must be further explored in future work. In this work it is thought that impurities on the surface of the powders (originating from the ionic liquid synthesis) played a role in preventing the growth of new LST grains from the infill onto existing LST grains, leading to large pores.

This came from observation of empty space surrounding agglomerates of particles which were likely matrix agglomerates which were surrounded by the infill after cold sintering and became empty space when the LST formed and was not able to stick to the surface of the existing LST. Methods to reduce the porosity thereby increasing the density in this method have been proposed in the Future work.

6.1 References

1   Z. Lu, H. Zhang, W. Lei, D. C. Sinclair and I. M. Reaney, *Chem. Mater.*, 2016, **28**, 925–935.

2   D. Berthier, A. Varenne, P. Gareil, M. Digne, C. P. Lienemann, L. Magna and H. Olivier-Bourbigou, *Analyst*, 2004, **129**, 1257–1261.

3   H. Muta, A. Ieda, K. Kurosaki and S. Yamanaka, *Mater. Trans.*, 2005, **46**, 1466–1469.

4   R. Boston, J. Guo, S. Funahashi, A. L. Baker, I. M. Reaney and C. A. Randall, *RSC Adv.*, 2018, **8**, 20372–20378.

7.0 Supplementary Information

7.1 XPS Reports

Below are the verbatim reports provided by Deborah Hammond which detail the collection of XPS data

Sheffield Surface Analysis Centre

surfaceanalysis.group.shef.ac.uk

Customer: Stephanie Mudd

Date: 5th June 2023

Analysis: XPS

XPS Analyis of $La_{0.15}Sr_{0.775}TiO_3$ Pellets (SSAC950n1)

Introduction

Pellets of $La_{0.15}Sr_{0.775}TiO_3$ have been prepared using an ionic liquid synthesis method before being calcined at 800 °C and sintered at 800-1325 °C under a reducing 5%H2/95%N2 atmosphere. The pellets have been submitted for XPS analysis with the oxidation states of titanium being or particular interest.

Experimental

The submitted samples were as described in the table below.

Samples
Baseline
CSES800a
CSES800b
CSES1000a
CSES1000b
CSIS800 a
CSIS800 b
CSIS1000a
NCSIS800a
SSI350

All analyses have been collected from the surface of the pellets as submitted and without any additional preparation. Consequently, the data will include effects by which the surface is different from the pellet bulk.

To avoid differential charging, the samples were electrically isolated from the sample holder by using a paper label insert between the samples and the sample holder. The pellets were then stuck to the paper label using double sided tape. The analyses were carried out using a Kratos Supra instrument with a monochromated aluminium source, and two analysis points per sample, of area 700 μm by 300 μm. For one area of each pair only Ti 2p and O 1s high resolution scans were collected. For the second area survey scans were collected between 1200 to 0 eV binding energy, at 160 eV pass energy, 1 eV intervals, and 300 seconds/sweep with one sweep being collected, and high-resolution Na 1s, La 3d, O 1s, Ti 2p, C 1s, Cl 2p and Sr 3d spectra collected at 20 eV pass energy and 0.1 eV intervals over an appropriate energy range, with one 300 second sweep for all spectra except the Ti 2p for which four sweeps were collected to improve the signal to noise for curve fitting and because the energy range was extended to include the Ti 2p satellites at higher binding energy. The C 1s spectrum energy range was extended to include K 2p peaks if present. Charge neutralisation of 0.4 A was used throughout.

A second pair of analyses were collected from CSIS800a as the initial Sr 3d data were significantly different to the other samples, but the second set of data was consistent with the first and so assumed to be okay.

The data collected was calibrated in intensity using a transmission function characteristic of the instrument to make the values instrument independent. The data can then be quantified using

theoretical Schofield relative sensitivity factors modified to account for instrument geometry, variation in penetration depth with energy and the angular distribution of the photoelectrons. The high-resolution spectra were all calibrated in eV by fixing the main C 1s peak to be 285.0 eV.

Results and Discussion

Although the titanium oxidation states were of most interest an overview of the samples as a whole has also been included. Table 1 shows the surface composition of each sample determined from the high-resolution scans collected. The survey scans were used to determine which elements were present and high-resolution spectra were collected based on recommendations from the Thermoscientific web site (xpssimplified.com). The elements detected were those expected - being lanthanum, strontium, titanium, oxygen, potassium, chlorine and carbon. The expected elements contribute a great many peaks to the XPS survey scans, consequently it is quite possible that small concentrations of other elements have been missed due to overlap with transitions from the bigger contributors.

These surface compositions have been determined by considering the signal intensity above a fitted background, with an adjustment for chlorine as described below. Note for the titanium spectra, the background has not been extended to include the satellite peaks seen at higher binding energy, an example of which is shown in Figure 1. Satellite peaks such as these have been reported in the literature, e.g. refs 1 and 2, but are not typically alluded to, and are not included in the recommended fitting for Ti 2p which has been used to determine the concentrations of Ti oxidation states present (ref 4). These satellite peaks may be of interest in the current context but further literature searching needs to be carried out.

Table 2 shows the La:Sr:Ti ratios determined from the XPS data, which show some variation between samples.

The results of curve fitting the La 3d, Sr 3d, C1s, O 1s and Cl 2p high resolution spectra are all given in Appendix A.

The lanthanum $3d^{5/2}$ peak positions and the extent of multiplet splitting (ref 3) suggests the lanthanum is present only as La_2O_3.

The chlorine high resolution spectra appeared to show four peaks. The pair of peaks at the higher binding is consistent with where metal chloride peaks would be expected and is thought to be the Cl 2p doublet. The lower binding energy pair is thought to actually be too low in binding energy to be chlorine but is instead the La 4p transition. Consequently, the chlorine contribution would be

exaggerated if only the intensity above the background was used. Instead, the Cl 2p curve fit (Table A6) has been used to determine how much of this intensity is chlorine and how much is lanthanum and the concentrations in Table 1 have been adjusted appropriately. This suggests that whilst all samples showed some chloride, the CSIS 800 samples, both a and b, showed a lot of chloride.

For most samples the binding energy for the Sr 3d$^{5/2}$ peak is consistent with SrO. For samples CSIS800 there appeared to be a second Sr environment. This was still seen when the analysis for this sample was repeated. However, given the very high surface chloride concentration seen for sample CSIS800a this second Sr environment could be $SrCl_2$ and this would be approximately consistent with the binding energies seen. The CSIS800 samples, both a and b, appear to have an increased surface strontium concentration compared to the baseline.

Table 1. Surface composition (at%) determined from high resolution XPS scans

Sample	Na	La	O	Ti	C	K	Cl	Sr
Baseline i	1.7	3.6	48.0	14.4	16.2	0.9	2.6	12.7
CSES800a i	2.7	2.5	47.1	15.4	18.6	1.0	1.3	11.4
CSES800b i	2.3	2.5	47.4	15.5	17.8	0.9	1.3	12.2
CSES1000a i	1.7	2.4	49.4	14.5	18.1	0.3	1.2	12.3
CSES1000b i	1.6	2.5	48.9	15.1	17.8	0.4	1.2	12.5
CSIS800 ai	0.8	1.7	39.7	10.4	21.0	0.3	9.9	16.2
CSIS 800a iii	1.6	2.1	44.8	11.8	11.7	0.3	10.4	17.3
CSIS 800a iv	1.6	2.1	42.9	11.8	11.6	0.3	11.8	17.8
CSIS800 b i	0.8	2.0	43.0	12.2	20.8	0.2	6.0	15.0
CSIS1000a i	1.2	2.0	48.0	12.6	22.6	<0.1	1.2	12.5
NCSIS800a i	2.0	1.8	46.0	15.8	18.4	0.7	1.2	14.1
SSI350 i	0.6	2.3	45.3	11.8	25.6	<0.1	1.1	13.2
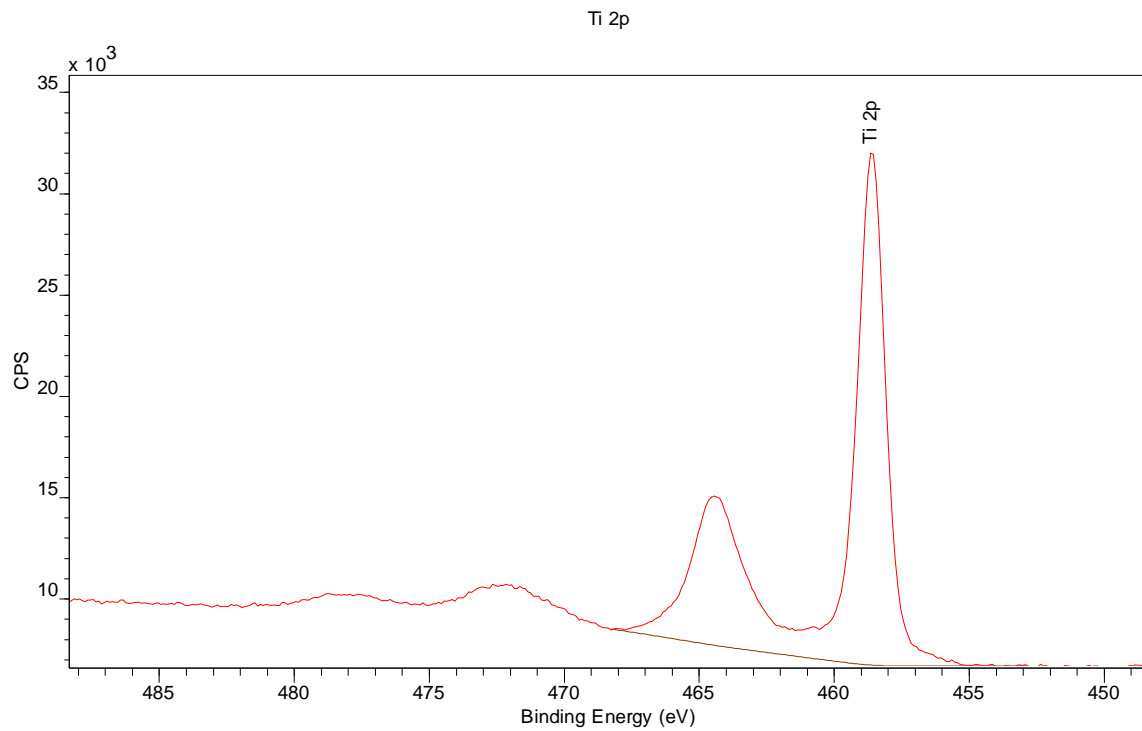
Figure 1. Example Ti 2p spectrum (baseline, area i) showing satellites and background used to determine surface composition.

Table 2. La:Sr:Ti ratios suggested by the surface composition data shown in Table 1

Sample	La	Sr	Ti
Baseline i	0.25	0.88	1
CSES800a i	0.17	0.74	1
CSES800b i	0.16	0.79	1
CSES1000a i	0.17	0.85	1
CSES1000b i	0.17	0.82	1
CSIS800 ai	0.17	1.55	1
CSIS 800a iii	0.18	1.47	1

CSIS 800a iv	0.17	1.51	1
CSIS800 b i	0.17	1.24	1
CSIS1000a i	0.16	0.99	1
NCSIS800a i	0.12	0.89	1
SSI350 i	0.19	1.12	1

The surface carbon concentration is small, and shows a small carbonate component which amounts to between 3% and 10% of the total surface. SrO reacts readily with CO_2 in the atmosphere to make $SrCO_3$, so there may also be a small concentration of strontium carbonate as well as strontium oxide.

It was of most interest to know the concentrations of different titanium oxidation states and the method published by Mark Biesinger has been used to determine this (reference 4). The major peak in the Ti 2p spectra falls at 458.6 ± 0.1 eV eV binding energy, consistent with Ti(IV) as would be expected. Any titanium metal, or Ti(0) would be expected at 454.1 eV, and Ti(III) and Ti(II) are expected between these two extremes at approximately 457.2 eV and 455.4 eV respectively. As can be seen from Figure 1 and the example Ti 2p curve fit shown in Figure 2 there is only a small intensity to the lower binding energy side of the main Ti(IV)peak. The very low intensity at binding energies consistent with Ti(0) or Ti(II) suggest neither is present at a detectable level. The spectra have been curve-fitted on the assumption there is Ti(III). However, there is insufficient Ti(III) to account for the high intensity between the two main peaks of the TiO2 doublet (Ti $2p^{3/2}$ and Ti $2p^{1/2}$). An additional doublet has been added to account for this. It is expected this is Ti(IV) related. The specific curve fits are given in Appendix A. The concentrations of Ti(IV) and Ti(III) they suggest are given in Table 3. There is some variation with experimental treatment.
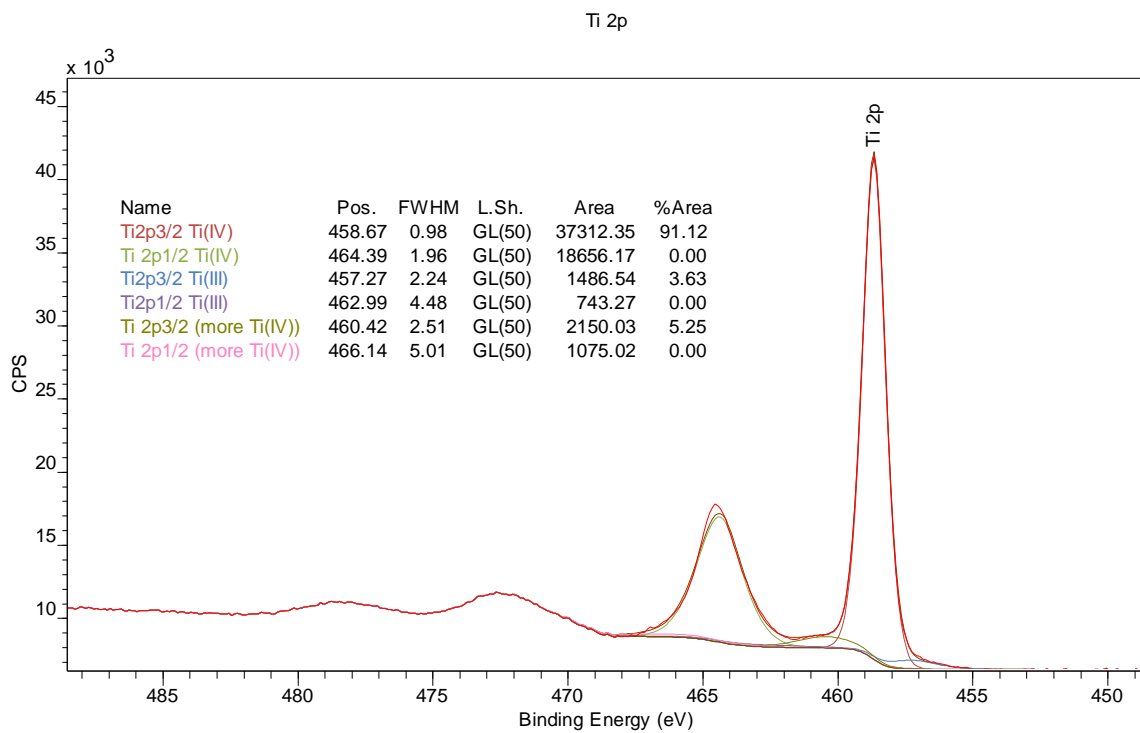
Figure 2. Example Ti 2p spectrum (baseline, area i) showing Ti(IV) and Ti(III) curve fit

Table 3. Ti(III) and Ti(IV) concentrations determined by curve fitting the Ti 2p spectra

Sample	Ti(IV)	Ti(III)
Baseline i	96.4	3.6
Baseline ii	96.0	4.0
CSES800a i	95.5	4.5
CSES800a ii	95.3	4.8
CSES800b i	94.1	5.9
CSES800b ii	94.4	5.6
CSES1000a i	93.9	6.1
CSES1000a ii	94.3	5.7
CSES1000b i	93.1	6.9
CSES1000b ii	93.7	6.3
CSIS800 ai	94.3	5.7
CSIS800 a ii	95.7	4.3
CSIS 800a iii	94.4	5.6
CSIS 800a iv	95.2	4.8
CSIS800 b i	93.6	6.4
CSIS800 b ii	94.6	5.4
CSIS1000a i	94.1	5.9
CSIS1000a ii	94.5	5.6
NCSIS800a i	94.0	6.0
NCSIS800a ii	92.7	7.4
SSI350 i	92.1	7.9

SSI350 ii	92.5	7.5

Conclusions

- The titanium oxide on the surface of the pellet was found to be predominantly Ti(IV) with a small concentration of Ti(III). However, Ti(0) and Ti(II) were not detected.
- Strontium was predominantly SrO, although there may also have been a small strontium carbonate component.
- On sample CSIS800a there was probably also strontium chloride, $SrCl_2$.
- Lanthanum was present predominantly as La_2O_3.
- Some variation in La:Sr:Ti ratio was seen as a function of treatment

References

1. X-ray Photoelectron Spectroscopy (XPS) studies of clean and hydrated TiO2 (rutile) surfaces. Volume 68, number 2.3 Chemical Physics Letters 1-5, December 1979
2. X-ray photoelectron spectroscopy data from lightly Pd doped TiO2 anatase nanoparticles Surf. Sci. Spectra 27, 024011 (2020); https://doi.org/10.1116/6.0000407 Mark H. Engelhard, Donald R. Baer, and Linxiao Chen
3. https://www.thermofisher.com/uk/en/home/materials-science/learning-center/periodic-table/lanthanide-rare-earth/lanthanum.html
4. M.C. Biesinger, L.W.M. Lau, A. Gerson, R.St.C. Smart, Resolving Surface Chemical States in XPS Analysis of First Row Transition Metals, Oxides and Hydroxides: Sc, Ti, V, Cu and Zn, *Applied Surface Science*, 257 (2010) 887-898.

http://www.xpsfitting.com/2008/09/titanium.html

Appendix A

Table A1. Results of curve-fitting the C 1s high resolution spectra

Sample	B.E. (eV)	%Area	B.E. (eV)	%Area	B.E. (eV)	%Area	B.E. (eV)	%Area
Baseline i	285.0	73.3	286.6	16.5	288.7	4.4	289.6	5.8
CSES800a i	285.0	73.6	286.6	16.6	288.6	4.5	289.6	5.3
CSES800b i	285.0	75.7	286.6	15.8	288.7	3.9	289.5	4.6
CSES1000a i	285.0	73.8	286.6	16.5	288.6	4.0	289.6	5.7
CSES1000b i	285.0	73.3	286.5	16.8	288.4	4.5	289.5	5.4
CSIS800 ai	285.0	73.0	286.8	13.0	288.6	3.2	289.7	10.7
CSIS800 b i	285.0	74.4	286.9	13.4		0.0	289.5	12.1
CSIS1000a i	285.0	77.6	286.9	10.6	288.9	3.0	289.8	8.7
NCSIS800a i	285.0	80.2	286.7	14.0		0.0	289.1	5.7
SSI350 i	285.0	78.1	286.5	9.3	288.5	3.5	289.6	9.1
CSIS 800a iii	285.0	66.0	286.8	13.2		0.0	290.0	20.8
CSIS 800a iv	285.0	61.6	286.9	17.6		0.0	289.9	20.8

C 1s

Name	Pos.	FWHM	L.Sh.	Area	%Area
C 1s	285.00	1.31	GL(30)	8019.90	69.55
C 1s	286.57	1.31	GL(30)	1809.94	15.69
C 1s	289.64	1.31	GL(30)	637.04	5.52
K2p	293.16	1.26	GL(30)	1544.25	3.39
K2p	295.88	1.26	GL(30)	772.13	1.69
C 1s	288.69	1.31	GL(30)	478.76	4.15

Sr 3p1/2

C 1s

K2p

CPS

Binding Energy (eV)
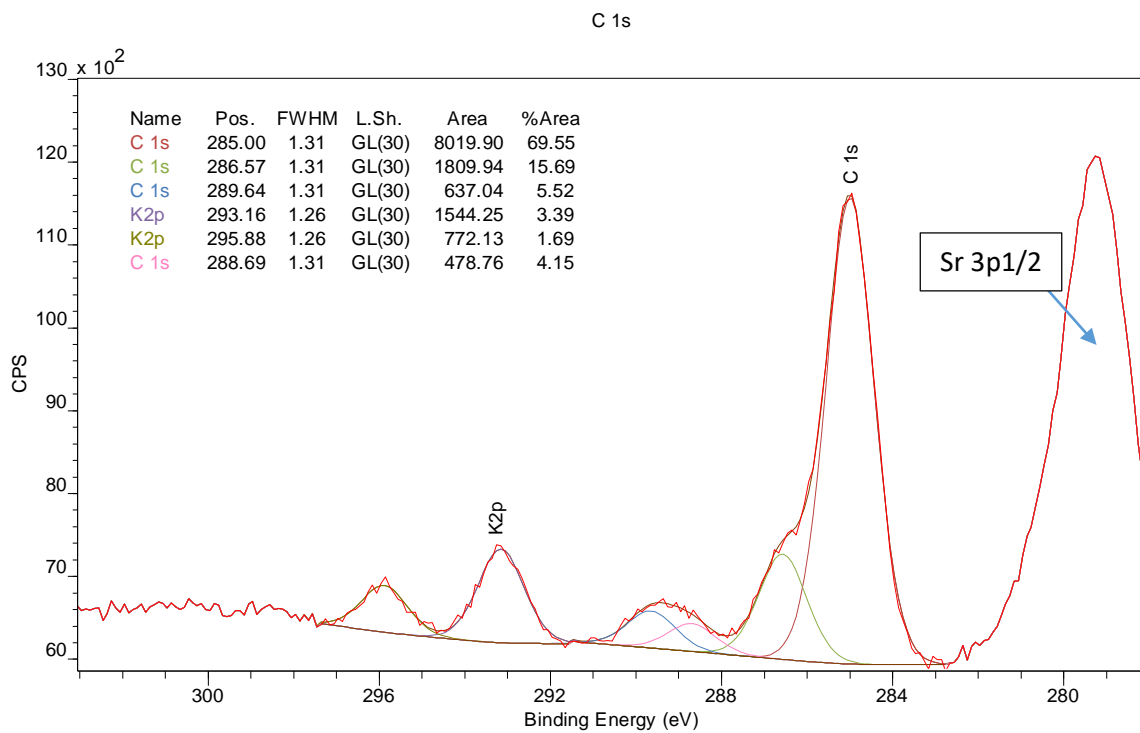
Figure A1. Example fitted C 1s spectrum from baseline sample, area i

Table A2. Results of curve fitting the Sr 3d high resolution spectra

Sample	B.E. (eV)	%At Conc	B.E. (eV)	%At Conc	B.E. (eV)	%At Conc	B.E. (eV)	%At Conc
Baseline i	133.0	60.0	134.8	40.0				
CSES800a i	133.0	60.0	134.7	40.0				
CSES800b i	133.0	60.0	134.8	40.0				
CSES1000a i	133.0	60.0	134.8	40.0				
CSES1000b i	133.1	60.0	134.8	40.0				
CSIS800 ai	133.0	39.1	134.7	26.1	134.0	20.9	135.7	13.9
CSIS 800a iii	133.3	37.3	135.0	24.8	134.2	22.8	136.0	15.2
CSIS 800a iv	133.3	37.1	135.0	24.7	134.3	22.9	136.1	15.2
CSIS800 b i	133.2	60.0	134.9	40.0				
CSIS1000a i	133.1	60.0	134.9	40.0				
NCSIS800a i	132.9	60.0	134.7	40.0				
SSI350 i	132.9	60.0	134.6	40.0				
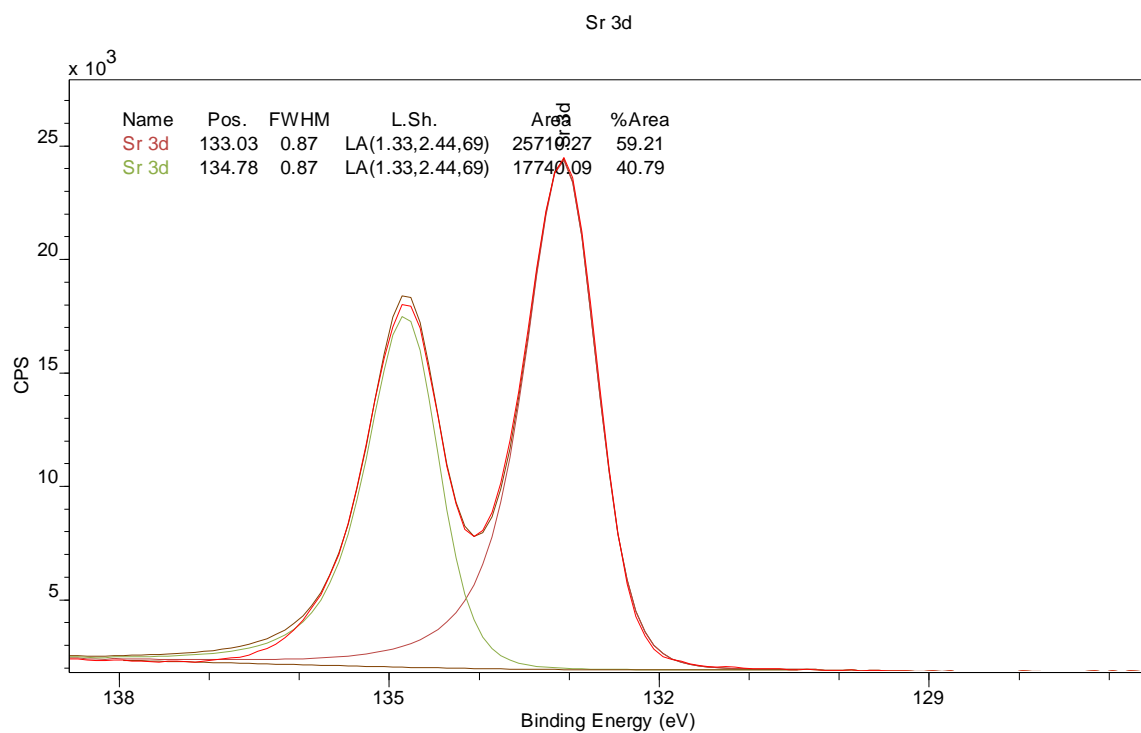
Figure A2. Example fitted Sr 3d spectrum from baseline sample, area i

Table A3. Results of curve fitting the La 3d high-resolution spectra, including the multiplet splitting – fitting of limited physical value

Sample	B.E. (eV)	%At Conc	B.E. (eV)	%At Conc	B.E. (eV)	%At Conc
Baseline i	834.5	29.6	837.1	50.7	839.1	19.7
CSES800a i	834.5	28.3	837.0	52.8	839.1	18.9
CSES800b i	834.5	33.5	837.1	44.2	839.0	22.3
CSES1000a i	834.5	32.6	837.0	45.7	839.0	21.7
CSES1000b i	834.4	33.9	837.0	43.6	839.0	22.6
CSIS800 ai	834.6	34.4	837.2	42.7	839.2	22.9
CSIS 800a iii	834.6	35.9	836.5	25.7	839.0	38.5
CSIS 800a iv	834.6	36.8	836.6	25.3	839.0	38.0
CSIS800 b i	834.5	35.9	837.1	40.2	839.1	23.9
CSIS1000a i	834.5	32.3	837.1	46.3	839.1	21.5
NCSIS800a i	834.7	33.1	837.5	44.9	839.4	22.0
SSI350 i	834.3	31.5	836.8	47.5	838.9	21.0
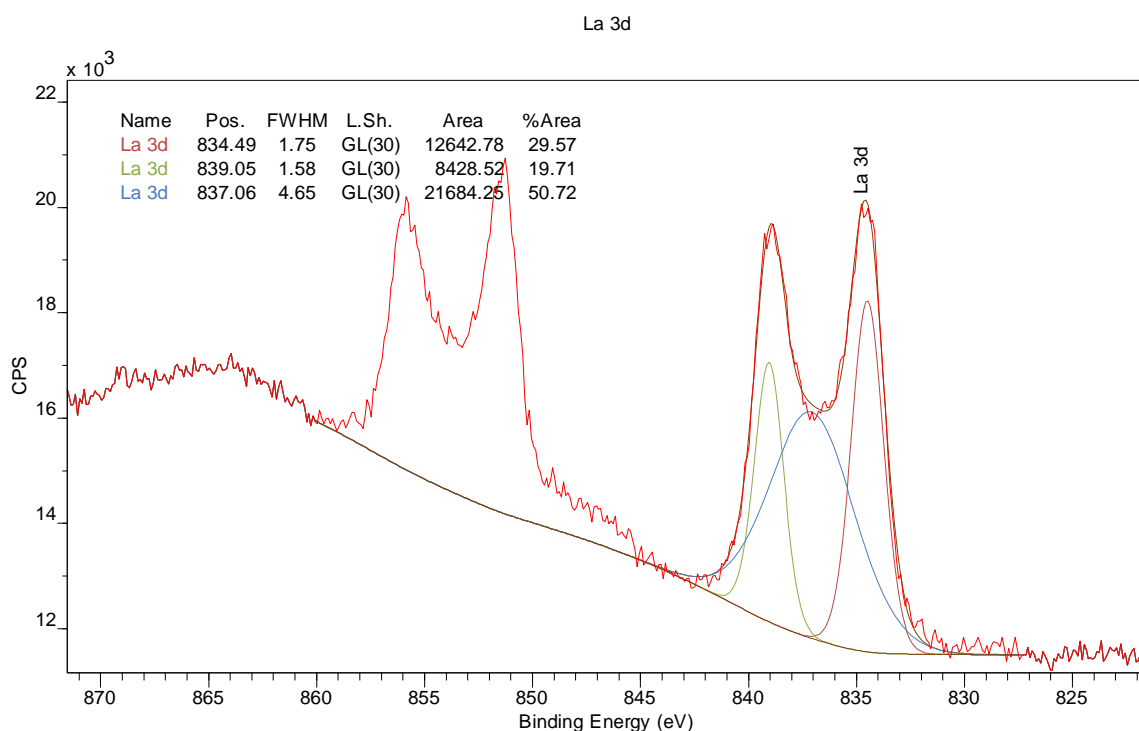
Figure A3. Example fitted La 3d spectrum from baseline sample, area i

Table A4. Results of curve fitting the Ti 2p high resolution spectra

Sample	Ti2p$^{3/2}$ Ti(IV)		Ti 2p$^{3/2}$ (more Ti(IV))		Ti2p$^{3/2}$ Ti(III)	
	B.E. (eV)	%At Conc	B.E. (eV)	%At Conc	B.E. (eV)	%At Conc
Baseline i	460.4	5.3	458.7	91.1	457.3	3.6
Baseline ii	460.3	5.1	458.6	90.9	457.2	4.0
CSES800a i	460.0	5.9	458.6	89.6	457.2	4.5
CSES800a ii	459.9	5.5	458.5	89.7	457.1	4.8
CSES800b i	459.9	6.0	458.6	88.1	457.2	5.9
CSES800b ii	459.9	5.8	458.6	88.6	457.2	5.6
CSES1000a i	459.6	8.7	458.7	85.2	457.3	6.1
CSES1000a ii	459.8	7.7	458.7	86.6	457.3	5.7
CSES1000b i	459.6	8.4	458.7	84.7	457.3	6.9
CSES1000b ii	459.6	7.7	458.6	86.0	457.2	6.3
CSIS800 ai	460.0	3.8	458.5	90.4	457.1	5.7
CSIS800 a ii	459.5	6.9	458.6	88.8	457.2	4.3
CSIS 800a iii	460.1	5.1	458.6	89.3	457.2	5.6
CSIS 800a iv	460.0	5.4	458.5	89.8	457.1	4.8
CSIS800 b i	460.1	4.1	458.7	89.5	457.3	6.4
CSIS800 b ii	459.9	6.4	458.9	88.1	457.5	5.4
CSIS1000a i	459.7	7.8	458.6	86.3	457.2	5.9
CSIS1000a ii	459.6	8.6	458.6	85.8	457.2	5.6
NCSIS800a i	460.3	6.6	458.9	87.4	457.5	6.0
NCSIS800a ii	459.6	7.0	458.5	85.7	457.1	7.4
SSI350 i	459.4	8.5	458.5	83.6	457.1	7.9
SSI350 ii	459.6	5.0	458.4	87.5	457.0	7.5

Table A5. Results of curve fitting the O 1s high resolution spectra

Sample	B.E. (eV)	%At Conc	B.E. (eV)	%At Conc	B.E. (eV)	%At Conc	B.E. (eV)	%At Conc
Baseline i	530.0	75.2	531.2	11.2	532.1	9.8	533.2	3.9
Baseline ii	529.9	74.4	530.9	10.4	531.8	10.8	532.9	4.4
CSES800a i	529.9	73.2	530.9	11.7	531.9	10.8	533.0	4.3
CSES800a ii	529.7	72.9	530.7	12.0	531.7	10.8	532.7	4.4
CSES800b i	529.9	72.3	530.8	12.7	531.8	10.7	533.0	4.3
CSES800b ii	529.9	74.2	530.8	11.8	531.7	9.8	532.8	4.3
CSES1000a i	530.0	65.7	531.1	15.9	532.1	12.6	533.2	5.8
CSES1000a ii	529.9	65.1	531.0	15.5	532.0	13.1	533.0	6.3
CSES1000b i	530.0	68.9	531.0	14.6	532.0	11.1	533.1	5.5
CSES1000b ii	529.8	70.2	530.7	14.4	531.7	10.4	532.8	5.0
CSIS800 ai	529.9	60.2	531.2	18.0	532.1	15.0	533.3	6.8
CSIS800 a ii	530.0	61.4	531.3	16.3	532.1	14.7	533.3	7.6
CSIS 800a iii	530.0	62.7	531.2	16.1	532.2	15.2	533.3	6.0
CSIS 800a iv	529.9	63.7	531.1	15.1	532.1	15.2	533.2	5.9
CSIS800 b i	530.1	65.0	531.3	16.4	532.2	13.1	533.4	5.5
CSIS800 b ii	530.2	65.0	531.3	15.9	532.2	13.2	533.5	5.9
CSIS1000a i	529.9	60.6	531.1	17.2	532.0	15.8	533.1	6.5
CSIS1000a ii	529.9	61.8	531.0	16.7	532.0	15.3	533.0	6.2
NCSIS800a i	530.5	85.8			532.2	10.0	533.4	4.2
NCSIS800a ii	530.3	86.5			532.1	9.6	533.3	3.9
SSI350 i	529.8	59.3	531.1	17.3	531.9	17.7	533.1	5.6

SSI350 ii	529.7	54.9	531.0	17.6	531.8	21.9	533.0	5.6

O 1s
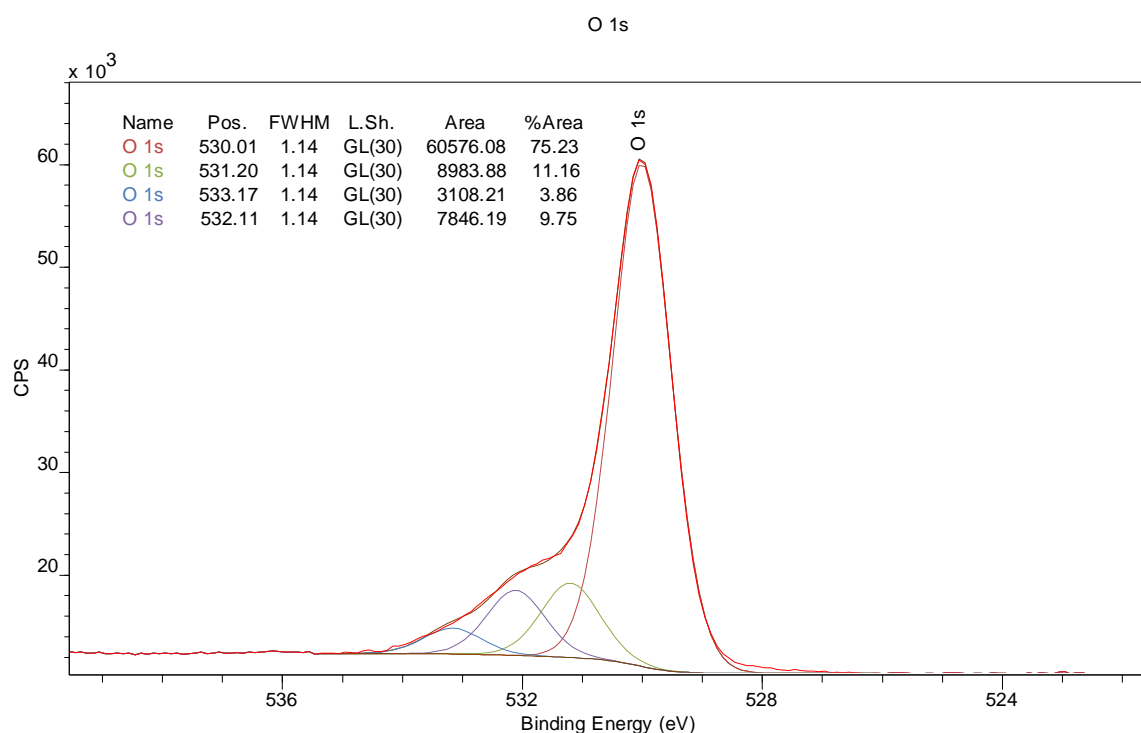
Figure A4. Example fitted O 1s spectrum from baseline sample, area i

Table A6. Results of curve fitting the Cl 2p high resolution spectra

	Metal Chloride							
	Cl 2p$^{3/2}$		Cl 2p$^{1/2}$		La 4p$^{3/2}$		La 4p$^{1/2}$	
Sample	B.E. (eV)	%At Conc	B.E. (eV)	%At Conc	B.E. (eV)	%At Conc	B.E. (eV)	%At Conc
Baseline i	198.4	42.1	200.0	21.1	195.6	24.6	196.6	12.3
CSES800a i	198.3	35.1	199.9	17.5	195.5	31.6	196.5	15.8
CSES800b i	198.3	34.5	199.9	17.3	195.5	32.1	196.5	16.1
CSES1000a i	198.3	32.6	199.9	16.3	195.5	34.0	196.5	17.0
CSES1000b i	198.3	32.8	199.9	16.4	195.6	33.9	196.6	16.9
CSIS800 ai	198.6	59.6	200.2	29.8	195.8	7.1	196.8	3.6
CSIS 800a iii	198.8	60.3	200.4	30.1	195.8	6.4	197.4	3.2

CSIS 800a iv	198.8	61.2	200.4	30.6	195.9	5.5	197.5	2.7
CSIS800 b i	198.5	56.0	200.1	28.0	195.7	10.7	196.7	5.3
CSIS1000a i	198.4	37.2	200.0	18.6	195.6	29.5	196.6	14.8
NCSIS800a i	198.3	41.0	199.9	20.5	195.5	25.7	196.5	12.8
SSI350 i	198.3	33.2	199.9	16.6	195.4	33.5	196.4	16.7
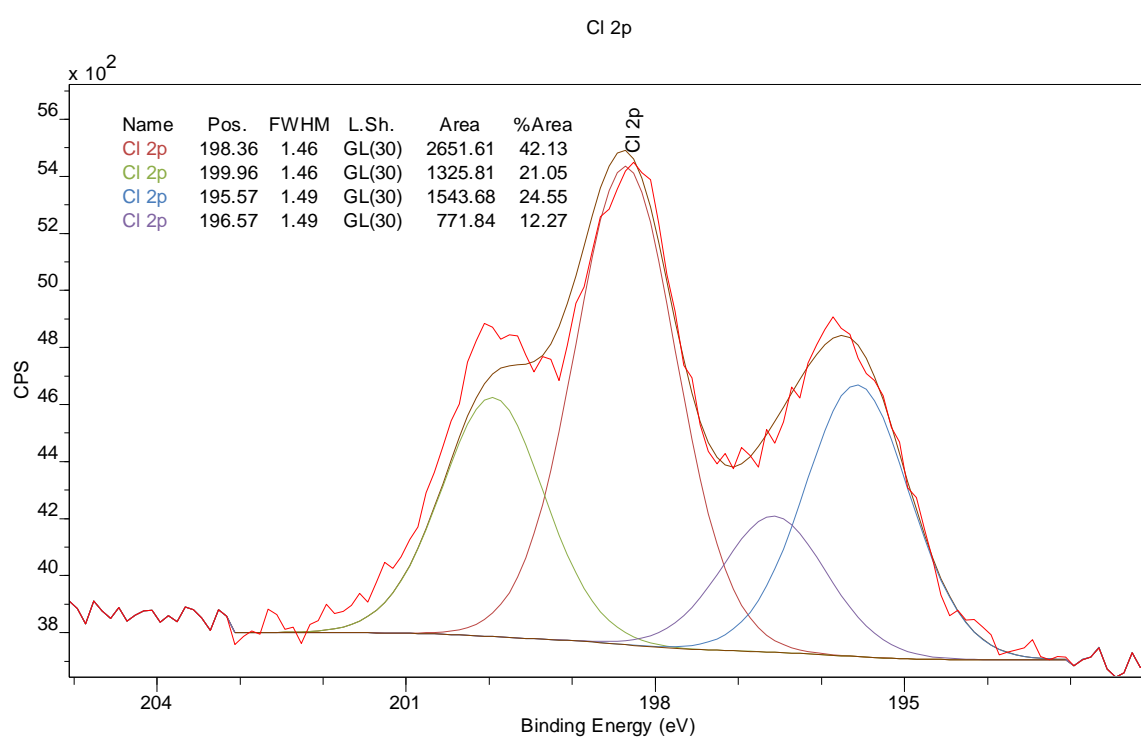
Figure A5. Example fitted Cl 2p spectrum from baseline sample, area i

Dr Debbie Hammond
Experimental Officer
Sheffield Surface Analysis Centre
Sheffield University

Interpretations of the data are given in good faith, but no liability is assumed for actions taken as a consequence of these interpretations.

Sheffield Surface Analysis Centre

surfaceanalysis.group.shef.ac.uk

Customer: Stephanie Mudd

Date: 17th August 2023

Analysis: XPS

XPS Analysis of (La,Sr)TiO$_3$ Powders and Pellets (SSAC719n2)

Introduction

A request was made to look again at the curve fitting of the Ti 2p high resolution spectra for the powder samples. Experimental detail as to how the data was collected has already been described in a previous memo (SSAC719n1)

Experimental

The submitted samples were as described in the table below.

Samples
Solid state powder
Cheap IL powder
Expensive IL powder
Solid state pellet
Cheap IL pellet
Expensive IL pellet

It was reported previously that the powder samples showed little intensity below the main Ti(IV) contribution, whilst the pellets showed some suggesting some contribution from lower oxidation states. Consequently, the Ti 2p high-resolution spectra from only the pellets were curve fitted and the results given in the previous memo. In summary, for the pellets whilst the majority of the titanium was present as Ti(IV) a small Ti(III) component was suggested, and also a very small Ti(0) component.

It has been attempted to curve fit the high-resolution Ti 2p spectra for the powder samples.

In order to do this, the fitting constraints used previously were revisited and small changes have been made, in particular to the fixed energy separation between the Ti 2p3/2 and Ti 2p1/2 peaks, to 5.7 eV for Ti (IV) and 5.2 eV for Ti(III). This is in line with the Biesinger paper and it was an error that for the previous memo 5.6 eV was used for Ti(III) and 5.2 eV was used for the proposed second pair of Ti(IV) peaks at higher energy in order to fit the spectral envelope. Unfortunately, these relatively small changes have made a more substantial change to the suggested %contribution of Ti(III) to the pellet samples, particularly the solid state and expensive IL pellets. The new values are given in Table 1 and the previous values given in Table 2.

What this does demonstrate is how sensitive the absolute values given are to the curve fitting parameters used. The trends in the data for the pellets have not changed. The data also suggests that whilst the Ti(III) contribution for the cheap IL are very similar for both powder and pellets, the contribution for the solid state and expensive IL powders are about half that of their respective pellets. Indeed, the %Ti(III) contribution from all the powders are very similar, as demonstrated in memo SSAC719n1 by the similarity of the spectra shown in Figure 4.

Table 1. % of titanium components determined by curve fitting

Sample	Ti(IV)	Ti2p (III)	Ti2p (metal)
Solid state powder a	93.6	6.5	
Solid state powder b	92.8	7.3	
Cheap IL powder a	92.7	7.3	
Cheap IL powder b	92.7	7.3	
Expensive IL powder a	93.2	6.8	
Expensive IL powder b	93.2	6.8	
Solid state pellet a	84.7	14.6	0.7
Solid state pellet b	84.9	14.4	0.7
Cheap IL pellet a	91.1	8.8	0.1

Cheap IL pellet b	92.8	7.2	0.0
Expensive IL pellet a	83.9	13.5	2.5
Expensive IL pellet b	84.7	12.3	3.1

Table 2. Previously reported results (SSAC791n1) % of titanium components

Sample	Ti(IV)	Ti(III)	Ti(0)
Solid state pellet a	89.5	9.1	1.4
Solid state pellet b	89.4	9.5	1.1
Cheap IL pellet a	92.9	7.1	0.0
Cheap IL pellet b	94.9	5.1	0.0
Expensive IL pellet a	88.1	8.0	3.9
Expensive IL pellet b	88.6	7.5	3.9
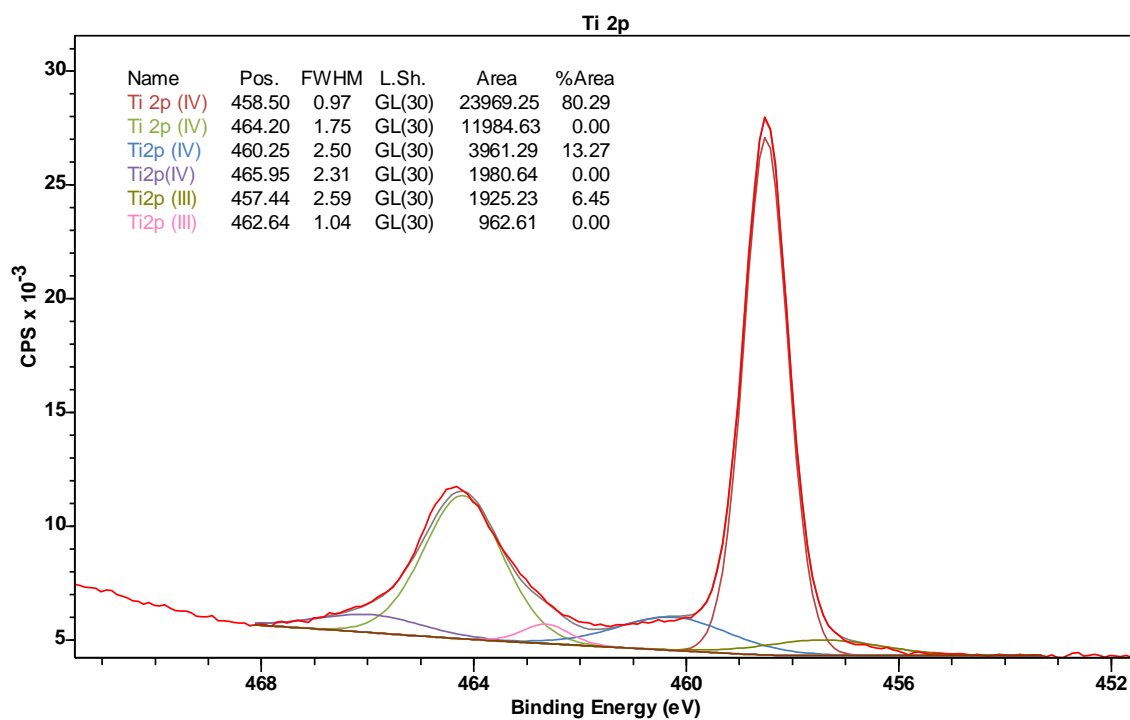
Figure 1. Curve fitted high resolution Ti 2p XPS spectrum for solid state powder.
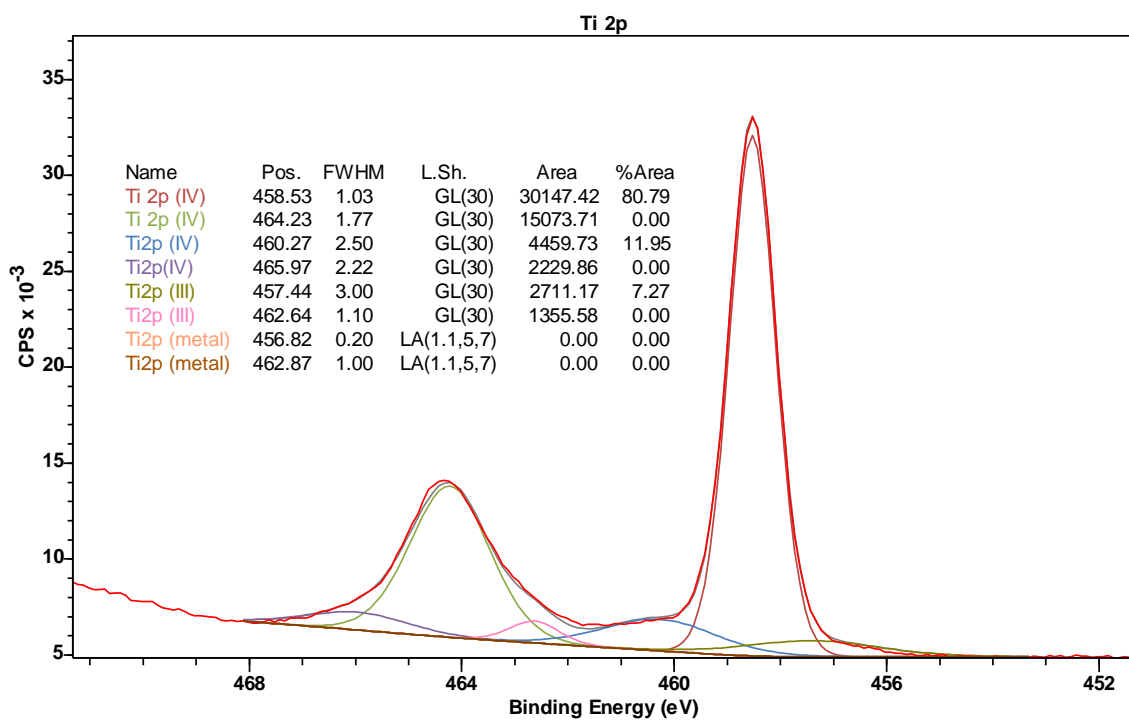
Figure 2. Curve fitted high resolution Ti 2p XPS spectrum for cheap IL powder.
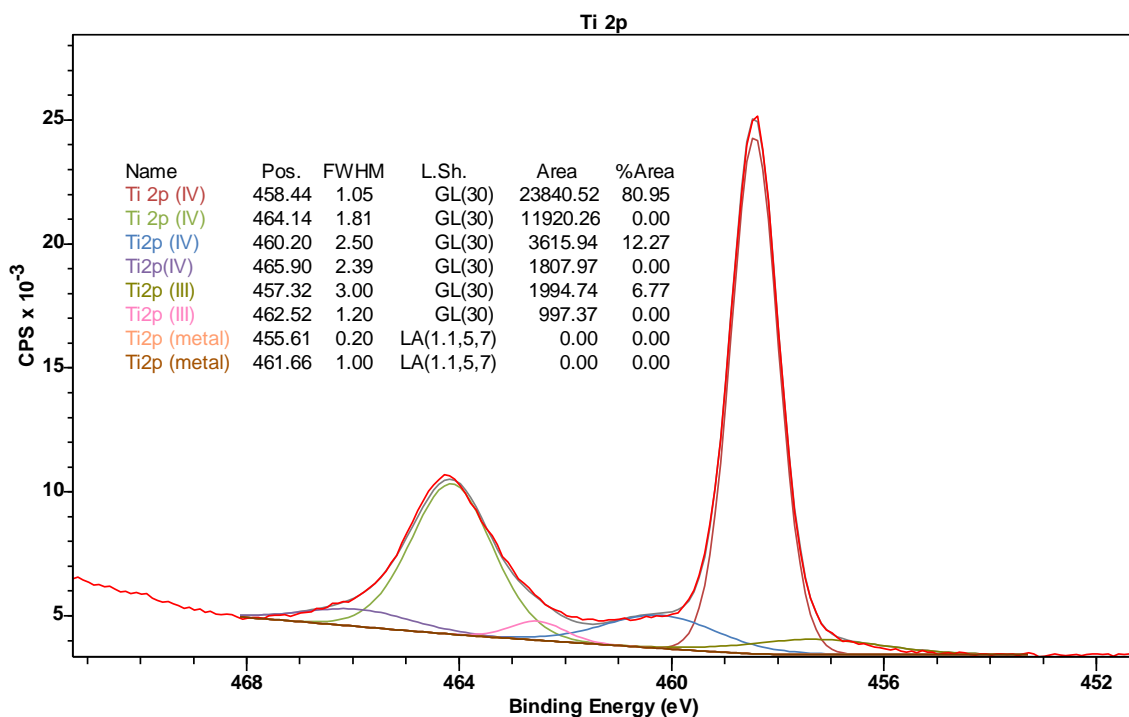
Figure 3. Curve fitted high resolution Ti 2p XPS spectrum for expensive IL powder.
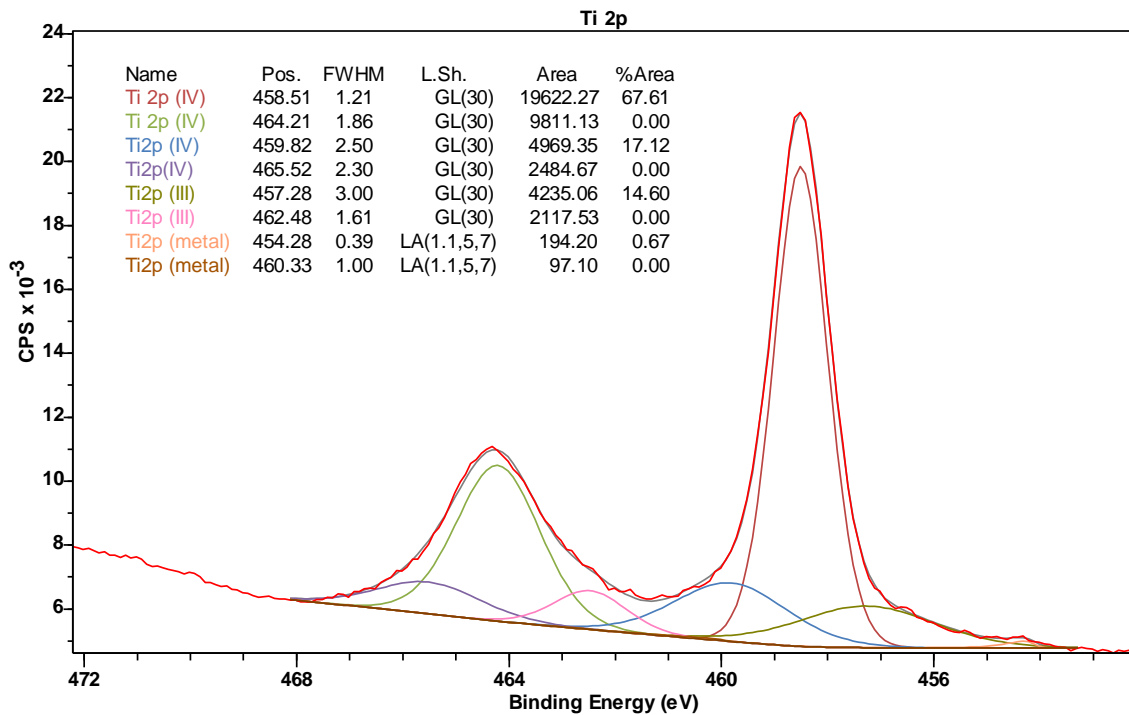
Figure 4. Curve fitted high resolution Ti 2p XPS spectrum for solid state pellet.
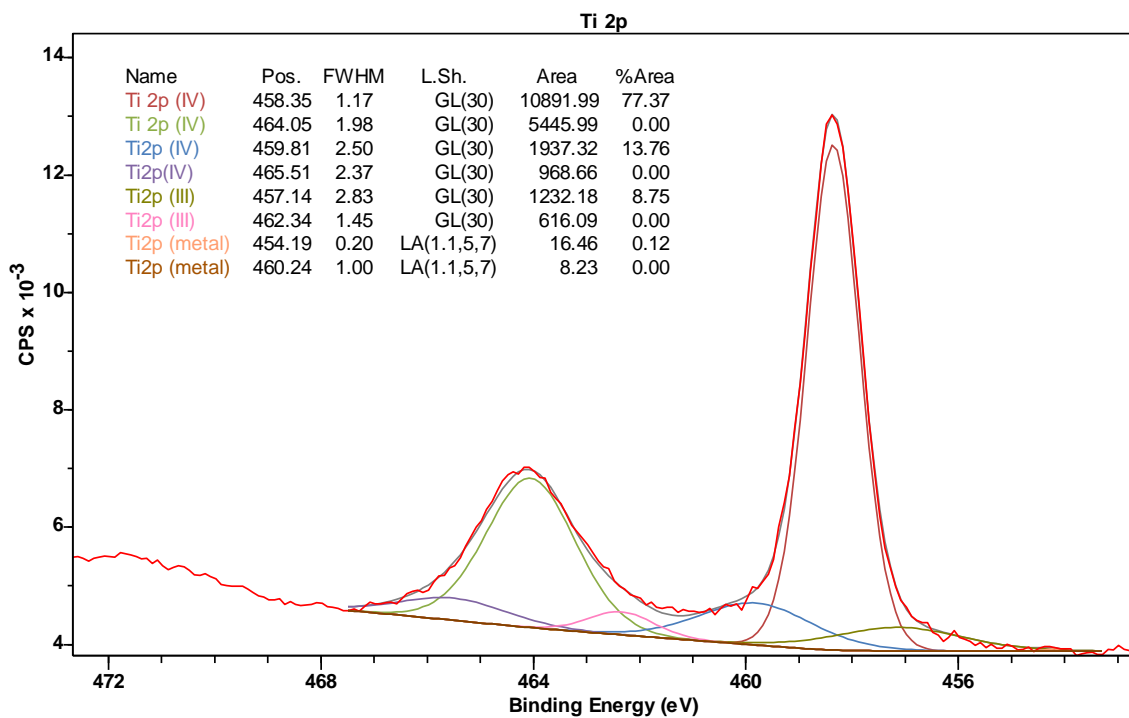
Figure 5. Curve fitted high resolution Ti 2p XPS spectrum for cheap IL pellet.
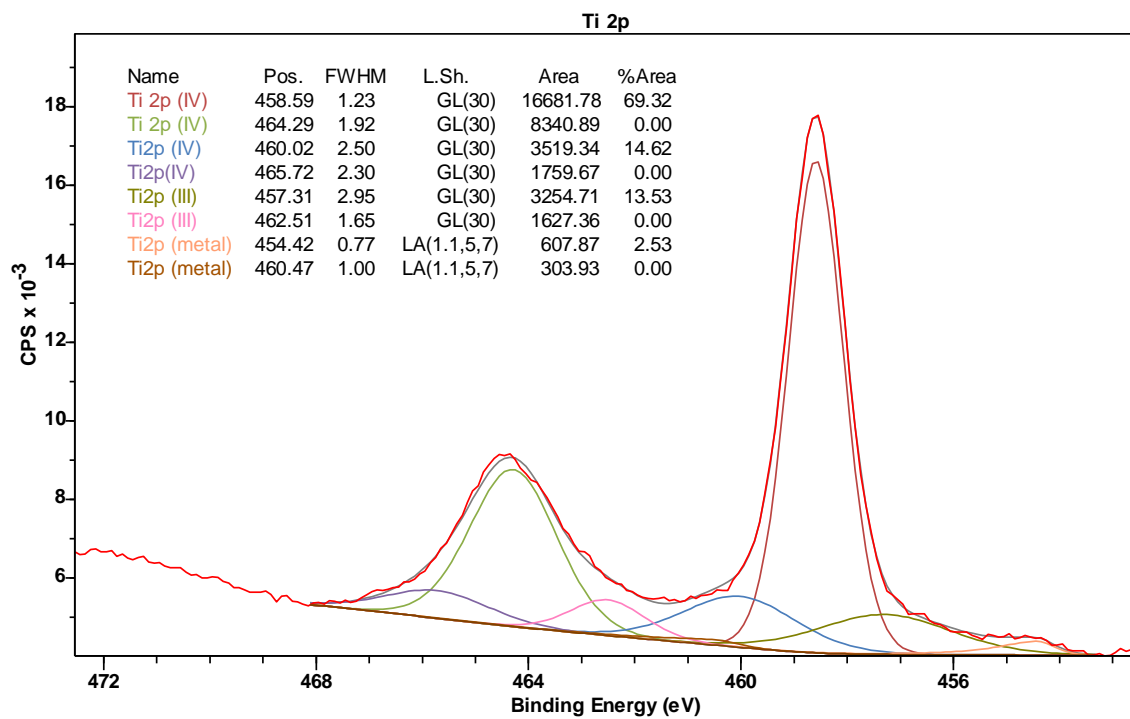
Figure 6. Curve fitted high resolution Ti 2p XPS spectrum for expensive IL pellet.

Conclusions

- The absolute values of %contribution of Ti(III) and Ti(0) to the high resolution spectra have been shown to be very sensitive to the fitting constraints used.
- The trends within the data are less sensitive, and consequently likely to be more reliable.
- The %Ti(III) within the powder samples appear to be similar for all powders , and approximately half that of the pellet samples for the solid state IL and expensive IL.
- The cheaper IL has a similar %Ti(III) contribution in both powder and pellet form.

Dr Debbie Hammond

Experimental Officer

Sheffield Surface Analysis Centre

Sheffield University

Interpretations of the data are given in good faith, but no liability is assumed for actions taken as a consequence of these interpretations.